X-Ray spectroscopie characterization of hot and dense plasmas created by intense lasers.

Nikolaos Kontogiannopoulos

To cite this version:

Nikolaos Kontogiannopoulos. X-Ray spectroscopie characterization of hot and dense plasmas created by intense lasers.. Physics [physics]. Ecole Polytechnique X, 2007. English. NNT : . pastel-00003578

HAL Id: pastel-00003578
https://pastel.hal.science/pastel-00003578

Submitted on 27 Jul 2010

THESIS

presented at École Polytechnique

to obtain the degree of

DOCTOR OF ECOLE POLYTECHNIQUE

specialization : physics

by

Nikolaos Kontogiannopoulos

Title of the thesis :

X-ray spectroscopic characterization of laser–produced hot dense plasmas

defended publicly in 6 December 2007 in front of the jury composed of :

Jean–Claude Gauthier	*President*
Anne Sylvie Gary	*Referee*
Jean–Francois Wyart	*Referee*
Patrick Audebert	
Victor Malka	
Claude Chenais–Popovics	*Invited*
Michel Poirier	*Research Director*

Acknowledgements

This thesis was realized in the laboratory LULI ("Laboratoire pour l'Utilisation des Lasers Intenses") of Ecole Polytechnique between 2004 and 2007. I would like to thank Francois Amiranoff director of laboratory for providing all the technical and material support and resources for implementing this work.

I thank all the members of the jury. Especially Anne Sylvie Gary and Jean–Francois Wyart who carried out the demanding work of being referees. Also, Jean–Claude Gauthier, Patrick Audebert and Victor Malka, who accepted to judge this work.

This work had the particular advantage to be accomplished, having as directors Claude Chenais–Popovics and Michel Poirier, which I gratefully thanks for their continuous help in every different problem that I found during my thesis.

My gratitude to the members of research group that I had the pleasure to work with : Serena Bastiani–Ceccoti, Jean–Raphael Marques, and Olivier Peurysse. Special thanks to Thomas Blenski the theoretical work of which was a invaluable support in accomplishing my thesis.

My grateful thanks to Frederic Thais. Apart from physics, its humor and its positive view gave to me a real reference to continue over the difficulties that I found during this work.

I would also like to thanks all the PhD students, researchers and technicians for making this laboratory a pleasant place to work in.

My special thanks to the PhD students Livia Lancia and Ana Mancic for the constructive discussions and fruitful collaboration that we had.

N. Kontogiannopoulos
Paris 2007

Contents

Introduction

In the beginning of the last century, the advent of quantum mechanics set the theoretical background in understanding the physical processes in atomic structure, chemical bonds, solid–state physics, particle physics and cosmology. It also noticeably opened the way to the investigation of a new state of the matter, the *plasma*, which is supposed to constitute a very large part of the universe. An accurate description of plasmas is, for instance, necessary to apprehend the mechanisms of the energy production inside the stars. Another qualitative revolution of this field occurred during the fifties. The development of the space technology made available extraterrestrial observatories, providing an enormous quantity of data and also the ground for new theoretical researches. In parallel, the digital computers gave for the first time a powerful tool to elaborate intricate theoretical models, opening new paths in the interpretation of the advanced astrophysical observations [1]. During the last three decades, the development of the laser technology has restated again the research in astrophysics. The power lasers gave the ability to reproduce in the laboratory the conditions found in the interior of the stars, providing a great progress in the evolution of plasma physics [2–4].

From the first steps in the parallel development of quantum mechanics and astrophysics, the understanding of the nuclear fusion as the energy production mechanism in the stellar interior has set the question of the ability to apply this physical process to produce energy in a terrestrial scale. Following the nature of the stars, it was made clear that the basic problem in such an adventure is the confinement of the high energetic plasmas providing the fusion reactions, and around this problem a new research field of the plasma physics was generated. Historically, the first scheme that appeared as an answer to the confinement problem was the Magnetic Confinement Fusion. The other scheme which appeared in parallel with the development of the power lasers is the Inertial Confinement Fusion (ICF) [5]. In ICF no external means of confinement is involved. Here, the confinement exclusively relies on the inertia of the mass. Briefly, in this scheme, power laser beams of very short pulse duration interact with the fusion target, heating it and producing a very fast expanding ablated plasma layer. Due to the conservation of the inertia the rest of the target is strongly compressed, and this implosion produces a very hot plasma with proper conditions to ignite a fusion reaction.

In the general context of the laser produced plasmas, a research field of particular importance is plasma spectroscopy, which is related to the study of the plasma atomic physics, and in particular to the interpretation of the plasma emission and absorption spectra. Plasma spectroscopy includes both the theoretical research to model the complicated physics involved in the determination of the emission and absorption properties of the plasma, as well as the experimental techniques used to check these sophisticated models. Its very importance consists in describing plasmas under conditions where the decisive phenomenon is the transfer of radiation through the plasma. Situations like this are encountered in both astrophysics in modeling the stellar atmospheres, and in ICF especially in the so–called indirect drive scheme. On the other hand the spectrum analysis provides very accurate informations about the state of the plasma (ionization state, density and temperature), and thus, spectroscopy is in general a very powerful diagnostic tool of plasma physics. During the last years, the use of plasmas to produce XUV sources [6] opened a new field of technological interest for plasma spectroscopy, as the extreme ultraviolet lithography (EUVL), which concerns the development of new generation microelectronics.

Model of stellar atmospheres

The laboratory–scale astrophysical plasmas produced by power lasers provide improved possibilities for developing our understanding of the stellar physics. Thus, in past years, an important effort has been done to study theoretically and experimentally the plasmas emissivity and opacity under conditions similar with those found in the stellar atmospheres [2–4].

In this context, the opacities of medium–Z elements have a particular importance, even if their abundance is low versus hydrogen and helium, because they rule the radiation energy transfer in stellar interiors [1]. This stems from the spectral characteristics of the radiation in the interior of the stars, in conjunction with the properties of the plasmas of medium–Z elements. In particular, assuming a Planckian radiation, and for the typical temperatures achieved in the stellar interior, it follows that the radiation maximum appears in the spectral range between 50 and 1000 eV (XUV range), where the medium–Z elements show a very rich absorption spectrum [7].

In the inner layers of stellar atmospheres the statistic of local thermodynamic equilibrium (LTE) can describe accurately the different interactions occurring between the plasma and the radiation [1], and the models of LTE plasmas opacities are very important. However, extended regions of the atmospheres are ruled by non local thermodynamic equilibrium statistics (NLTE), and the development of accurate atomic physics models for describing the dynamic behavior of such plasmas is also crucial in understanding the behavior of the stars.

Indirect scheme of Inertial Confinement Fusion

Mainly two different schemes are used to generate the energy flux and the pressure required to drive an Inertial Confinement Fusion (ICF) with lasers, as shown in Figure I.1 [5]. In the direct drive approach, a number of laser beams heats directly the fusion capsule (Fig. I.1(a)). The beam energy is absorbed by electrons in the outer low density corona. Then the electrons transport the energy to the inner material to drive the ablation and the resulting implosion. The problem with this scheme stems from the limitations in irradiating symmetrically and uniformly the capsule : hydrodynamic instabilities as the Rayleigh–Taylor instability (RTI) develop and impair the regular implosion and ignition of the target.

To overcome these difficulties the indirect ICF method was introduced, which is based on the hohlraum target shown in Fig. I.1(b). The hohlraum is an empty cavity composed of a high–Z material as gold, with a cylindrical symmetry along the horizontal axis, in the interior of which is placed the fusion capsule. In the indirect scheme, the laser beams heat the inner wall of the cavity, and the produced plasma converts the laser energy into an intense x–ray radiation field. The x–ray radiation then drives the heating of the fusion capsule. The conversion of the laser light takes place in an optically thin high temperature layer formed on the surface of the inner wall. The temperature of the hohlraum is determined by the radiation heat wave propagating through the optically thick plasma layer in its interior, and which is builded by the diffusion of the x–rays. The thermal properties of this optically thick layer rule also the confinement of the radiation field in the cavity empty space, which after multiple absorption and re–emission processes tends to become uniform.

The main advantage of the hohlraum targets is the symmetrical irradiation of the capsule by the x–ray field, which improves the implosion drive with respect to the electrons drive of the direct scheme, especially as concerns RTI [8,9]. However, the price one has to pay consists in the loss of energy (coupling efficiency), as a large fraction of the incident laser energy is used to thermalize the hohlraum. The crucial parameter for both the advanced coupling efficiency and irradiation symmetry is the opacity of the material composing the hohlraum, which determines the conversion of the laser beam energy and the radiation confinement.

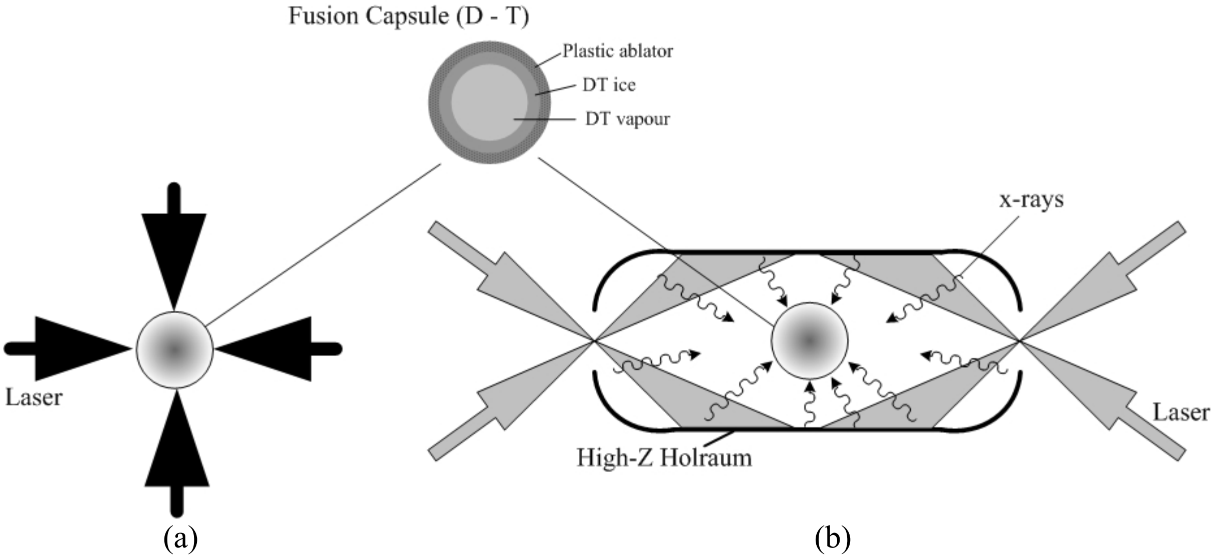

Figure I.1 Different schemes of the D–T capsule drive (a) Direct drive scheme, (b) Indirect drive scheme with the *hohlraum* configuration.

The study of the opacities has been introduced also in the context of the indirect ICF with the sophisticated fusion capsules that have been proposed. The x–ray radiative drive depends strongly on the spectral opacity of the ablator material, and optimized ablator mixtures of plastics with higher–Z materials as copper (Cu) prove to give improved implosion efficiencies [5].

Purposes of the present work

The theoretical research for the description of the absorption and emission spectrum of medium and high–Z elements plasmas has led to the development of atomic physics codes simulating different plasma statistics. Their common characteristic is the description of the atomic structures with the superconfiguration formalism, which provides the ability to calculate in a reasonable computation time the very complicated emission and absorption spectra of these plasmas. Two such codes employed in our experiments are the NLTE code TRANSPEC/AVERROES developed by O. Peyrusse [10,11], and the LTE code SCO developed by T. Blenski *et al.* [12–14].

The first part of our work is aimed at the study of the emissive properties of low–density plasmas of rare gases, which can be used to benchmark the TRANSPEC/AVERROES code. The code gives the ability to simulate the emission spectrum of multicharged ions of medium and high–Z elements plasmas. In our experimental work we measured the x–ray emission spectra of laser irradiated xenon and krypton gas, characterizing independently the heating conditions (density, temperature) of the produced NLTE plasmas with the Thomson scattering technique. The present experiment was focused in analyzing with TRANSPEC/AVERROES the time–resolved emission spectrum of the plasmas in the XUV range. Previous time–resolved measurements of the xenon plasma performed by our research group showed that in the keV range the emission spectrum does not change with time [15]. In the XUV spectral range, however, we expect the emission spectrum to be more sensitive to the variations of the plasma density and temperature, and thus, to measure time variable emission spectra. A main motivation of our work is exactly to follow these variations with TRANSPEC/AVERROES, providing to the code well characterized experimental data in a spectral range of particular theoretical interest.

The second part of the present work concerns the characterization of the opacities in the XUV spectral range of medium–Z elements plasmas mixtures. We performed an experiment with thin solid foils of zinc sulfide irradiated by the intense x–ray field confined in the interior of a spherical gold cavity. The experimental data were analyzed with the code SCO, which statistical nature is appropriate to describe medium–Z elements mixtures, that may exhibit very complex structures difficult to unravel with fully detailed atomic codes. The zinc sulfide was chosen due to the homogeneous plasma mixture provided by a chemical compound, and because its components show discrete non–overlapping absorption features in the experimental spectral range. The plasma heating conditions were characterized independently by measuring the XUV absorption of x–ray irradiated aluminium foils, which can be accurately analyzed with the detailed atomic code HULLAC [16].

Structure of the thesis

The first two chapters give an outline of the theory involved in the study of the emission and absorption plasma spectroscopy. Chapter 1 describes the different atomic processes occurring in a plasma. The LTE and the NLTE statistics ruling the equilibrium of the atomic processes are presented. Then, we give a brief description of the different codes of plasma atomic physics used in the analysis of our experimental data, namely HULLAC, SCO and TRANSPEC/AVERROES. In Chapter 2 the macroscopic theory of the radiation transport through a plasma is given. We describe also the self–similar model of Basko and the view factor approach, which permit us to calculate the heating conditions of the absorption foils achieved in the interior of the spherical gold cavity.

Chapter 3 gives a description of the instruments used for realizing the two experiments, as well as the technical characteristics of the LULI2000 laser facility used to perform the experiments. Chapter 4 presents the experiment realized to characterize the emission spectra of the xenon and krypton plasmas in NLTE, as well the analysis of the experimental data with TRANSPEC/AVERROES. Finally, the experiment for measuring the absorption spectrum of the ZnS plasma mixture and the analysis of the experimental data with the code SCO are given in Chapter 5.

References of Introduction

[1] D. Mihalas, Stellar atmospheres, W. H. Freeman and Company (1978).

[2] L. B. Da Silva *et al.*, Absorption Measurements Demonstrating the Importance of $\Delta n = 0$ Transitions in the Opacity of Iron, Phys. Rev. Lett **69**, 438 (1992).

[3] F. J. Rogers and C. A. Iglesias, Science **263**, 50 (1994).

[4] C. Chenais–Popovics *et al.*, Astrophys. J., Suppl. Ser. **127**, 275 (2000).

[5] S. Atzeni, J. Meyer-Ter-Vehn, The Physics of Inertial Fusion, Beam plasma interaction, Hydrodynamics, Hot dense matter, pp. 302 – 303, Oxford Science Publications, 2004.

[6] S. Fujioka *et al.*, Opacity effect on Extreme Ultraviolet Radiation from Laser–Produced Tin Plasmas, Phys. Rev. Letters **95**, 2350041 (2005).

[7] C. Chenais–Popovics, Astrophysics in laboratory : Opacity measurements, Laser Part. Beams **20**, 291 (2002).

[8] J. D. Lindl, Development of the indirect–drive approach to inertial confinement fusion and the target physics basis for ignition and gain, Phys. Plasmas **2**, 3933 (1995).

[9] J. D. Lindl *et al.*, The physics basis for ignition using indirect–drive targets on the National Ignition Facility, Phys. Plasmas **11**, 339 (2004).

[10] O. Peyrusse, A superconfiguration model for broadband spectroscopy of non–LTE plasmas, J. Phys. B : At. Mol. Opt. Phys. **33**, 4303 (2000).

[11] O. Peyrusse, A model for the simulation of nonequilibrium line transfer in laboratory plasmas, Phys. Fluids B **4**, 2007 (1992).

[12] T. Blenski, A. Grimaldi and F. Perrot, Hartree–Fock statistical approach to atoms and photoabsorption in plasmas, Phys. Rev. E **55**, R4889 (1997).

[13] T. Blenski, A. Grimaldi and F. Perrot, A superconfiguration code based on the local density approximation, J. Quant. Spec. Radiat. Transfer **65**, 91 (2000).

[14] J. C. Pain and T. Blenski, Self-consistent approach for the thermodynamics of ions intense plasmas in the superconfiguration approximation, J. Quant. Spec. Radiat. Transfer **81**, 355 (2003).

[15] C. Chenais–Popovics *et al.*, X-ray emission of a xenon gas jet plasma diagnosed with Thomson scattering, Phys. Rev. E **65**, 0464181 (2002).

[16] A. Bar–Shalom *et al.*, HULLAC, an integrated computer package for atomic processes in plasmas, J. Quant. Spec. Radiat. Transfer **71**, 169 (2001).

Chapter 1 Elements of plasma atomic physics

1.1 Introduction

This chapter presents some basic elements of the atomic physics involved in the study of laser produced laboratory plasmas. First, the description of the different atomic processes taking place in a hot–dense plasma is given. Then, we discuss the different thermodynamic regimes ruling the plasmas state. Two situations may be involved in our experiments: the local thermodynamic equilibrium (LTE) and the non–local thermodynamic equilibrium (NLTE), where one uses collisional radiative equations to describe the populations kinetics. Sophisticated theoretical models are implemented as post–processors of plasma atomic physics codes, in order to obtain the plasmas emission and absorption spectra. The unresolved transition arrays and the super–transition–arrays formalisms may be used extensively in the codes calculating the synthetic spectra of medium and high–Z elements plasmas, and an outline of these powerful approaches is given. After an enumeration of the elementary radiative and collisional processes involved in the plasma, we describe briefly the different atomic codes used in the analysis of the experimental data, as well as the post–processors accounting for the statistical and radiative properties of such plasmas.

1.2 Plasma atomic processes

The plasma components, namely the ions, electrons, and photons, interact through electromagnetic fields, transferring energy from one particle to the other, and thereby changing their states. To determine the macroscopic behavior of the plasma, a classification of the different interactions is necessary. In plasma spectroscopy the processes of the greatest interest are those in which an ion interact with an electron and/or a photon, and which result in changing the excitation or ionization state of the ion. The ion–ion interactions (collisions, formation of molecular states), usually less probable than electron–ion and photon–ion interactions, are not considered here. We may classify these processes according to the variation (bound–free) or not (bound–bound) of the ionization state of the ion, as shown in Table 1–I.

The atomic processes can be also classified with respect to the participation (radiative) or not (collisional) of a photon in the interaction, and the emission and absorption spectra originate directly from such radiative processes. The spectra are composed of a discrete and a continuous part. The former results from the bound–bound radiative processes. In the formation of the latter contribute the bound–free and the free–free transitions of the electrons (not given in the table). Though the free–free transitions are not important for the plasmas conditions relevant to our work, they are described briefly at the end of this section.

bound–bound		bound–free	
direct process	inverse process	direct process	inverse process
photoabsorption	spontaneous decay (+ stimulated emission)	photoionization	radiative recombination (spontaneous + stimulated)
e-impact excitation	e-impact de–excitation	e-impact ionization	three body recombination
-	-	autoionization	dielectronic recombination

Table 1 – I Classification of the different atomic processes changing the state of the plasma ions.

The quantity that describes the contribution of a given process to the variation of the plasma state is its transition rate giving the number of reactions per unit time. When a target and a projectile is involved, this rate can be computed from the cross section of the elementary process and the statistical distribution of the projectiles (electrons or photons). The radiative rates and the collisional cross–sections are calculated from the basic equations of quantum mechanics.

1.2.1 Detailed balance principle

As seen in Table 1–I, every atomic process occurring within a plasma has its inverse, and a remarkable property is that the rate expressions of the two processes are correlated in a very simple way via the detailed balance principle [1–3]. In its elementary form, the detailed balance principle requires that the rate of any process at a given electron (and/or photon) energy is equal to the rate of the inverse process for the corresponding velocity class (when an electron is involved) and/or frequency interval (for a photon). In its integrated form, the detailed balance principle states that the rates of the processes

$$A_i^{+\zeta} + p_1 + \ldots \Leftrightarrow A_j^{+\zeta'} + p_2 + \ldots \tag{1.1}$$

are such that

$$R_{ij} N_i N_1 \ldots = R'_{ji} N_j N_2 \ldots \tag{1.2}$$

where R_{ij} (resp R'_{ji}) is the rate coefficient for the direct (resp. inverse) process, and N_i is, for instance, the density of ions in the state *i assuming local thermodynamic equilibrium*. Examples of application of the detailed balance can be found in [1–3]. The detailed balance principle greatly simplifies the calculations of the transition rate coefficients, since once the rate coefficient of an atomic process is known, the inverse coefficient can be found directly from Eq. (1.2) if the electrons (or the photons) are at thermal equilibrium, without any hypothesis on the LTE or NLTE status of the ionic level populations.

1.2.2 Bound–bound processes

Spontaneous decay and resonant photoabsorption

In the spontaneous decay one observes the transition from a discrete excited ionic state *j* to a lower ionic state *i*, with simultaneous emission of a photon. In the presence of an external electromagnetic field, *stimulated emission* also contributes to the $j \to i$ transition. The inverse process is the resonant photoabsorption. The emission and absorption of photons between bound states of an ion of charge ζ reads

$$A_i^{+\zeta} + \hbar\omega \Leftrightarrow A_j^{+\zeta} \tag{1.3}$$

The coefficients for spontaneous emission A_{ji}, photoabsorption B_{ij}, and stimulated emission B_{ji}, obey the well-known Einstein relations [3]. It is interesting to note that stimulated emission was discovered by Einstein in 1916 precisely by applying the detailed balance principle to a two-level atom in thermal equilibrium with radiation.

Electron impact excitation and de–excitation

In the process of electron impact excitation a collision between an electron and an ion of charge ζ takes place, inducing the excitation of a bound electron from a low energy state i to a high energy j, while the free electron loses the energy $\Delta E_{ji} = E_j - E_i$. The impact de–excitation is the inverse process. Both processes affect only the excitation state of the ion, and not its ionization degree. This collisional process can be schematized as

$$A_i^{+\zeta} + e \Leftrightarrow A_j^{+\zeta} + e \tag{1. 4}$$

To illustrate the detailed balance in a simple case, if we denote their rate coefficients by $E(\zeta, i \rightarrow \zeta, j)$ and $D(\zeta, j \rightarrow \zeta, i)$, respectively, this principle in its integrated form gives

$$\frac{D(\zeta, j \rightarrow \zeta, i)}{E(\zeta, i \rightarrow \zeta, j)} = \frac{g_{\zeta,j}}{g_{\zeta,i}} \exp(-\frac{\Delta E}{k_B T_e}) \tag{1. 5}$$

where $g_{\zeta,i}$, $g_{\zeta,j}$ are the statistical weights of the two bound states, T_e is the temperature of the free electrons, assuming their velocity distribution is Maxwellian, and k_B is the Boltzmann constant .

1.2.3 Bound–free processes

Photoionization and radiative recombination

The process of photoionization is the result of the interaction between a photon and an ion. Here, the photon is absorbed by the ion and a bound electron is transferred into the continuum. The inverse process where a free electron is captured in a bound state of the ion with the simultaneous emission of a photon is called radiative recombination. Stimulated radiative recombination must also be considered in the presence of an external field. These processes are described as

$$A_i^{+\zeta} + \hbar\omega \Leftrightarrow A_j^{+\zeta+1} + e \tag{1.6}$$

and, using detailed balance, their cross–sections are connected by the Einstein–Milne relations [3]

$$\frac{\sigma_{ph}(\zeta, i \rightarrow \zeta+1, j; \hbar\omega)}{\sigma_{rr}(\zeta+1, j \rightarrow \zeta, i; E_e)} = \frac{2mc^2 E_e}{(\hbar\omega)^2} \frac{g_j}{g_i} \tag{1.7}$$

where σ_{ph} and σ_{rr} are, respectively, the cross sections of photoionization and radiative recombination, with (ζ, i) we denote the less-charged ion state and with $(\zeta + 1, j)$ the ionized state, and $E_e = \hbar\omega - E_{ji}$ is the free electron energy. Photoionization is an important process mainly in optically thick plasmas, where the mean free path of the photons is shorter than the plasmas dimensions, so that the intensity of the local field induces a sufficiently large rate of photoionization with respect to electron impact ionization rate. In optically thin plasmas photoionization is less important than photoabsorption.

Electron impact ionization and three–body recombination

Electron impact ionization is one of the most important processes in hot plasmas. Here the collision of a free electron with an ion transfers a bound electron in the continuum and the ion charge state increases. The inverse process is the three–body recombination, where two free electrons collide simultaneously with an ion, one of them being captured, while the other takes away the released energy. The three–body recombination requires the presence of two free electrons, and thus this process, proportional to N_e^2, becomes important only at high electron densities . These processes can be written

$$A_i^{+\zeta} + e \Leftrightarrow A_j^{+\zeta+1} + e + e \tag{1.8}$$

Here, we denote the rate coefficients of impact ionization and three–body recombination by $I(\zeta,\ i\rightarrow\zeta+1,\ j;T_e)$ and $R^{(3)}(\zeta+1,\ j\rightarrow\zeta,\ i;T_e)$, respectively. Assuming the free electrons obey a Maxwell distribution, the detailed balance gives

$$\frac{I(\zeta,i\rightarrow\zeta+1,j;T_e)}{R^{(3)}(\zeta+1,j\rightarrow\zeta,i;T_e)} = 2\left(\frac{mc^2k_BT_e}{2\pi(\hbar c)^2}\right)^{3/2}\frac{g(\zeta+1,j)}{g(\zeta,i)}\exp(-\frac{E_{\zeta+1,j}-E_{\zeta,i}}{k_BT_e}) \tag{1.9}$$

Autoionization and dielectronic recombination

In the processes of autoionization and dielectronic recombination doubly excited ion states are involved. A doubly excited ion denoted by $A^{+\zeta}_{n'l',n''l''}$ (n', n'' are the principal and l', l'' the orbital quantum numbers) is characterized by two excited electrons, one in a low energy state $n'l'$ and the other in a high energy state $n''l''$. The doubly excited species can lose an electron through autoionization when an internal electronic interaction process takes place, if the initial ion energy is above the ionization potential. The inverse process is called dielectronic recombination.

The detailed balance principle applied to the reaction

$$A_0^{+(\zeta+1)} + e \Leftrightarrow A^{+\zeta}_{n'l',n''l''} \tag{1.10}$$

is written, in its integrated form, as

$$\frac{R^{*(d)}(\zeta+1\rightarrow\zeta;n'l',n''l'';T_e)}{Au(\zeta;n'l',n''l''\rightarrow\zeta+1)} = \frac{1}{2}\frac{g_{\zeta;n'l',n''l''}}{g_{\zeta+1}}\left(\frac{2\pi(\hbar c)^2}{mc^2k_BT_e}\right)^{3/2}\exp(-E_{n'l',n''l''}/(k_BT_e)) \tag{1.11}$$

where $R^{*(d)}(\ \zeta+1\rightarrow\ \zeta;\ n'l',n''l'';\ T_e)$ and $Au(\zeta;\ n'l',n''l''\rightarrow\ \zeta+1)$ are the dielectronic recombination and autoionization rate coefficients respectively The dielectronic recombination depends strongly on the plasma density. In fact, at high plasma densities the continuum lowering cuts out the highly excited ionic levels, leaving less phase space for the dielectronic recombination. Therefore, this process is mainly significant in relatively low densities plasmas.

1.2.4 Free–free processes (*Bremsstrahlung* radiation)

The bremsstrahlung radiation emission takes place when an electron moving close to an ion is accelerated by the Coulomb field, emitting a photon. In the inverse bremsstrahlung the simultaneous interaction of a free electron with the Coulomb field of an ion and the radiation field induces the absorption of a photon by the free electron. Both these processes are characterized as free–free transitions to recall the initial and the final states of the radiating electrons.

The bremsstrahlung radiation and its inverse process become significant for low–Z plasmas (hydrogen, helium) which are fully ionized and where the free electrons transitions are the main radiation mechanism. In medium and high–Z plasmas at relatively low temperatures (partially charged ions) bremsstrahlung produces a low continuous background, the main radiation mechanisms being the bound–bound and bound–free transitions.

1.3 Plasma statistical physics

1.3.1 Local Thermodynamic Equilibrium

In thermodynamic equilibrium the state of the plasma is specified uniquely by two thermodynamic variables (like the absolute temperature and the density) via the well known equations of statistical mechanics. However, this situation is not valid in astrophysics and laboratory plasmas when electron–ion collisions or photon–ion interactions have a small probability. The problem lies in the deviations from the thermal distribution of the plasma photons. This mainly results from the ability of the photons to escape from the plasma without being reabsorbed; this occurs, for example, in the corona stellar regions (and also in many laboratory plasmas), where the photon mean free path is larger than the plasma dimensions. As a result, in a plasma some particles may obey thermal distributions (possibly ions and much more probably electrons), something that is ensured by their relatively high collisional rates [2].

In this situation the plasma statistics can be described with the model of local thermodynamic equilibrium (LTE). In LTE model we assume that locally the plasma particles are in thermodynamic equilibrium, even though the photons deviate from it, and thus they can be characterized by a temperature and density determining their distributions. LTE is a strictly local theory and does not permit to correlate the conditions of separate plasma regions, let say by radiation exchange, and thus, we should understand that the plasma parameters of temperature and density have a purely local scope [3].

For LTE to be valid, two conditions should be fulfilled [4] : (1) The collisions mean free paths of the particles, and mainly of the electrons, should be smaller than the dimensions of the gradients exhibiting the thermodynamic parameters, and (2) the photons mean free path should not exceed strongly the gradients dimensions. The former ensures that within the volume of the locally characterized plasma a large number of particles collisions take place which tends to thermalize its behavior. The latter means that the photons interacting locally with the particles come from a region with not very different thermodynamic properties. The non local radiation tends to drive the particles distributions away from their equilibrium state, competing the particles collisions. Concerning the global characteristics of the plasma these conditions are equivalently fulfilled when it has a high density, and it is optically thick.

At thermodynamic equilibrium, the populations of the plasma particles are ruled respectively by the Maxwell, Boltzmann, and Saha distributions for the free electrons, the ionic levels and the ionization stages.

Maxwell velocity distribution

The probability at thermodynamic equilibrium that a free electron of mass *m* and temperature T_e has a velocity in the range of (*u*, *u* + *du*) is given by the Maxwell velocity distribution

$$f(u)du = (\frac{m}{2\pi k_B T_e})^{\frac{3}{2}} \exp(-mu^2 / 2k_B T_e) 4\pi u^2 du \tag{1.12}$$

where k_B is the Boltzmann constant. The above relation assumes that quantum statistics (Fermi-Dirac for electrons) is not required, i.e., that the electron gas is not degenerated. This is true if the electron temperature is much greater than the Fermi energy scaling as $n_e^{2/3}$, where n_e is the electron density, e.g., $k_B T >> 0.1$ eV if $n_e = 10^{20}$ cm^{-3}. This hypothesis is always acceptable for the experimental conditions considered in this work. The Maxwell distribution is characterized by the most probable speed,

$$u_0 = (2k_B T_e / m)^{\frac{1}{2}} \tag{1.13}$$

and the root mean square speed, $\left\langle u^2 \right\rangle^{\frac{1}{2}} = (3k_B T_e / m)^{\frac{1}{2}}$.

Boltzmann excitation equation

At thermodynamic equilibrium with temperature T_e, the population distribution of the different bound ionic states is determined by the Boltzmann law,

$$\frac{N_{\zeta,i}}{N_{\zeta,0}} = \frac{g_{\zeta,i}}{g_{\zeta,0}} \exp(-\frac{E_{\zeta,i} - E_{\zeta,0}}{k_B T_e}) \tag{1.14}$$

where $N_{\zeta,i}$ represents the density of ζ–charged ions in a excited level *i* ($N_{\zeta,0}$ is the density of the ζ–charged ion in its ground state); $g_{\zeta,i}$, $g_{\zeta,0}$ are, respectively, the statistical weights of the excited and the ground level, accounting for the degenerate sublevels (the $2J + 1$ *m*–states in the absence of a magnetic field), and $\Delta E_{i0} = E_{\zeta,i} - E_{\zeta,0}$ is the energy of the excited level above the ion ground state.

Saha ionization equation

The Saha law specifies the populations in the different ionization states. It is derived from a minimization of the free energy of the ions and electrons, assuming that the electrons form an ideal gas of non-degenerated particles. Assuming the ion densities of two successive ionization states ζ, and $(\zeta + 1)$ are N_ζ, $N_{\zeta+1}$ their ratio is given by

$$\frac{N_{\zeta+1}}{N_\zeta} = \frac{2}{n_e} \left(\frac{2\pi m k_B T_e}{h^2} \right)^{\frac{3}{2}} \frac{z_{\zeta+1}(T_e)}{z_\zeta(T_e)} \exp\left(-\frac{E_{I\zeta}}{k_B T_e} \right) \tag{1.15}$$

where $E_{I\zeta}$ is the ionization potential of the ζ–charged ion, T_e is the electron temperature, and $z_\zeta(T)$ the partition function

$$z_\zeta(T) = \sum_i g_{\zeta,i} \exp(-\frac{E_{\zeta,i}}{k_B T}) \qquad (1.16)$$

the sum being carried upon the bound levels of the ζ–charged ion.

1.3.2 Non–Local Thermodynamic Equilibrium–Collisional Radiative Model

Non–local thermodynamic equilibrium (NLTE) characterizes a plasma when at least one of the particles distribution functions deviates from the corresponding thermal distribution; explicitly, when the occupation number of the bound atomic levels do not follow the Boltzmann distribution, or an ionization state density deviates from the Saha value, or a velocity distribution is non–Maxwellian [2]. Even if the ions in the plasma obey LTE conditions as described above, the photons do not usually follow Planck's law.

The main cause of the existence of NLTE regimes is the ability of the photons to escape from the plasma (optically thin) and the fact that collision rates are not much higher than radiative rates. Due to this loss of energy the plasma particles participating in the photons emission (ions in bound–bound and bound–free, or electrons in free–free radiative transitions) deviate from their thermal distribution, and, when the plasma density is relatively low, the collisional processes can not compensate this deviation. Other reasons can be the rapid temporal variation in a plasma not being in a steady state, or transport processes due to the steep gradients of the plasma parameters. It is important to notice that because the NLTE situations are mainly due to the non–Planckian behavior of the radiation field, the frontier between LTE and NTLE states is never very clear.

The distributions functions of the plasma particles under NLTE conditions cannot be found in an analytical form from basic principles, as with in LTE. Here, we have to write down explicitly the kinetic equations ruling the statistics of the plasma particles. The state density of a specific particle (ion, electron, or photon) can be obtained by solving rate equations, taking into account all the processes that increase or decrease its population.

In the standard NLTE modeling approach we account in detail for the different atomic states, while the free electrons are still assumed to have a Maxwellian distribution due to their high collision rates in hot plasmas [5]. So, the ionization distribution and the bound level populations are determined by solving a system of rate equations taking into account all the collisional and radiative processes. The general form of the rate equation is

$$-\frac{dN_i}{dt} = N_i \sum_j R_{i\to j} - \sum_j N_j R_{j\to i} \qquad (1.17)$$

where $R_{i\to j}$ is the total transition rate from the level i to j($R_{j\to i}$ stands for the inverse processes), and N_i is the i–level population density (N_j for j–level).

1.4 Calculation of complex plasma spectrum–Superconfigurations approach

In order to calculate the plasma emission or absorption spectra one has to determine the atomic structures of the different plasma species, accounting for their atomic states, as well as the transitions rates of all the atomic processes which connect these states. In plasma conditions it is often possible to ignore the interactions between configurations. Then, the atomic states are described using the fine structure levels, where each state of a configuration

C is characterized by the two quantum numbers *JM*. This approach, which is known as the detailed level accounting (DLA), becomes unrealistic for the calculation of the spectrum of medium and high–Z elements plasmas due to the huge number of configurations and detailed levels involved in the accounting of the collisional and radiative rates.

In this case a statistical description of both the states and the corresponding transitions is necessary. Such a statistical description to arrays of detailed transitions between two configurations has been proposed in the so called UTA and SOSA approaches by J. Bauche, C. Bauche-Arnoult and M. Klapisch [7-9]

These approaches have been motivated by unresolved structures due to the bound-bound transitions observed in plasmas experiments. In plasmas the unresolved spectral structures appear naturally from the emission of a large number of spectral lines in a narrow band due to their finite spectral width (Doppler broadening, Stark effect). This situation corresponds to the high number of transitions from close energy states of two configurations. In this case the statistical treatment of the transitions is justified. The notion of the UTA (intermediate coupling Unresolved Transition Array) or the SOSA (relativistic Spin–Orbit–Split–Arrays) is used when one represents them by their continuous envelope as a function of the photon energy. In this model the first three moments of the transitions are necessary; the zero–moment determining the transitions amplitude, the first moment the energy and the second–moment the width. These moments are written formally,

$$\mu_0^{(C)} = M_0^{(C)} \tag{1.18.a}$$

$$\mu_1^{(C)} = M_1^{(C)} / M_0^{(C)} \tag{1.18.b}$$

$$\mu_2^{(C)} = M_2^{(C)} /(M_0^{(C)} - (\mu_1^{(C)})^2) \tag{1.18.c}$$

The terms M_i are the transitions strengths,

$$M_i^{(C)} = \frac{4\pi^2 a_{fine}}{3} P_C \sum_{n_E \in C, m_E \in C'} (E_{m_E} - E_{n_E})^i \left| \langle n_E | \hat{D} | m_E \rangle \right|^2 \tag{1.19}$$

where a_{fine} is the fine structure constant, P_C is the configuration probability, E_{m_E} and E_{n_E} are the states energies, and $\left|\langle n_E |\hat{D}| m_E \rangle\right|$ is the transition dipole matrix element. Let us note that in Eq. (1.19) the use of a common P_C probability before the summation upon the levels is an approximation essential to simplify the formalism: in principle such probability depends on E_{n_E} and should be kept under the sum expression. The approximation of a common P_C (Boltzmann factor) is justified when the level energy spread is much smaller than the plasma temperature. Using such an approximation, closed forms have been derived by Bauche *et al* [7-9] for the sum appearing in expression (1.19).

However even with a statistical approach to detailed levels within the configurations we still face the problem that the number of configurations can be extremely large. An answer to this problem is the superconfiguration (SC) treatment of the bound states together with the super–transition–arrays (STA) method proposed first by A. Bar–Shalom [6]. A SC Ξ is defined as a collection of configurations the energies of which are close, in particular their difference should be less than kT_e. The transitions between two SCs, Ξ and Ξ′, are obtained as in the UTA or SOSA approach in a statistical approach performing an average over all the possible one–electron transitions, $\alpha \rightarrow \beta$, between the configurations belonging to Ξ and Ξ′, forming in this manner a super–transition–array (STA). In this way the STA is a natural extension of the unresolved transition arrays method (UTA). The extension of the UTAs formalism to the STA model is however not straightforward since now the averaging should take into account also the dependence of the probability factor P_C on the configuration average energy E_C. In fact, to obtain the transitions $\alpha \rightarrow \beta$, additionally to the states of the configurations in Eq. (1.19), we have now to account for all the configurations belonging to the superconfigurations Ξ and Ξ',

$$M_i^{(\Xi)} = \frac{4\pi^2 a_{fine}}{3} \sum_{C\in\Xi, C'\in\Xi';} P_C \sum_{n_E\in C, m_E\in C'} (E_{m_E} - E_{n_E})^i \left| \langle n_E | \hat{D} | m_E \rangle \right|^2 \tag{1.20}$$

The STAs are characterized by their three first moments defined similarly to Eq. (1.18). The important point in the superconfiguration method is a simplified treatment of the P_C probability allowing one to calculate the moments of Eq. (1.20) using a recursive method and avoiding direct summations over all configurations C and C'.

1.5 Atomic codes of plasma physics

1.5.1 The code HULLAC

The code HULLAC calculates the atomic structure as well as the cross sections of the collisional and radiative atomic processes within the detailed level formalism. In its standard version of ref. [10], these data are post–processed by a collisional radiative model in order to compute the emission and absorption spectra of NLTE plasmas. The theoretical framework of the code is the first order perturbation theory with a central field, applied on the relativistic description of the Dirac equations.

The atomic relativistic states are obtained from the many-electron Dirac Hamiltonian,

$$H = H' + H_{Breit} + H_{QED} \tag{1.21}$$

The multi–electron Dirac Hamiltonian operator H' written in atomic units ($\hbar = e = m = 1$) is

$$H' = \sum_i (h_i^D - \frac{Z}{r_i}) + \sum_{i<j} \frac{1}{r_{ij}} \tag{1.22}$$

where h_i^D is the kinetic part of a single–electron Dirac Hamiltonian, and the terms H_{Breit} and H_{QED} are included to account for the Breit interactions and QED corrections, respectively. The central field principle consists in splitting the hamiltonian in a spherically symmetric part H_0 and in a perturbation H_1

$$H_0 = \sum_i (h_i^D + U(r_i)) \tag{1.23}$$

$$H_1 = \sum_{i<j} \frac{1}{r_{ij}} + \sum_i (\frac{Z}{r_i} - U(r_i)) \tag{1.24}$$

where the parametric potential $U(r_i)$ is inserted in the zero order hamiltonian in order to obtain a first order perturbation as small as possible.

The relativistic orbitals (four component spinors) obtained from the solution of the Dirac equation,

$$(h_i^D + U(r_i))\varphi_{nljm} = \varepsilon_{nlj}\varphi_{nljm} \tag{1.25}$$

are characterized by the set of quantum numbers *nljm*, and the *N*–electron zero order solutions are constructed from the antisymmetrical products of the orbitals. The parametric potential involved in Eq. (1.25) is [11],

$$U(a,r) = \frac{1}{r}\left(\sum_{s=1}^{N} q_s f(l_s, a_s, r) + I\right) \tag{1.26}$$

where,

$$f(l_s, a_s, r) = e^{-a_s r} \sum_{k=0}^{2l_s+1}\left(1 - \frac{k}{2l_s + 2}\right)\frac{(a_s r)^k}{k!} \tag{1.27}$$

In Eqs. (1.26), (1.27) the index s runs over the different shells, where q_s is the occupation number and l_s the orbital quantum number of the shell; I is the degree of ionization plus one, and the parameter a_s is proportional to the inverse of the shell radius. The solutions of H' are calculated by adjusting the parameter a_s of $U(r)$ in order to obtain minimum first order configuration energies. The Breit and QED terms of the Hamiltonian are considered as second order perturbations. The first order mixed configuration energies and wavefunctions obtained are then used for the calculation of the radiative transitions rates and the cross sections of the collisional excitation, ionization and photoionization. The inverse process rates are obtained by detailed balance.

In the present work, the code HULLAC is employed in the analysis of the XUV absorption spectrum of radiatively heated Al or ZnS plasmas in LTE. The code calculates for the different ion species their energy levels and the oscillator strengths of the transitions. In order to calculate the plasma opacity, these data are used here assuming a Saha–Boltzmann population distribution for the ionic level populations. The necessary plasma parameters (matter density, temperature) determining the LTE statistics are calculated theoretically with the radiation hydrodynamic code MULTI [12]. The results of MULTI with the LTE statistics permit to simplify the calculation of the synthetic absorption spectrum, providing an estimation of the different ion species abundances, as well as of the different transitions participating in the spectral range of interest. For instance, in our experimental conditions for aluminium, and in the spectral range of 20 – 200 Å where the absorption is measured, its spectrum is mainly formed by the 2*p*–3*s* and 2*p*–3*d* transitions of the ionic sequence Al^{4+}–Al^{8+}.

Figure 1.1 shows the opacity spectrum of an Al plasma calculated by HULLAC for typical density and temperature values achieved in our experiment. In the spectral range of 50 – 150 Å, we can see the very rich absorption spectrum of Al composed of the bound–bound transitions of different ions, and which are superimposed on the photoionization continuum (bound–free transitions).

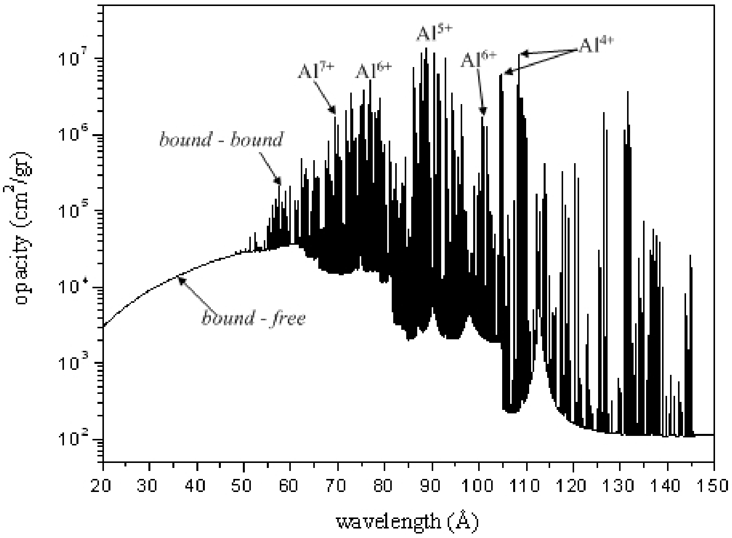

Figure 1.1 Al plasma opacity calculated by HULLAC [10] for $\rho = 2$ mg/cm^3 and $T_e = 20$ eV (calculated with natural line widths).

1.5.2 The code SCO

The code SCO (Superconfiguration Code for Opacity) [13–15] is based on the formalism of superconfigurations (SC) [6] to calculate the absorption spectra of plasmas in LTE conditions. The self–consistent–field (SCF) calculation of the potential and wavefunctions in each superconfiguration is performed using a version of the Density–Functional Theory or the statistical Hartree–Fock (HF) equations proposed by T. Blenski *et al.* [13] in the framework of the SC formalism. The SCF ion–cell model [16] is completed by accounting for the static screening of the free electrons, the contribution of which is described by the Thomas–Fermi model. In this way, the average energies of the bound electrons are obtained, and the configuration free energy can be calculated.

The basic quantity calculated by the code is the photoabsorption cross–section, and this is accomplished by the SC treatment of the bound–bound and bound–free transitions of all the ions. For the determination of the super–transition–arrays [6] the code does not calculate detailed lines for each SC but uses instead a statistical approach resulting in unresolved transition structures [7–9] (UTA or SOSA). The free–free transitions (inverse bremsstrahlung) can be calculated with the classical approach of the Kramer cross–section, or in a quantum mechanical approach with the free wavefunctions of the Average Atom (AA) model.

The information needed to construct the SCs used in the absorption spectrum calculations is generated within the frame of the AA model. In particular, this model provides the approximate values of the one–electron states which are used to group shells close in energy (energy dispersion less than k_BT) in supershells. The AA populations and their variance give an estimation of the SCs that have to be included in the calculation, and this choice is accomplished automatically by the code. Then, the electronic structure of the selected SCs is obtained self–consistently. The choice of the SCs number, and thus the division of the ion states in supershells, is refined and iteratively repeated until the convergence of the spectrum: when the calculated spectrum does not vary the SCs number is sufficient and the procedure ends. The relativistic effects are included with the Pauli approximation [16], and the orbital relaxation corrections are taken into account for all relevant transitions [14].

The code SCO is used in our work to analyze the XUV absorption spectrum of a zinc sulfide (ZnS) plasma mixture in LTE. Here, the ion–cell model is used for all the elements of the mixture so that all the ions are screened by a plasma having the same electron density [15]. The free electrons density is calculated with the Thomas–Fermi model of mixtures [17], and thus the corresponding effective masses of the different elements are obtained. The ions of the mixture are represented by hundreds of SCs, the structures of which are calculated self–consistently in a neutral atomic sphere corresponding to the effective mass of the element.

The code SCO calculates the absorption spectrum of each element separately as well as the total absorption of the mixture. However, the charge distribution of each element is ruled by the Saha–Boltzmann law, which involves the total electron density (i.e. electrons coming from both Zn and S); in this way the opacity associated to each component depends on the presence of the other one. Figure 1.2 shows the opacities of the zinc (dashed line) and sulfur (full line) calculated by SCO [13–15], using for both plasmas : $\rho = 2$ mg/cm^3 and $T_e = 20$ eV. For these typical plasma parameters of our experiment, in the range of 20 – 150 Å, the spectrum is formed mainly by the $2p$–$3s$ and $2p$–$3d$ transitions of S^{5+}, S^{6+} ions, as well as by the $3d$–$4f$ transitions of the zinc ions in the sequence of Zn^{5+}–Zn^{8+}. The code predicts that the sulfur and zinc ions transitions appear in distinct spectral ranges, ensuring the ability to study simultaneously the absorption properties of the mixture components.

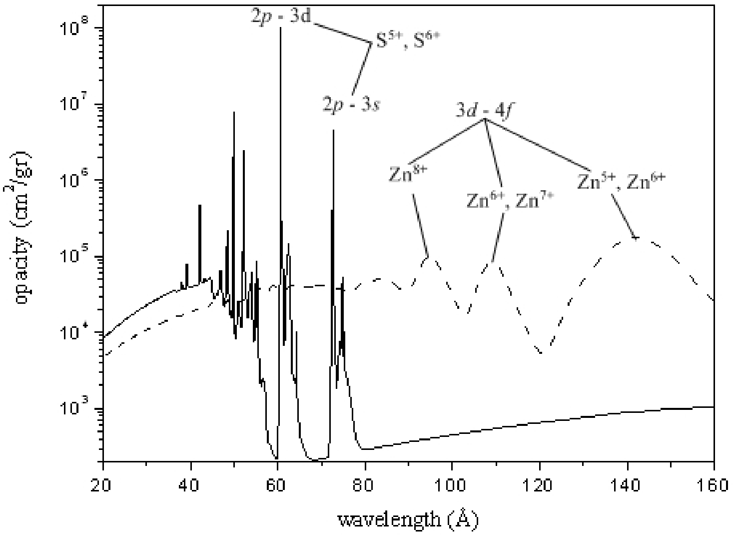

Figure 1.2 Opacities calculated by SCO [13–15] for $\rho = 2$ mg/cm^3 and $T_e = 20$ eV; full line : sulfur plasma, dashed line : zinc plasma.

1.5.3 The code TRANSPEC/AVERROES

The code TRANSPEC/AVERROES developed by O. Peyrusse [5] implements a NLTE collisional radiative model (CRM) supported by the superconfiguration (SC) formalism [6] for the description of the ions states. This model permits to simulate the complex emission and absorption spectra of medium and high–Z elements plasmas under NLTE. The code is divided in two parts. The first part, the code AVERROES, calculates the collisional and radiative rates of the different atomic processes, as well as the mean energies and variances of the super–transition arrays. Then, these quantities are used by a standard time–dependent CRM such as TRANSPEC [18–19] that calculates the plasma kinetic populations to obtain the synthetic emission spectrum.

Concerning the calculations of the atomic orbitals, AVERROES uses the following approximations :

1. The calculations are performed within the “isolated atom” model. In particular, no static screening by the free electrons is introduced in the atomic potential. Furthermore, the orbitals are not confined into a finite ion–cell.
2. The orbitals are non relativistic, and the corrections to the radial Schrodinger equation are introduced with the Pauli approximation described in [20].
3. Exchange contribution to the atomic potential is calculated with the local density approximation.

To calculate the synthetic emission spectrum, the code can be used either in a single–cell mode, assuming an homogeneous plasma, or as a post–processor of a hydrodynamic code as MULTI [12]. In the second case the hydro–code gives in a tabulated format the spatial and temporal profiles of the plasma parameters, and thus provides the evolution of the plasma cells used by TRANSPEC.

The TRANSPEC/AVERROES package is used in the analysis of the XUV emission of the xenon and krypton NLTE plasmas (Chapter 4). The time–resolved emission spectrum of each element is measured in the range of 20–200 Å, and the code is used to simulate the transitions structures n = 5–4 and 4–4 of the xenon, as well as the structures n = 4–3 and 3–3 of the krypton. In our work the kinetic code TRANSPEC is used in single–cell mode, and the plasma parameters are measured with the Thomson scattering technique providing their average values. Simultaneously, the x–ray spectrum of the elements is measured in the keV range. In particular, the xenon spectrum is studied in the range of 12 – 15 Å where the $3d$–$4f$ transitions appear, and that of krypton in the range 6 – 8 Å corresponding to the 2–3 and 2–4 transitions. In this range, and under the given experimental conditions, the rich emission spectra of the elements are of particular interest by themselves, and the synthetic spectra calculated by the code permit to analyze them, identifying the transitions of the different ions. Moreover, this identification of the ionic species can provide an independent means of inferring the heating conditions of the laser irradiated plasmas.

References of Chapter 1

[1] D. Salzman, Atomic Physics in Hot Plasmas, Oxford University Press, 1998.

[2] J. Oxenious, Kinetic Theory of Particles and Photons–Theoretical Foundations of Non–LTE Plasma Spectroscopy, Springer–Verlag, 1986.

[3] D. Mihalas, Stellar atmospheres, W. H. Freeman and Company (1978).

[4] Y. B. Zel'dovich, Y. P. Raizer, Physics of Shock Waves and High-Temperature Hydrodynamic Phenomena, Academic Press, 1966.

[5] O. Peyrusse, A superconfiguration model for broadband spectroscopy of non–LTE plasmas, J. Phys. B : At. Mol. Opt. Phys. **33**, 4303 (2000).

[6] A. Bar–Shalom *et al.*, Super–transition–arrays : A model for the spectral analysis of hot, dense plasma, Phys. Rev. A **40**, 3183 (1989).

[7] C. Bauche–Arnoult, J. Bauche, M. Klapisch, Variance of the distribution of energy levels and of the transition arrays in atomic spectra, Phys. Rev. A **20**, 2424 (1979).

[8] C. Bauche–Arnoult, J. Bauche, M. Klapisch, Variance of the distribution of energy levels and of the transition arrays in atomic spectra. II. Configurations with more than two open subshells, Phys. Rev. A **25**, 2641 (1982).

[9] C. Bauche–Arnoult, J. Bauche, M. Klapisch, Variance of the distribution of energy levels and of the transition arrays in atomic spectra. III. Case of spin-orbit-split arrays, Phys. Rev. A **31**, 2248 (1985).

[10] A. Bar–Shalom *et al.*, HULLAC, an integrated computer package for atomic processes in plasmas, J. Quant. Spec. Radiat. Transfer **71**, 169 (2001).

[11] M. Klapisch, *et al.*, The 1*s*-3*p* K, 3-like x-ray spectrum of highly ionized iron, J. Opt. Soc. Am. **67**, 148 (1977).

[12] R. Ramis, R. Schmalz and J. Meyer–Ter–Vehn, MULTI – A computer code for one – dimensional multigroup radiation hydrodynamics, Comp. Phys. Communications **49**, 475 (1988).

[13] T. Blenski, A. Grimaldi and F. Perrot, Hatree–Fock statistical approach to atoms and photoabsorption in plasmas, Phys. Rev. E **55**, R4889 (1997).

[14] T. Blenski, A. Grimaldi and F. Perrot, A superconfiguration code based on the local density approximation, J. Quant. Spec. Radiat. Transfer **65**, 91 (2000).

[15] J. C. Pain and T. Blenski, Self-consistent approach for the thermodynamics of ions intense plasmas in the superconfiguration approximation, J. Quant. Spec. Radiat. Transfer **8**, 355 (2003).

[16] T. Blenski, K. Ishikawa, Pressure ionization in the spherical ion–cell model of dense plasmas and a pressure formula in the relativistic Pauli approximation, Phys. Rev. E **51** 4869 (1995).

[17] A. F. Nikiforov, V.G. Novikov, V.B. Uranov, Quantum–Statistical Models of Hot Dense Matter, Birkhauser Verlag, Basel–Boston–Berlin, 2005.

[18] O. Peyrusse, A model for the simulation of nonequilibrium line transfer in laboratory plasmas, Phys. Fluids B **4**, 2007 (1992).

[19] O. Peyrusse, X–ray spectroscopy studies using the TRANSPEC code, J. Quant. Spectrosc. Radiat. Transfer **51**, 281 (1994).

[20] R.D. Cowan, The theory of atomic structure and spectra, Berkeley, CA, University of California Press.

Chapter 2 Radiation transfer through a plasma–Cavities thermal radiation and solid foil heating

2.1 Introduction

To compare the experimental absorption of radiatively heated zinc sulfide (ZnS) plasmas in local thermodynamic equilibrium (LTE) to opacity calculations, the hydrodynamic and radiative properties of the plasma have to be calculated. The ion populations and energy distribution involved in the opacity computation of an LTE plasma depend on its temperature and density which can be derived from the hydrodynamic behavior. To simulate the hydrodynamics of an absorption foil heated by a gold cavity, we have to determine the radiation confined in the interior of the cavity which heats the absorption foil. In a following stage, we have to simulate the hydrodynamic behavior of the radiatively heated absorption foil. In §2.2, we give some basic elements on radiation transfer through a plasma. Then, we describe the hydrodynamic code MULTI [1] used to simulate the interaction of a plasma with a radiation field. In paragraph 2.3, we present the Basko self–similar model [2], which, in conjunction with a geometric approach [3], describes the flux distribution inside the cavity, and thus determine the heating conditions of the absorption foil.

2.2 Radiation transfer problem

When a high temperature field interacts with a plasma, the energy transport by thermal radiation through the heated plasma becomes significant. The plasma emissivity and opacity depend explicitly on its parameters (temperature, matter density). The plasma parameters are strongly affected by the radiation field through the transport of energy and momentum. In such a case, we are talking about the non linear coupling between the hydrodynamics and the radiation transfer, which in general constitutes a difficult problem if solved analytically. In paragraph 2.2.1 we present the basic theory describing the coupling of a transported radiation field with an expanded plasma. Then, based on this model, we describe the approach used by the hydro code MULTI [1].

2.2.1 Hydrodynamics–radiation equations coupling

Elements of fluid mechanics

The basic equations ruling the dynamics of a fluid follow from the conservation laws of mass, momentum and energy [4]. When the motion of a fluid is represented in fixed coordinates – Euler representation – these equations are, if the macroscopic description holds,

$$\frac{\partial}{\partial t}\rho + \overline{\nabla}\cdot(\rho\overline{u}) = 0 \tag{2.1.a}$$

$$\left(\frac{\partial}{\partial t} + \overline{u}\overline{\nabla}\right)\overline{u} = -\frac{1}{\rho}\overline{\nabla}p \tag{2.1.b}$$

$$\left(\frac{\partial}{\partial t}+\overline{u}\overline{\nabla}\right)e+p\left(\frac{\partial}{\partial t}+\overline{u}\overline{\nabla}\right)\frac{1}{\rho}=-\frac{1}{\rho}\overline{\nabla}\overline{q}+\frac{1}{\rho}S \tag{2.1.c}$$

where ρ is the density, p the pressure, and $\overline{u}$ the velocity of a moving fluid cell measured in the fixed frame. In Eq. (2.1.c) e is the specific energy, the vector $\overline{q}$ is the heat conduction current, and the function S represents all the external energy sources interacting with the fluid. To obtain a system in a closed form, Eqs. (2.1) have to be completed by the equations of state for the pressure and the specific energy, usually given as a function of the density and the temperature : $p=p(\rho,T)$, $e=e(\rho,T)$.

The Lagrange representation is the equivalent form that take the fluid equations when we define a spatial frame of reference moving with the fluid, and thus we describe the behavior of individual fluid elements rather than fixed space points. In a one dimensional planar geometry, the Lagrangian coordinate of a fluid element is given usually in terms of the fluid mass that separates this element from a spatial point of reference [5]. If the Eulerian coordinate of this reference point coincides with the beginning of the fixed frame (x_{ref} = 0), the transformation defining the Lagrangian coordinates is

$$m(x)=\int_{0}^{x}\rho(x')dx' \tag{2.2}$$

Re–expressing the spatial derivates in term of m, and using the fact that the partial time derivative $(\partial/\partial t)_{Lagrange}$ in the Lagrange system is by definition equal to the total time derivative $(\partial/\partial t+u\partial/\partial x)_{Euler}$ in the Euler system, Eqs. (2.1) are written

$$\frac{\partial\rho}{\partial t}=-\rho^{2}\frac{\partial u}{\partial m} \tag{2.3.a}$$

$$\frac{\partial u}{\partial t}=-\frac{\partial p}{\partial t} \tag{2.3.b}$$

$$\frac{\partial e}{\partial t}+p\frac{\partial u}{\partial m}=-\frac{\partial q}{\partial m}+\frac{1}{\rho}S \tag{2.3.c}$$

The Lagrange equations, which take a simple form in the planar geometry, are used extensively when we have strong fluid compressions, or when we want to trace the variations of different fluid species. Additionally, this form provides particular advantages as concerns the application of numerical integration methods, and therefore many hydrodynamic codes use this representation.

Plasma opacity and emissivity

The interaction of a radiation field with a plasma is ruled by the energy transfer into, or from the field due to the emission and absorption of radiation by the plasma. Its description in an atomic scale would require to account for the different radiative processes described in Chapter 1. Macroscopically, we define two coefficients which characterize the absorption and emission properties of the plasma : the opacity and the emissivity [6]. These coefficients are determined by the different atomic processes taking place during the plasma–field interaction, and generally they appear as very complicated functions of the frequency (when spectral lines are present). Their determination from first principles, in an atomic scale, concerns the development of sophisticated models of plasma atomic physics, which constitute the theoretical background of the present work. Here, we restrict to give their definitions, and for this we refer to Figure 2.1 showing a differential element of a plasma interacting with a radiation field.

The plasma *opacity*, $\chi(\bar{r},\hat{n},v,t)$, is defined such that a plasma element of area *dA* and length *dl*, removes, within a frequency range *dv* in a time interval *dt*, from a radiation field with specific intensity $I(\bar{r},\hat{n},v,t)$ propagating into a solid angle *dω* in the direction $\hat{n}$ normal to *dA*, an amount of energy,

$$d\mathrm{E} = \chi(\bar{r},\hat{n},v,t)I(\bar{r},\hat{n},v,t)dAdld\omega dvdt \tag{2.4}$$

The dimensions of the opacity are cm^{-1}; $(1/\chi)$ is the definition of the *mean free path*, which provides a measure of the distance over which a photon propagates before it is removed from the field.

In the general definition of Eq. (2.4), opacity includes both the absorption and the scattering processes occurring in the interaction of the radiation with the plasma. Those processes can be considered as independent and this is represented by the following sum

$$\chi(\bar{r},\hat{n},v,t) = \kappa(\bar{r},\hat{n},v,t) + \sigma(\bar{r},\hat{n},v,t) \tag{2.5}$$

where κ and σ are, respectively, the absorption and scattering coefficients. When the scattering processes are negligible, opacity is identified with the absorption coefficient, and in the following the term opacity is used to characterize κ; that is, opacity characterizes explicitly the radiation removal due to its absorption by the plasma.

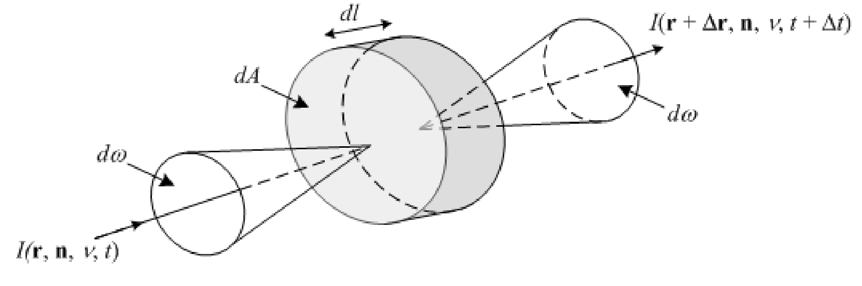

Figure 2.1 Transport of radiation through a plasma element.

The plasma emissivity $\eta(\bar{r},\hat{n},v,t)$ gives the amount of energy emitted from a plasma element of area *dA* and length *dl*, in the direction $\hat{n}$ and into a solid angle *dω*, within a frequency range d*v* in a time interval *dt*,

$$d\mathrm{E} = \eta(\bar{r},\hat{n},v,t)dAdld\omega dvdt \tag{2.6}$$

The dimensions of the emissivity are ergs cm^{-3}sr^{-1}hz^{-1}sec^{-1}.

Equation of radiation transfer

The equation determining the transport of radiation through a plasma can be obtained with the aid of Fig. 2.1 [6]. Assuming a plasma element of area *dA* and length *dl*, which is characterized by a specific opacity χ and emissivity η, we want to calculate the amount of energy passing through it, and which is carried by the radiation field. Let $I(\bar{r},\hat{n},\nu,t)$ be the specific intensity of the incident radiation field on the plasma element, and $I(r+dr,\hat{n},\nu,t+dt)$ the specific intensity of the radiation emerging from it, in direction $\hat{n}$ and into a solid angle $d\omega$, after a time interval *dt*. Taking into account all the interactions between the field and the plasma element, the energy passing through it is equal to the incident energy plus the amount created by emission, minus the amount absorbed, or

$$\begin{aligned}&[I(r+dr,n,\nu,t+dt)-I(\bar{r},\hat{n},\nu,t)]dAd\omega d\nu dt\\&\qquad=[\eta(\bar{r},\hat{n},\nu,t)-\kappa(\bar{r},\hat{n},\nu,t)I(\bar{r},\hat{n},\nu,t)]dldAd\omega d\nu dt\end{aligned} \tag{2.7}$$

Taking the Taylor expansion of the term $I(r+dr,\hat{n},\nu,t+dt)$ with respect to *dl*, and using $\Delta t=\Delta l/c$, from Eq. (2.7) we obtain the transfer equation

$$[c^{-1}(\partial/\partial t)+(\partial/\partial l)]I(\bar{r},\hat{n},\nu,t)=\eta(\bar{r},\hat{n},\nu,t)-\kappa(\bar{r},\hat{n},\nu,dt)I(\bar{r},\hat{n},\nu,t) \tag{2.8}$$

or, expressing the derivate $\partial/\partial l$, which is taken along the propagation direction of the rays, in terms of an orthogonal coordinates system,

$$[c^{-1}(\partial/\partial t)+(\hat{n}\bar{\nabla})]I(\bar{r},\hat{n},\nu,t)=\eta(\bar{r},\hat{n},\nu,t)-\kappa(\bar{r},\hat{n},\nu,t)I(\bar{r},\hat{n},\nu,t) \tag{2.9}$$

In our study, we are interested in one dimensional planar medium. Further, under the conditions of the produced plasmas, the matter velocity is expected to be much smaller than the velocity of light (*u*/*c* << 1), and the time derivative in Eq. (2.9) can be dropped out. This holds because the variation time scale of the radiation field is very small in comparison with the time scale of the plasma motion, and the field “sees” the fluid to be at rest. With this assumption, and if we use the Lagrange variable of Eq. (2.2), the one dimensional planar version of Eq. (2.9) is written

$$\mu\partial I(m,\mu,\nu,t)/\partial m=\kappa'(m,\mu,\nu,t)[I_S(m,\mu,\nu,t)-I(m,\mu,\nu,t)] \tag{2.10}$$

where $\mu=\cos\theta$ is the direction cosine determining the angular distribution of the photons, and $\kappa'\equiv\kappa/\rho$ is the plasma massive opacity. The function $I_S\equiv\eta/\kappa'$ is the definition of the *source function* of the plasma, which is an equivalent description of its emissivity [6].

For the description of the radiation field, the quantities having a particular importance are the zero, first and second order angular moments of the specific intensity, which define, respectively, the radiation energy density, flux and pressure,

$$U(z,\nu,t)=c^{-1}\int_{-1}^{1}I(z,\mu,\nu,t)d\mu \tag{2.11}$$

$$S(z,\nu,t)=\int_{-1}^{1}I(z,\mu,\nu,t)\mu d\mu \tag{2.12}$$

$$P_R(z,\nu,t)=\frac{2\pi}{c}\int_{-1}^{1}I(z,\mu,\nu,t)\mu^2 d\mu \tag{2.13}$$

Eq. (2.13) gives the scalar into which the radiation pressure tensor reduces in a one–dimensional planar geometry. Using the definitions of Eq. (2.11)–(2.13), the zero and first angular moments of the transfer equation give

$$c\partial S(z,\nu,t)/\partial z=\kappa(z,\nu,t)[U_S(z,\nu,t)-U(z,\nu,t)] \tag{2.14.a}$$

and

$$c\partial P_R(z,\nu,t)/\partial z=-\kappa(z,\nu,t)S(z,\nu,t) \tag{2.14.b}$$

The term U_S in Eq. (2.14.a) is the energy density corresponding to the plasma source function. The interpretation of this equation is straightforward : it states that the energy flow through a surface containing a volume element (the divergence of the flux) is equal to the total energy emitted into, minus the total energy absorbed from the field by the plasma.

The description of the radiation transport in the form of Eq. (2.14) has the advantage that the angular variable is eliminated, reducing the dimensionality of the problem. Due to this the introduction of the radiation moments is a widely used method to solve the transfer equation. The question arising is whether Eq. (2.14) can be solved as a differential equation system. A simple inspection confirms that this is not possible, because the n moment of the transfer equation introduces also the $n+1$ moment of the specific intensity; thus, one more relation is necessary, a difficulty known as the *closure problem*. The basic method applied to obtain the moment equations in a closed form is to eliminate the radiation pressure variable P_R, using the variable Eddington factors, $f=P_R/U$ [6]. We return to this point in paragraph 2.2.2, where the specific approach used by the physical model of code MULTI [1] is discussed.

Coupling of the plasma hydrodynamics with the radiation field

As we noticed in the introduction, the hydrodynamics of the plasma and the transferred radiation field show a twofold coupling. Here, we are interested in the transfer of energy and momentum between the radiation field and the plasma, which appear explicitly in the equations ruling the plasma hydrodynamics. In the one dimensional planar geometry the energy transfer term Q is written

$$Q=\int_0^\infty\Big(\int_{-1}^{1}\kappa(I_S-I)d\mu\Big)d\nu \tag{2.15}$$

Its interpretation follows easily from the zero–moment of the transfer equation; it describes the net energy transfer rate per unit volume between the plasma and the radiation field. The net momentum transfer rate per unit volume R between the plasma and the field is

$$R=\frac{1}{c}\int_0^\infty\Big(\int_{-1}^{1}(\eta-\chi I)\mu d\mu\Big)d\nu \tag{2.16}$$

and for $u/c \ll 1$, R can be ignored. So, the only equation that has to be modified is the energy equation of the plasma fluid, which becomes

$$\frac{\partial e}{\partial t} + p\frac{\partial u}{\partial m} = -\frac{\partial q}{\partial m} + \frac{1}{\rho}(S+Q) \qquad (2.3.c')$$

2.2.2 MULTI one dimensional radiation hydrodynamic code

The MULTI (MULTIgroup MULTIlayer) code developed by R. Ramis *et al.* [1], simulates the hydrodynamics of a one dimensional plasma coupled with a radiation field. The code is based on a finite set of difference equations, which result from the physical model describing the coupling of the plasma with the radiation, as follows :

- the spatial variation of the plasma fluid motion, and of the radiation transport through it, are described in discrete cells, while the temporal variation is calculated in discrete time steps sampling the evolution of the plasma–radiation coupling.
- the frequency domain is optimally divided in discrete groups.

This is achieved by the *multigroup* approach of the plasma emissivity and opacity, which is a powerful extension of the simplified *single mean opacity* approximation used to solve the *non grey* radiation transfer problem [6].

Physical model of the radiation field–plasma coupling

As we saw in paragraph 2.2.1, for a "static" ($u/c << 1$) and one dimensional planar plasma, the Lagrange representation of the equations describing its coupling with an intense radiation field are given by (2.3a, b, c') and (2.10). The equations of state for the pressure and the internal energy, required to close the hydrodynamic system of equations, are provided to the code in a tabulated format using the data of the SESAME library [7]. The term q in Eq. (2.3.c′) represents the heat flux carried by electrons, and in the quasi–equilibrium limit is given by the Fourier law

$$q = -\overline{K}T^{5/2}\partial_x T \qquad (2.17)$$

In our case the conductivity K is given by Spitzer formula [8],

$$\overline{K} = \frac{10.16\varepsilon\delta_t {k_B}^{7/2}}{\sqrt{m_e} e^4 Z_i \log\Lambda}, \qquad \varepsilon\delta_t \approx 0.095\frac{Z_i + 0.2410.16}{1+0.24Z_i} \qquad (2.18)$$

where k_B is the Boltzmann constant, m_e, e the mass and the charge of electron, Z_i the plasma mean ionization number, and $\log\Lambda$ the Coulomb logarithm. The term S, is the energy rate per unit volume deposited on the medium from external sources. The code model gives the ability to integrate various sources as a laser beam, a Planckian radiation, or even the radiation obtained in a tabulated format from another simulation performed with MULTI.

Equations of the physical model

a) multigroup method

In the multigroup method, the spectrum is divided into a number of frequency intervals. Then, the photons of the radiation field, which belong into a specific frequency interval ($\nu^g{}_a$, $\nu^g{}_b$), are further distributed with regard to their propagation direction. To this end, the range of the propagation angle is divided into a number of direction cosines intervals, each of which covers a specific range ($\mu^g{}_a$, $\mu^g{}_b$). The photons of a specific frequency and direction cosines interval define a *group* of the radiation field. Within each group the frequency and angular dependence of the radiation quantities can be eliminated, defining the zero and first mean group moments (group energy density, flux) describing the radiation field,

$$U_g(m,t) = \frac{1}{c}\left(\int_{\mu^g{}_a}^{\mu^g{}_b}\int_{\nu^g{}_a}^{\nu^g{}_b} I(m,\mu,\nu,t)d\nu d\mu + \int_{-\mu^g{}_a}^{-\mu^g{}_b}\int_{\nu^g{}_a}^{\nu^g{}_b} I(m,\mu,\nu,t)d\nu d\mu\right) \tag{2.19.a}$$

$$S_g(m,t) = \int_{\mu^g{}_a}^{\mu^g{}_b}\int_{\nu^g{}_a}^{\nu^g{}_b} I(m,\mu,\nu,t\nu)\mu d\nu d\mu + \int_{-\mu^g{}_a}^{-\mu^g{}_b}\int_{\nu^g{}_a}^{\nu^g{}_b} I(m,\mu,\nu,t)\mu d\nu d\mu \tag{2.19.b}$$

where, in the planar geometry, (μ_a, μ_b) and ($-\mu_a$, $-\mu_b$) characterize the photons of the group propagating, respectively, to the right and to the left.

Taking the zero and first moments of the transfer equation and making the proper substitution of Eq. (2.19.a), (2.19.b), we obtain the group version of Eq. (2.14), which as we explained do not form a close set. To obtain these equations in a closed form, the code assumes that the function of the specific intensity results as a first order perturbation of the Planckian specific intensity,

$$I = I_p - \frac{\mu}{\kappa}\frac{\partial I_p}{\partial T}\partial_m T \tag{2.20}$$

an hypothesis that is strictly valid for LTE plasmas. With this assumption the system of Eq. (2.14) is reduced to the group version of the Feautrier equations [9,10],

$$\partial_m S_g(m,t) = c\kappa_P(\rho,T)(U_{P,g} - U_g(m,t)) \tag{2.21.a}$$

$$f_g c\partial_m U_g(m,t) = -\kappa_R(\rho,T)S_g(m,t) \tag{2.21.b}$$

where

$$f_g = \frac{(\mu^g{}_a)^2 + \mu^g{}_a\mu^g{}_b + (\mu^g{}_b)^2}{3} \tag{4.21.c}$$

is the group Eddington factor [1], and

$$\kappa^g{}_P = \int_{\nu^g{}_a}^{\nu^g{}_b} \kappa I_P d\nu \Bigg/ \int_{\nu^g{}_a}^{\nu^g{}_b} I_P d\nu \tag{2.22.a}$$

$$\kappa^g{}_R = \int_{\nu^g{}_a}^{\nu^g{}_b} \partial I_P/\partial T\, d\nu \Bigg/ \int_{\nu^g{}_a}^{\nu^g{}_b} \kappa^{-1}\partial I_P/\partial T\, d\nu \tag{2.22.b}$$

are, respectively, the group Planck and Rosseland mean opacities [9]. Eq. (2.21) now form a closed set between the group quantities of the radiation flux and the mean energy. Further, the group energy coupling term of Eq. (2.3.c′) is written

$$Q_g(m,t) = c\rho(m,t)\kappa^g{}_P(\rho,T)(U_{P,g} - U_g(m,t)) \tag{2.23}$$

Now, the Eq. (2.3) and (2.21), taking into account the term of Eq. (2.23), define a closed system of differential equation describing the coupling of the plasma hydrodynamics with the radiation field, and which can be solved for each group, provided the group mean opacities. In the radiation hydrodynamics simulations of the present work, these data are calculated with the code POTREC [11] and they are given in a tabulated format to be used by the code MULTI.

b) Spatial – temporal discretization

In the one dimensional planar problem the plasma in the Lagrange representation is defined by two boundary values m_L and m_R. The spatial discretization is obtained by dividing the Lagrangian coordinate m between these boundaries, and thus the plasma, in N discrete subintervals, called "cells", which are not necessarily equal. In matter units the width of each cell is Δm_i. The $N + 1$ boundary surfaces lying between two successive cells are called "interfaces". The difference equation with respect to the discrete matter variable are obtained by attributing at each cell a discrete set of hydrodynamics and radiation quantities. From this point of view, it is assumed that the quantities characterizing a flux (like velocity, radiation flux) are known on the interfaces, while all the other quantities are known in the cells.

Further, the time evolution of the radiation–plasma interaction is calculated in discrete times, replacing the differential term of the rate equations with difference temporal operators of finite step width Δt_i.

Simulations performed with MULTI

In the calculations performed to analyze the data of the ZnS absorption experiment, the code MULTI is used twice. First, it simulates the interaction of the laser beam with the conversion foil generating the x–ray source. From this way, we obtain the radiation that fills the cavity. Then, we perform a second simulation with MULTI by coupling to the absorption foil the radiation calculated in the first step with the Basko model and the view factor approach. The calculation of the radiation which is confined by the cavity and heats the absorption foil is the subject of the following paragraph.

2.3 Radiation confinement in the interior of an open spherical gold cavity

The confinement of the radiation field in the interior of a cavity can be viewed as the composite result following from the heating of its wall and the radiation reemission accompanying this heating. Though these phenomena are strongly correlated, we approach them separately in the following paragraphs. First, we analyze the energy exchange inside the cavity, which determines the heating of each wall element. Then, we study the behavior of a single wall element due to the radiation incident on it, which determines its radiation reemission. Finally, we calculate the total radiation heating the absorption foil.

2.3.1 Energy exchange in the cavity interior

The energy exchange inside the cavity is described in Figure 2.2. This figure shows a spherical cavity with open sections having a direct correspondence with the cavities used in the experiment. In particular, the cavity contains two holes with area A_H (i.e. the diagnostic holes, one of which is covered by the absorption foil, $A_H = A_F$), and an external source occupying an area A_S, and which irradiates the interior of the cavity with a flux $S_0(\vec{r},t)$. For the cavity used in the experiment this radiation flux corresponds to the x–ray emission at the rear side of the conversion foil heated by the main beam. If the wall material of the cavity participating in the radiation confinement has an area A_W, the simple geometrical formula follows

$$A_C = A_W + A_S + 2A_H \tag{2.24}$$

where A_C is the equivalent area of a closed spherical cavity with the same radius.

Let us consider a differential wall element at an arbitrary point $P(\vec{r})$. The radiation energy incident on this element is the sum of the radiation emitted from the source S_s and the radiation emitted from all the other wall elements S_i. This energy is balanced by the energy absorbed by the wall element S_w, and the reemitted energy from it S_r. The energy balance in term of radiation fluxes is written

$$S_i(\vec{r},t) + S_s(\vec{r},t) = S_r(\vec{r},t) + S_w(\vec{r},t) \tag{2.25}$$

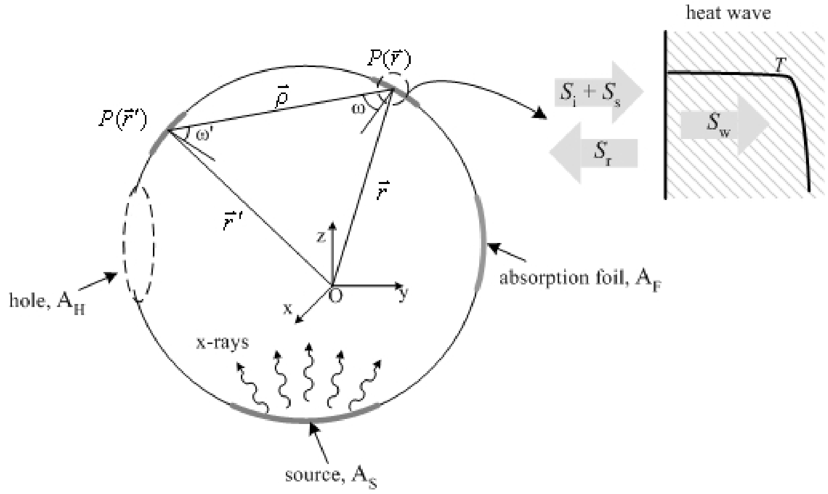

Figure 2.2 Schemes showing the energy exchange occurring in the interior of an open spherical cavity, between two arbitrary wall elements and the external radiative source. The magnified wall part gives the energy balance within a single wall element.

where

$$S_i(r,t) = \int_{A_w} \frac{S_r(\vec{r}\,',t)}{\pi} \Psi_\upsilon(\vec{r},\vec{r}\,')dA' \tag{2.26}$$

$$S_s(r,t) = \int_{A_s} \frac{S_0(\vec{r}\,',t)}{\pi} \Psi_\upsilon(\vec{r},\vec{r}\,')dA' \tag{2.27}$$

$$S_r(\vec{r},t) = R(\vec{r},t)[S_i(\vec{r},t) + S_s(\vec{r},t)] \tag{2.28}$$

assuming a Lambertian (isotropic) radiation emission within the cavity for both the external source and each wall element acting as radiator.

Eq. (2.26) gives S_i the incident flux on a wall element located at $P(\vec{r})$ due to the radiation emitted from all the wall material of the cavity. Similarly, Eq. (2.27) gives S_s the incident flux at $P(\vec{r})$ due to the radiation emitted from all the area occupied by the external source. Finally, Eq. (2.28) is the definition of the reemission factor $R(\vec{r},t)$ characterizing the emission properties of the material. The *view factor* $\Psi_\upsilon(\vec{r},\vec{r}')$ appearing in Eq. (3), (5) is defined by [3],

$$\Psi(\vec{r},\vec{r}') = \cos\omega\cos\omega' / \rho^2 \tag{2.29}$$

where ω, ω' are, respectively, the angles forming the normal of the surfaces at the points $P(\vec{r})$, $P'(\vec{r}')$ with the direction PP', and $\rho = |PP'|$ (see Fig. 2.2). This geometrical quantity describes the energy coupling between two arbitrary wall elements, determining both the emission direction from the one element and the solid being seen the other element along this direction. For the geometry of a spherical cavity, the view factor between any two points on its surface is constant,

$$\Psi(\vec{r},\vec{r}') = \pi / A_C \tag{2.30}$$

In the case of a Lambertian source assumed above, this property implied from the spherical symmetry of the cavity has two consequences : (1) the interior of the cavity is irradiated uniformly from the source, and (2) due to this uniform irradiation from the source, but also from the rest of the cavity wall, each wall element has the same temperature. Further, the integral expressions (2.26), (2.27) can now be greatly simplified. To this end, we define the fractional area coefficients :

$$\eta_W = A_W / A_C \tag{2.31.a}$$

$$\eta_S = A_S / A_C \tag{2.32.b}$$

Using these definitions and Eq. (2.30), we obtain from Eq. (2.26)–(2.28),

$$S_i(t) = \eta_W S_r(t) \tag{2.33}$$

$$S_s(t) = \eta_S S_0(t) \tag{2.24}$$

$$S_w(t) = \eta_S S_0(t) - S_r(t)(1 - \eta_W) \tag{2.35}$$

Equation (2.33) gives the flux incident on a wall element due to the flux emitted from all the wall material. In a case of a cavity without holes (including the source area), and thus without energy losses, η_W = 1, and as a consequence $S_i(t) = S_r(t)$. Therefore, for an open cavity system, the coefficients η_W, η_S should be viewed as an equivalent statement of the energy conservation expressed in terms of fluxes.

Finally, and more importantly, with the assumption of isotropic radiators, and due to the symmetry of the spherical cavity stated in Eq. (2.30), the wall material in the cavity interior can be characterized by a single radiative temperature and flux. (This is clearly underlined in Eq. (2.33)–(2.35) where the explicit spatial dependence characterizing each wall element is eliminated). So, the initial three–dimensional energy exchange problem in the interior of the cavity has been transformed into the equivalent one–dimensional problem of a wall element heating, which is analyzed in the next paragraph.

2.3.2 Radiation reemission of the cavity wall–Basko scaling law

The interaction of the x–ray radiation field confined in the interior of the cavity and a single cavity wall element can be described with Figure 2.3 [12]. Here, we assume a planar solid material coming in contact at $t = 0$ with an x–ray radiation field (Fig. 2.3(a)). For a high–Z material, as gold, the heating of the wall forms an optical thick plasma layer on its surface, which absorbs totally the incident x–ray radiation. Thus, the deposited energy on the wall surface is transmitted into the body of the material by diffusion [13,14]. For high temperatures the dominant heat transport mechanism is the radiation conduction. A non linear supersonic heat wave propagates into the solid material (Fig. 2.3(b)). As the thickness of the heated region increases its propagation velocity decreases, while at the same time a plasma expansion wave is formed in the solid–vacuum interface (Fig. 2.3(c)). When the velocity of the heat wavefront becomes sonic, it is overtaken by the expansion wave front and a shock wave is formed. This situation with the heat wave preceded by a shock wave and the simultaneous expansion of the plasma is known as the ablative heat wave.

The ablative heat wave formed into a planar medium due to the non linear radiation heat conduction was studied in [13]. In particular, it was proved that for a high–Z material, as gold, the non linear heating problem is self–similar, if the specific internal energy ε, and the mean Rosseland free path l_R, of the material are non linear functions of its temperature T, and density ρ,

$$\varepsilon = \varepsilon_* T^{\mu} V^{\nu} \tag{2.36.a}$$

$$l_R = l_* T^{\mu_R} V^{\nu_R} \tag{2.36.b}$$

where $V=1/\rho$ is the specific volume, and $\varepsilon_*, \mu, \nu, l_*, \mu_R, \nu_R$ fitting parameters. The self–similar behavior of the heat transport through the medium permits to determine scaling laws between the absorbed energy by the medium and its temperature, or equivalently its radiative flux [2,3,15].

In our analysis, the description of the reemitted flux due to the medium heating is given by the scaling law proposed by Basko [2],

$$S_r(t) = K_r [E_w(t)]^{a} [S_w(t)]^{\beta} \tag{2.37.a}$$

where $E_{\rm w}$ defined by

$$S_w(t) = \frac{\partial E_w(t)}{\partial t} \tag{2.37.b}$$

is the total energy absorbed by the wall, and K_r, α, β are constants related with the physical properties of the wall material. These parameters can be calculated using the ablative heat wave self–similar solution of Pakula and Sigel [13].

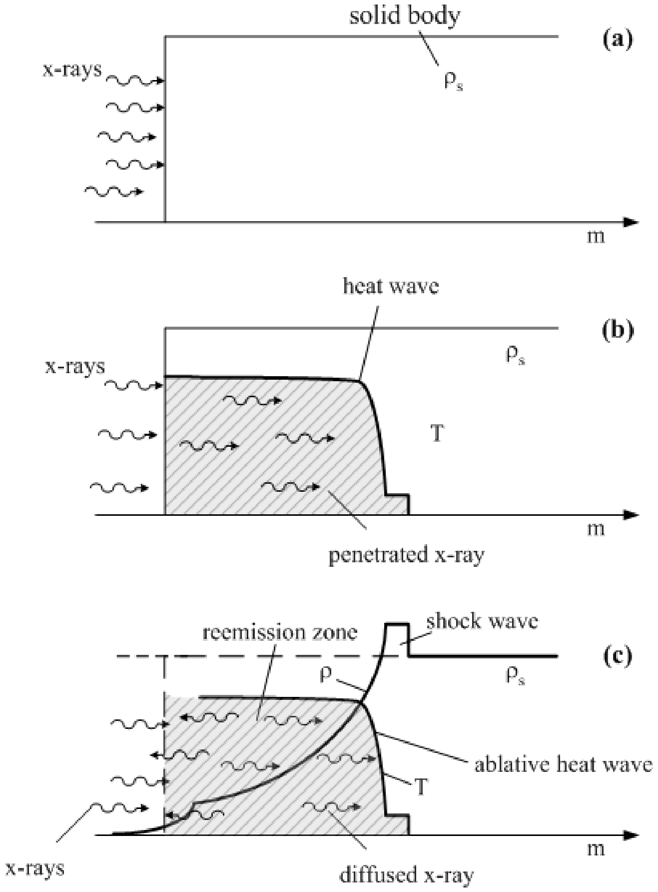

Figure 2.3 Formation of the ablative heat wave. (a) initial situation; (b) propagating heat wave; (c) ablative heat wave.

For the range of the temperature and matter density achieved in the gold cavities in our experiment (10 eV ≤ T ≤ 50 eV, $0.05\rho_s \le \rho \le 0.5\rho_s$; ρ_s, gold solid density), the scaling law parameters are [16]:

$$K_r = 4.7, \qquad a = 0.416 \ , \qquad \beta = 0.794$$

Using the energy exchange formulated in Eq. (2.35), Eq. (2.37.a) can be written in the equivalent form,

$$\frac{dE_w}{dt} + K_r(1-\eta_w)(E_w)^{\alpha}(\frac{dE_w(t)}{dt})^{\beta} = \eta_s S_0(t) \tag{2.38}$$

where the flux is measured in 10^{14} J/cm^2/sec. Eq. (2.38) is a non linear ordinary differential equation describing the time evolution of the absorbed energy by a wall element, given the source flux heating it. This equation is integrated numerically, replacing the time derivates with time difference operators, in order to obtain an equivalent non linear algebraic equation. Having calculated $E_w(t)$, the reemitted flux from a heated wall element and its equivalent radiative temperature are directly obtained by Eq. (2.37).

2.3.3 Total radiation flux coupled with the absorption foil

Now, we can calculate the total radiation flux heating the absorption foil. A simplified scheme illustrating the radiation coupling with the absorption foil is given in Figure 2.4. This figure shows that the flux heating the absorption foil is the sum of : (1) the directly coupled flux due to the radiation emitted from the rear of the conversion foil, and (2) the coupled flux due to the radiation emitted from the cavity wall.

For the flux heating the absorption foil due to the cavity wall emission, starting from Eq. (2.26) one obtains in a similar manner with Eq. (2.33),

$$S_{i,Wall}(t) = \eta_W S_r(t) \tag{2.40}$$

Also, for the flux heating the absorption foil due to its direct coupling with the conversion foil is

$$S_{i,CFoil}(t) = \eta_S S_0(t) \tag{2.41}$$

Thus, the total flux heating the absorption foil is

$$S_{i,TOTAL}(t) = \eta_W S_r(t) + \eta_S S_0(t) \tag{2.42}$$

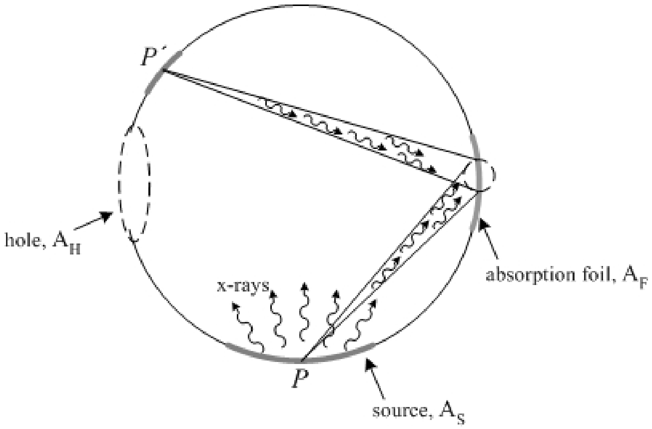

Figure 2.4 Total coupling scheme of the cavity radiation with the heated absorption foil.

Here, it would be useful to introduce the coupling factor α giving the ratio between the total flux heating the absorption foil and the total flux emitted at the rear of the conversion foil:

$$\alpha(t) \equiv \frac{S_{i,TOTAL}(t)}{S_0(t)} = \eta_S[\frac{\eta_W R(t)}{1-\eta_W R(t)} + 1] \tag{2.43}$$

Having calculated α, the hydrodynamic behavior of the absorption foil can be simulated with MULTI by driving it with the x–ray source flux weighted by the factor α. This is particularly important when $S_{i,CFoil} > S_{i,Wall}$, that is when the absorption foil is mainly heated by the source flux directly coupled with it. In this case, the weighted x–ray source, apart from the correct heating flux, involves in the simulation the source spectral distribution calculated by the code, and this description is more accurate than an equivalent Planckian radiator with its temperature obtained by the Stefan–Boltzmann law ($T_R = \sqrt[4]{S_{i,TOTAL} / \sigma}$, σ Stefan constant and T_R the radiative temperature).

References of Chapter 2

[1] R. Ramis, et al., MULTI – A computer code for one–dimensional multigroup radiation hydrodynamics, Comput. Phys. Commun. **49**, 475 (1988).

[2] M. Basko, An improved version of the view factor method for simulating inertial confinement fusion holraums, Phys. Plasmas **3**, 4148 (1996).

[3] G. D. Tsakiris, Energy redistribution in cavities by thermal radiation, Phys. Fluids B **4**, 992 (1992).

[4] L. Landau, E. Lifchitz, Physique Theorique, Tome 6 : Mecanique des fluides, Editions MIR (1989).

[5] Ya. B. Zel'dovich, Physics of Shock Waves and High–Temperature Hydrodynamic Phenomena, Academic Press, 1966.

[6] D. Mihalas, Stellar atmospheres, W. H. Freeman and Company (1978).

[7] B. I. Bennet *et al.*, Los Alamos report LA-7130 (1978).

[8] L. Spitzer, Physics of fully ionized plasmas, Whisley Interscience, 1962.

[9] D.Mihalas and B. Weibel Mihalas, Foundation of Radiation Hydrodynamics, Oxford University Press, 1984.

[10] P. Feautrier, C. R. Acad. Sc. **258**, 3189 (1964).

[11] A. Mirone et *al.*, Non–LTE opacity calculations with the $n - l$ splitting for radiative hydrodynamic codes, J. Quant. Spec. Radiat. Transfer **58**, 791 (1997).

[12] R. Sigel, "Laser Generated Intense Thermal Radiation", in Handbook of Plasma physics, North–Holland Editions, 1991.

[13] R. Pakula, R. Sigel, Self-similar expansion of dense matter due to heat transfer nonlinear conduction, Phys. Fluids **28**, 232 (1985).

[14] N. Kaiser, J. Meyer-ter-Vehn, and R. Sigel, The x–ray driven heating wave, Phys. Fluids B **1**, 1747 (1989).

[15] M. Murakami, J. Meyer-Ter-Vehn, Radiation symmetrization in indirectly driven ICF targets, Nucl. Fussion **31**, 1333 (1991).

[16] H. Merdji, Etude par spectroscopie d'absorption des opacities et des proprietes radiatives des plasmas chauds, These, Ecole Polytechnique, 1998.

Chapter 3 Laser and Instrumentation

3.1 Introduction

This chapter presents the techniques used in the experiments that we have performed in the installations of the LULI laboratory. First, we discuss the technical characteristics of the LULI2000 power lasers. Then, a description of the targets used in the experiments is given. We proceed with the presentation of the diagnostic instruments and their characteristics, as well as the corrections we had to apply on the measurements. Finally, we give the description of the auxiliary devices involved in the realization of the experiments.

3.2 LULI2000 laser facility

The experiments presented in this work were performed at the LULI2000 laser facility. Two main power laser chains are located in the laser hall, and in the experimental hall are found the vacuum chamber, the laser frequency doubling and the focusing system. In the following paragraphs, a brief description of the different stages is given.

3.2.1 Laser beam chains

The front–end stage of the laser consists of a Nd^{+3} doped YLF (Yttrium Lithium Fluoride) infrared crystal oscillator which emits at 1.053 μm. The oscillator output is pre–amplified and split in two laser beams of ~ 2.5 10^6 W (i.e., 4 mJ energy, 1.5 ns pulse duration), delivered into the amplification stage of each chain.

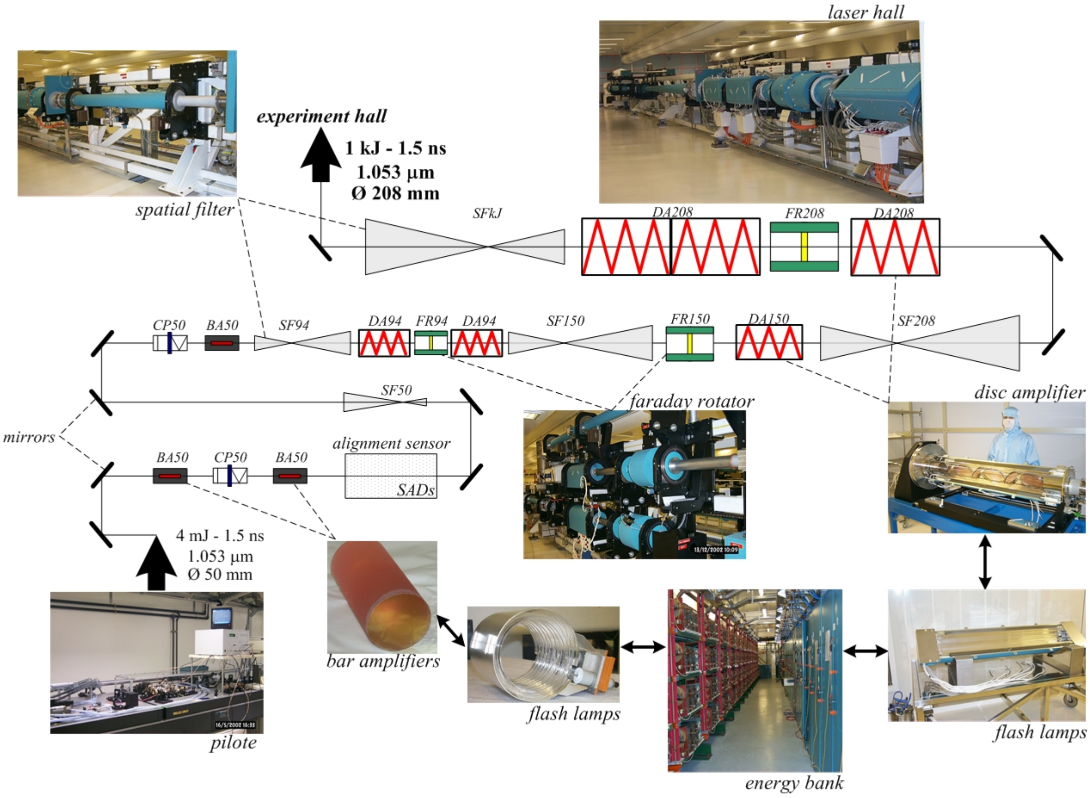

Figure 3.1 Schematic of the different stages composing the laser beam chain.

The structure of the amplification stage, shown in Figure 3.1, is composed of 4 substages of Nd^{+3} doped phosphate glass amplifiers [1]. Three bar amplifiers of 50 mm diameter (BA50) build the first substage, and the next three ones are disc amplifiers of 94, 150 and 208 mm diameter, respectively (DA94, DA150 and DA208). The laser pumping for rods and disks is obtained with a system of flash lamps filled with xenon gas, which emits a continuum spectrum covering the spectral range between the UV and the infrared. These flash lamps are supplied by the energy bank. The transfer of the laser beam is provided by a series of spatial filters (SF50, SF94, SF150, SF208 and SFkJ) adapting the beam diameter between the different substages. The power disc amplifiers (DA94, DA150 and DA208) are isolated with three Faraday Rotators (FR94, FR150 and FR208) which ensure the protection of the previous stages from the reflected power signals. The output of each laser chain has the following characteristics :

1. Flat–top pulse shape with 208 mm diameter.
2. 0.6 10^{12} W power at 1.053 µm wavelength
   (typical characteristics used : 1 kJ energy, 1.5 ns pulse duration).

3.2.2 Focalization of the laser beam–KDP crystal and random phase plate

In the experimental hall are the vacuum chamber and the systems delivering the power laser beams to the targets (see Fig. 3.2). In the vacuum chamber are placed the targets interacting with the laser beams, and also the different x–ray diagnostic instruments. Each power laser beam passes through a KDP frequency doubling crystal and is focused into a target by coupling a focus lens with a random phase plate (RPP).

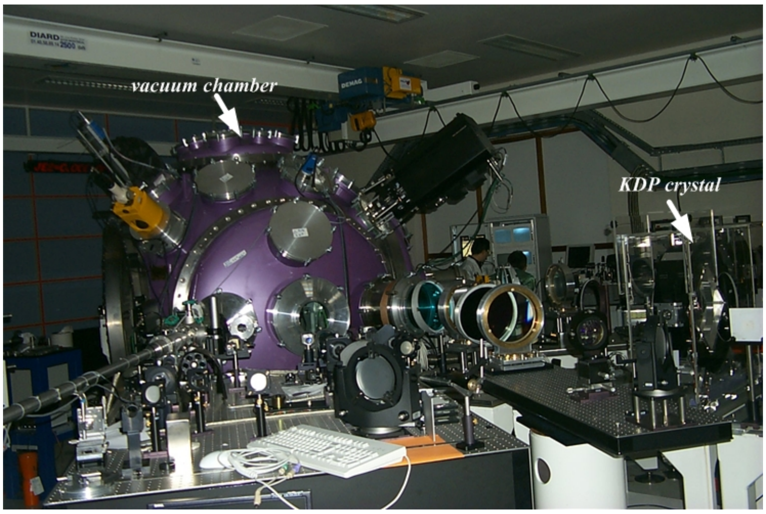

Figure 3.2 LULI2000 experimental hall.

KDP frequency doubling crystal

The YLF front–end stage emits a laser beam at 1.053 µm wavelength. However, due to many aspects – in particular the energy transport efficiency in the laser plasma interaction, the hydrodynamic behavior of the targets – experiments have shown that it is better to use laser pulses at shorter wavelengths [2,3]:

1. the heat front penetrates deeper within the target as the critical density is higher for shorter wavelengths.
2. the fast electrons production is reduced; so, the transport of energy is mainly due to thermal electrons, reducing consequently the target pre–heating.

For these reasons, each laser beams passes through a KDP crystal which doubles its frequency to obtain laser pulses at 0.53 μm wavelength. This conversion is due to the non linear behavior of the crystal material, and its energy efficiency depends on the crystal orientation. Figure 3.3 gives the conversion efficiency of the laser energy at 0.53 μm as a function of the orientation of the crystal x–axis.

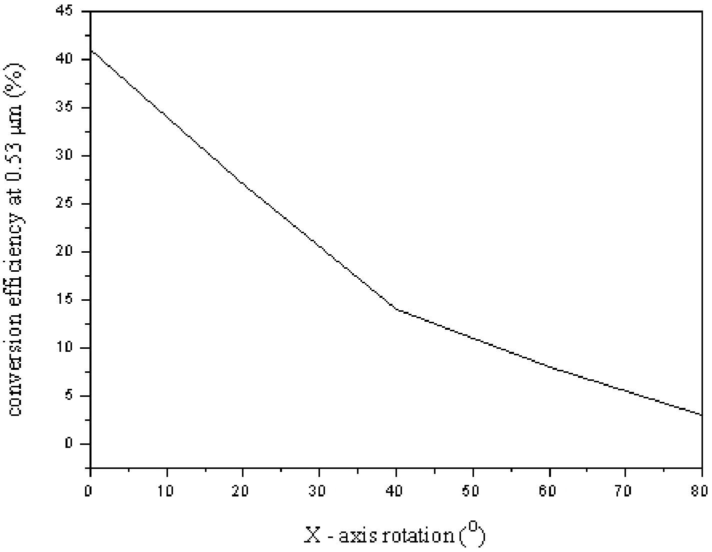

Figure 3.3 Energy conversion efficiency at 0.53 μm wavelength as a function of the angle of the KDP crystal x–axis.

Random Phase Plate (RPP)

The spatial distribution of the laser energy delivered on the targets is strongly related to the irradiation spatial uniformity of the laser wave front. Non–homogeneous focal spots with hot punctual areas are usually formed on targets irradiated directly with short wavelength lasers, due to interferences in the coherent laser beam [4]. This problem can be solved by coupling a random phase plate (RPP) with the focus lens of the laser beam to obtain a smoother focal spot. The RPP is composed of a two–dimensional array of small glass transmitting areas, each of which applies a phase shift of 0 or π rad, randomly chosen [5]. These glass areas act as diffracting elements and divide the laser beam into small beamlets with different phases, which are superimposed in the focal plane. The resulting intensity distribution consists of very closely spaced peaks bounded by the spatial distribution function of a single diffracting element. Now, due to the small spatial scale of the laser peaks, the plasma inhomogeneities are efficiently smoothed by thermal lateral conduction in the laser–matter interaction. The envelope function that modulates the spatial distribution on the focal plane is of the form $(\sin x / x)^2$ [6], and therefore the intensity distribution is

$$I(x,y) \sim I_o(x,y) \cdot [\frac{\sin(\pi d_x x / \lambda f)}{\pi d_x x / \lambda f}]^2 [\frac{\sin(\pi d_y y / \lambda f)}{\pi d_y y / \lambda f}]^2 \tag{3.1}$$

where $I_o(x,y)$ is the random distribution of the beamlets peaks, λ is the wavelength of the laser beam, f the focal length, x, y are the Cartesian coordinates measured on the focal plane, and d_x, d_y are the dimensions of the glass element. From Eq. (3.1) it follows that, for a given focal length f, the dimensions of the smoothed focal spot is determined by a proper choice of the dimensions of the RPP elements.

3.3 Targets description

3.3.1 Gas–jet for spectral emission characterization

The gas–jet targets are used here to measure the emission spectrum of xenon and krypton plasmas in non local thermodynamic equilibrium. The gas–jet targets were introduced in the research field of the laser produced plasmas for the advantages that they provide with respect to thin solid foil targets : (1) the large scale uniform produced plasmas, and (2) a plasma density adjustable with the gas pressure [7].

(a) (b)

Figure 3.4 (a) Image of the nozzle assembly in the experimental chamber. (b) Schematic cross–section of the nozzle.

In our experiment the gas–jets are produced by a cylindrical copper nozzle with a conical output aperture ending with a 1 mm diameter hole. The nozzle is supplied by a variable gas pressure backing system and its operation is controlled with a fast electro–valve (see Fig. 3.4). The spatial distribution of the gas–jet density of the nozzle was measured independently as a function of the gas pressure with a Mach–Zehnder interferometry experiment performed with helium and argon gas [7] (see also Appendix B). Figure 3.5 gives a typical experimental density profile obtained for a 20 bar pressure argon gas–jet, at 1 mm distance from the nozzle. The density shows a parabolic–like spatial variation as a function of the radius – measured from the center of the nozzle – with ~ 0.5 mm diameter plateau at its maximum where it is rather constant. Measurements for different pressures corresponding to the conditions of the xenon–krypton experiment, gave that the density maximum varies in the range of $2\ 10^{18} - 6\ 10^{18}$ cm^{-3}.

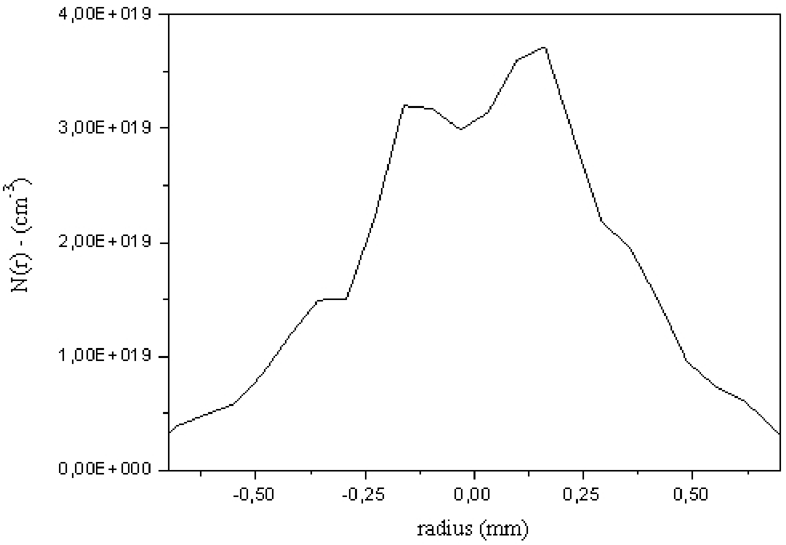

Figure 3.5 Neutral density profile of 20 bars argon gas–jet at 1 mm distance from the nozzle.

3.3.2 Spherical gold cavity for absorption spectra measurements

In the experimental study of the absorption of zinc sulfide (ZnS) plasmas, the absorbing foils are heated by the x–ray radiation confined in the interior of a spherical gold cavity. The image of the gold cavity is shown in Figure 3.6. Three holes are drilled in the 1.2 mm diameter cavity : at the front side, there is a 700 μm diameter hole covered with a 130 nm thick gold conversion foil which transforms the coherent laser beam energy into the incoherent x–ray radiation heating the cavity. At the lateral sides are two diagnostic holes of 250 μm diameter; one of them is covered by the absorption foil (see Fig. 3.6). They define the “diagnostic axis” along which the radiation probing the absorption plasma is propagating. The absorption foils are composed of thin solid ZnS or aluminium foils coated on both sides by carbon tampers. The thickness of the absorption materials is : 48.9 nm for ZnS and 74 nm for aluminium, which corresponds for both materials to 20 μg/cm^2 areal mass, and the carbon tampers are 35.3 nm thick corresponding to 8 μg/cm^2 areal mass.

The cavities were manufactured following a technology developed at the Max Planck Institut für Quantenoptik (MPQ) located in Garching bei München, Germany. The gold cavities are made in four different steps. First of all, a mandrel is machined in a copper block by a very precise lathe. In a way, the designed shape is the “negative” geometry of the cavity, i.e., basically a sphere. In a second step, the copper sphere is covered with a 13 μm thick gold layer in a deposition process. The next step of the process is the drilling of the holes. The final step consists in dissolving this copper filling the cavity in an acid bath that does not react with gold. At this stage, thin foils are simply-glued on the front wall, and the cavity is mounted on the target holder.

As we can imagine, the inner surface quality of the cavity is very important for the physics phenomena during the laser and x-ray interaction. In case of bad roughness, the effective area is modified and all kind of hydrodynamics perturbations are possible. In the process used, this quality depends of the quality of the lathe turning. For this, progressive actions of polish are made increasingly fine before covering with the gold layer.

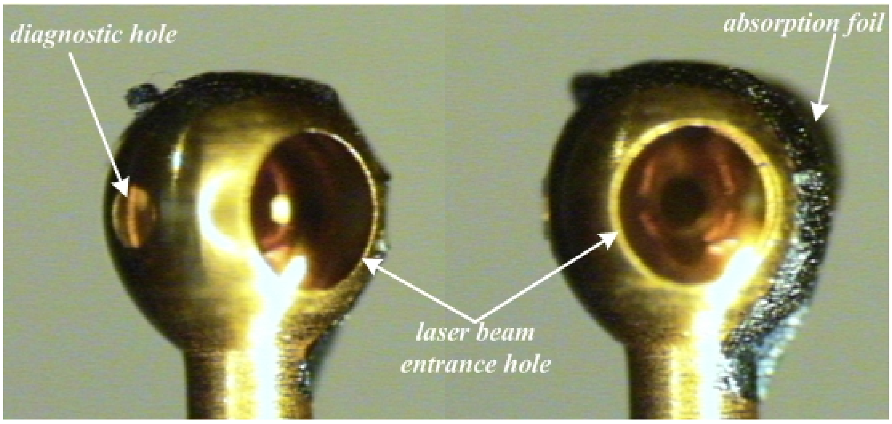

Figure 3.6 A spherical gold cavity of 1.2 mm diameter. The left image shows the entrance hole and the one of the two diagnostic holes; the absorption foil covering the second diagnostic hole appear in the image at the right.

3.4. Diagnostic instruments

3.4.1 Bragg crystal spectrograph

In the xenon–krypton experiment the time–integrated x–ray emission spectra in the keV range are measured with a double flat Bragg crystal spectrograph composed of a TlAP (thallium–hydrogen–phthalate) and an ADP (ammonium–dihydrogen–phosphate) crystals. The TlAP crystal permits to record the $3d$–$4f$ transitions of xenon in the range of 12 – 15 Å, and the ADP crystal the 2–3 and 2–4 transitions of krypton in the range of 6 – 8 Å.

Description of the spectrograph operation

The schematic of the spectrograph cross–section is given in Figure 3.7(b). It contains two independent 60 mm plates for mounting the crystals. The first plate forms a fixed angle of 60° with the plane of the recording device, and the second can be rotated at any angle using a micro–rotator. In this experiment the TlAP crystal is mounted at the fixed plate and the ADP crystal on the rotating plate. The plasma x–ray radiation enters in the device through a window composed of two slits of 4 mm length and 200 μm width. These slits prevent the generation of interference patterns on the crystal borders. In our experiment the dispersed radiation is recorded by a Kodak DEF film mounted on the spectrograph in a film cassette.

The operation of the spectrograph is based on the Bragg interference patterns obtained by a plane crystal. The condition for an incident x–ray, with a specific wavelength λ and an incident angle θ, to be reflected by constructive interference by the crystal lattice is given by the Bragg law,

$$m\lambda = 2d\sin\theta \tag{3.2}$$

where m is the diffraction order, and d is the lattice constant, i.e. the distance between the planes of the crystal structure; for the crystals used in the experiment, (1) $2d_{TlAP} =$ 25.9 Å, and (2) $2d_{ADP} =$ 10.648 Å.

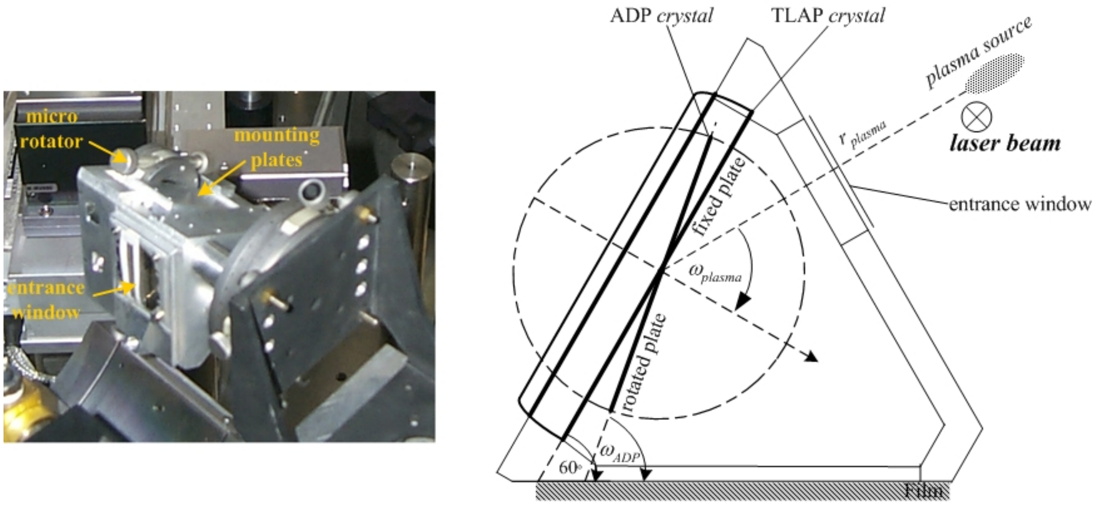

(a) (b)

Figure 3.7 (a) Image of the double Bragg crystal spectrograph. (b) Spectrograph cross–section (the alignment of the spectrograph with respect to the elliptic focal spot of the xenon–krypton gas–jet plasma is also shown).

The alignment of the spectrograph with respect to the gas–jet plasma is done by taking into account the simultaneous recording of the two spectral ranges of interest, as well as the operation of the Thomson scattering diagnostic (cf. §3.4.3). The spectrograph should not block the solid angle defined by the collecting lens of the Thomson diagnostic, ensuring the proper recording of the dispersed x–ray radiation. These constraints are fulfilled by the following positioning parameters (see Fig. 3.7(b)) :

- Distance between the plasma source and the center of the rotated crystal : r_{plasma} = 11.65 cm.
- angle of the plasma with the normal to the fixed crystal : $\omega_{plasma} = 60.55^{o}$.
- angle of the rotated crystal (ADP) with the plane of the film : $\omega_{ADP} = 70^{o}$.

Using these positioning parameters, in the next paragraph we calculate the spectral dispersion of the spectrograph.

Spectral Resolution

The operation of the spectrograph is limited by the geometrical characteristics of the different components involved on the spectrum recording procedure, namely by the size of the plasma and the film grain. To determine the effect of these parameters on the spectral resolution the calculation of the crystal dispersion is necessary.

a) Bragg crystal dispersion

The crystal dispersion is defined as the derivative of the recording position x of a ray reflected by the crystal, with respect to the wavelength λ of the incident ray on the crystal,

$$D(\lambda) = \frac{dx(\lambda)}{d\lambda} \tag{3.3}$$

From the geometry of Figure 3.8 we obtain

$$x(\theta) = \frac{y_o}{\tan(a+\theta)} \tag{3.4}$$

where α is the angle of the crystal with respect to the recording device, θ is the Bragg angle of the incident ray, and y_o is the distance from the film to the *plasma image*, symmetric of the plasma with respect to the crystal plane.

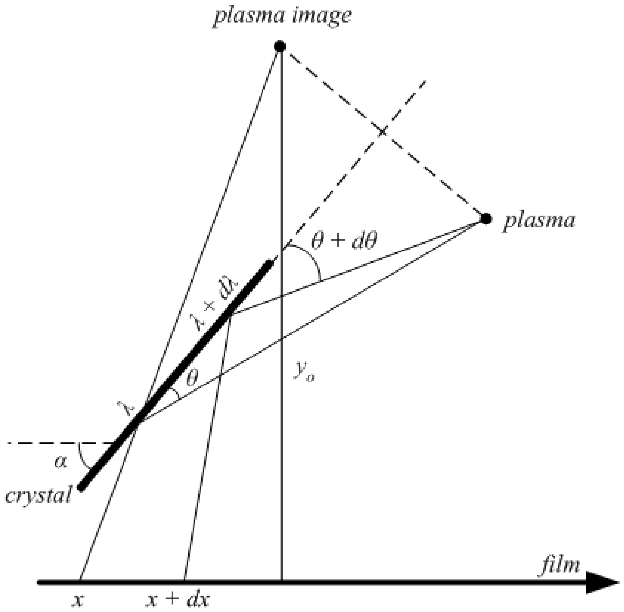

Figure 3.8 Calculation of the Bragg crystal dispersion with the image geometrical method.

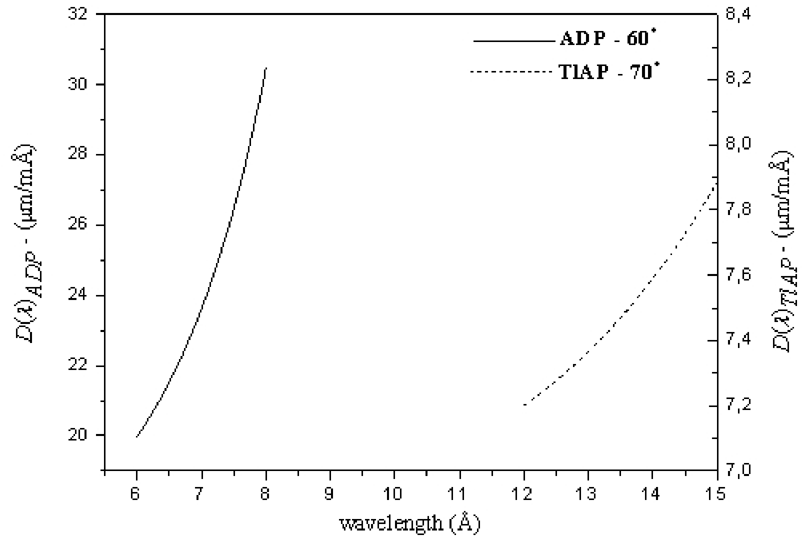

Figure 3.9 Dispersion curve of the ADP crystal in the range of 6 – 8 Å (full line), and of the TlAP crystal in the spectral range of 12 – 15 Å (dashed line); the crystal angles with respect to the film plane are, respectively, 60° and 70°.

Differentiating Eq. (3.4) with respect to θ and using the variable transformation,

$$d\lambda = 2d\cos\theta\, d\theta \tag{3.5}$$

we find

$$D(\lambda) = \frac{y_o}{2d} \frac{1}{\sin^2(\alpha + \arcsin(\frac{\lambda}{2d}))\sqrt{1-(\frac{\lambda}{2d})^2}} \tag{3.6}$$

The dispersion curves of the two crystals calculated for the experimental alignment parameters are given in Figure 3.9. As can be seen, in the spectral ranges of interest the dispersion for both crystals show a non linear monotonic variation with the wavelength. In particular, the dispersion of the ADP crystal varies in the range of 20 – 30 μm/mÅ and the dispersion of the TlAP crystal varies in the range of 7.2 – 7.9 μm/mÅ. This means that the position of the reflected rays on the film is a non linear function of the wavelength, which should be taken into account in the calibration of the spectra.

b) geometrical limitations of the spectral resolution

Due to the finite size of the plasma source and the film grain, a dispersed ray with wavelength λ is recorded at a non punctual area on the film, characterized by a length Δx in the dispersion direction. For a specific wavelength λ, the spectral resolution is given by the formula

$$\Delta\lambda = \frac{\Delta x}{D(\lambda)} \tag{3.7}$$

where $D(\lambda)$ is the dispersion of the crystal. Thus, to determine the spectral resolution in the case of the xenon–krypton experiment we have to account for : (1) the 1.6 μm diameter grain of the Kodak DEF film, and (2) the elliptical focal spot of the plasma characterized by a 150 μm minor and 1 mm major axis (cf. §3.5.4).

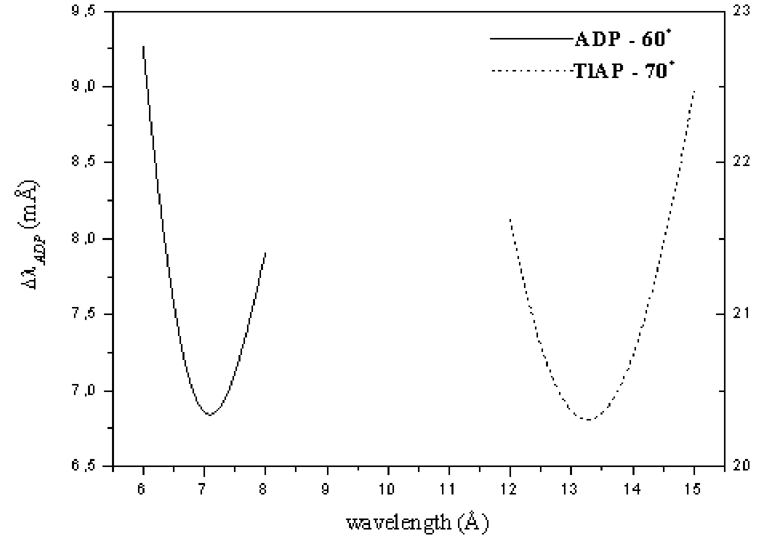

Figure 3.10 Spectral resolution curve of the ADP crystal in the range of 6–8 Å (full line), and of the TlAP crystal in the range of 12–15 Å (dashed line).

Concerning the film grain, and taking into account the variation of $D(\lambda)$ summarized in Fig. 3.9, we find that the spectral resolution that it imposes is ~ 0.2 mÅ for the TlAP and ~ 0.6 mÅ for the ADP crystal. This elliptical shape of the laser focal spot heating the plasma has been chosen to optimize the spectral resolution by setting the minor ellipse axis perpendicular to the plasma–crystal axis. Given the orientation and the positioning parameters, the variation of the spectral resolution with the wavelength has been calculated for both crystals, and the results are given in Figure 3.10. Both curves are symmetric around an absolute minimum, which for the TlAP crystal appears at 13.2 Å, and for the ADP crystal at 7 Å; the curves shape is imposed by the functional behavior of $\Delta x(\lambda)$. In the spectral ranges where the two crystals are used, the mean value of the resolution is ~ 22 mÅ for the TlAP crystal, and ~ 8 mÅ for the ADP crystal, determined by the 150 μm minor axis dimension of the heated plasma. In every case the limitation imposed by the film grain is much smaller and can be ignored.

Crystal reflectivity

In the keV x–ray range covered in our experiment, the reflectivity is strongly dependent on the wavelength of the scattered radiation, even for an ideal crystal structure. This implies the spectral dependency of the dispersed radiation intensity, that should be taken into account as "correction" in the procedure applied to deduce the intensity of the plasma emission from the recorded signal.

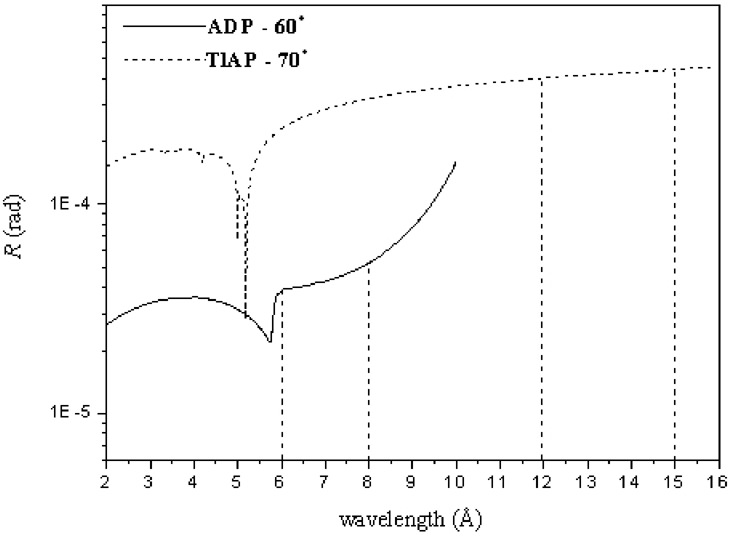

Figure 3.11 Integrated reflectivity of the ADP (full line) and the TlAP crystal (dashed line).

The quantity used to characterize the spectral response of the crystal is the *integrated spectral reflectivity* as is defined in the Darwin–Prins model [8]. Let I_o and I be the incident and the reflected intensity, respectively. The integrated reflectivity R is calculated by integrating the ratio I/I_o over the diffraction line profile of the reflected radiation, which in the case of the Darwin–Prins model is supposed to be a Lorentzian. Then R is given by

$$R = \frac{\pi}{2}\omega I(0)/I_o \qquad (3.8)$$

where $I(0)$ is the peak intensity, and ω the profile full width at half maximum (FWHM) of the reflected radiation. From Eq. (3.8), the intensity of the incident radiation can be calculated from the reflected peak intensity and the integrated reflectivity of the crystal. The integrated reflectivity of the ADP and the TlAP crystal are given in Figure 3.11[8,9]. As we can see for both crystals, and in the spectral ranges of interest, the reflectivity shows a very small variation with the wavelength with no discontinuities: R_{ADP} varies in the range of $3\ 10^{-5} - 5\ 10^{-5}$ rad, and $R_{TlAP} \sim 4\ 10^{-4}$ rad. The reflectivity corrections can be approximated by second order polynomials.

3.4.2 Transmission grating XUV spectrograph

The measurement of the time–resolved x–ray spectra in the range of 20 – 200 Å are performed in both experiments with a transmission grating spectrograph coupled to a streak camera (cf §3.5.1). In the case of the xenon–krypton experiment this spectral range covers the unresolved transmission structures n = 5–4 and 4–4 of the xenon, as well as the structures n = 4–3 and 3–3 of the krypton emission spectrum. In the case of the ZnS experiment this spectral range contains the absorption structures 2*p*–3*s* and 2*p*–3*d* of sulfur and the structures 3*d*–4*f* of zinc.

Description of the spectrograph operation

The setup of the XUV spectrograph given in Figure 3.12 is based on the SPARTUVIX model [10]. It consists of a spherical mirror, which acts as the plasma radiation collecting element, and a transmission grating placed in the optical path between the mirror and the detector, which is the dispersive element of the spectrograph. For our spectrograph, a nickel (Ni) mirror of R = 5200 mm curvature radius and a gold transmission grating of 2000 lines/mm are used.

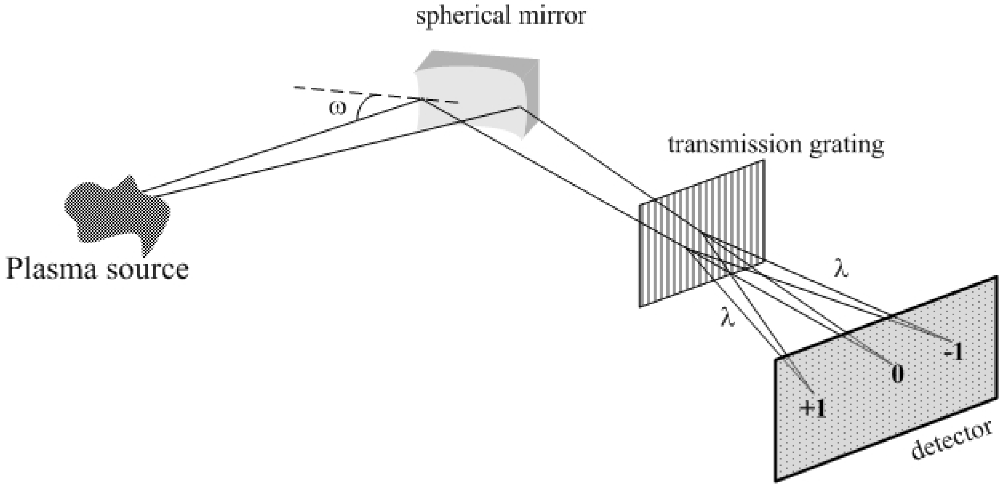

Figure 3.12 Schematic of the XUV spectrograph disposition.

The dispersion equation of the transmission grating can be obtained by reference to Fig. 3.13. In this figure is given a part of a transmission grating periodic structure, with distance d between two neighboring slits. Assuming a radiation wave front incident on the grating with angle θ_o, we determine the variation of the transmitted wave front as a function of the direction angle θ. According to the Fresnel principle each slit of the grating acts as a secondary wave source, with its angular distribution described by the Fresnel–Kirchhoff diffraction integral [6]. All these sources are coherent, and their phase at a distant observation point differ from each other by integral multiples of $d.p$, where

$$d \cdot p \equiv BL - AK = d\left(sin\theta - sin\theta_o\right) \tag{3.9}$$

is the total path difference at the observation point between the light passing from two neighboring slits (see Fig. 3.13). The total intensity distribution results from the interference between all the secondary sources, and it is given by the formula

$$I(p) = I_o[\frac{\sin(N \cdot kdp/2)}{\sin(kdp/2)}]^2[\frac{\sin(kap/2)}{kap/2}]^2 \tag{3.10}$$

where I_o is the intensity of the incident wave, $k = 2\pi/\lambda$ its wavenumber and N is the number of the grating slits. The first term of Eq. (3.10) describes the interference between the wave fronts of the secondary sources, and the second term is a slow varying envelope function of the interference distribution, due to the diffraction of each single secondary source. The former presents its maxima when the denominator $\sin(kdp/2)$ vanishes :

$$p = \frac{m\lambda}{d} \qquad ,m = 0, \pm 1, \pm 2,... \tag{3.11}$$

and from Eq. (3.9) we obtain

$$\frac{m\lambda}{d} = sin\theta - sin\theta_o \tag{3.12}$$

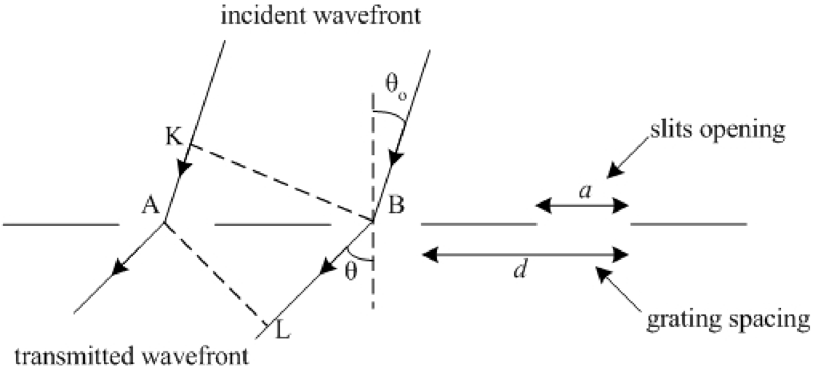

Figure 3.13 Simplified scheme of a transmission grating periodic structure.

Eq. (3.12) is the corresponding Bragg law of the transmission grating describing its behavior as a dispersive element. For an incident wave front perpendicular to the transmission grating, and for small dispersion angles, Eq. (3.12) simplifies to

$$m\lambda = d\frac{x}{\sqrt{x^2 + {l_{gd}}^2}} \approx d\frac{x}{l_{gd}} \tag{3.13}$$

where m is the dispersion order, x is the recording position on the detector of a transmitted ray measured in the dispersion direction, and l_{gd} is the distance *transmission grating–detector* (see also Fig. 14 below). So, in this limiting case, the recording position on the detector of a dispersed ray is a linear function of the wavelength.

Spectrograph alignment and spectral resolution

a) determination of the spectral resolution parameters

The spectral resolution of the XUV spectrograph is limited by : (1) the intrinsic resolving power of the grating, (2) the finite size of the detector elements, and (3) the finite size of the plasma source in conjunction with the geometry of the spectrograph disposition.

The intrinsic spectral resolution of the grating is given by the formula [6,11],

$$\frac{\Delta\lambda}{\lambda} = \frac{1}{mN} \tag{3.14}$$

where m is the dispersion order, and N the number of the grating slits illuminated by the plasma radiation collected by the mirror. In our case the intrinsic grating resolution in the spectral range of 20 – 200 Å is ~ 3 mÅ. Due to this fine resolving power, the transmission grating does not introduce limitations on the spectrograph resolution, and its contribution can be ignored.

The spectral resolution $\Delta\lambda$ due to the finite size Δx of the plasma recorded image on the detector – determined from the dimensions of the detector elements and the plasma size – can be calculated readily from Eq. (3.13),

$$\Delta\lambda = \frac{d}{l_{gd}} \Delta x \tag{3.15}$$

The detector of the streak camera coupled to the grating in both experiments has a constant recording minimum dimension Δx_{det}= 100 μm. The minimum size associated to the finite size of the source is given by

$$\Delta x_{source} = G \cdot \Delta s \tag{3.16}$$

where Δs is the diameter of the source, and G is the magnification factor of the spectrograph setup. Consequently, the spectral resolution determined by the detector and the source depends explicitly on the geometry of the setup as described hereunder.

b) choice of the XUV spectrograph alignment parameters

The geometrical parameters of the spectrograph are shown in the detailed scheme of Figure 3.14. The distance *plasma source–detector* is determined by the mechanical properties of the experimental chamber (l_{pd} = 1065 mm). To optimize the spectrograph for our experimental conditions, we have to determine the parameter l_{gd} in conjunction with the different distances: distance *plasma source–mirror* (l_{pm}), *mirror–transmission grating* (l_{mg}), *mirror–detector* (l_{md}), and with the incidence angle ω.

Concerning the operation of the spherical mirror, the distances *plasma source–mirror* (l_{pm}) and *mirror–detector* (l_{md}) are related by the following relationships [12],

$$\frac{1}{l_{pm}} + \frac{1}{l_{md}} = \frac{2}{R\sin\omega} \tag{3.17.a}$$

$$l_{md} = G \cdot l_{pm} \tag{3.17.b}$$

where R is the curvature radius of the spherical mirror and G the magnification factor of the disposition. The best dispersion is obtained by maximizing the distance l_{md}, i.e. minimizing the distance l_{mg}. So, we fixed l_{mg}=65 mm from mechanical arguments. Then, expressing the parameter l_{gd} as a function of G, one obtains

$$l_{gd} = l_{md} - l_{mg} = (1+G)\frac{R}{2}\sin\omega - l_{mg} \tag{3.18}$$

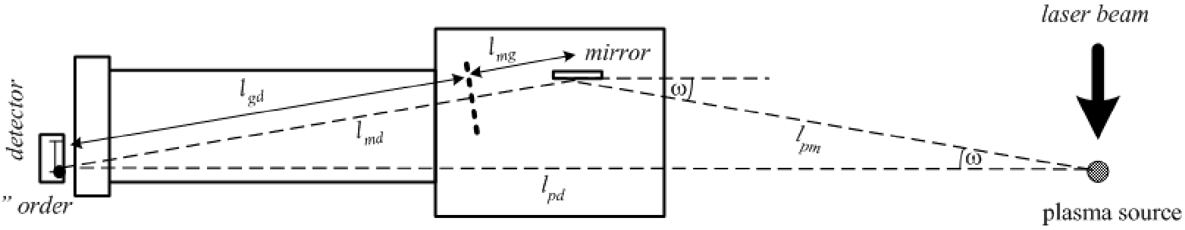

Figure 3.14 Top view of the XUV spectrograph disposition in the experimental chamber where are shown the alignment geometrical parameters (G = 1).

Further, the incident angle ω is related to the magnification factor G by the non linear formula

$$l_{pd} = \frac{1+G}{G}\frac{R}{2}\sin\omega\sqrt{1+G^2+2G\cos(2\omega)} \tag{3.19}$$

The numerical evaluation of Eq. (3.18), (3.19) permits to calculate the distance l_{gd}. With Eq. (3.15), the spectral resolution is also a function of G.

c) calculation of the spectral resolution

We can now evaluate the magnitude of the spectral resolution introduced by the detector elements and the source. We calculate them numerically, in the case of the xenon–krypton experiment, where the plasma source diameter is Δs = 200 μm. The full line of Figure 3.15 is the spectral resolution due to the source calculated with the non linear system of Eq. (3.15)–(3.19) for different values of G in the range of 0.1 – 2; the dashed line is the spectral resolution due to the detector elements (Δx_{det}= constant = 100 μm) calculated respectively with the Eq. (3.15), (3.18) and (3.19).

The resolutions have the same order of magnitude and therefore we have to take both into account for the calculation of the total spectral resolution, according to the quadratic formula

$$\Delta\lambda = \sqrt{\Delta\lambda_{source}{}^2 + \Delta\lambda_{\det}{}^2} \tag{3.20}$$

The result is given in Figure 3.16, where is shown also the variation of the incident angle on the crystal. The spectral resolution takes its minimum value of 2.3 Å for G = 0.7. However, as the spectral resolution around the absolute minimum varies slowly, the magnification factor has been set to G = 1 in order to make the alignment easier and more accurate. For this value of G the spectral resolution is 2.4 Å. Furthermore, the incident angle is 6°, and as we will see in the paragraph concerning the mirror reflectivity, this value imposes the acceptable low limit of 20 Å on the spectrograph bandwidth.

A similar analysis in the case of ZnS experiment, where the diameter of the plasma source determined by the diagnostic hole of the gold cavity is Δs = 250 μm (see Chapter 5) and Δx_{det}= 100 μm, gives for G = 1 a spectral resolution of 2.7 Å and an incident angle of 6°.

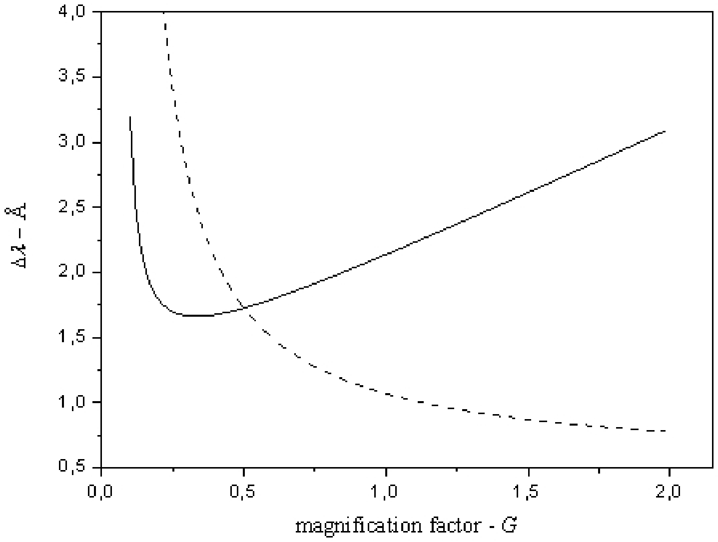

Figure 3.15 Numerical results calculated for the parameters of the xenon–krypton experiment. Full line : spectral resolution due to the finite size of the plasma source (Δs = 200 μm), dashed line : spectral resolution due to the finite size of the detector elements (Δx_{det} = 100 μm)

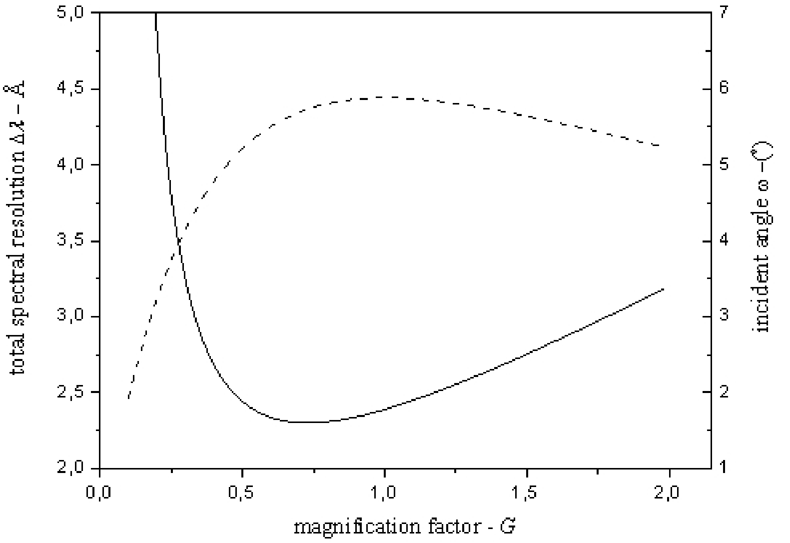

Figure 3.16 Full line : total spectral resolution calculated with Eq. (3.20), dashed line : incident angle of the x–rays on the spherical mirror.

These data have been checked during the xenon–krypton experiment. For this we have measured the slope of the K–edge of a beryllium (Be) absorption filter. Figure 3.17 gives the recorded emission spectrum of a gold foil irradiating a 1 μm thick Be filter, around the spectral range of the Be K–edge. The figure shows also the theoretical transmission curve of the filter obtained from the tabulated data of CXRO [13]. The slope of the K–edge is found around 5 Å corresponding to a spectral resolution of 2.5 Å, in good agreement with the theoretical value.

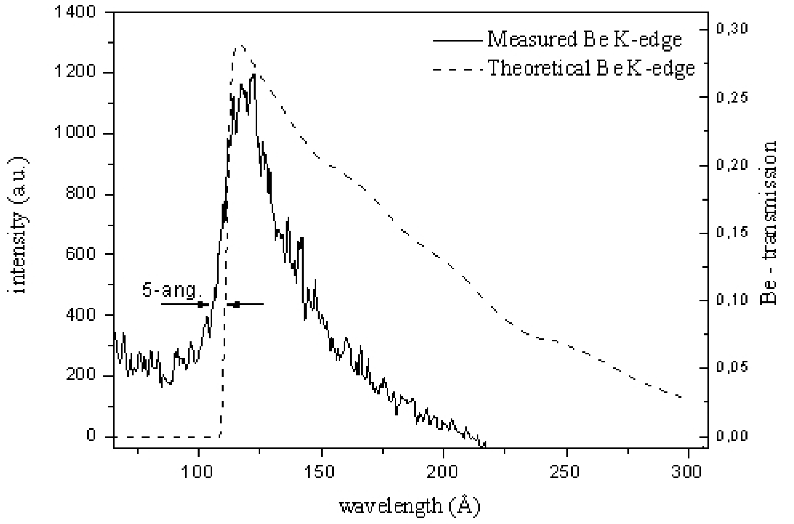

Figure 3.17 Measurement of the slope enlargement of the Be filter K–edge due to the spectral resolution.

Grating transmission efficiency

The transmission efficiency is defined as the ratio of the photons transmitted through the grating to the incident photons. In the case where the grating wires are assumed to be totally opaque, this attenuation is ruled by the radiation distribution given by Eq. (3.9). However, in the keV range a fraction of the incident radiation is transmitted through the grating wires, and is subject to an attenuation and a phase shift which depend on the refraction index and the thickness of the wire. So now, one should take into account, additionally to the formal description of Eq. (3.10), the interference between the radiation penetrating through the wires and the radiation which is transmitted freely through the grating slits.

The above statements are included in the model of Schnopper [14,15]. According to this, the transmission efficiency as a function of the radiation wavenumber k, and for a given dispersion order m, is given by

$$\tau_m(k) = [\frac{\sin(Nm\pi)}{N\sin(m\pi)}]^2[\frac{\sin((a/d)m\pi)}{m\pi}]^2(1+e^{-2k\beta z}-2e^{-k\beta z}\cos(k\delta z)) \tag{3.21}$$

where a, d are respectively the slit and spacing dimensions; β is the imaginary part of the wire refraction index, δ is its real part, and z is the thickness of the wire. The first term in Eq. (3.21) is the normalized N–slits interference pattern of Eq. (3.10), and in our case is equal to 1 due to the integer values of m. The second term is the modulation factor of the transmitted radiation due to the single slit diffraction pattern, and the last term represents the interference between the radiation transmitted through the wires with the radiation transmitted through the slits. Further, applying twice Eq. (3.21), one can show that the ratio of the mth–order to the 1st–order transmission efficiency is

$$\frac{\tau_m}{\tau_1}=[\frac{\sin((a/d)m\pi)}{m\sin((a/d)\pi)}]^2 \tag{3.22}$$

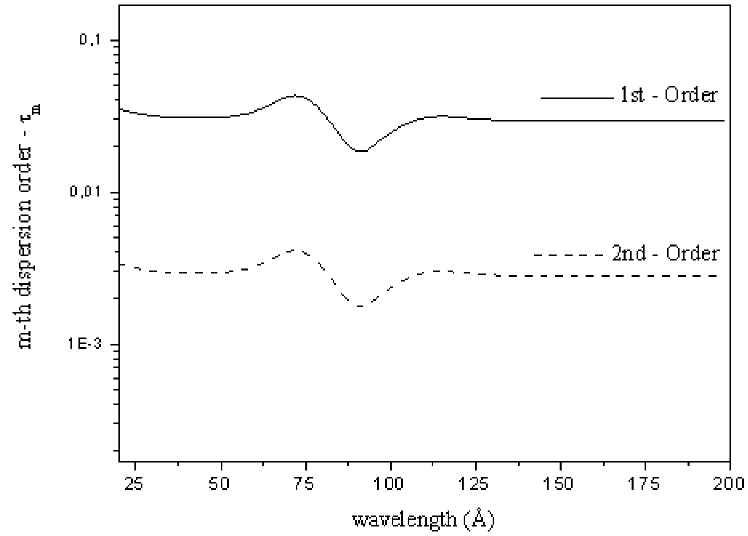

Figure 3.18 Transmission efficiency calculated for the 1st and the 2nd–dispersion order of a gold grating with 2000 lines/mm, 2200 Å thick wires and 0.6 cyclic ratio.

In both experiments the spectrograph uses a gold transmission grating with a cyclic ratio *a*/*d* = 0.6 and 2200 Å thick wires. For these values, and using the gold refraction index obtained form the tabulated data of CXRO [13], the transmission efficiency is calculated by Eq. (3.21) for the first and the second dispersion order and shown in Figure 3.18. A first remark is that the efficiency of both dispersion orders is almost constant in the spectral range of 20 – 200 Å, except the interval of 60 – 100 Å where weak variations are observed. Further, the efficiency of the 2nd–order represents 10% of the 1st–order, which can be verified easily from Eq. (3.22). This implies that the incident radiation on the detector results from the superposition of different dispersion orders. Therefore, to deduce the intensity of the incident radiation on the grating from the radiation recorded on the detector a deconvolution procedure is necessary. The description of this procedure is given in the following paragraph where the spectral corrections that should be applied on the measured spectra are presented.

Spectral corrections

a) mirror reflectivity

The reflectivity of the spherical mirror depends on the wavelength and the angle of the incident radiation (“grazing angle”). This dependency should be taken into account to obtain the intensity level of the measured spectrum. Figure 3.19 gives the reflectivity of the Ni–mirror for a 6° grazing angle; the curve is obtained from the tabulated data of CXRO [13]. In the spectral range between 20 and 200 Å the reflectivity of the mirror shows a weak variation, and a sharp decrease giving a zero reflectivity below 20 Å. This implies that the mirror acts as a filter cutting the hard x–ray radiation. This characteristic prevents the saturation of the spectrograph detectors from the high energetic photons; indeed, we had to take this into account for the choice of the spectrograph magnification factor and the grazing angle of the mirror.

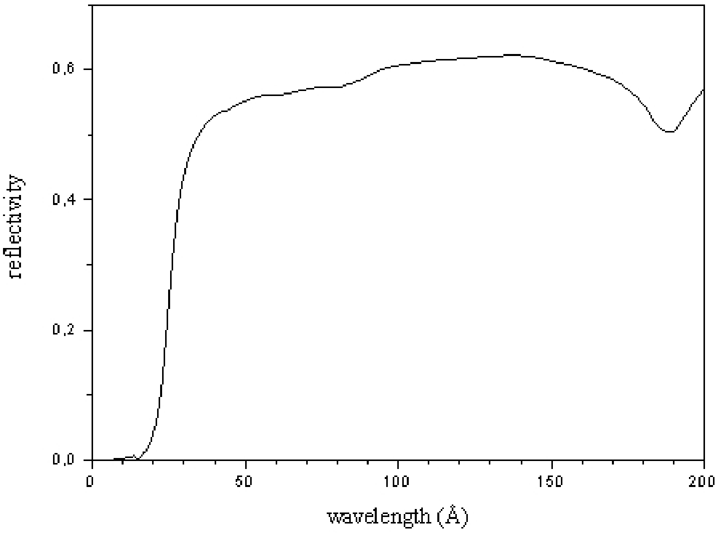

Figure 3.19 Reflectivity of the spherical mirror for a 6^{o} grazing angle. The mirror is composed of a 80 nm nickel layer deposited on a SiO_2 substrate; the curve is obtained from the CXRO data [13].

b) deconvolution of higher dispersion orders

As the superposition of the different dispersion orders have to be eliminated to deduce the intensity of the incident radiation, a deconvolution procedure has to be applied on the recorded spectrum to subtract the higher dispersion orders. The incident radiation on the detector, $I_{det}(\lambda)$, results from the superposition of the different dispersion orders, weighted by the mth–order efficiency τ_m of the grating, or

$$I_{\det}(\lambda)=\sum_{m=1}^{\infty}\tau_m(\lambda/m)\cdot I_o(\lambda/m) \tag{3.23}$$

where $I_o(\lambda)$ is the incident radiation on the grating. If the detector is characterized by a spectral response $H(\lambda)$, then the measured radiation recorded by the detector is $I_{rec}(\lambda)=H(\lambda)\cdot I_{\det}(\lambda)$, and Eq. (3.23) gives

$$I_{rec}(\lambda)=\sum_{m=1}^{\infty}H(\lambda/m)\cdot\tau_m(\lambda/m)\cdot I_o(\lambda/m) \tag{3.24}$$

To deduce $I_o(\lambda)$ from the measured quantity $I_{rec}(\lambda)$, we re–write Eq. (3.24) as

$$I_o(\lambda)=\frac{1}{H(\lambda)\cdot\tau_1(\lambda)}[I_{rec}(\lambda)-\sum_{m=2}^{\infty}H(\lambda/m)\cdot\tau_m(\lambda/m)\cdot I_o(\lambda/m)] \tag{3.25}$$

The problem with Eq. (3.25) is that, except the known quantity $I_{rec}(\lambda)$, it involves also the unknown functions $I_o(\lambda/m)$. This can be overcome by a recursive procedure that takes advantage of the low limit λ_o of the spectrograph bandwidth imposed by the spherical mirror (λ_o = 20 Å for our application). Due to this, there is a spectral range between $\lambda_o - 2\lambda_o$ in which the dispersed radiation recorded by the detector is equal to the 1st dispersion order of $I_o(\lambda)$. Thus, in a first step we calculate from Eq. (3.25)

$$I_o(\lambda) = \frac{1}{H(\lambda)\cdot\tau_1(\lambda)}[I_{rec}(\lambda)] \qquad ,\lambda \in [\lambda_o,\, 2\lambda_o]$$

Then, because $I_o(\lambda)$ is known in the range of $\lambda_o - 2\lambda_o$, in a second step we get

$$I_o(\lambda) = \frac{I_{rec}(\lambda)}{H(\lambda)\cdot\tau_1(\lambda)} - (\frac{H(\lambda/2)}{H(\lambda)})\cdot(\frac{\tau_2(\lambda/2)}{\tau_1(\lambda)})\cdot I_o(\lambda/2) \qquad ,\lambda \in [2\lambda_o,\, 3\lambda_o]$$

and recursively we find for the *n*–th step

$$I_o(\lambda) = \frac{I_{rec}(\lambda)}{H(\lambda)\cdot\tau_1(\lambda)} - \sum_{m=2}^{n}[(\frac{H(\lambda/m)}{H(\lambda)})\cdot(\frac{\tau_m(\lambda/m)}{\tau_1(\lambda)})\cdot I_o(\lambda/m)] \qquad ,\lambda \in [n\lambda_o,\, (n+1)\lambda_o] \tag{3.26}$$

The contribution of m–th dispersion order on the measured radiation is weighted by the ratio τ_m/τ_1. This poses a limit on the deconvolution steps, as we can drop out the terms for which $\tau_m/\tau_1 << 1$. In our case, from Eq. (3.22) we find that this holds for m > 2, and thus the deconvolution can be reduced to the first two dispersion orders.

3.4.3 Thomson scattering diagnostic

Thomson scattering was introduced in the domain of laser produced plasmas as a diagnostic method to measure the density and the electronic temperature, using the scattered laser light due to the plasma ionic and electronic fluctuations [16,17] (see Appendix A). In the xenon–krypton experiment this technique provides the independent measurement of the plasma parameters, which are used for the theoretical calculations of the plasmas emission spectrum (cf §4.4).

A top view of the experimental setup is given in Figure 3.20 [18]. The laser beam, which interacts with the gas–jet to produce the plasma, acts on the same time as the probing beam of the Thomson diagnostic (Thomson “self–scattering” approach). The scattered light by the produced plasma is collected by a *f* = 300 mm achromatic lens at an angle of 135° with respect to the propagation direction of the laser beam. The scattered light is then driven to a 50/50 beam splitter producing two independent beams to analyze simultaneously the ionic and the electronic scattering spectra. One of the beams reflected by the splitter is driven to the spectrograph analyzing the electronic spectrum. In its optical path a *f* = 500 mm lens is placed properly to focus the beam on the entrance slit of the spectrograph coupled with the streak camera. Similarly, the beam transmitted through the splitter is focused by a *f* = 700 mm lens to the spectrograph analyzing the ionic spectrum.

The measurement of the ionic scattering spectrum is performed with a high resolution SOPRA spectrograph. The spectrograph is composed of a curved mirror and a reflection grating of 1200 lines/mm. Its operational range covers a narrow bandwidth of ± 5 nm around the wavelength of the plasma producing laser beam (0.53 μm) with a resolution of 0.2 nm. These characteristics permit to measure unambiguously the two ionic satellites, which appear very close to the laser frequency. The dispersed light is coupled to the entrance window of a achromatic IMACON Hatland S20 streak camera, which permits to measure the time evolution of the ionic scattering spectra with a speed of 200 ps/mm.

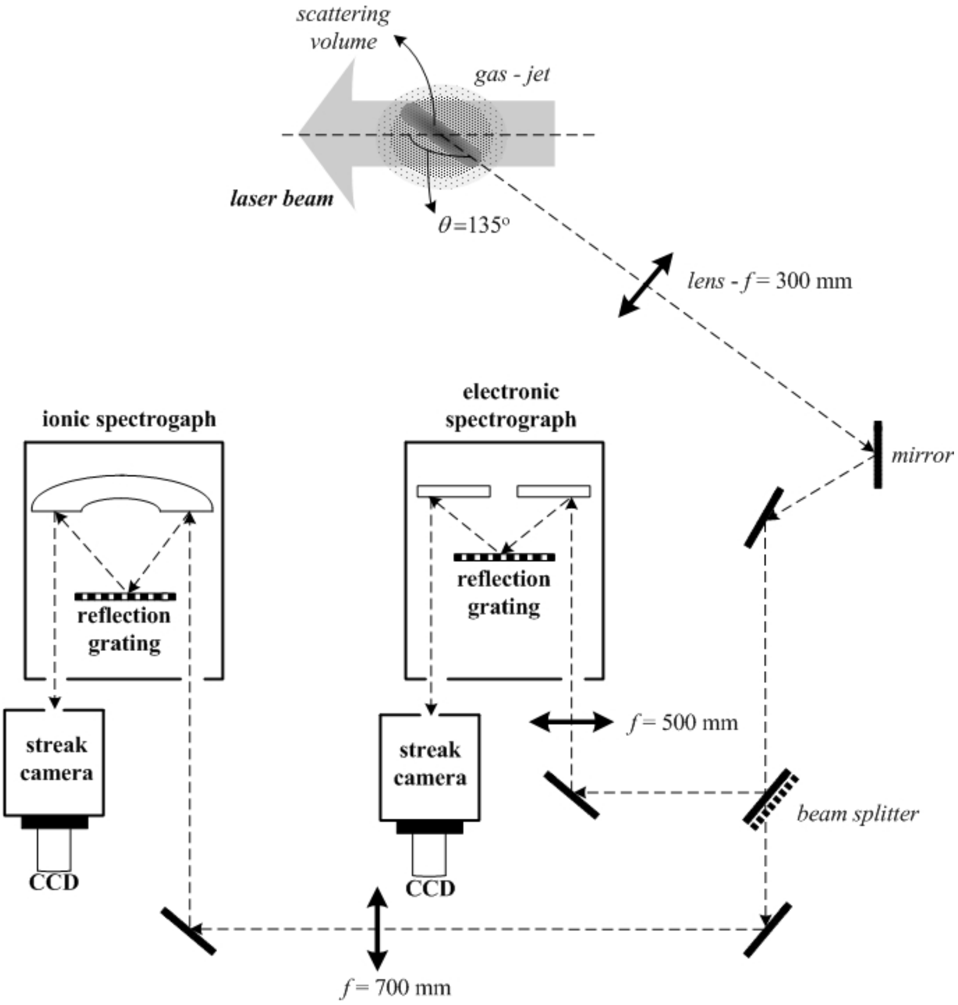

Figure 3.20 Top view scheme of the experimental setup of the Thomson scattering diagnostic.

For the measurement of the electronic scattering spectrum a medium resolution SPEX spectrograph is used, which is composed of two plane mirrors and a reflection grating of 100 lines/mm. The spectrograph operates in a bandwidth of 400 – 700 nm with a resolution of 6.4 nm. Thus, it covers the interval where the electronic satellites of the scattering spectrum are expected to appear, due the range of plasma parameters obtained under the given experimental conditions. The output of this spectrograph is also time–resolved by using a second achromatic IMACON Hatland S20 streak camera. The time resolved spectra of both spectrographs are recorded with two 12-bit CCDs of 512x512 pixel resolution.

The power level of the ionic satellites exceeds strongly that of the electronic satellites, inducing the saturation of the electronic spectrograph. This problem is solved by placing an interference filter in front of the electronic spectrograph. The light scattered in a spectral bandwidth ± 5 nm around the laser wavelength (ionic spectral range) is strongly attenuated and almost 100% of the light out of this bandwidth is transmitted.

The wavelength calibration of the spectrographs has been realized using the characteristic emission lines of a mercury lamp. The dispersion constant of the ionic spectrograph was found equal to 0.02 nm/pixel and the corresponding one for the electronic spectrograph is equal to 0.26 nm/pixel.

3.5 Auxiliary devices and other diagnostics

3.5.1 Streak Camera

The measurement of the XUV spectra time evolution is performed by coupling the XUV spectrograph with a Kentech x–ray streak camera. The streak is optimized to operate in the x–ray range of 0.1 – 10 keV covering the spectral range of our experiments (0.1 – 1 keV). This paragraph gives the description of the device operation, and the corrections applied to extract the measured spectra from the recorded images.

Description of the device operation

A scheme of the streak camera showing the main operational characteristics of the device is given in Figure 3.21. Initially, the x–rays falling on the cathode generate photoelectrons which are accelerated in the high electric field region between the cathode and the grid. The electrons, passing through the grid, converge spatially due to the operation of the focus cone. The focused electrons pass through a small opening on the anode and they are inserted in the region of the deflection plates. There, a variable electric field is applied to the electrons which are deflected perpendicularly to their propagation direction. Thus, the photoelectrons sweep the phosphor surface and produce a fluorescence light signal. This signal is then amplified by the intensifier providing an intensity level that can be detected by the CCD camera. The deflection electric field is produced by superposing a bias with a ramp voltage, which are adjusted externally to control the sweep speed of the device.

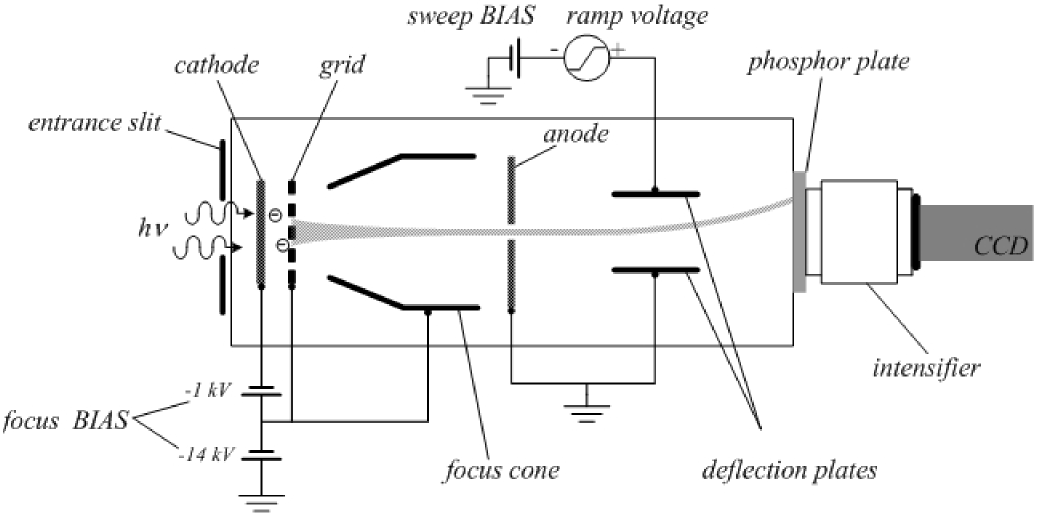

Figure 3.21 Scheme of the Kentech streak camera.

If a narrow slit is placed in front of the streak, perpendicular to the deflection direction, its image will appear on the phosphor with a magnification factor of 2. The slit is aligned with the dispersion direction of the transmission grating, so that the deflection of this image permits to record the time evolution of the XUV spectrum.

In our experiments a complex structure x–ray cathode is used, with a Cesium Iodide (CsI) semiconductor as active material. It is composed of a 1200 Å thick solid CsI layer of 0.225 g/cm^3 density plus a very thin aluminium layer (250 Å thick). The aluminium layer ensures mainly the electrical conductivity of the cathode, but it also participates to the photoelectrons generation. This composite structure is deposited on a 1000 Å thick Lexan ($C_5H_7O_2$) layer of 2.06 g/cm^3 density which serves as a high x–ray transmission mechanical support.

The photoelectron generation is due to the interaction of x–ray photons with the cathode. The x–ray photons fall on the cathode from the Lexan side, which acts like an energy filter, and passing through interact with the CsI layer (CsI, aluminium). The deposited x–ray energy is converted initially to photoelectrons and to Auger electrons within the body of the photocathode. These internal electrons cause subsequently the excitation of secondary electrons, mainly by carrying the electrons from the valence to the conducting band. Nearly all the deposited energy of the x–ray photons is converted to secondary electrons; only a small fraction escapes from the photocathode in the form of fast primary electrons and fluorescence radiation.

The CsI cathode was chosen due to the high yield of secondary electrons with respect to other materials, as gold (Au) and palladium (Pd) also used to fabricate cathodes in the spectral range of 0.1 – 10 keV [19,20].

Time resolution and spectrum image deformation

(a) time resolution

The time resolution of the XUV spectrograph is determined by the characteristics of the streak camera, in conjunction with the geometrical properties of the spectrograph setup. The limiting factor of the streak operation is mainly the deflection speed. This parameter determines whether the generation at two different times of two photoelectrons on the cathode is recorded at two discrete spatial points on the phosphor plate. In Figure 3.22 is given the time evolution of the phosphor plate sweep, for different ramp voltages applied on the deflection plates, as it was measured by the manufacturer [20]. During the phosphor plate sweep, the deflection speed determined by the slope of the curves can be assumed as being constant. The different nominal values of the deflection speed are summarized in the first column of Table 3–I.

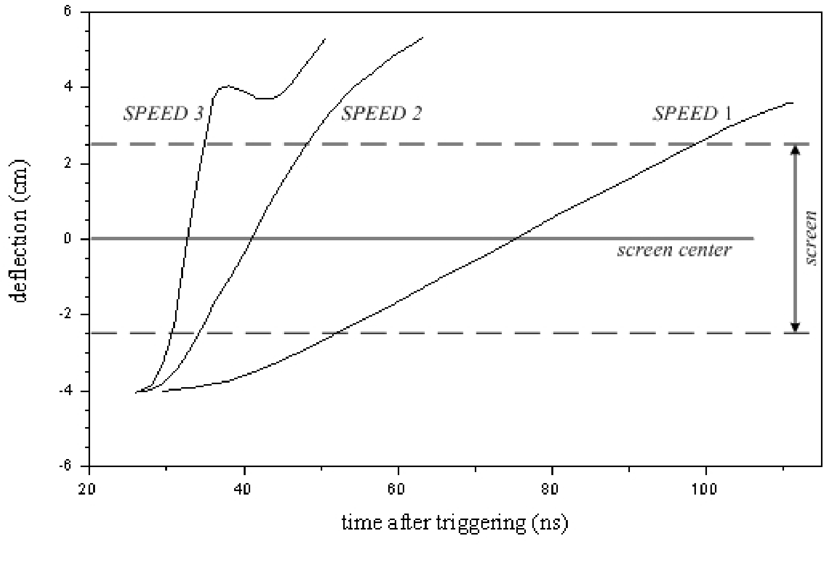

Figure 3.22 Time evolution of the electron beam deflection for different ramp voltages [20].

Given the value of the deflection speed, the time resolution of the spectrograph is determined by the pixel size of the CCD camera, as well as by the width of the entrance slit. The columns 3–5 of the table give the resolution limitations due to the different CCD cameras and the slit used in the experiments. In every case, the limitations of the CCDs are negligible and the time resolution is determined by the width of the entrance slit.

label	Speed (mm/ns)	time resolution (ps)		
		ARP CCD (19 μm)	ANDOR CCD (13 μm)	entrance slit (200 μm)
1	1.2	16	11	167
2	4	5	3	50
3	13.5	1.4	1	15

Table 3–I Time resolution imposed by the components of the XUV spectrograph calculated for the different sweep speeds of the streak camera.

(b) spectrum image deformation

The intensifier adds a radial aberration on the recorded spectrum image which has to be corrected to measure the time evolution of the spectra. The model describing this deformation can be understood with the help of Figure 3.23. In Fig. 3.23(a) the geometrical equivalent of a proper image is given, characterized by a rectilinear coordinates grid. Due to the operation of the intensifier, the measured image takes the form of the curvilinear grid given in Fig. 3.23(b). Taking as a reference the center of the intensifier (C), the polar coordinates on the two images of a given point *P*, are related with the following transformation

$$r' = r - \alpha r^3 \tag{3.27.a}$$

$$\theta' = \theta \tag{3.27.b}$$

where α is the deformation parameter. From Eq. (3.27), we see that the intensifier changes the radial position of the measured image points, but not their angular position. Once the parameter α is known, the correction is simply performed by the inverse transformation of Eq. (3.27).

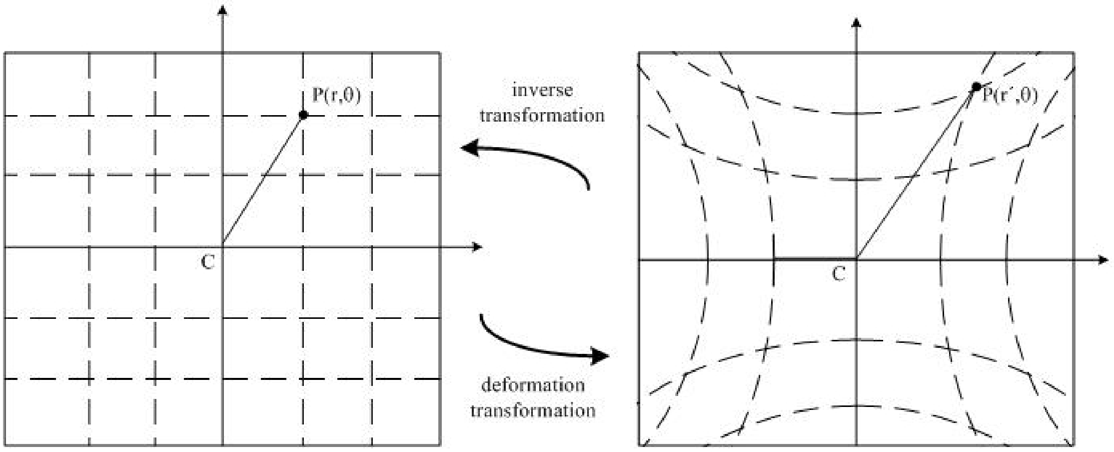

(a) (b)

Figure 3.23 Modelization of the intensifier deformation. (a) Proper spectrum image, (b) deformed spectrum image.

The correction is performed using a special utility developed in the IDL environment. A two–step procedure is applied. First, a curvilinear grid calculated by the code is superimposed on the deformed images. Adjusting the deformation parameter α, and comparing the fit of the calculated grid to the spectrum image, an estimation of the intensifier deformation is obtained (see Fig. 24(a)). In a second step, the code calculates the inverse transformation of Eq. (3.27) for a matrix of a discrete number of points (16 radial x 32 angular), following the corrected polar coordinates. Then, the polar coordinates of all the image points are calculated from the inverse transformation matrix with an interpolation procedure, giving the corrected image (see Fig. 24(b)).

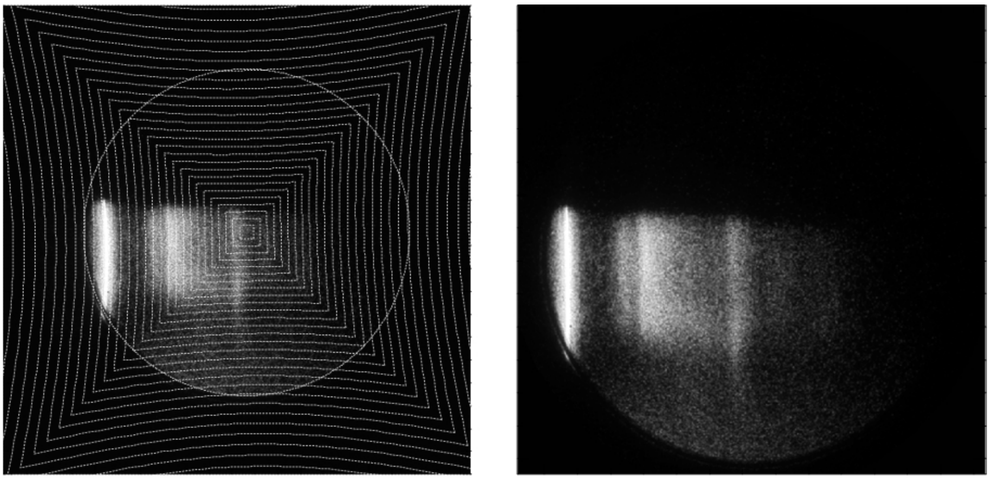

(a) (b)

Figure 3.24 Correction of the intensifier deformation applied on a recorded XUV spectrum image.

Spectral response

The sensitivity of the cathode with the energy of the incident photons has to be included in the spectral corrections, to deduce the intensity of the measured spectrum. The spectral response of the cathode is mainly determined by the behavior of the CsI and the aluminium layers, which are the active photoelectric materials. However, in order to describe it properly we also have to take into account the absorption of Lexan, which determines the number of photons falling on CsI (CsI, aluminium).

The spectral dependence of the photoelectrons generation is described by the phenomenological model of Henke [19,21]. The number of the secondary photoelectrons emitted per incident photon, or "quantum yield", from the back side of a CsI layer is given by

$$Y_{CsI}(E) = (a_{CsI}\kappa_{CsI}(E)E\rho_{CsI})e^{-(l_{CsI}\kappa_{CsI}(E)\rho_{CsI})} \tag{3.28}$$

where E is the energy of the incident photon, $\kappa_{\mathrm{CsI}}(E)$ is the absorption coefficient of CsI, ρ_{CsI} its matter density, l_{CsI} is the thickness of the CsI layer, and a_{CsI} is a constant coefficient depending on the nature of the material. Given the incident radiation, which interacts with the material generating the primary electrons, the linear term of Eq. (3.28) is proportional to the escaping secondary electrons. The exponential term represents the attenuation of the incident photons due to the interactions within the CsI body. As the escaping secondary electrons come from a very thin layer at the back side of the CsI body (of the order of 100 – 200 Å), the photons penetration length l_{CsI} provides, in a first approximation, that the primary electrons are generated within this layer.

Taking into account the attenuation of the aluminium and Lexan layers, as well as the photoelectron generation within the aluminium body, the extension of Eq. (3.28) is written [21,22],

$$Y_{Cath}(E) = [(a_{CsI}\kappa_{CsI}(E)E\rho_{CsI})e^{-(l_{CsI}\kappa_{CsI}(E)\rho_{CsI})} + a_{Al}\kappa_{Al}(E)E\rho_{Al}]e^{-(l_{Lexan}\kappa_{Lexan}(E)\rho_{Lexan}+l_{Al}\kappa_{Al}(E)\rho_{Al})} \quad (3.29)$$

The significance of the additional parameters appearing in the above equation is evident, and we mention only that a_{Al} is a coefficient depending on the nature of aluminium. The curve of Eq. (3.29) for the nominal values of the cathode parameters (thickness, density) used in the experiments is shown in Figure 3.25 (full line). The transmissions and the opacities of the materials (CsI, aluminium and Lexan) are obtained from the tabulated data of CXRO [13]. Also, the material coefficients were calculated by the research group of C. Reverdin during the absolute calibration measurements performed on various CsI cathodes at the LURE synchrotron [22].

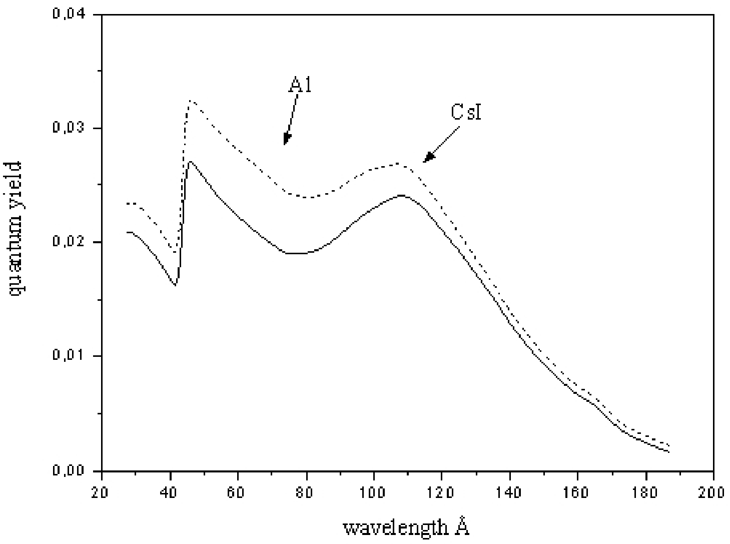

Figure 3.25 Quantum yield spectral response of the CsI cathode (CsI, aluminium). Full line : Yield calculated with the nominal values of the cathode materials. Dashed line : Yield calculated by supposing a 25% oxidation of the aluminium layer (Note : given the Lexan thickness, the response in the range of 40 – 90 Å is determined mainly by the aluminium layer and above 90 Å by the CsI layer)

The problem with the application of the Henke model is the change that the cathode experiences with time. These long–scale changes are caused by the unavoidable contact of the cathode with the atmosphere during its use. The affecting mechanisms are mainly : (1) the oxidation of the aluminium layer, and (2) the hydration of the CsI layer. The oxidation of the aluminium layer results in the formation of a Al_2O_3 coat on the cathode, which changes its photoemission efficiency. The dashed curve of Fig. 3.25 is a typical example of this behavior. This curve is calculated by supposing that the alumimium layer of the cathode is composed of 75% pure aluminium and of 25% Al_2O_3, with all the other parameters unchanged. Though the shape of the curve does not change significantly, there is a variation in the relative ratio of the observed structures, especially at low wavelengths where the quantum yield is mainly determined by the aluminium photoemission. The other affecting mechanism is the absorption of atmospheric water vapor by the hydrophilic CsI surface. Due to this, there is a variation of the CsI effective surface area, or equivalently a variation of its photoemission [20]. This mechanism is more difficult to be modeled, and we mention only that, in fact, it causes a change on the ratio between the photoemissions efficiencies of the CsI and aluminium layers.

The cathode used in the experiments is not calibrated. Even if the cathode is under a nitrogen atmosphere as long as possible, unavoidable changes in its sensitivity limit the accuracy of the corrected XUV spectra. We will discuss this point further in Chapter 4, where we will analyze the influence of the cathode model on the correction of the xenon–krypton plasma XUV emission spectrum.

3.5.2 CCD Cameras

The charge coupling device (CCD) camera is a structure of small photodiodes arranged in series of rows and columns, as is shown in Figure 3.26(a). Each element ("pixel") captures a small fraction of the image. The whole image is obtained by scanning the structure of the discrete photodiodes. The operation of the CCD is based on the doubled function carried out by the pixel: the transformation of the image photons into charges, with pixel acting as photodiode, and the charge storage due to its capacitor–like behavior, as described in more details hereunder.

The CCD cameras are usually fabricated using the metal–oxide–semiconductor (MOS) technology. A cross section of a typical MOS structure is shown in Fig. 3.26(b). It contains a *p*–type silicon substrate ("body") where the photoelectric generation of electron–hole pairs takes place. Over the substrate, a thin layer of silicon dioxide (SiO_2) is grown insulating the body of the semiconductor from the high conduction poly silicon layer, which forms the device electrodes. The poly silicon layer is developed in three insulated spatial regions covering the body of the semiconductor, forming three electrodes which are necessary for the production of the electric signals controlling the device operation.

Applying a high bias voltage on the gate electrode, and a low bias voltage on the coupling electrodes, the pixel operates as a photosensitive MOS capacitor. In this mode the mobile holes of the substrate are repulsed from the region under the gate, leaving the negative charges of the fixed acceptors ions. Thus, a space charge region is formed, and a potential well which confines the photoelectrons generated by the incident photons. The photoelectrons enhance the formed channel under the SiO_2, and this procedure is continued, with the pixel charge to increase as more photons interact with the semiconductor, till the saturation of the capacitor occurring at the full of the potential well.

Inverting the bias of the electrodes, the charge stored on each element is transferred sequentially to its neighbor. Therefore, by applying a proper clocking scheme on the coupling electrodes of the pixels, the charges are shifted, one row at a time, to the shift register. This structure is equivalent with a row of the CCD array, with the same number of pixels, but is masked so that no photon can fall on it. In this way the produced charged pattern of the image area is scanned and can be further processed digitally.

A main limitation on the operation of the CCD is imposed by the thermally generated electron–hole pairs in the depletion region of the body. These electrons give a fog signal which is known as dark current (as it is the only signal produced by the semiconductor when it is not exposed in light). Dark current is added on the accumulated photoelectrons as intrinsic noise signal, and should be as low as possible. As the thermal charge generation is an exponential function of the semiconductor temperature, this is achieved by decreasing the operational temperature of the CCD.

The technical characteristics of the different CCD cameras used in our experiments are summarized in Table 3–II. The Andor CCD provides a minimum operational temperature of ~ -20^{o} due to its internal cooling capability. Concerning the thermal oriented limitations, this camera gives excellent measurement conditions, as for a diminution of the temperature in the range between 0^o and -20^o its dark current is decreased of ~ 90%. In our conditions of laser shots at very low repetition rate (a shot per hour), the ARP and COHU cameras which operate at room temperature can be used. The background signal is acceptable when these devices are gated with a small acquisition duration.

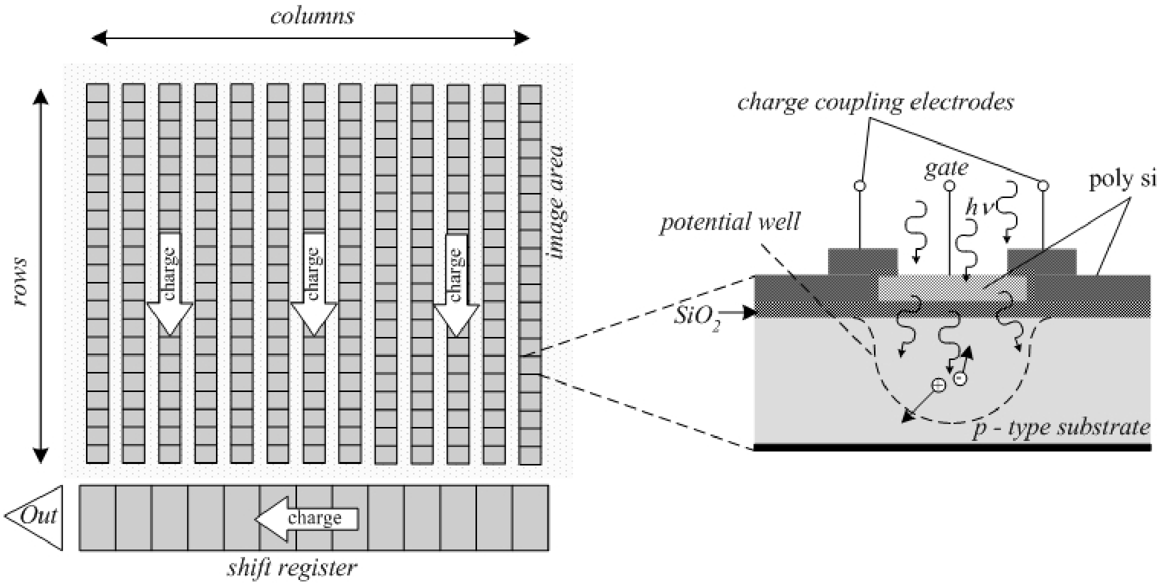

(a) (b)

Figure 3.26 (a) Top view of a typical CCD array structure. (b) Single pixel cross–section where is shown the internal electronic operation.

CCD	pixels (H)x(V)	pixel size (µm) (H)x(V)	image area (mm) (H)x(V)	used for
ANDOR – 16 bit	1024 x 1024	13.3 x 13.3	13.3 x 13.3	streak
ARP – 12 bit	521 x 512	19 x 19	-	streak / pinhole (main beam)
COHU – 8 bit	732 x 290	9.2 x 16.8	6.4 x 4.8	pinhole (backlight)

Table 3–II : Technical characteristics of the CCD cameras used in the experiments (for the pinholes cameras, the CCDs are directly exposed to x–rays).

3.5.3 Kodak DEF film

In the xenon–krypton experiment the time–integrated x–ray spectra measured by the Bragg spectrograph are recorded on a double emulsion direct exposure film (DEF) of Kodak [23]. This film was chosen due to its high sensitivity in the spectral range of 1 – 10 keV, which covers the spectral range of interest in our experiments.

A cross–section of the film structure is shown in Figure 3.27(a). It is composed of two 13 µm thick photosensitive emulsion layers which are deposited above and below a 185 µm thick polyester ($C_5H_4O_2$) substrate. As is shown in Figure 3.27(b), each emulsion layer is protected with a 1 µm thick overcoat, and consists of an heterogeneous system of 1.6 µm diameter AgBr grains imbedded in a gelatin layer. The AgBr grains are the active photosensitive material, and the body of the emulsion layer can be viewed as an overlay of AgBr monolayer surfaces, with the emulsion gelatin diffused between them. For the spectral range used here, the polyester substrate absorbs the x–ray photons and only one emulsion is involved in the photographic process.

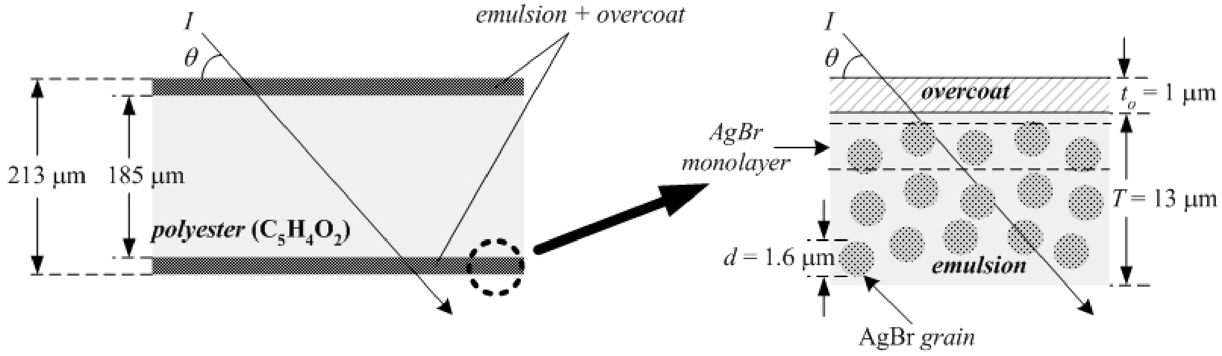

(a) (b)

Figure 3.27 (a) Structure of the double–emulsion DEF film of Kodak. (b) Cross–section of the photosensitive emulsion layer.

The x–ray spectrum is obtained by deducing the incident radiation intensity from the optical density of the film. To this end, the semiempirical model of Henke is used, which permits to characterize the response of the film in the x–ray range, taking into account the energy and the propagation direction of the incident radiation [23–25]. This model is based on a phenomenological description of the physical processes taking place during the exposure of the film, from which it follows that the optical density of the film D is related to the intensity of the incident radiation I by a universal function,

$$\alpha D = \varphi(\beta I) \tag{3.30}$$

where the parameters α, β are :

$$\alpha = \frac{\mu' / \sin\theta}{1 + \mu' d_o / \sin\theta} \tag{3.31.a}$$

$$\beta = [1 - \exp(-\mu_1 d)]\exp(-\mu_o t_o / \sin\theta) \tag{3.31.b}$$

and where :

μ', μ_1 and μ_o are, respectively, the energy dependent linear absorption coefficients of the heterogeneous emulsion layer, of the AgBr grain, and of the overcoat layer,
d_0 is the effective depth of the AgBr monolayer surface,
d is the diameter of the AgBr grain,
t_o is the thickness of the overcoat layer,
and θ, is the angle of the incident radiation with respect to the film surface (see Fig. 3.27(b))

The form of the universal function results by a fitting of calibration data, and in the case of a thin emulsion film of thickness T (that is, for an emulsion body which does not absorb all the incident photons) Eq. (3.30) becomes [24],

$$\alpha D = a \ln\left[\frac{1 + b\beta I}{1 + b\beta I \exp(-\mu' T / \sin\theta)}\right] \tag{3.32}$$

where

$$a = 0.68\ \mu\text{m}^{-1} \qquad \text{and} \qquad b = 1.69\ \mu\text{m}^{2}$$

are two semiempirical parameters obtained by the calibration of the film[1] [23].

These parameters, or equivalently the calibration data, are affected by the exposure conditions as well by the development conditions of the film. Due to this, a strict process was followed during the experiment. First, the exposed film in the experimental chamber was protected from visible light by a 7 μm thick beryllium filter. After the exposure to the x–ray radiation, the film was developed, fixed and washed with constant temperature solutions at 20^{o}. Then, the film was scanned, and the measured optical density was transformed into the incident radiation intensity (photons/μm^{2}), with a software utility using Eq. (3.32) based on the Henke model [23].

3.5.4 Pinhole cameras

A x–ray pinhole camera records on a detector device (film, or CCD) the time and spectral integrated image of a plasma source, with a spatial resolution which is determined by the diameter of the entrance hole of the camera. This diagnostic instrument permits to estimate indirectly the focal spot of the laser beam, by measuring the dimensions of the produced x–ray plasma source. A simplified scheme of a pinhole camera is given in Figure 3.28. The dimension D of the recorded image on the detector is related to the plasma dimension d by the formula

$$D = Gd \tag{3.33}$$

where the magnification G of the instrument is

$$G = \frac{R}{r}[1 + \frac{t}{d}(\frac{r}{R} + 1)] \approx \frac{R}{r} \tag{3.34}$$

The dimension of the pinhole is mainly determined by the size and the luminosity of the plasma source. Further, the range of the spectral integration is defined by the filters placed in front of the pinhole, which mainly reject the visible light and soft x–rays (sub–keV). A common practice is to use a pinhole with different entrance holes of various diameters, in front of which are placed different filters.

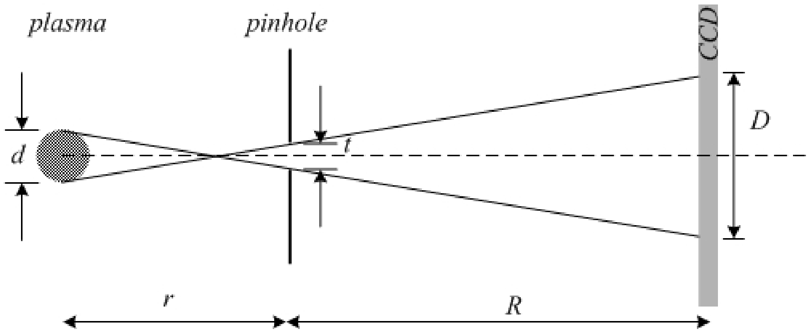

Figure 3.28 Scheme of the pinhole camera operation principle.

---

[1] We have to notice at this point, that the contribution to the optical density of the second emulsion layer becomes important for photons energy above 4000 eV, and therefore in our case it can be ignored [31]

This setup is used in both experiments for the pinhole monitoring the laser beam heating the targets to produce the measured plasmas. This pinhole contains three entrance holes of 5, 10 and 20 μm diameter, respectively, arranged in a triangle of 1mm side. The spectral range is determined by a beryllium filter of 23 μm thickness in front of the ARP CCD that is used as recording device. A typical recorded image obtained for a 500 μm diameter focal spot is given in Figure 3.29(a).

The laser beam producing the backlight in the experiment for the characterization of the ZnS absorption (cf. §5.2.1), is monitored by a single–hole pinhole camera of 23 μm diameter. In this case the temporal and spectral integrated image was recorded on a COHU CCD camera, in front of which a composite filter is placed containing a 23 μm thick Be plus 100 μm thick Mylar layer. A typical image obtained for an elliptical plasma source (150 μm x 1mm size) is given in Fig. 3.29(b)

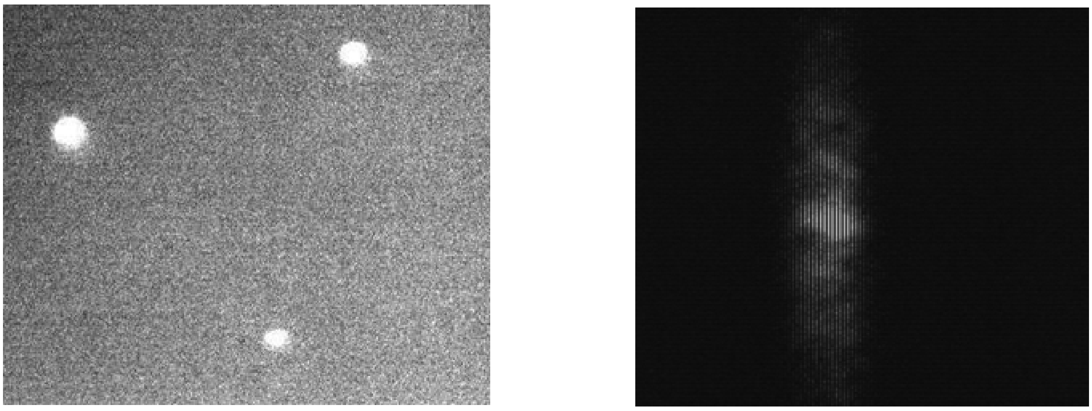

(a) (b)

Figure 3.29 (a) Image of the three–hole pinhole camera monitoring the main beam of LULI facility. (b) Image of the single–hole camera monitoring the backlight laser beam in the ZnS experiment.

3.5.5 Streak camera differential pumping system

To accelerate the photoelectrons of the streak camera a high intensity electric field is necessary, which is produced by applying a high voltage (1 kV) on the very closely spaced photocathode and grid. To avoid an electric breakdown the operation of the streak under very low pressure conditions is necessary ($< 10^{-4}$ mbar). Generally, the low pressure inside the vacuum chamber is provided by a permanently installed pumping mechanism. This system contains two pumping turbines and can give pressures of the order of 10^{-5} mbar. The problem with the gas–jet target is that its injection in the vacuum chamber induces a sharp increase of the pressure, which cannot be compensated quickly enough by the permanent pumping system. Indeed, from the measurements performed with a Pirani gauge sensor, it was found that after the injection of the gas–jet the pressure becomes ~ 10^{-3} mbar.

To overcome this problem, a differential pumping system was designed and constructed, the operational principle of which is shown in Figure 3.30. The system is composed of an external pumping turbine, and a small chamber in which the streak is placed (streak chamber). The streak chamber is in contact with the experimental chamber through a narrow window of 500 μm width x 30 mm length, and with the external pumping turbine through two pipes. The flow of the pipes is controlled by the two mechanical valves V1, V2. With V1 closed and V2 open, the streak chamber is isolated from the external turbine, and its space is pumped through the narrow window by the principal pumping system. When the pressure inside the streak chamber becomes of the order of 10^{-3} mbar, V1 is opened and V2 is closed and the streak chamber is pumped with the external turbine. Under these conditions, the system ensures that the gas flow *streak chamber–external turbine* exceeds adequately the flow *experimental chamber–streak chamber*, keeping the pressure of the streak chamber in an acceptable level for the streak operation.

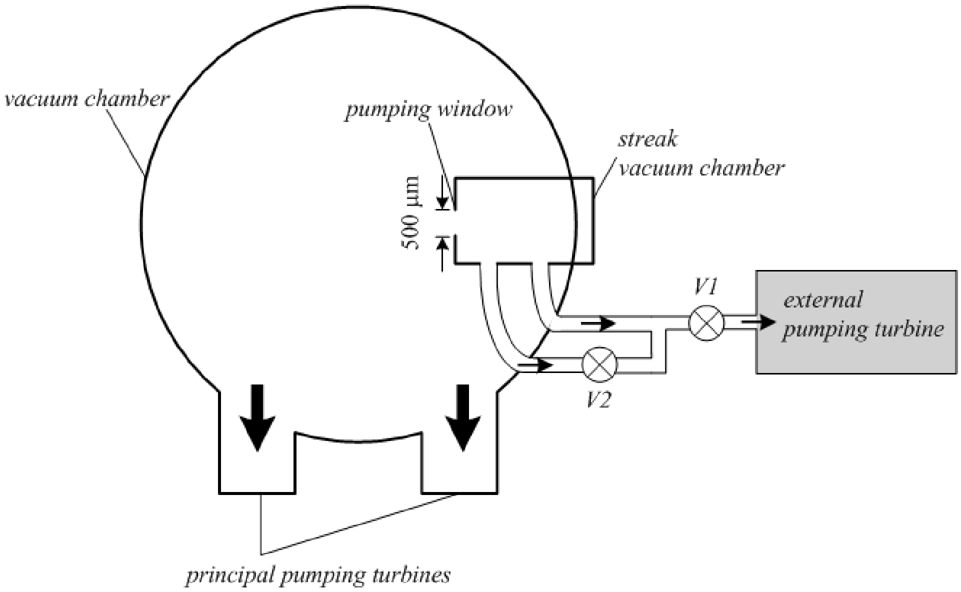

Figure 3.30 Schematic presenting the operational principle of the differential pumping system providing the low pressure conditions of the streak camera.

References of Chapter 3

[1] J.P. Zou *et al.*, Analyse et Correction de Surface d'Onde de la nouvelle installation LULI2000 : état d'avancement du projet «CSO», LULI Rapport Scien. 2004 – 2005, p. 86.

[2] F. Amiranoff, *et al.*, Experimental Transport Studies in Laser-Produced Plasmas at 1.06 and 0.53 µm, Phys. Rev. Lett. **43**, 522 (1979).

[3] Garban–Labaune *et al.*, Effect of Laser Wavelength and Pulse Duration on Laser-Light Absorption and Back Reflection, Phys. Rev. Lett. **48**, 1018 (1982).

[4] Y. Kato *et. al.*, Random Phasing of High-Power Lasers for Uniform Target Acceleration and Plasma Instability Suppression, Phys. Rev. Lett. **53**, 1057 (1984).

[5] C. B. Burckhardt, Use of a Random Phase Mask for the Recording of Fourier Transform Holograms of Data Masks, Appl. Optics **9**, 695 (1970).

[6] M. Born, E. Wolf, "Principles of optics", Pergamon Press (1993).

[7] V. Malka, *et. al.*, Characterization of neutral density profile in a wide range of pressure of cylindrical pulsed gas–jet, Rev. Sci. Instrum. **71**, 2329 (2000).

[8] B. L. Henke, E. M. Gullikson, J. C. Davis, X-Ray Interactions : Photoabsorption, Scattering, Transmission and Reflection at E = 50-30,000 eV, Z = 1-92, At. Data Nucl. Data Tables **54**, 181 (1993).

[9] A. Burek, Crystals for astronomical x-ray spectroscopy, Space Sci, Instrum. **2**, 53 (1976).

[10] J. L. Bourgade *et al.*, SPARTUVIX : A time-resolved XUV transmission grating spectrograph for x-ray laser research, Rev. Sci. Instrum. **59**, 1840 (1988).

[11] M. Chaker *et al.*, Calibrated soft x-ray spectrograph using transmission grating, pinhole and film, Rev. Sci. Instrum. **60**, 3386 (1989).

[12] F. Gilleron, Étude du transfert radiatif et de l'opacité d'un plasma créé par rayonnement X, thesis École Polytechnique, 2000.

[13] Center for X-ray Optics (CXRO), X-Ray Interaction With Matter Tabulated Data, http://henke.lbl.gov/optical_constants/.

[14] H. W. Schnopper *et al.*, Diffraction grating transmission efficiencies for XUV and soft x rays, Appl. Optics **16**, 1088 (1977).

[15] H. Bräuniger, P. Predehl, K. P. Beuermann, Appl. Optics **18**, 368 (1979).

[16] E. M. Campell *et al.*, Laser Part. Beams **9**, 209 (1991).

[17] S. H. Glenzer *et al.*, Thomson scattering from laser plasmas, Phys. Plasmas **6**, 2117 (1999).

[18] J-R Marques *et al.*, Mesure par diffusion Thomson de l'évolution de la température et de la densité électronique de plasmas de xénon ou de krypton créés par laser, Rapport LULI (2003).

[19] B. L. Henke, J. P. Knauer, K. Premaratne, The characterization of x-ray photocathodes in the 0.1 – 10 keV photon energy region, J. Appl. Phys. **5**, 1509 (1981).

[20] Re–entrant x–ray streak camera – Operation and description, Kentech Instruments Ltd.

[21] C. Reverdin, *et al.*, Absolute brightness measurements at the LURE synchrotron with a bolometer and application to the absolute calibration of the photodiodes and photocathodes, Laser and Particle Beams **12**, 573 (1994).

[22] Reverdin *et al.*, Sensibilité spectrale des photocathodes XUV minces en transmission, rapport interne CEA/DIF (1993).

[23] Henke *et al.*, High energy x-ray response of photographic films: models and measurement, J. Opt. Soc. Am. B **3**, 1540 (1986).

[24] Henke *et al.*, Low-energy x-ray response of photographic films. I. Mathematical models, J. Opt. Soc. Am. B **1**, 818 (1984).

[25] Henke *et al.*, Low-energy x-ray response of photographic films. II. Experimental characterization, J. Opt. Soc. Am. B **1**, 828 (1984).

Chapter 4 X–ray emission spectroscopy of xenon and krypton plasmas in NLTE conditions

4.1 Introduction

Plasmas in non local thermodynamic equilibrium (NLTE) are of primary interest for astrophysics in understanding and describing extending parts of the stellar atmospheres [1]. NLTE conditions are found, also, in many different research fields of laboratory plasma applications, such as the inertial confinement fusion (ICF) [2] and the development of x–rays sources. The global approach for the description of plasmas in NLTE is the collisional radiative model, in which the populations kinetic equations are solved using the transitions rates obtained from atomic codes. The situation, unfortunately, becomes complicated when the atomic number of the elements is increased. The medium and high–Z elements demand an enormous computation time to solve the kinetic equations with a detailed level accounting of their transitions and energy levels. To overcome this problem, an effort was done recently to integrate the superconfigurations approach and the formalism of the super–transitions–arrays (STA) [3], initially introduced in the context of LTE plasmas, in the NLTE statistics of the collisional radiative models [4,5].

This theoretical research has to be supported by spectroscopic experiments. The main characteristic of such experiments is the independent determination of the plasma parameters (n_e, T_e) used by the codes for simulating the emission spectra. The experimental technique mostly applied for this purpose is the Thomson scattering diagnostic. In this category of experiments, we could refer to the study of plasmas generated by laser irradiated gold targets [6,7], the study of holraums plasmas [8], as well as the experiments performed by our research group with the plasmas produced by laser irradiated xenon gas–jet targets [9].

The present work [10], should be viewed as the continuation of the study of well–characterized gas–jet plasmas reported in ref. [9], with the extension to the spectroscopic study of the XUV domain. This is an open field to benchmark the complex NLTE plasma models integrated in the package of the code TRANSPEC/AVERROES [4,5], as very few experimental data have been reported for medium and high–Z elements. A previous first attempt in analyzing the XUV spectroscopy of NLTE gas–jet plasmas [11] showed that the dynamics of the system affects strongly its XUV emission, and that for a proper study its time evolution should be taken into account. In our experiment, the emission spectra of laser produced xenon and krypton gas–jet plasmas in NLTE conditions are studied. For each element, we record simultanesouly its time–resolved emission spectrum in the XUV, and its time–integrated emission spectrum in the keV spectral range. Our focusing on the time evolution of only the XUV emission is due to the negligible time variation that the emission spectrum exhibits in the keV spectral range [9].

The study of the keV x–ray emission spectrum is included in our experiment for two reasons. First, both xenon and krypton emit a very rich spectrum challenging for the analysis with the code TRANSPEC/AVERROES. The spectra are composed of the xenon $3d$–$4f$ unresolved structures of the different ions species around the closed–shell Ni–like (Xe^{26+}) ion [9] and the krypton nl – n'l' transitions (for n=2, n'=3,4) from Mg–like (Kr^{24+}) to F–like (Kr^{27+}) ion [12,13]. Moreover, for both elements, these spectra are the link with the experiments previously performed by our team, and they can provide an independent estimation of the produced plasma state.

4.2 Experimental setup

4.2.1 Laser beam and gas–jet targets

The top–view of the experimental setup used to measure the xenon and krypton plasma emission spectra is shown in Figure 4.1. A 1 mm diameter nozzle is placed at the center of the vacuum chamber, producing the gas–jet targets. For both gas types, the pressure of the backing system feeding the nozzle varies in the range of 1.3 – 7.0 bar. The density profile of the gas–jet targets was characterized by performing a Mach–Zehnder interferometry experiment [14]. The measurements gave a super–gaussian density profile of about 1 mm width at a 750 μm distance from the exit plane of the nozzle. At this height the maximum of the density profile varies with the backing pressure from 1.7 to $9\text{x}10^{18}$ cm^{-3}.

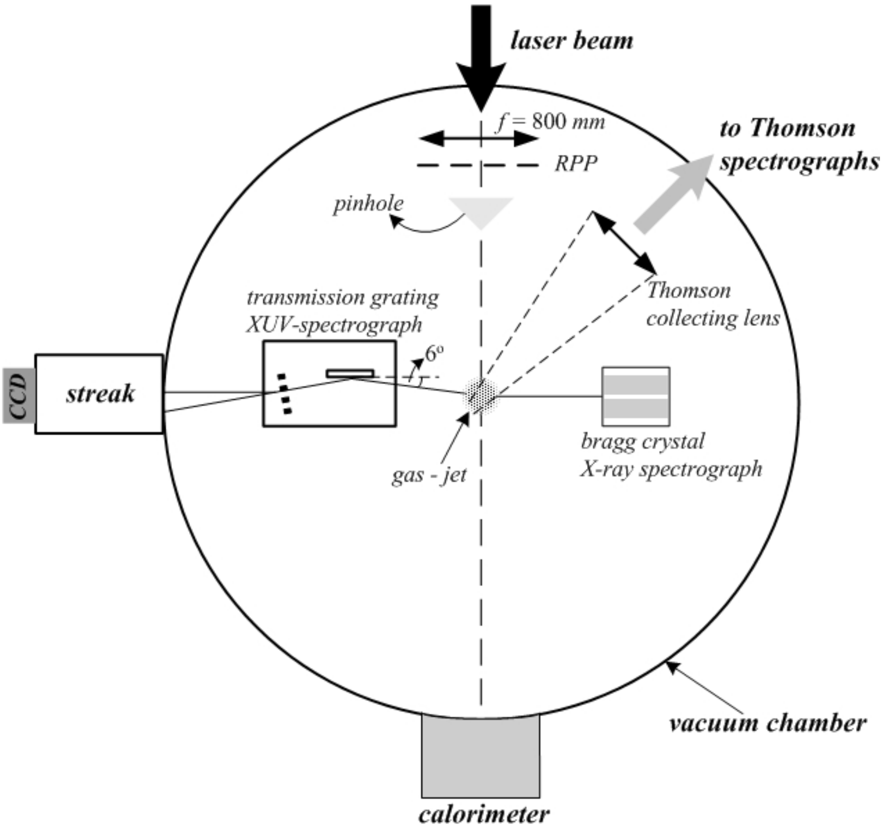

Figure 4.1 Top view of the experimental chamber.

A 1.5 ns duration flat–top neodymium laser pulse passes through a KDP crystal of frequency doubling efficiency of about 45%. The energy of the frequency doubled laser beam (λ = 0.53 μm) was varied in the range of 100 – 400 J. The laser beam is focused on the gas–jet by coupling a f = 800 mm lens with a random phase plate (RPP) of 0.37 mm x 4.2 mm element size. This coupling produces on the target an elliptic focal spot of 1 mm horizontal size at 50% of the laser intensity maximum, and of 150 μm vertical size at 10% of the laser intensity maximum. The laser beam is focused on the gas–jet at a distance of 750 μm from the exit plane of the nozzle. Thus, the focal spot width is equal to the width of the gas–jet. This choice ensures the absence of cold gas around the produced plasma, which absorbs the emitted x–ray radiation [11].

4.2.2 Diagnostic instruments

Thomson scattering diagnostic

A *f*/6 lens collects the laser light scattered by the produced plasma at 135° angle with respect to the propagation direction of the laser beam. The self–scattered radiation is driven to the Thomson diagnostics located outside of the vacuum chamber (see §3.4.3). The combination of the collecting lens with the Thomson disposition, defines a probing volume of 50 μm height x 200 μm width x 300 μm length (see Fig. 4.2(a)).

The analysis of the electronic and ionic satellites permits to determine the time evolution of the plasma parameters (mean ionization number, ion density, electron temperature). The scattering parameter α determining the Thomson scattering regime, depends on the propagation wavelength of the laser beam in the plasma and the probing angle along which the scattered radiation is collected (see Appendix A). For the frequency doubled laser (λ = 0.53 μm), and for the expected range of the electronic density (~ 10^{19} cm^{-3}), the choice of the probing angle ensures that $\alpha \sim 1.7 \geq 1$, i.e. a collective behavior of the plasma for the scattering process.

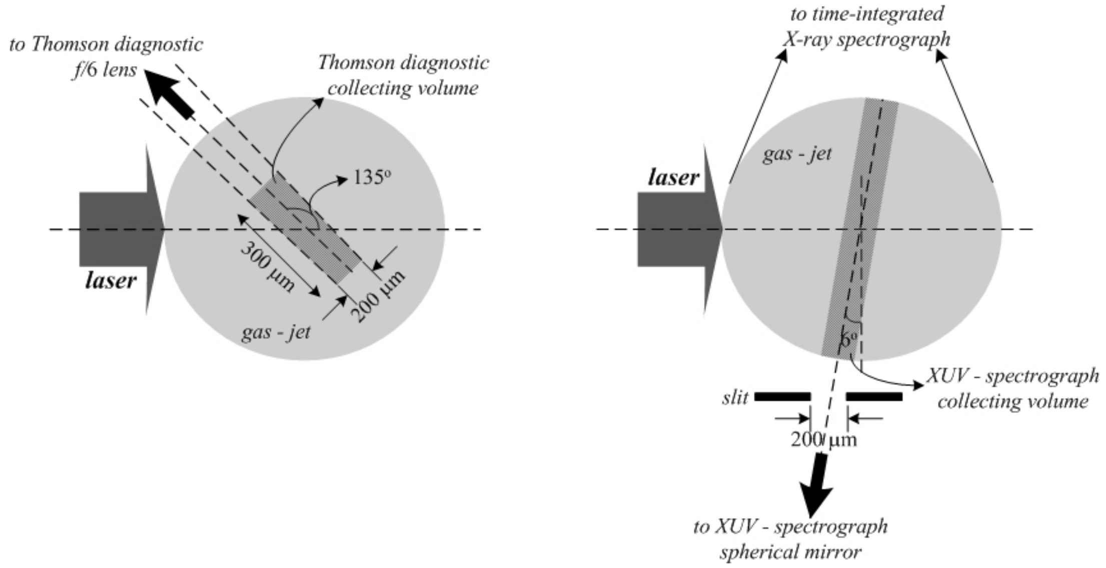

(a) (b)

Figure 4.2 Schemes of the plasma regions probed by the diagnostics : (a) Collecting volume of the Thomson diagnostic. (b) Collecting volume of the XUV and the x–ray spectrographs.

X–ray spectroscopic diagnostics

The measurement of the xenon–krypton plasma x–ray emission spectra is realized with two spectrographs permitting the simultaneous recording of the emitted radiation in the keV and the sub–keV (XUV) range. The time–integrated spectra in the keV range are measured with the double Bragg crystal spectrograph described in paragraph 3.4.1. The time–resolved XUV spectra are measured by coupling the transmission grating XUV spectrograph described in paragraph 3.4.2 with a streak camera. These diagnostic instruments are placed in opposite positions almost perpendicularly to the propagation direction of the laser beam (see Fig. 4.1).

As shown in the zoomed top–view of Figure 4.2(b), a slit of 200 μm width is placed on the recording axis of the XUV spectrograph which forms a 6° angle with the normal to the laser axis. The slit and the spherical mirror of the spectrograph, define a collecting volume of 200 μm width along the instrument line of sight. The slit determines the width of the plasma projection along the dispersion direction of the XUV spectrograph, and this limitation is very important for two reasons. First, the time–resolved recording of the XUV spectrum does not allow to monitor different spatial regions of the plasma. The slit, defining a narrow probing plasma volume almost perpendicular to the laser axis, provides that the spectrograph measures the emitted radiation of a fairly homogeneous plasma. Second, this reduced spatial projection improves the spectral resolution of the instrument (for the specific setup $\Delta\lambda$ = 2.4 Å, see §3.4.2)

The dispersion direction of the Bragg crystal spectrograph lies in a plane perpendicular to the laser axis. The diagnostic probes almost all the spatial region occupied by the produced plasma (Fig. 4.2(b)). The extension of the plasma along the laser axis is spatially resolved by a slit of 200 μm width placed perpendicularly to the laser axis. As the slits are located closer to the recording film than to the plasma, the spatial resolution is rather poor (~ 0.5 mm). The spectral resolution is limited by the 150 μm small axis of the elliptical laser focal spot, and is 22 mÅ for the TlAP crystal, and 8 mÅ for the ADP crystal (see §3.4.1). So, the formation of the plasma image on the film, in the direction parallel to the laser axis, is realized with very poor spatial resolution, and this implies the mutual overlapping of the radiation emitted from different spatial regions of the plasma.

Pinhole camera

The focal spot of the produced plasma is monitored with a x–ray pinhole camera. This pinhole is composed of three entrance holes of 5, 10 and 20 μm diameter arranged in a triangle of 1 mm side. The recording device is an ARP CCD camera, and a 23 μm thick beryllium filter is used to bound the spectral integration range of the instrument. The arrangement *plasma source–pinhole–CCD* lies in the same plane as the propagation direction of the laser beam, and it forms a 36^o angle with the horizontal plane of the experimental chamber, i.e. with the main laser beam axis. The distance *plasma source–pinhole* is set to 170 mm, and the distance *pinhole–CCD* to 600 mm. Thus, the nominal value of the magnification factor is ~ 3.5.

In parallel with the main diagnostic instruments, a calorimeter is used to measure the absorption of the laser energy by the plasma. The calorimeter was calibrated by measuring the energy of the laser beam without the gas–jet. The measurements gave that, when the backing pressure of the gas–jet increases from 1.3 to 7 bar, the energy absorbed by the plasma varies from 28% to 55% .

4.3 X–ray spectra data processing

4.3.1 Emission spectra in the keV range

Wavelength calibration

The wavelength calibration of the xenon–krypton plasma emission spectra in the keV range is performed by approaching the non linear dispersion function of the Bragg crystal spectrograph by a second order polynomial :

$$\lambda = a_2 \cdot (pixel)^2 + a_1 \cdot pixel + a_0 \tag{4.1}$$

Eq. (4.1) gives the wavelength of an incident photon on the film as a function of its recording position along the dispersion axis, given in pixels.

In a first step, the dispersion coefficients a_2, a_1, are calculated by analyzing the emission spectrum of an aluminium plasma independently measured. This choice is justified by the well characterized spectral lines composing the aluminium spectrum in the range of 6 – 8 Å, and which correspond to the transitions n=1 → 2, 3 of the hydrogen–like and the helium–like aluminium ions [15]. The ADP crystal records these lines at the first dispersion order, and the TlAP at the second dispersion order, respectively.

The determination of an offset coefficient a_0 is necessary for each different measurement : this coefficient accounts for a small relative shift of the recorded spectrum along the dispersion axis occurring during the film digitizing process. It can be determined by the identification of an emission structure for each measured spectrum. This procedure is performed by using previous experimental characterizations of the xenon and krypton plasma emission spectra, in the same spectral range [9,11,13].

a) Krypton plasma emission spectrum (6 – 8 Å)

Figure 4.3 shows two typical raw spectrum images obtained by the ADP crystal. The emission spectrum of an aluminium plasma, produced by focusing a 45 J energy laser beam on a 50 μm thick aluminium foil, is given in Fig. 4.3(a); Fig. 4.3(b) gives the emission spectrum of a 4 bar pressure krypton gas–jet heated by 230 J energy laser. In both images, the wavelength dispersion is recorded along the horizontal axis, and along the vertical axis we obtain the projection of the plasma spatial expansion along the propagation axis of the laser beam.

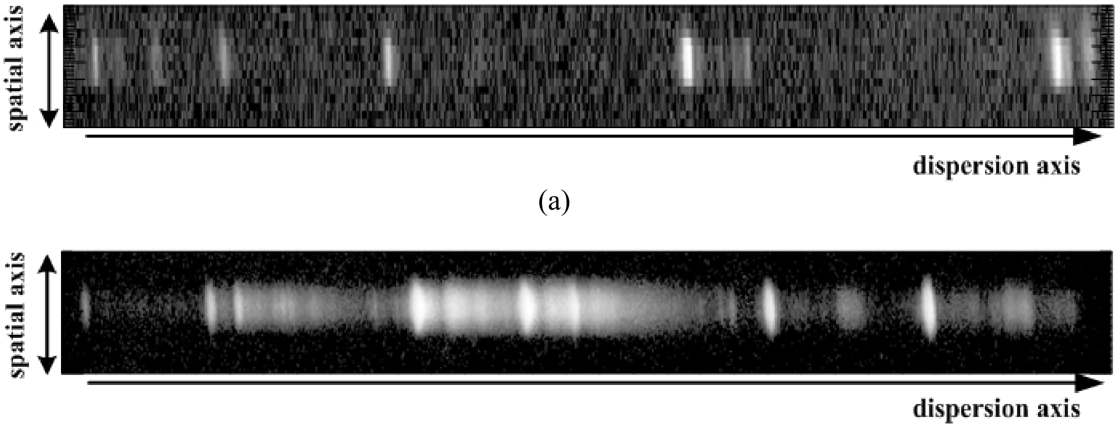

(a)

(b)

Figure 4.3 Raw images of the recorded spectra dispersed by the ADP crystal. (a) Aluminium plasma emission spectrum, (b) Krypton plasma emission spectrum.

spectrum line	λ(Å)	ion	lower level	upper level
Lyβ	6.052	Al^{12+} (H)	1s	$3p\ P_{3/2}$
Heβ	6.634	Al^{11+} (He)	$1s^2\ {}^1S_0$	$1s3p\ {}^1P_1$
Heα	7.757	Al^{11+} (He)	$1s^2\ {}^1S_0$	$1s2p\ {}^1P_1$

Table 4–I Aluminium plasma transition used to calibrate the wavelength axis of the krypton plasma emission spectrum.

First, the aluminium spectrum profile (dashed line of Fig. 4.4) is calibrated by identifying the three characteristic hydrogen and helium–like transition lines given in Table 4–I providing the dispersion coefficients a_2, a_1. The offset coefficient a_0 for each specific shot is then obtained by using the $2p^6$–$2p^5 3d$ (3D) transition line of the Ne–like (Kr^{26+}) ion appearing on the krypton emission spectrum at 6.88 Å [11,13] (see also Table 4–VII in § 4.5.2). The calibrated krypton spectrum is shown as the full line curve of Figure 4.4.

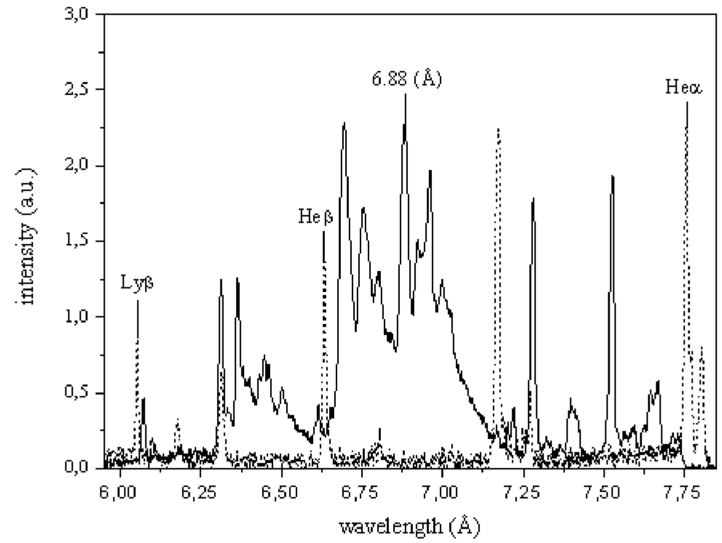

Figure 4.4 Wavelength calibration of the spatial and time–integrated spectrum profiles obtained by the recorded images of Fig. 4.3. Full line : krypton spectrum profile, dashed line : aluminium spectrum profile. (the characteristic lines used for the wavelength calibration are marked).

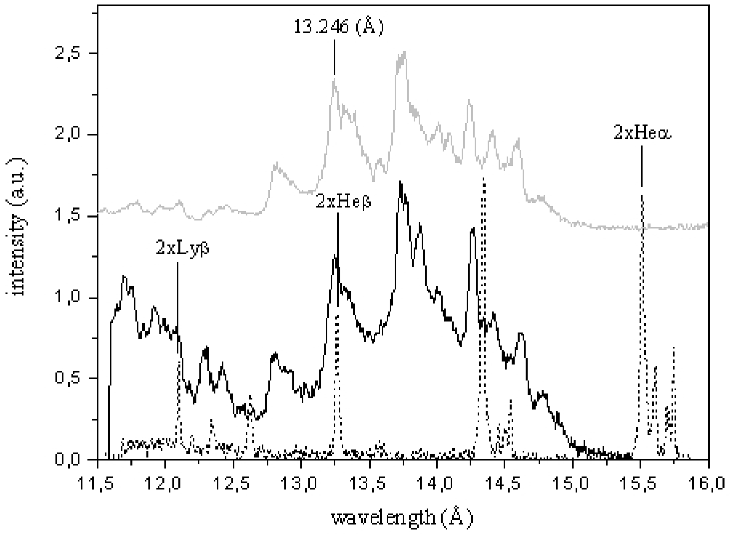

Figure 4.5 Wavelength calibration of the xenon and aluminium space and time–integrated spectrum profiles measured with the TlAP crystal. Full black line : measured xenon spectrum profile. Dashed line : measured aluminium spectrum profile. Full grey line : xenon plasma emission spectrum studied in [9].

b) Xenon plasma emission spectrum (11 – 16 Å)

The wavelength calibration of the xenon spectrum is performed in a similar manner. The dispersion coefficients a_2, a_1 of the TlAP crystal setup are calculated by using the aluminium transition lines of Table 4–I, but which appear now in the second dispersion order of the crystal (lines : 2xLyβ = 12.104Å, 2xHeβ = 13.268 Å and 2xHeα = 15.514 Å). Then, the offset coefficient a_0 is calculated by identifying the peak of the Fe–like (Xe^{28+}) 3*d*–4*f* transition array appearing at 13.246 Å [9]. A typical example of the xenon spectrum calibration is given in Figure 4.5. This common graph gives the xenon and aluminium plasma emission spectra measured with the TlAP crystal, and the xenon plasma emission spectrum studied in [9].

Intensity calibration

The procedure applied to calibrate the intensity scale takes into account the spectral responses of the spectrograph components. First, by using the model of Henke, the optical density of the exposed DEF film is converted into the exposure of the incident radiation [16]. Then, the radiation flux of the emission spectra is corrected for the spectral response of the Be (7 µm thick) and the Mylar (10 µm thick) filters, which are placed in front of the film in order to reduce the recorded noise (mainly by cutting off the visible light). In a next step, the incident intensity on film measured in photons/Å/µm^2, is converted to the intensity reflected by the crystals, measured in photons/Å/sr, taking into account the spectrograph geometry. Finally, the intensity reflected by the crystals is transformed into incident intensity (photons/Å/sr) by using the integrated reflectivities of the ADP and the TlAP crystals [17,18]. The spectral response of the spectrograph components are summarized in Figure 4.6. A typical example of the transformation from the measured optical density to the spectrum intensity, applied on a xenon plasma emission spectrum, is given in Fig. 4.7.

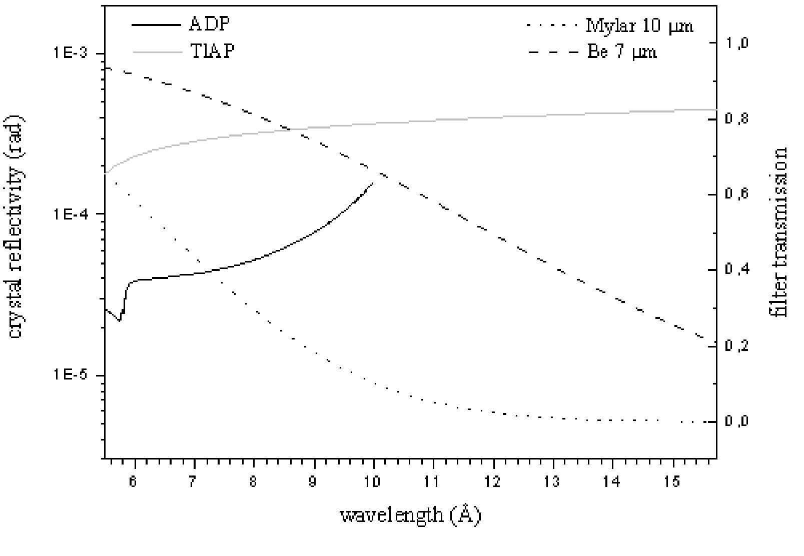

Figure 4.6 Integrated reflectivity curves of the ADP (full black line) and the TlAP (full gray line) crystals; transmission curves of 7 µm thick Be (dashed line), and of 10 µm thick Mylar filter (dotted line).

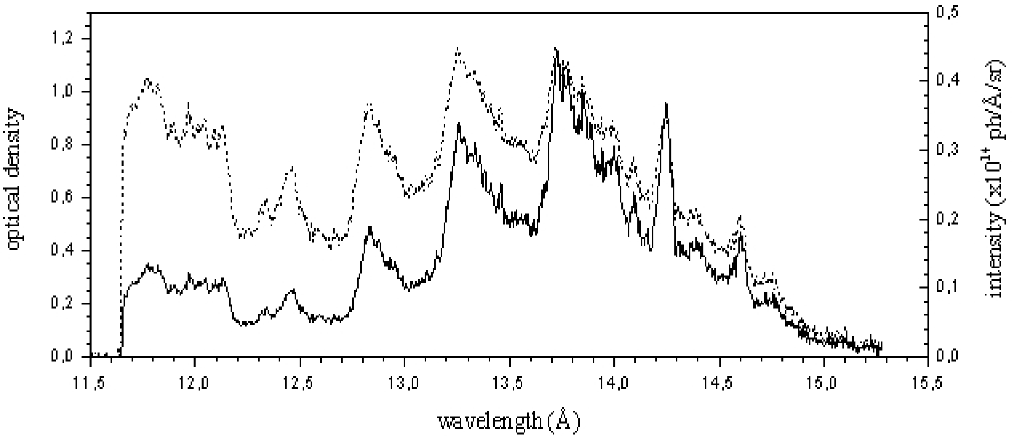

Figure 4.7 Transformation from the measured optical density to intensity for a xenon emission spectrum, applying the spectral corrections of the spectrograph components; full line spectrum intensity, dashed line : optical density.

4.3.2 XUV emission spectra

Figure 4.8 shows two typical time–resolved spectrum images of the xenon and krypton plasma emission recorded with the XUV spectrograph. In Fig. 4.8(a) is given the emission spectrum obtained by heating a 2 bar pressure xenon gas–jet with a 355 J energy laser beam, and in Fig 4.8(b) the spectrum of a 4 bar pressure krypton gas–jet heated by a 230 J energy laser. The time evolution of the measured spectra is recorded along the vertical axis, and the spectral dispersion along the horizontal axis.

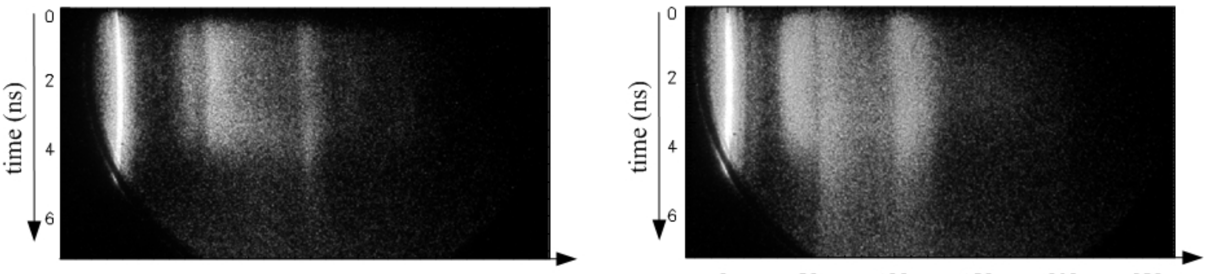

(a) (b)

Figure 4.8 Time–resolved XUV emission spectrum images. (a) Emission spectrum of a 2 bar pressure xenon gas–jet heated by a 355 J energy laser, (b) emission spectrum of a 4 bar pressure krypton gas–jet heated by a 230 J energy laser.

First, the spectrum images are corrected for the deformation introduced by the intensifier (see Chapter 3). Then, the time and wavelength axis of the spectra are calibrated. Finally, the spectra are corrected for the responses of the spectrograph components affecting the intensity of the measured radiation. The time/wavelength calibration, and the intensity correction are described analytically in the next two paragraphs.

Time–wavelength calibration

From the dispersion relationship of the XUV spectrograph, it follows that the dispersion axis can be calibrated by using a simple linear formula,

$$m\lambda = a_1 \cdot pixel + a_0 \tag{4.2}$$

where m is the dispersion order, and a_1 is the dispersion coefficient determined by the geometry of the spectrograph setup. The offset coefficient, a_0, represents a small relative shift, from shot to shot, of the zero transmission order, and it does not depend on the dispersion properties of the spectrograph. The wavelength calibration, as it is formulated in Eq. (4.2), is reduced to the calculation of the dispersion coefficient a_1, while the variable coefficient a_0 is deduced easily by the zero transmission order of each spectrum. To calculate a_1, some special shots were performed on xenon gas–jet with a 1 μm thick Be filter placed in front of the spectrograph. By measuring the absorption K–edge introduced by the Be filter on the xenon emission spectrum at 110.85 Å [19], we found that the dispersion coefficient for the specific experimental setup is, a_1 = 0.423 Å/pixel (see Fig. 4.9).

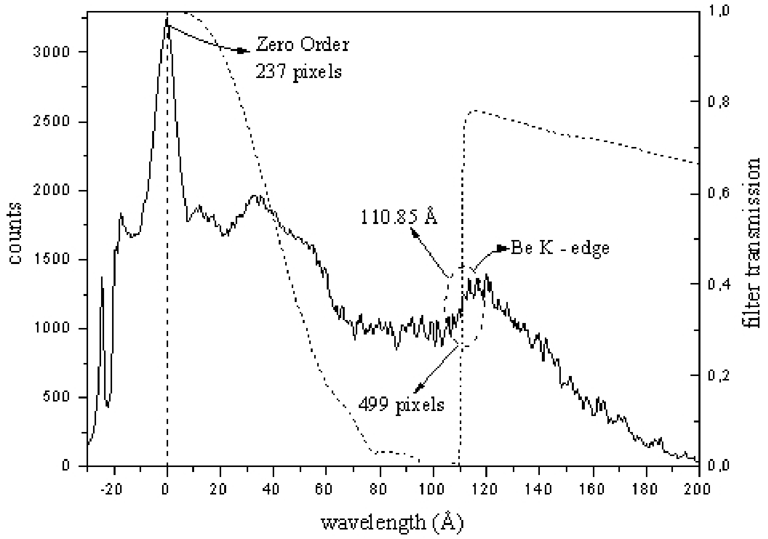

Figure 4.9 Calculation of the dispersion coefficient a_1 of Eq. (4.2). Full line : emission spectrum profile of a 4 bar pressure xenon gas–jet heated by a 400 J energy laser. Dashed line : 1 μm Be filter transmission curve. Be filter K–edge appears on the recorded xenon spectrum at pixel 499; the zero transmission order of the specific spectrum appears at pixel 237.

To calibrate the time axis, the signal position on the CCD camera (counted in pixels) has to be associated with the time characteristics of the streak camera. First, the recording position of the signal on the CCD should be transformed to its recording position on the phosphor plate. For this, we have to take into account the magnification of the intensifier (G_{int} = 4/5) and the magnification of the fiber optics configuration (G_{fo} = 1/3), which connects the intensifier with the CCD. Then, the spatial position of the measured event on the phosphor plate is correlated with its recording time using the deflection speed of the streak. The ARP CCD camera used in the experiment has a pixel size of 19 μm, which corresponds to a width of 0.072 mm on the phosphor plate along the time axis. The manufacturer gives for the deflection speed used in the experiment the nominal value of 4 mm/ns. Thus, the nominal value of the time coefficient for the configuration streak–intensifier–CCD is 0.019 ns/pixel.

Intensity corrections

The components of the XUV spectrograph affecting the spectral variations of the intensity of the recorded spectrum are : (1) the spherical Ni–mirror, (2) the transmission grating convolving the different dispersion orders, and (3) the cathode of the streak camera. The cathode response (full line) and the mirror reflectivity (dotted line) are given in Figure 4.10. The cathode response is calculated with the Henke model [20], assuming a structure composed of a 1200 Å thick Cesium Iodide (CsI) plus a 250 Å thick aluminium layer deposited on a 1000 Å thick Lexan layer (see §3.5.1). The Ni–mirror reflectivity is obtained from the tabulated data of CXRO [19] for a grazing angle of 6^o (see §3.4.2). The correction procedure applied on the recorded spectrum can be divided in two parts. First, the deconvolution of the 2nd–dispersion order of the grating is performed, with the cathode response being applied step by step at each corrected spectrum interval, according to the analysis of paragraph 3.4.2. Then, the spectrum is corrected for the Ni–mirror response. A typical example of the corrections applied on the emission spectrum profile of a xenon plasma is given in Figure 4.11; the profile is sampled at 0.63 ns after the beginning of the signal emission from the spectrum image of Fig. 4.8(a). The peaks of the corrected spectrum appearing above 170 Å represent an artificial signal produced by the application of the cathode response on the spectrum noise, and thus, this spectral range should be excluded from our analysis.

The question arising here concerns the accuracy of the cathode response calculated with the Henke model [20] for the assumed cathode composition. As we saw in paragraph 3.5.1, in fact, the cathode is subject to long–scale changes affecting its spectral response. We recall that these changes are the hydration of the CsI layer, and the oxidation of the aluminium layer causing the formation of an Al_2O_3 layer on the cathode. The proper determination of the these variations necessitates the fitting of the Henke model with the experimental data obtained by an absolute calibration of the cathode [21,22], a process not applied to our cathode (uncalibrated).

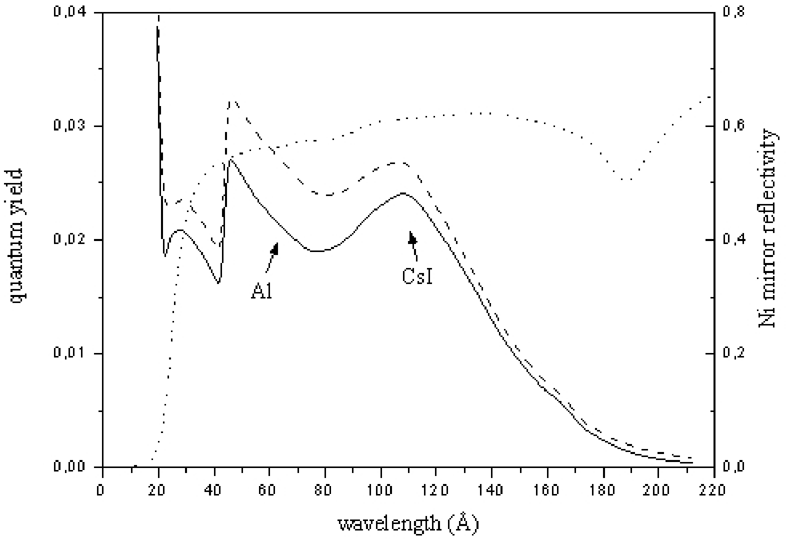

Figure 4.10 Spectral response curves of the XUV spectrograph components. Quantum yield of the CsI photocathode by using the nominal values of the manufacturer (full line), or by assuming a 25% oxidation of the aluminium layer (dashed line); dotted line : reflectivity of the 80 nm thick spherical Ni–mirror for a 6^o grazing angle.

However, the potential changes of the cathode do not vary significantly the shape of the corrected spectrum. In Fig. 4.10 are compared the responses of a cathode with and without oxidation, the aluminium layer being 25 % oxidized. Applying the two cathode responses on the uncorrected spectrum profile of Fig. 4.11, we obtain the results given in Fig. 4.12. The two spectra show a negligible deviation between the measured emission structures only above 60 Å. In the following, we apply on the measured spectra the response calculated for the cathode nominal values, neglecting the oxidation, supposing that hydrated CsI has the same spectral response as CsI.

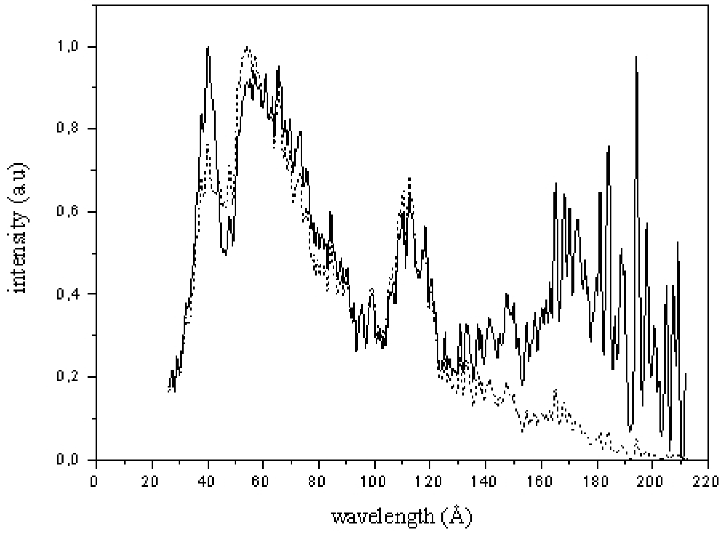

Figure 4.11 Intensity corrections applied to a spectrum profile obtained 0.63 ns after the beginning of the signal emission, from the xenon plasma XUV emission spectrum of Fig. 4.8(a). Dashed line : uncorrected spectrum, full line : corrected spectrum.

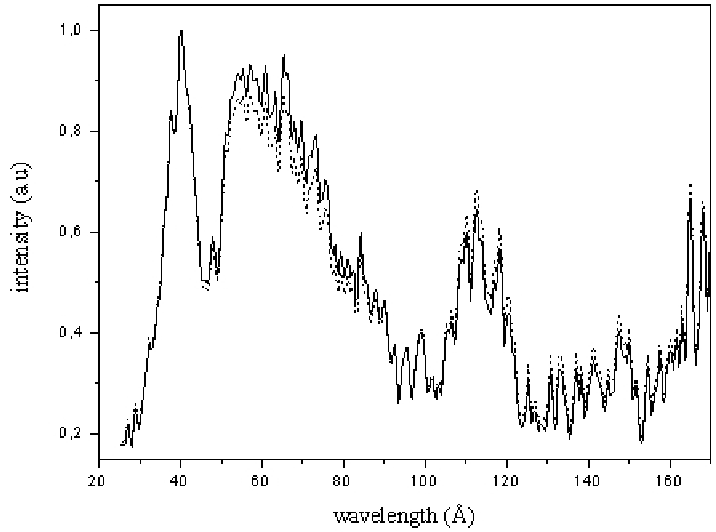

Figure 4.12 Comparison of the spectra obtained by applying the two cathode responses of Fig. 4.10 on the uncorrected spectrum profile of Fig. 4.8(a). Full line : Spectrum obtained by the response of a cathode calculated with the manufacturer values. Dashed line : Spectrum obtained by the response of a 25 % oxidized aluminium layer cathode.

4.4 Determination of the plasma parameters–Thomson scattering spectra analysis

4.4.1 Helium plasma parameters

During the xenon–krypton plasma x–ray emission spectra measurements campaign, a number of shots was performed with a helium gas to calibrate the ion density of the gas–jet targets [9,23]. The ion density of the helium gas–jet plasma can be derived from the parametrical fit of its electronic spectrum giving the plasma electron density, because, under the given experimental conditions the helium plasma is fully ionized. Helium gas was chosen, because its neutral density depends only on the adiabatic parameter γ which is the same for all the monatomic gases (γ = 5/3); hence, it permits to deduce the ion density of the xenon–krypton plasmas. These measurements were performed additionally to the Mach–Zehnder experiment [14], and they provide a more accurate estimation of the ion density, obtained under the same experimental conditions as the emission spectra of xenon and krypton. The outline of the Thomson scattering theory is given in Appendix A, and the description of the Mach–Zehnder experiment is given in Appendix B.

Figure 4.13 shows a typical example of the spectrum images recorded by the Thomson spectrographs, in the case of a 7 bar pressure helium gas–jet heated by a 350 J energy laser beam. The image of Fig. 4.13(a) is a time–resolved electronic scattering spectrum, and that of Fig. 4.13(b) an ionic scattering spectrum. In both images the wavelength is recorded along the horizontal axis, and along the vertical axis is recorded the time evolution of the spectra.

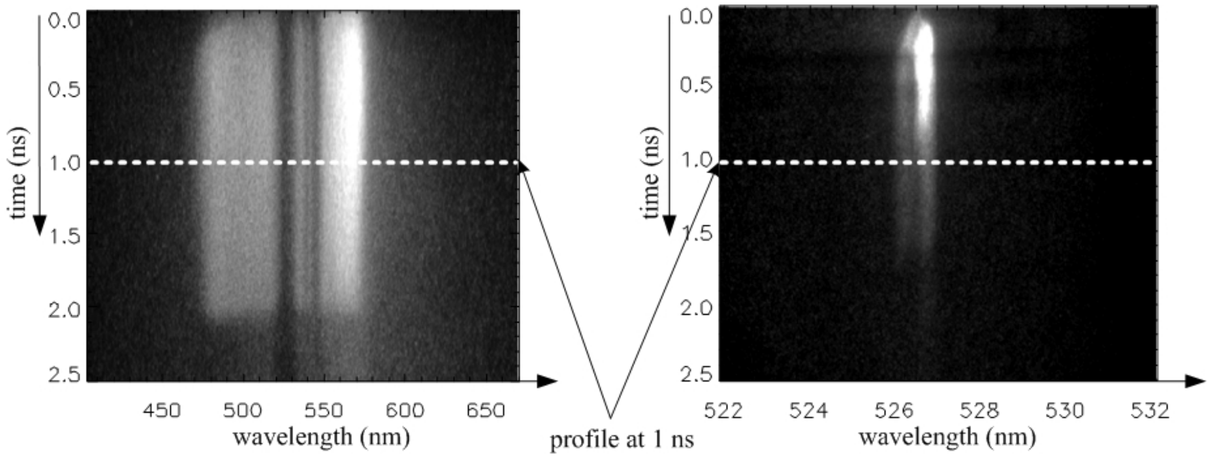

(a) (b)

Figure 4.13 Recorded images of the time–resolved Thomson scattering spectra of a 7 bar pressure helium gas–jet heated by a 350 J energy laser beam. (a) Electronic spectrum, (b) ionic spectrum.

In Fig. 4.13(a) we can observe the two electronic satellites on both sides of a dark spectral band appearing around the laser wavelength (0.53 μm). This zone is highly attenuated by an interference filter placed in front of the electronic spectrograph which transmits almost 100% out of this narrow spectral region. The instantaneous appearance of the electronic satellites after the laser pulse indicates a fast ionization of the plasma. As times evolves, and during the heating of the plasma by the laser, a slight decrease of the distance between the outer borders of the satellites is observed. This implies a slow decrease of the electron density which can be explained by the plasma expansion [23].

In Fig. 4.13(b), the formation of the ionic satellites indicate that the increase of the electron temperature occurs in the first 100 ps after the beginning of the signal emission. Then, for the remaining plasma heating duration, the position of the satellites does not vary. In a first approximation, the ionic resonance frequency ω_{ac} of a non–isothermal plasma ($T_e >> T_i$) is [24]

$$\omega_{ac} \cong k\sqrt{\frac{k_B}{m_i}\langle Z\rangle T_e} \tag{4.3}$$

where k_B is the Boltzmann constant, m_i the ion mass and k the ionic perturbation wavenumber. Thus, and since the helium plasma is fully ionized ($<Z> = 2$), its electron temperature during its heating remains constant. Finally, an interesting feature of the ionic spectrum is that the satellite appearing above λ_{laser} (red satellite) shows a higher intensity in comparison with the satellite below λ_{laser} (blue satellite). This behavior could be attributed either to the presence of a Brillouin instability [23], or to a drift velocity of the electrons [25].

Figure 4.14 gives the lineouts obtained from the spectrum images of Fig. 4.13, 1 ns after the beginning of the signal emission (dotted lines), integrated on a 100 ps window. In order to determine accurately the plasma parameters the theoretical calculation of its spectral density function is necessary [25], using as input parameters the electron density, the electron temperature and the mean ionization number of the plasma [6]. The spectral density function is calculated for a collisionless plasma, assuming a maxwellian velocity distribution of the plasma species [25]. To take into account the spectral resolution of the instruments, the theoretical electronic spectrum is convolved with a gaussian of 64 Å full width at half maximum (FWHM), and the ionic spectrum with a gaussian of 2 Å FWHM.

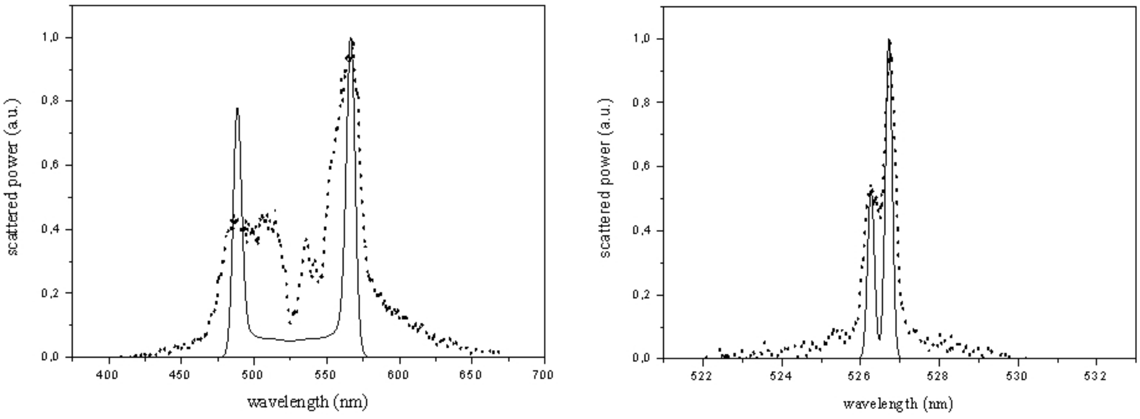

(a) (b)

Figure 4.14 Comparison of the experimental Thomson scattering spectra (dotted lines) obtained at 1 ns after the beginning of the signal, with the theoretical spectra (full lines) calculated for $n_e = 1.8\ 10^{19}$ cm^{-3}, $ZT_e = 126$ eV. (a) Electronic spectrum, (b) ionic spectrum.

Generally, the theoretical spectra are fitted parametrically with the experimental spectra by varying simultaneously the electron density, the electron temperature and the mean ionization number of the plasma [6,26]. The fit of the ionic spectrum provides the product $<Z>T_e$ (see Eq. (4.3)). The fit of the electronic spectrum gives n_e, with T_e a small correction on the determination of the electronic satellites frequencies ω_{oe}, according to the Bohm–Gross dispersion relationship [27],

$$\omega^2{}_{oe} \cong \omega^2{}_{pe} + (3k_B T_e / m_e)k^2 \tag{4.4}$$

where

$$\omega_{pe} = \sqrt{n_e e^2 / \varepsilon_o m_e} \tag{4.5}$$

is the electron plasma frequency, e and m_e are the electron charge and mass, ε_o the vacuum dielectric constant, and k the electron perturbation wavenumber.

For the fully ionized helium plasma ($<Z> = 2$), the fit of the ionic spectrum provides the electronic temperature, and given T_e the electronic spectrum gives directly n_e, from which the plasma ion density is calculated ($n_i = n_e/2$). The best fit is obtained for : $n_e = 1.8\ 10^{19}$ cm^{-3} and $ZT_e = 126$ eV; thus for $T_e = 63$ eV (full lines of Fig. 4.14). So, the ion density of a 7 bar pressure helium gas is $n_i = 0.9\ 10^{19}$ cm^{-3}. Repeating this procedure for different times around 1 ns, the decrement rate of the electron density was found about 0.15 10^{19} cm^{-3}.

The measurements of the xenon–krypton plasma emission spectra are obtained for gas backing pressures in the range of 1.3 – 4 bar. Extrapolating from the helium measurement the ion density for these pressures, we find that it varies in the range of 1.67 10^{18} – 5.14 10^{18} cm^{-3}. The comparison of the ion density obtained by the Thomson scattering with the results of the Mach–Zehnder experiment is given in Table 4–II. The results show a good agreement, and the small deviation at the high pressure (~ 14 %) could be attributed to the different conditions under which the two experiments were performed.

P **(bar)**	**He Thomson -** n_i **(cm^{-3})**	**Mach–Zehnder -** n_i **(cm^{-3})**
1.3	1.67 10^{18}	1.95 10^{18}
2	2.57 10^{18}	3 10^{18}
4	5.14 10^{18}	6 10^{18}

Table 4–II Ion density extrapolated from the Helium Thomson measurement, and the Mach–Zehnder interferometry experiment, for the pressures of the the xenon–krypton gas–jets.

4.4.2 Xenon and krypton plasmas parameters

Analysis of xenon Thomson scattering spectra

Figure 4.15 gives a typical example of the time–resolved electronic and ionic Thomson scattering spectra obtained for a xenon gas–jet of 1.3 bar pressure heated by a 400 J energy laser. The time evolution shows the same characteristics as for helium. The distance between the outer borders of the electronic satellites decreases, implying the decrease of n_e (see Fig. 4.15(a)). After the plasma fast ionization, and during its heating by the laser pulse, the distance of the ionic satellites does not change (see Fig. 4.15(b)). However, no qualitative result can be deduced, as both $<Z>$ and T_e defining the ionic satellites position may vary with time. Also, the red ionic satellite of Fig. 4.15(b) is more intense in comparison with the blue one, indicating the presence of a Brillouin instability, or the electrons drift velocity.

The electronic and ionic spectrum profiles (100 ps time integration), obtained from Fig. 4.15, 1 ns after the beginning of the signal emission, are given in Figures 4.16(a), (b) (dotted lines). Unlike helium, for the xenon plasma $<Z>$ is not fixed, and in order to fit the theoretical calculations it is represented as a function of the parameter n_e

$$\langle Z(n_e)\rangle = \frac{n_e}{n_i} \tag{4.6}$$

provided that the plasma ionic density is determined independently. The ionic density is an explicit function of the gas pressure and it is given by the helium Thomson scattering and the Mach–Zehnder measurements. With measured the ionic density, we apply the same procedure as used for helium. Fitting the electronic spectrum we obtain n_e, with T_e being a correction parameter of the electronic satellites position (see Eq. (4.4)). The simultaneous fit of the ionic spectrum gives $<Z>T_e$ and T_e, as $<Z>$ is specified via Eq. (4.6). The best fit is obtained for $n_e = 2\ 10^{19}$ cm^{-3} and $<Z>T_e = 6000$. For 1.3 bar pressure it gives $n_i = 1.67\ 10^{18}$ cm^{-3} (see Table 4–II); thus $<Z> = 12$ and $T_e = 500$ eV.

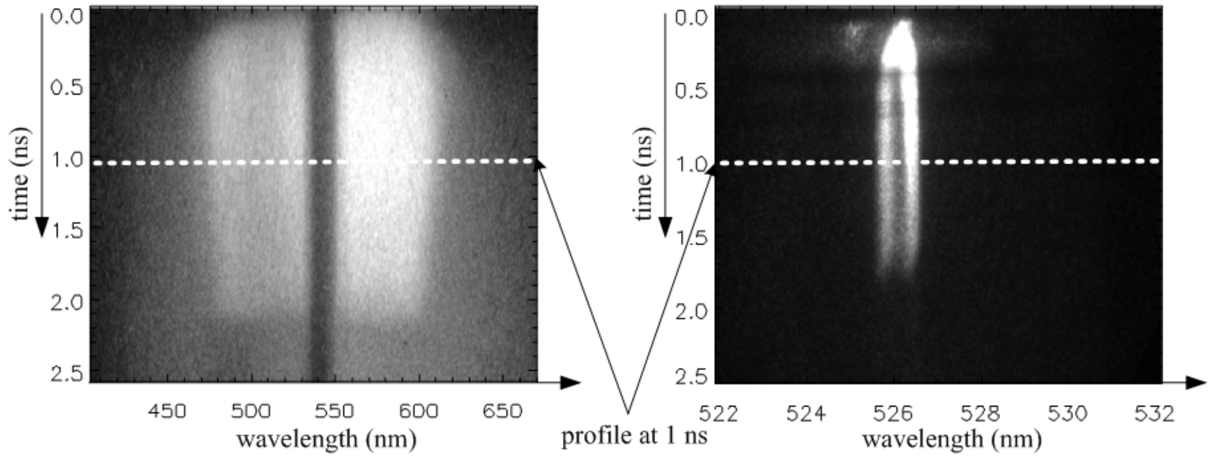

(a) (b)

Figure 4.15 Recorded images of the time–resolved Thomson scattering spectra of a 1.3 bar pressure xenon gas–jet heated by a 400 J energy laser beam. (a) Electronic spectrum, (b) Ionic spectrum.

At first sight, the result exhibits manifest incompatibilities. The low value of the mean ionization number cannot be explained for this high plasma temperature; this erroneous value of $<Z>$ is confirmed also by the analysis of the xenon x–ray emission spectrum which gives roughly $<Z> \sim 26 - 28$ (cf. §4.5.1). As the only independent parameter of the above analysis is n_i, a possible explanation of this result is the overestimation of n_i giving a low $<Z>$ via Eq. (4.6). To understand this, we notice that the extrapolation of n_i for the different pressures of the xenon gas–jet was done : (1) assuming a linear relationship between the gas backing pressure and the produced jet density, and (2) using as reference the measured density of the helium plasma. However, the linearity assumption may give errors when the pressure of the xenon gas–jet is very low, compared to the 7 bar pressure of the helium reference. The same argument holds for the reference densities obtained from the argon gas Mach–Zehnder measurements; here the density is measured in a 20 bar argon gas–jet. It has to be mentioned that the linearity n_i (P) has been checked for higher pressures than the 1.3 – 4 Bar range used in our experiment.

This hypothesis seems to explain the results of the Thomson analysis. Table 4–III summarizes the xenon plasma parameters obtained by the Thomson scattering spectra under different pressure and laser energy conditions. The fifth column gives $<Z>$ calculated with n_i obtained from the helium reference density (the corresponding T_e is given in the sixth column). As the xenon pressure increases and gets closer to the helium pressure, $<Z>$

increases and its value is more consistent with the independent estimation obtained by the x–ray emission spectra.

Another incoherence is that, for a quasi constant energy, we expect an increase of the plasma heating for an increasing gas pressure, i.e. an increase of both <*Z*> and T_e. So the variation of the temperature with the pressure is not physically correct.

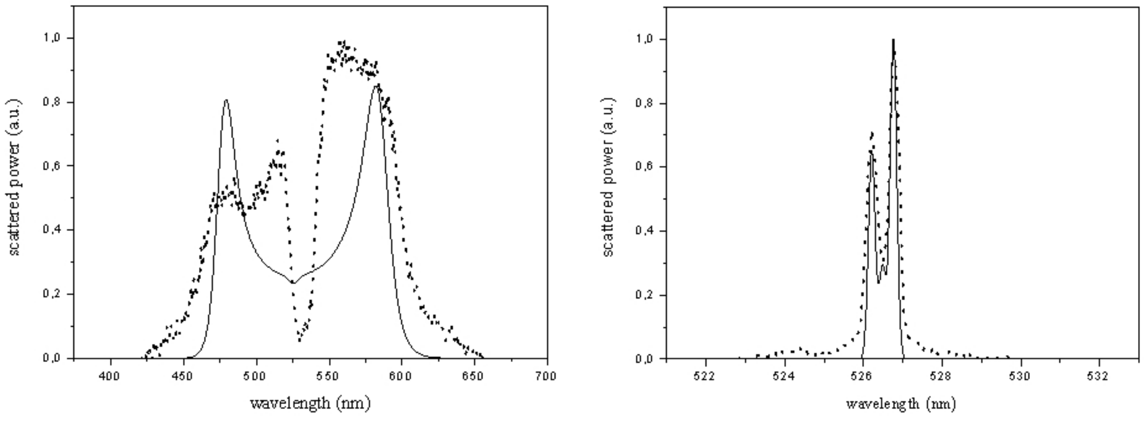

(a) (b)

Figure 4.16 Comparison of the experimental xenon Thomson scattering spectra (dotted lines) obtained at 1 ns after the beginning of the signal, with the theoretical spectra (full lines) resulting from the calculation of the spectral density function for $n_e = 2.0\ 10^{19}$ cm^{-3}, $<Z>T_e$ = 6000. (a) Electronic spectrum, (b) ionic spectrum.

			Thomson n_i - reference			x-ray spectra <*Z*> - reference		
P (bar)	*E*(*ω*) (J)	n_e(x10^{19} cm^{-3})	n_i(x10^{18} cm^{-3})	<*Z*>	T_e (eV)	<*Z*>	T_e (eV)	n_i(x10^{18} cm^{-3})
1.3	400	2.0	1.67	12	500 ± 160	26	231 ± 77	0.77
2	380	3.75	2.57	15	463 ± 51	27	250 ± 28	1.39
4	350	12.5	5.14	24.3	390 ± 41	28	340 ± 36	4.46

Table 4–III Xenon plasma parameters for different values of the gas–jet pressure and the laser energy used in the experiment. The values of the plasma parameters correspond to the Thomson spectra measured 1 ns after the beginning of the signal emission.

An alternative approach to our problem would be to use the <*Z*> values given by the x–ray spectrum. In this case, T_e follows directly from the ionic part of the Thomson scattering spectrum. Then, n_e is obtained by fitting the electronic spectrum, and n_i results simply from Eq. (4.6). The results obtained with this method are given in columns 7–9 of Table 4–III. It should be noted that, in this approach, <*Z*> and T_e increase with the gas pressure, which is physically correct.

Unfortunately, the <*Z*> values obtained by the x–ray spectra must be used with special care, for, there is an intrinsic lack of coherence between the Thomson and the Bragg crystal x–ray spectrograph diagnostics. First, the x–ray spectrograph measures the plasma radiation in a narrow spectral band. Thus, the obtained spectrum is not the result of the radiation emitted from the whole plasma, but only from these regions which are hot enough to emit in the specific range (non–homogeneous plasma). In addition, the x–ray spectrum is space and time integrated. Therefore, it is possible to measure in space (and in time) a higher charged plasma, specially at the plasma side heated by the laser, and which is probed by the x–ray spectrograph but not by the Thomson diagnostic. Due to this, we expect, in fact, that the x–ray spectrograph "sees" a higher temperature plasma with respect to the Thomson diagnostic, giving an overestimation of the average charge.

Given the limitations of each approach, we choose to use the <*Z*> of the x–ray spectrum for the low pressures of the gas–jet, and the self–consistent Thomson analysis for the high pressures. So, for the spectrum of Fig. 4.15 from Table 4–III we have : $n_e = 2.0\ 10^{19}$ cm^{-3}, $T_e =$ 231 eV, <*Z*> = 26. The theoretical curves calculated for these parameters are shown as the full lines in Fig. 4.16.

The width of the electronic satellites in Fig. 4.16(a) is clearly underestimated by the theoretical spectrum. As the calculations are performed for a plasma characterized by a single n_e, this implies the presence of density gradients which could be attributed to : (1) the radial variation of the gas–jet density distribution predicted by the Mach–Zehnder experiment, and (2) the open geometry expansion of the plasma. The same situation is observed in the ionic spectrum of Fig. 4.16(b). In fact, the minimum and maximum value of <*Z*>T_e, for which an acceptable fit is obtained between the theoretical and the experimental satellites, are, respectively, 4000 and 8000 (see Fig. 4.17). This could be attributed to the variation of T_e, assuming in a first approximation that the variation order of <*Z*> is negligible. The plasma temperature gradients calculated for constant <*Z*> are given in columns 6 and 8 as deviations from the temperature mean value.

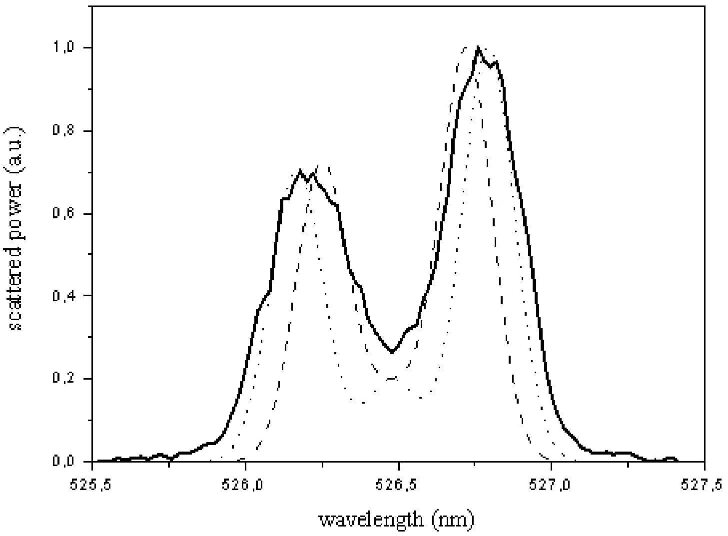

Figure 4.17 Variation limits of <*Z*>T_e for which an acceptable fit of the xenon ionic scattering spectrum is obtained. Full line : experimental ionic spectrum of Fig. 4.16(b). Dashed line : Theoretical curve calculated for <*Z*>T_e = 4000. Dotted line : Theoretical curve calculated for <*Z*>T_e = 8000.

Analysis of krypton Thomson scattering spectra

Figure 4.18 shows the two lineouts (dotted lines) of a Thomson scattering spectrum obtained for a 2 bar pressure krypton gas–jet heated by a 390 J energy laser beam; the profiles are sampled at 1 ns after the beginning of the signal emission and correspond to 100 ps time integration. A striking characteristic of Fig. 4.18(a) is the very wide spectral range of the electronic satellites indicating the presence of density gradients. The simultaneous parametrical fit of the spectra gives : $n_e = 6\ 10^{19}$ cm^{-3} and <*Z*>T_e = 4750. For $n_i = 2.57\ 10^{18}$ cm^{-3} obtained from Table 4–II, we find that <*Z*> = 23, and T_e = 203 eV. The mean ionization number given by the analysis of the krypton x–ray emission spectra is ~ 26 (cf. §4.5.2). Since this value is expected to be overestimated, the <Z> value obtained here from the helium reference density seems acceptable.

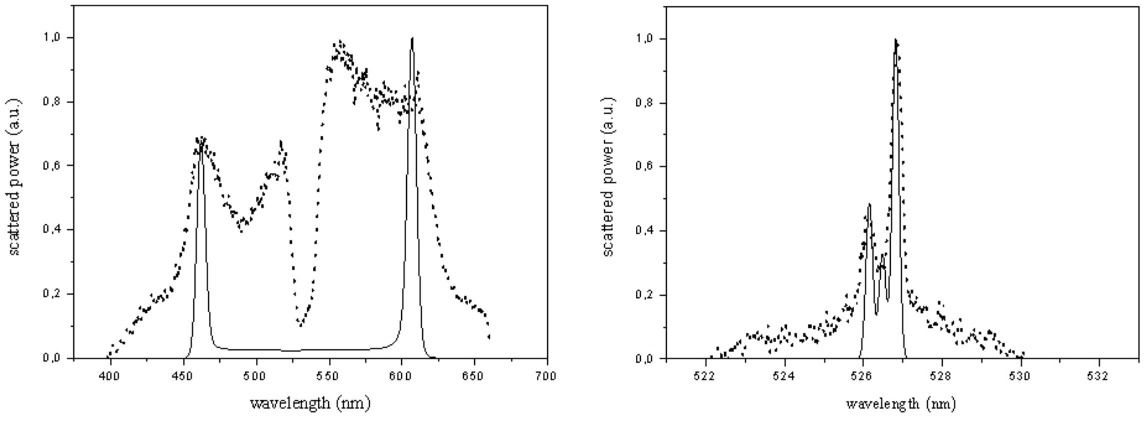

(a) (b)

Figure 4.18 Comparison of the experimental krypton Thomson scattering spectra (dotted lines) obtained at 1 ns after the beginning of the signal, with the theoretical spectra (full lines) resulting by the calculation of the spectral density function for $n_e = 6.0\ 10^{19}$ cm^{-3}, $ZT_e = 4750$. (a) Electronic spectrum, (b) Ionic spectrum.

P (bar)	$E(\omega)$ (J)	<Z>	n_e(x10^{19} cm^{-3})	T_e (eV)
1.3	370	21	3.5	203 ± 60
2	390	23	6.0	203 ± 32
4	230	23	12.0	171 ± 43

Table 4–IV Krypton plasma parameters for different values of the gas–jet pressure and the laser energy used in the experiment. The values of the plasma parameters result by analyzing the scattering spectra at 1 ns after the beginning of the signal emission.

The theoretical curves calculated for these parameters are shown as the full lines in Fig. 4.18. In Fig. 4.18(a), the underestimation of the electronic satellites width is obvious. From Fig. 4.18(b) we find for the product term $<Z>T_e$ a fit tolerance of ±750. For constant <Z> this implies that the plasma exhibits temperature gradients of ± 32 eV. Repeating the same procedure for the Thomson scattering spectra obtained under different pressure and energy conditions, we obtain the results summarized in Table 4–IV.

4.5 Characterization of the x–ray emission spectra in the keV range

4.5.1 Xenon plasma emission spectra

The time–integrated xenon plasma emission spectra in the keV range were measured for different gas–jet pressures and laser energies. These spectra, measured at the center of the gas jet, are presented in Figures 4.19, 4.20. In the spectral range of 12 – 15 Å, the xenon shows a rich emission spectrum composed of various transition structures. These structures correspond to the 3*d*–4*f* unresolved transitions arrays (UTA) emitted by different ion species around the closed–shell Ni–like (Xe^{26+}) ion [9]. The ions identified in our spectra belong to the iso–electronic sequence from Ni–like (Xe^{26+}) to V–like (Xe^{31+}). As in [9], Ni–like lines are observed around 14.24 Å and 14.6 Å corresponding, respectively, to the transitions from the $4f_{5/2}$ and the $4f_{7/2}$ *jj*–coupled spin orbital. Also, Co–like (Xe^{27+}), Fe–like (Xe^{28+}) and Mn–like (Xe^{29+}) ions UTAs are identified around 13.744 Å, 13.246 Å and 12.83 Å. However, in our case some additional structures are observed corresponding to the 3*d*–4*f* UTAs of higher charged ions. In particular, as the gas–jet pressure and the laser energy are increased, the transitions of the Cr–like (Xe^{30+}) and V–like (Xe^{31+}) ions appear, respectively, around 12.41 Å and 12.06 Å. Finally, the Cu–like (Xe^{25+}) ion UTA observed in [9], is identified also in our case around 14.39 Å, but only for low pressure and laser energy conditions.

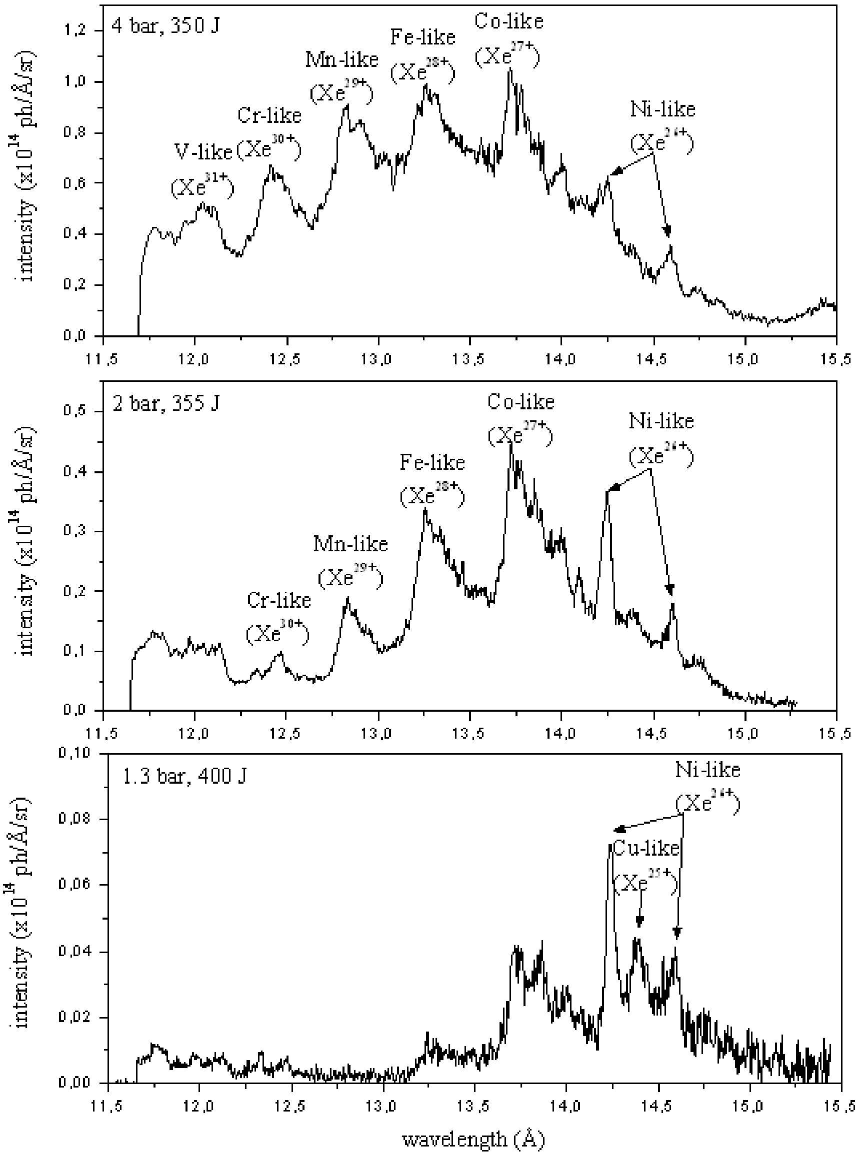

Figure 4.19 Variation of the xenon plasma x–ray emission spectrum with the experimental conditions; spectra obtained for similar laser energy and different gas–jet pressure.

Given the good reproducibility of the spectra, from shot to shot, we can follow the variations of the observed structures due to the changes of the gas–jet pressure and the laser energy. The absolute intensity level of the emission spectrum increases with the gas pressure and the laser energy, and this behavior can be explained by the increased absorbed energy from the produced plasmas. Further, it is interesting to investigate the variations of the ionic populations due to the different experimental conditions. So, we analyze the relative changes of the different emission structures intensities.

Fig. 4.19 gives the comparison of three spectra obtained under different gas–jet pressure and similar laser energy conditions. For 1.3 bar pressure, the spectrum is composed of the transitions from Cu–like (Xe^{25+}) to Fe–like (Xe^{28+}) ions; the Ni–like (Xe^{26+}) transitions from the $4f_{5/2}$ *jj*–coupled spin orbital, and the Cu–like (Xe^{25+}) transitions are dominant. As the pressure is increased to 2 bar, the ion features up to Cr–like (Xe^{30+}) appear clearly. Co–like (Xe^{27+}) ion transitions are now dominant, with a significant contribution of Ni–like (Xe^{26+}) and Fe–like (Xe^{28+}) ions features. The decrease of the Cu–like (Xe^{25+}) contribution (its ion feature is hardly identified), in addition to the appearance of higher charged ions, indicate clearly the shift of the ion population distribution to a higher ionization state. Concerning the variation of the intensity and the plasma ionization state, the increase of the pressure overcomes the small decrease of the energy. This proves the strong influence of the gas–jet pressure on the properties of the produced plasma. Increasing the pressure to 4 bar, a further increase of the plasma ionization state is observed. The Co–like (Xe^{27+}) and Fe–like (Xe^{28+}) ions transitions are still dominant, but now there is a significant contribution of the Mn–like (Xe^{29+}) and Cr–like (Xe^{30+}) ions features. Also, the V–like (Xe^{31+}) and the Ni–like (Xe^{26+}) ions contribute now almost equivalently.

The changes of the spectrum induced by the variation of the laser energy at constant gas pressure of 2 bar are shown in Fig. 4.20. For 120 J energy (dashed line), the emission features from Cu–like (Xe^{25+}) to Co–like (Xe^{27+}) appear. The dominant contribution stems from the $4f_{5/2}$ *jj*–coupled spin orbital transitions of the Ni–like (Xe^{26+}) ion, and the Cu–like (Xe^{25+}) transitions. Increasing the energy to 355 J (full line), as we mentioned above, the Co–like (Xe^{25+}) becomes dominant and the ion features up to the Cr–like (Xe^{30+}) appear in the spectrum. Thus, the plasma ionization state increases with the laser energy.

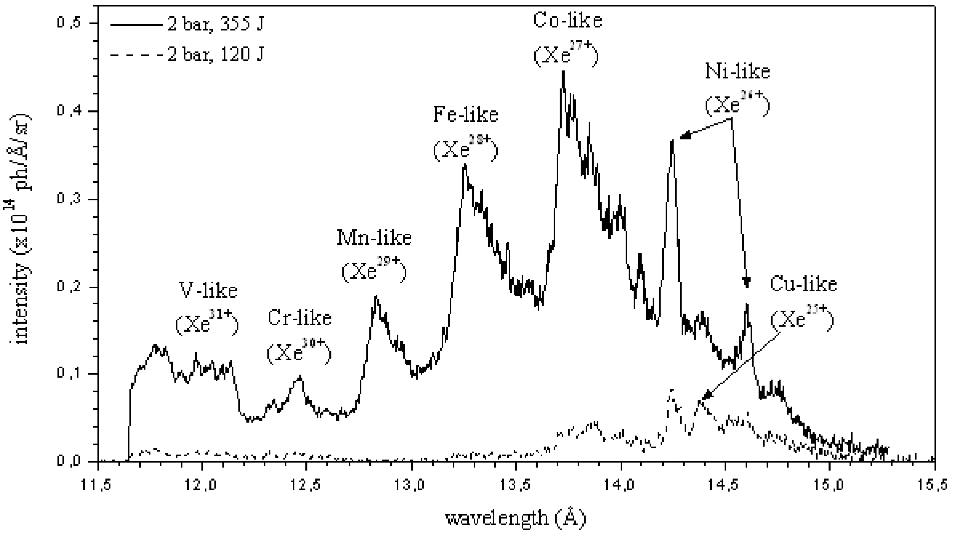

Figure 4.20 Variation of the xenon plasma x–ray emission spectrum with the experimental conditions; spectra obtained for the same gas–jet pressure and different laser energy.

An explicit calculation of the plasma ionic fractions would require to model each individual ion complex spectrum with the spin–orbit–split array method (SOSA) [28], and to perform a least–square–fit procedure with the experimental data, ajdusting the ion population distribution [9,29]. Such an analytical calculation would provide the quantitative determination of the ionic fractions. More simply, one can get a very rough estimation of the ions populations, supposing that the relative intensities of the ions features are proportional to the ionic fractions. This assumption is valid if the oscillator strengths of the main transitions involved for the different ionic stages are of the same order of magnitude. For each spectrum of Fig. 4.19, the relative intensity ratio of the peak corresponding to each ionic structure is calculated, and the results are summarized in Table 4–V (the ratio of the maximum spectrum feature is fixed to 1). These distributions permit to estimate roughly the plasmas mean ionization number, and from Table 4–VI we see that under the specific experimental conditions (pressure, laser energy) the xenon plasmas average charge takes values in the interval of 26 – 28.

Isoelectronic sequence Ion charge	Cu–like 25	Ni–like 26	Co–like 27	Fe–like 28	Mn–like 29	Cr–like 30	V–like 31
1.3 bar, 400 J	0.63	1	0.57	-	-	-	-
2.0 bar, 355 J	-	0.82	1	0.76	0.42	0.22	-
4.0 bar, 350 J	-	0.59	1	0.93	0.86	0.63	0.5
2.0 bar, 120 J	0.86	1	0.6	-	-	-	-

Table 4-V Relative intensity ratios of the different ions features of the xenon spectra under different experimental conditions of the gas–jet pressure and the laser energy.

Experimental conditions	1.3 bar, 400 J	2.0 bar, 120 J	2.0 bar, 355 J	4.0 bar, 350 J
$\langle Z \rangle$	26	25.9	27.4	28.3

Table 4–VI Xenon plasma mean ionization number assuming that the relative intensities of the ions features and the ionic fractions are proportional.

4.5.2 Krypton plasma emission spectra

The time–integrated krypton plasma emission spectra measured at the center of the gas–jet for different pressures and laser energies are summarized in Figure 4.21. The identification of the observed transition structures is based on the results of a previous work realized by our research group on the characterization of the krypton plasma emission spectrum in the keV range [11,13]. This work is based on a detailed level accounting (DLA) calculation of the different ions contributing to the emission spectrum, which is performed with the atomic code HULLAC [30]. The results of [13] corresponding to the transitions identified in our spectra are summarized in Table 4–VII. The second and the third column of the table contain, respectively, the experimental and the theoretical wavelengths of the transitions identified in [13]. In the first column are given the labels of the transitions identified in Fig. 4.21. In the range of 6 – 8 Å the krypton plasma emission spectrum contains many structures coresponding to the the n*l* – n'*l*' transitions (for n=2, n'=3,4) from Na–like (Kr^{25+}) to F–like (Kr^{27+}) ion [12,13].

As in xenon, it is worthwhile to investigate the variations of the krypton plasma emission spectrum with the pressure and the laser energy as shown in Fig. 4.21. A first remark concerns the absolute increase of the spectrum intensity with the increase of the gas–jet pressure and the laser energy. In the preceding paragraph we saw that this is due to the increase of the absorbed energy from the produced plasma.

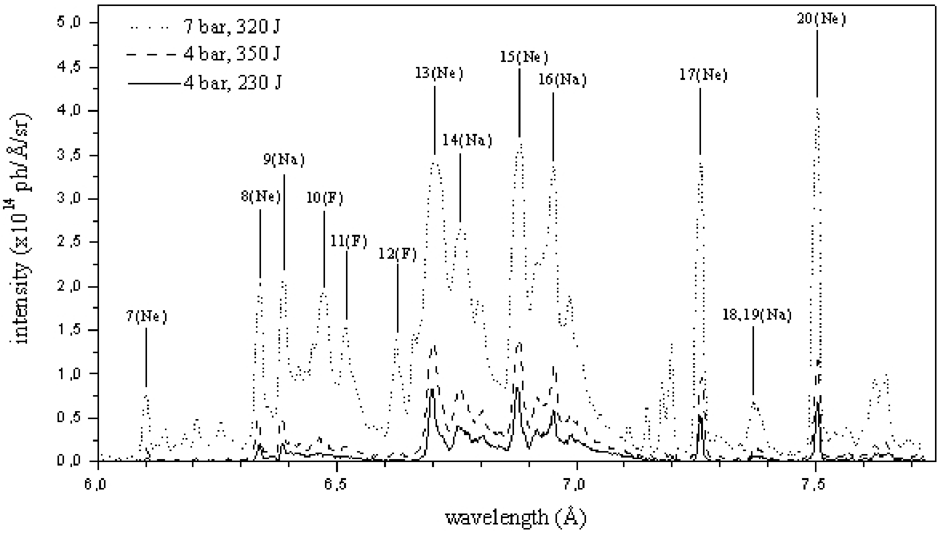

Figure 4.21 Variation of the krypton plasma x–ray emission spectrum with the the gas–jet pressure and the laser energy.

Further, and with regard to the induced variations on the plasma ions populations, we could mention the following. At 4 bar gas–jet pressure and 230 J laser energy (full line of Fig. 4.21), the observed emission structures correspond to the transitions of the Na–like (Kr^{25+}) and the Ne–like (Kr^{26+}) ions. The dominant spectral features are : the Ne–like (Kr^{26+}) $2p^6$–$2p^53d$ (label 13, 15) and the $2p^6$–$2p^53s$ (labels 17, 20) transitions, as well as the Na–like (Kr^{25+}) $2p^63d$–$2p^53d^2$ transitions (labels 14, 16). Around 6.35 Å it is observed a significant contribution of the Ne–like (Kr^{26+}) $2s^22p^6$–$2s2p^63\mathrm{d}$ transitions (labels 8, 9). Finally, there is a small contribution of the Ne–like (Kr^{26+}) $2s^22p^6$–$2s2p^63d$ transitions (label 7), and of the Na–like (Kr^{25+}) $2p^63d$–$2p^53s3d$ (label 18) and $2p^63d$–$2p^53s3p$ (label 19) transitions. Keeping constant the pressure, and increasing the energy at 350 J, the spectrum shown as the dashed curve in Fig. 4.21 is obtained. The general shape of the spectrum does not change, as the transitions observed for 230 J are still present, and their relative intensity ratio remains constant. However the spectrum shows a small contribution of the F–like (Kr $^{27+}$) $2p^5$–$2p^43d$ transitions (labels 10–12). This indicates that the increase in the energy results in a higher ionization state.

We see a similar behavior with the variation of the gas–jet pressure (full and the dotted line curves of Fig. 4.21). The intensity of the F–like (Kr^{27+}) transitions (labels 10–12), shows a significant increase, as they become almost equivalent with the Ne–like (Kr^{26+}) transitions (labels 8, 9). Finally, as with xenon, and with regard to the intensity level and the ionization state of the plasma, the increase of the pressure overcomes the small decrease of the laser energy.

Concerning the estimation of the krypton mean ionization number, the procedure followed in the case of the xenon gas would be helpless here, for, the identified ions give various discrete emission features with different intensities[2]. However, and inasmuch as we observe only three ionic charge states, roughly speaking, the mean ionization number of the krypton plasma is $\langle Z \rangle \approx 26 \pm 1$.

---

[2] A formal approach to calculate the ionic fractions is given in [11], applying the method presented in [9]. There, a least–square–fit is performed on the measured spectra, using the data calculated with the detailed atomic code HULLAC[30].

label	λ_{exp}(Å)	λ_{th}(Å)	ion	gA_{th}	lower level	J^{low}	upper level	J^{up}	E^{up}
7 (E2s)	6.102	6.0910	Kr^{26+} (Ne)	0.544(12)	2s^{2}2p^6	0	2s2p^{6}3d	2	16417.9
8 (3A)	6.335	6.3238	Kr^{26+} (Ne)	0.511(14)	2s^{2}2p^6	0	2s2p^{6}3d	1	15813.2
9 (3B)	6.382	6.3732	Kr^{26+} (Ne)	0.144(14)	2s^{2}2p^6	0	2s2p^{6}3d	1	15690.7
		6.3843	Kr^{25+} (Na)	0.493(14)	2s^{2}2p^{6}3s	0.5	2s2p^{6}3s3p	1.5	15663.3
		6.3913	Kr^{25+} (Na)	0.986(14)	2s^{2}2p^{6}3p	1.5	2s2p^{6}3p^2	1.5	16210.3
10	6.462	6.4590	Kr^{27+} (F)	4.54(14)	2p^5	1.5	2p^{4}3d	2.5	15482.3
		6.4645	Kr^{27+} (F)	2.98(14)	2p^5	1.5	2p^{4}3d	1.5	15469.1
11	6.515	6.5184	Kr^{27+} (F)	1.02(14)	2p^5	1.5	2p^{4}3d	2.5	15341.3
12	6.624	6.6193	Kr^{27+} (F)	3.07(14)	2p^5	0.5	2p^{4}3d	1.5	15552.3
13 (3C)	6.699	6.6929	Kr^{26+} (Ne)	2.89(14)	2p^6	0	2p^{5}3d	1	14941.2
14	6.753	6.7386	Kr^{25+} (Na)	2.91(14)	2p^{6}3d	2.5	2p^{5}3d^2	1.5	16026.9
	6.740	6.7414	Kr^{25+} (Na)	3.94(14)	2p^{6}3d	1.5	2p^{5}3d^2	1.5	16001.5
		6.7494	Kr^{25+} (Na)	5.20(14)	2p^{6}3d	2.5	2p^{5}3d^2	3.5	16003.0
		6.7511	Kr^{25+} (Na)	2.45(14)	2p^{6}3p	1.5	2p^{5}3p3d	2.5	15376.4
		6.7534	Kr^{25+} (Na)	6.06(14)	2p^{6}3d	2.5	2p^{5}3d	2.5	15994.3
	6.770	6.7629	Kr^{25+} (Na)	2.22(14)	2p^{6}3s	0.5	2p^{5}3s3d	1.5	14786.6
		6.7912	Kr^{24+} (Mg)	3.69(14)	2p^{6}3s3d	2	2p^{5}3s3d	3	16070.9
		6.7980	Kr^{24+} (Mg)	2.57(14)	2p^{6}3s^2	0	2p^{5}3s 3d	1	14710.3
	6.800	6.8067	Kr^{24+} (Mg)	2.04(14)	2p^{6}3s3d	2	2p^{5}3s3d	3	16037.4
15 (3D)	6.880	6.8755	Kr^{26+} (Ne)	2.17(14)	2p^6	0	2p^{5}3d	1	14544.4
		6.9191	Kr^{25+} (Na)	2.29(14)	2p^{6}3d	1.5	2p^{5}3d	2.5	15620.5
	6.928	6.9283	Kr^{25+} (Na)	3.46(14)	2p^{6}3d	2.5	2p^{5}3d	2.5	15620.5
		6.9468	Kr^{25+} (Na)	2.84(14)	2p^{6}3d	1.5	2p^{5}3d	2.5	15563.0
16		6.9473	Kr^{25+} (Na)	1.18(14)	2p^{6}3s	0.5	2p^{5}3s3d	1.5	14394.1
	6.953	6.9501	Kr^{25+} (Na)	2.78(14)	2p^{6}3d	2.5	2p^{5}3d^2	3.5	15575.3
17 (3F)	7.268	7.2670	Kr^{26+} (Ne)	0.109(14)	2p^6	0	2p^{5}3s	1	13760.7
18	7.376	7.3733	Kr^{25+} (Na)	0.230(14)	2p^{6}3d	2.5	2p^{5}3s3d	3.5	14749.5
	7.380	7.3827	Kr^{25+} (Na)	0.169(14)	2p^{6}3d	2.5	2p^{5}3s3d	2.5	14732.3
19	7.387	7.3892	Kr^{25+} (Na)	0.188(14)	2p^{6}3p	0.5	2p^{5}3s3p	1.5	13993.7
20 (3G)	7.504	7.5022	Kr^{26+} (Ne)	0.158(14)	2p^6	0	2p^{5}3s	1	13329.4

Table 4–VII Identification of the different ions and their corresponding atomic transitions contributing to the observed emission features of the krypton plasma (cf Ref [11,13]).

4.6 Analysis of the x-ray spectra with TRANSPEC/AVERROES

Having determined the parameters of the xenon and krypton plasmas, and after the independent estimation of their state obtained additionally from the preceding discussion of their keV x–ray spectra, we can calculate their synthetic emission spectra with the code TRANSPEC/AVERROES [4,5]. In paragraph 4.6.1 we compare the theoretical spectra of TRANSPEC/AVERROES with the experimental spectra in the keV range. Then, in paragraph 4.6.2 we extend our analysis in the XUV spectral range.

4.6.1 Calculation of the synthetic emission x-ray spectra in the keV range

Xenon plasma emission spectra

Figure 4.22 shows the xenon plasma emission spectrum measured for a 2 bar pressure gas–jet heated by a 355 J energy laser beam (dotted line). The theoretical spectrum (full line) is calculated with plasma parameters : $n_i = 2.57\ 10^{18}\ \mathrm{cm}^{-3}$, $<Z> = 27$, $T_e = 330$ eV. The density is given by the Thomson diagnostic and $<Z>$ by the x–ray spectrum. The temperature corresponds to the maximum value of the time evolution scheme that we assume to obtain after 1 ns the Thomson temperature $T_e \approx 260$ eV. Thus, we include an estimation of the Bragg spectrograph time integration (see also the discussion in §4.6.2).

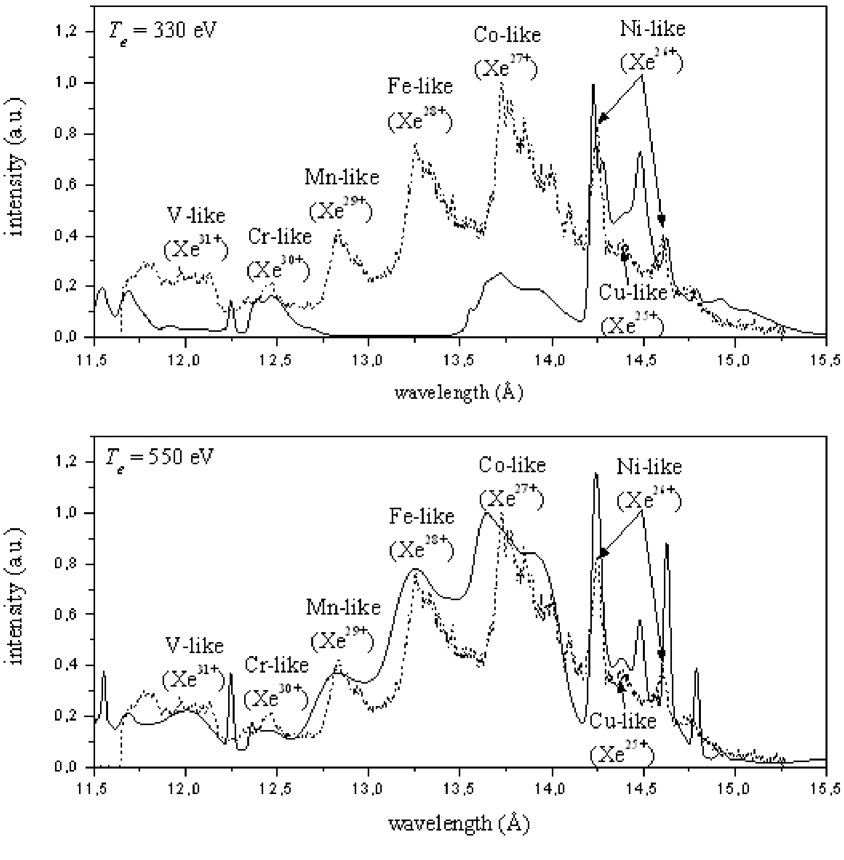

Figure 4.22 Xenon plasma emission spectrum of a 2 bar pressure gas–jet heated by a 355 J energy laser (dotted line), compared with the TRANSPEC/AVERROES [4,5] calculations for $n_i = 2.57\ 10^{18}\ \mathrm{cm}^{-3}$, $T_e = 330$ eV, 550 eV (full lines).

Adjusting the intensity level of the synthetic spectrum to fit the Ni–like (Xe^{26+}) features, we see that the code reproduce well their relative ratio. However, the synthetic spectrum underestimates strongly the Co–like (Xe^{27+}) ion features, and does not gives at all the measured Fe–like (Xe^{28+}) and Mn–like (Xe^{29+}) transitions structures. Keeping constant n_i, and increasing T_e we gradually obtain a better agreement between the theoretical and the experimental spectrum. Fitting the intensity of the theoretical spectrum to the Co–like (Xe^{27+}) emission features, we obtain the best convergence with the experimental spectrum for T_e = 550 eV. For this temperature, the code reproduces very well all the ions features from Co–like (Xe^{27+}) to Mn–like (Xe^{30+}), overestimating, however, the Ni–like (Xe^{26+}) transitions.

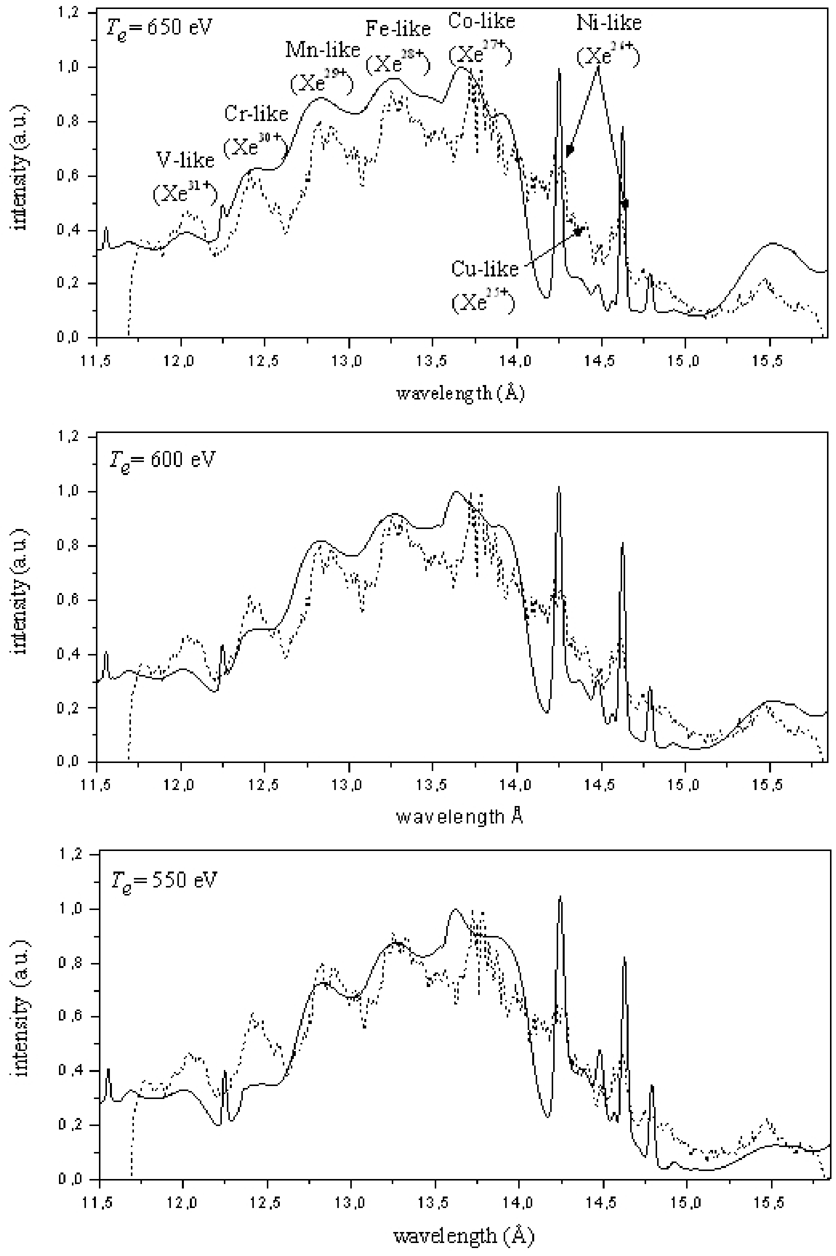

Figure 4.23 Xenon plasma emission spectrum of 4 bar pressure gas–jet heated by a 350 J energy laser (dotted line), compared with the TRANSPEC/AVERROES [4,5] calculations for n_i = 5.14 10^{18} cm^{-3}, T_e = 550, 600, 650 eV (full lines).

The xenon plasma emission spectrum obtained from a 4 bar pressure gas–jet heated by a 350 J energy laser is given in Figure 4.23 (dotted line). Similarly, the theoretical spectrum calculated for the Thomson scattering parameters (n_i = 5.14 10^{18} cm^{-3}, T_e = 390 eV, <Z> = 24.3) gives an average charge too low to reproduce the different emission features. Fig. 4.23 gives the theoretical spectra calculated, respectively, for T_e = 550, 600, 650 eV (full lines). The comparison with the experimental spectrum is performed by adjusting the intensity to fit the Co–like (Xe^{27+}) ion transitions. For T_e = 550 eV, the code reproduces the transitions ratio of the ions from Co–like (Xe^{27+}) to Mn–like (Xe^{29+}), but the contributions of the Cr–like (Xe^{30+}), V–like (Xe^{31+}) ions is underestimated. Keeping constant n_i, and increasing T_e, a better agreement is gradually observed for the high charged ions (Cr–like (Xe^{30+}), V–like (Xe^{31+})). To obtain a convergence for the Cr–like (Xe^{30+}) transitions, the temperature should be increased to 650 eV. At this temperature, however, there is a slight overestimation of the Fe–like (Xe^{28+}), Mn–like (Xe^{29+}) ion features. Also, it should be stressed that the code, for the specific temperature range, gives a strong overestimation of the Ni–like (Xe^{26+}) ion transitions.

From the above discussion two important remarks follow : (1) the theoretical spectra show a better convergence with the experimental for temperatures higher than those given by the Thomson diagnostics, and (2) even at “high” temperatures, we cannot obtain a convergence with all the observed emission features of the different ions species for a single temperature value.

Concerning the explanation of the very high temperature required we could invoke the instrinic lack of coherence between the Thomson and the Bragg spectrograph diagnostics, discussed in paragraph 4.4.2. We recall that this stems mainly from the different temporal and spatial operation scales of the two diagnostics. In particular, the larger spatial probing and the time integration of the Bragg spectrograph result in measuring a higher temperature plasma with respect to the Thomson diagnostic. This deviation is additionally enforced due to the narrow spectral range of the Bragg spectrograph, which does not give an overall image of the state of a non–homogeneous plasma, as the Thomson diagnostic does. Indeed, in the range 11 – 15 Å, only the ions Xe^{25+} to Xe^{31+} can contribute. The other ion stages do not emit in this spectral range.

The second remark could be explained by the presence of temperature gradients. The code TRANSPEC in the single–cell mode used in our analysis, calculates the populations kinetics and the synthetic spectrum with single temperature and density values, thus assuming a purely homogeneous plasma. However, the x–ray spectrum is not expected to correspond to an homogeneous plasma due to its space and time integration scale (spatial non homogeneity, temporal evolution). Our qualitative estimation is confirmed by the measurements of the Thomson diagnostic, which are time–resolved and obtained with a finer scale of spatial probing. Their analysis show the time evolution of the plasma parameters (especially for the electron density), and most important, it proves that at a given time the plasma exhibits both temperature and density spatial gradients.

Krypton plasma emission spectra

Figure 4.24 gives the krypton emission spectrum measured for a 4 bar pressure gas–jet heated by a 230 J energy laser (dotted line). The detailed level accounting analysis of the krypton spectrum performed elsewhere [13] shows that the spectrum exhibits a breakdown of the *LS*–coupling, and the UTAs are split into discrete unresolved sub–bands. Due to this, the synthetic spectra is calculated with TRANSPEC/AVERROES with the spin–orbit–split arrays (SOSA) formalism [28]. As in xenon, the synthetic spectrum does not reproduce the observed emission features for the temperature given by the Thomson diagnostic (n_i = 5.12 10^{18} cm^{-3},

T_e = 170 eV). The best convergence is obtained for the theoretical spectrum calculated with T_e = 500 eV (full line in Fig. 4.24). Now, the code reproduces well the Na–like and Ni–like transitions 13, 15, 16 (see Table 4–VII). However, an overestimation and an underestimation of the intensity levels is observed for the transitions (8, 9) and (17, 20), respectively.

Concerning the difference between the temperature of the Thomson diagnostic and the temperature used to obtain an acceptable convergence with measured x–ray spectrum, we could invoke the justification made for the xenon plasma. The deviations observed for the high temperature theoretical spectrum could be partly attributed to the gradients of the plasma cancelling the single–cell approach (single value temperature–density plasma) used by TRANSPEC. On the other hand, the observed deviations could be also attributed to the poor treatment of the coupling between the populations kinetics and the radiation field provided by SOSA. Here, the use of the detailed level accounting (DLA) approach could provide a better convergence.

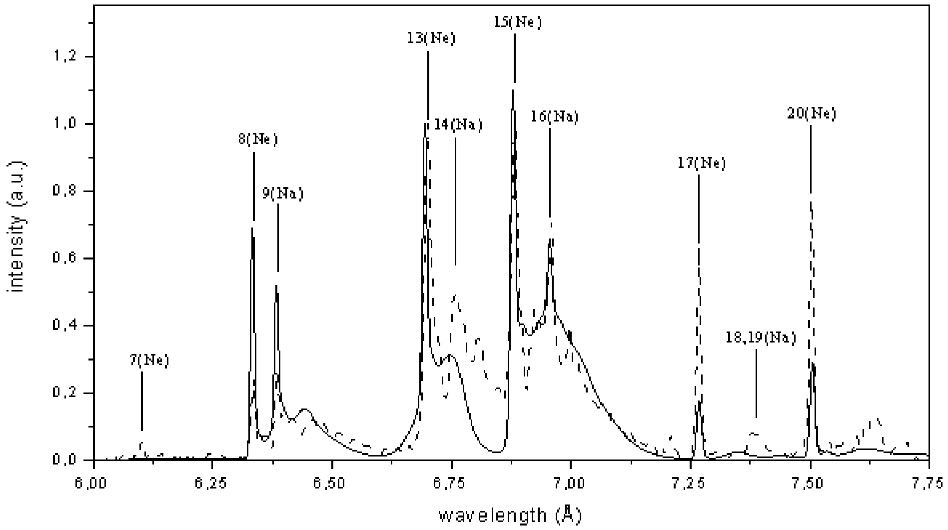

Figure 4.24 Krypton plasma emission spectrum of 4 bar pressure gas–jet heated by a 230 J energy laser (dotted line), compared with the TRANSPEC/AVERROES [4,5] calculations for n_i = 5.14 10^{18} cm^{-3}, T_e = 500 eV (full line).

4.6.2 Calculation of the XUV emission spectra

Xenon plasma emission spectra

The time–resolved XUV emission spectrum of a 2 bar pressure xenon gas–jet heated by a 355 J energy laser is recorded in the spectrum image of Figure 4.25. To study its time evolution, three lineouts of ~ 200 ps time integration width are sampled at different times, which are given as the dotted lines in Fig. 4.26. The specific samples were chosen as they provide a complete description of the emission time evolution.

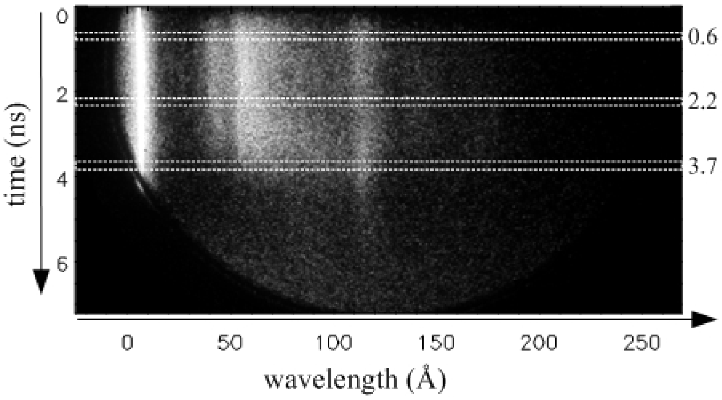

Figure 4.25 Spectrum image of 2 bar pressure xenon gas–jet heated by 355 J energy laser. The scheme gives the positions of the lineouts obtained to trace the time evolution of the spectrum.

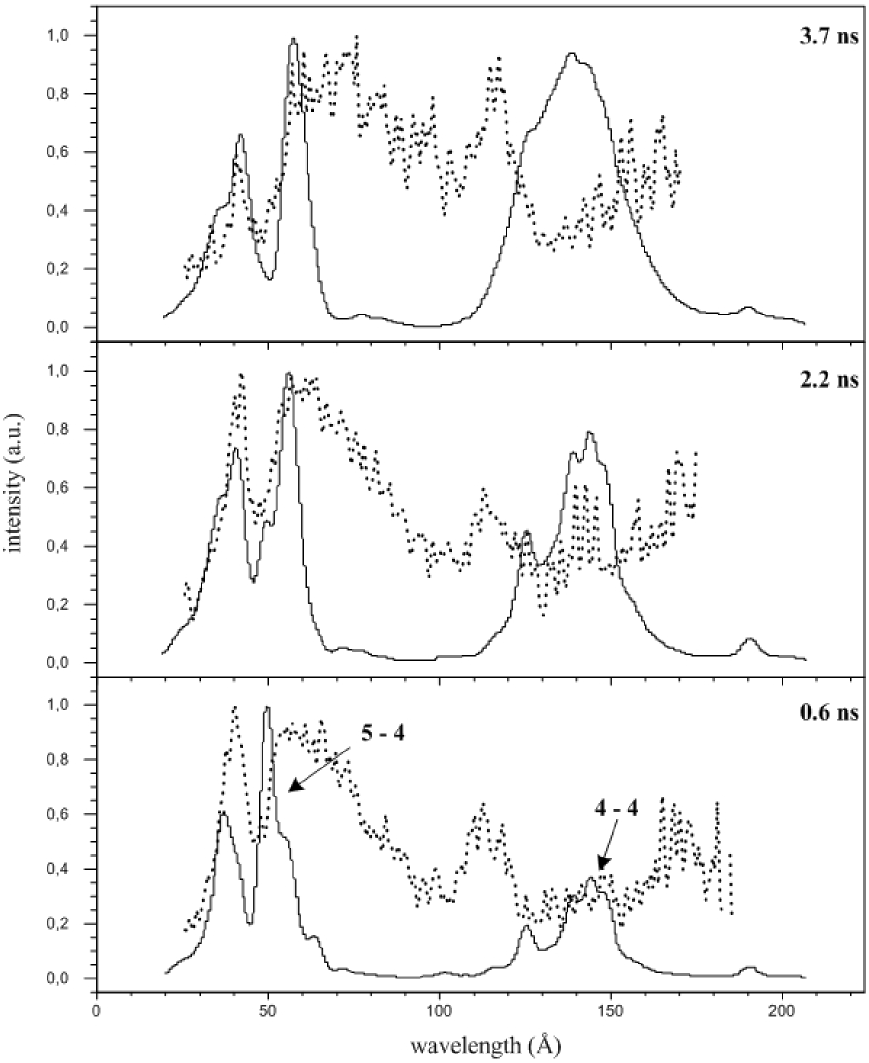

Figure 4.26 Xenon XUV emission spectrum profiles obtained from a 2 bar pressure gas–jet heated by a 355 J energy laser (dotted lines), compared with the calculations of TRANSPEC/AVERROES (full lines).

In the spectral range of 20 – 160 Å the xenon plasma gives a rich emission spectrum, which could be separated in three structures : the sharp structure around 40 Å, the wide structure appearing in the range of 46 – 90 Å, and the structure around 112 Å. The time evolution of the spectrum is shown in Fig. 4.26. Initially, the structure at 40 Å is dominant. As time evolves up to 2.2 ns, its intensity level remains constant, but around 3 ns it decreases strongly. The structure in the range of 46 – 90 Å has a dominant contribution almost all over the measured time interval. From 0.63 ns to 2.2 ns only a small variation of the structure intensity is observed. Only at the end of the measured signal, the structure changes ($t > 3.5$ ns). In particular, at 3.7 ns, the portion of the structure in the range of 46 – 75 Å decreases more than the range of 75 – 96 Å. So, the range 40–96 Å looks like a plateau. The structure around 112 Å increases at late times (see t=3.7 ns), reaching the same level of intensity as the plateau 40–96Å.

For the calculation of the synthetic XUV emission spectrum with the code TRANSPEC/AVERROES the time evolution of the plasma parameters has to be taken into account. The Thomson diagnostic for the specific measurement, and at 1 ns after the beginning of the signals emission, gives $n_i = 2.57\ 10^{18}$ cm^{-3} and $T_e = 260$ eV. A first estimation of the plasma parameters is obtained using a simplified time evolution scheme (see Fig. 27) :

1. The ionic density maintains a constant value.
2. The electron temperature shows a 0.2 ns fast rise to a maximum temperature ($T_e = 330$ eV), followed by a 0.25 ns duration plateau. Then, the temperature decays with a slope giving a total duration of 4.5 ns (observed emission mean duration). The maximum temperature is chosen to obtain at 1 ns, and for the assumed temperature slope, the Thomson temperature $T_e = 260$ eV.

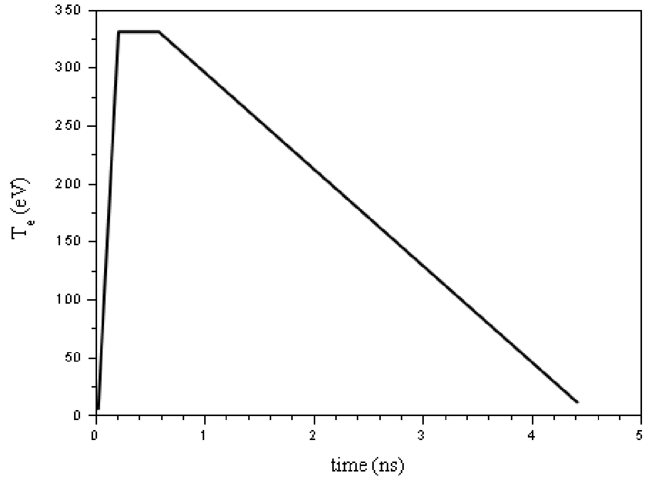

Figure 4.27 Time evolution of the electronic temperature. This evolution scheme is deduced by using the Thomson diagnostics measurements of a 2 bar pressure xenon gas–jet heated by 355 J energy.

The theoretical profiles calculated at 0.6 ns ($T_e = 290$ eV), 2.2 ns ($T_e = 170$ eV) and 3.7 ns ($T_e = 60$ eV) are shown as the full lines in Fig. 4.26. The theoretical spectrum is composed of 5–4 and 4–4 transitions structures. The 5–4 transitions structure is split in two discrete sub–bands around 40 and 50 Å, respectively. With regard to their peak wavelengths, the sub–band around 40 Å coincides clearly with the experimental structure. The sub–band around 50 Å coincides with the border of the wide band measured in the range of 46 – 90 Å, underestimating, however, its width. Finally, the code cannot reproduce the measured structure around 112 Å, and the wide unresolved emission structure observed in the range of 70 – 100 Å.

Taking as reference the intensity peak of the 5–4 transitions, the code at 0.6 ns reproduces the relative intensity of the sub–band around 50 Å, but it underestimates the relative intensity of the sub–band around 40 Å. The 4–4 transitions structure shows an ambiguous coincidence with the measured spectrum, but no conclusion can be inferred due mainly to the low signal to noise ratio (SNR) of the measured signal. As time evolves to 2.2 ns, a relative increase of the sub–band around 40 Å is observed, and the code 5–4 transitions show an improved agreement with measured spectrum in the range of 30 – 60 Å. Also, the measured spectrum shows a clear transition structure around 145 Å, which coincides with the 4–4 transitions structure of the code. However, this structure appears for a very narrow time interval. So, it could be an artificial signal due to the cathode response in conjunction with the low SNR (see §4.3.2). At 3.7 ns the 5–4 transitions are well reproduced by the code in the range of 30 – 60 Å, including their relative intensity ratio.

Krypton plasma emission spectra

Figure 4.28 gives the time evolution of the krypton plasma XUV emission spectrum measured for a 4 bar pressure gas–jet heated by a 230 J energy laser (dotted lines). As with xenon gas, the krypton plasma gives a rich and time–variable emission spectrum.

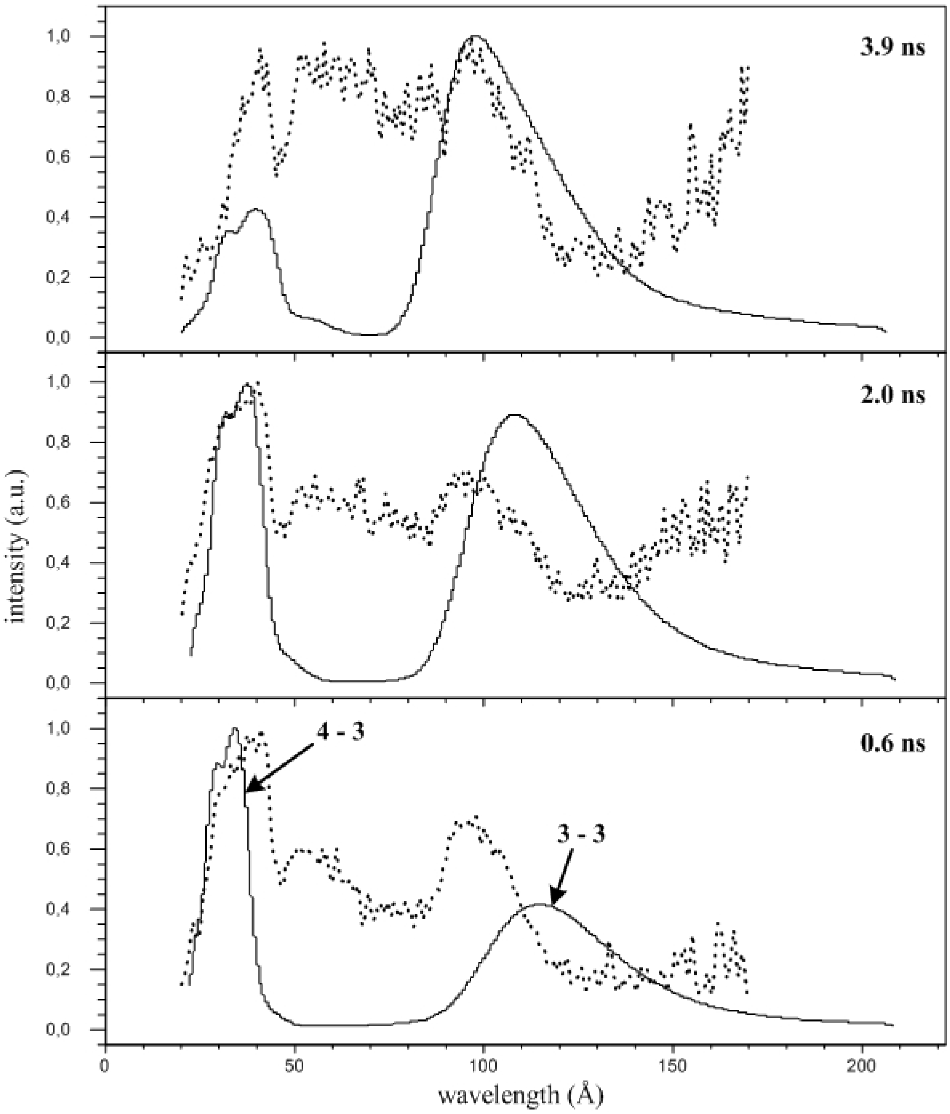

Figure 4.28 Krypton XUV emission spectrum profiles obtained from a 4 bar pressure gas–jet heated by a 230 J energy laser (dotted lines), compared with the calculations of TRANSPEC/AVERROES [4,5] (full lines).

Initially, at 0.6 ns three emission structures are clearly observed : the sharp dominant structure around 35 Å, the low intensity structure in the range of 45 – 65 Å, and the wide structure in the range of 85 – 120 Å with a significant contribution to the spectrum emission. As time evolves up to 2.0 ns, the three structures do not vary significantly. The formation of a plateau in the range of 50 – 85 Å is caused by the relative increase of the intensity in the range of 70 – 85 Å. At the end of the measured signal ($t > 3.5$ ns) a strong change is observed at low wavelengths. Indeed, in the profile probed at 3.9 ns, a decrease of the structure around 35 Å is observed, which intensity becomes equivalent to the intensity level of the rest of the spectrum.

To calculate the synthetic emission spectra we use the estimation obtained by the Thomson analysis ($n_i = 5.12\ 10^{18}$ cm^{-3}, $T_e = 170$ eV), and the time evolution scheme applied for the xenon. The results are shown in Fig. 4.28 as full lines. At 0.6 ns there is a very good agreement at low wavelengths; the code reproduces the dominant structure around 35 Å composed of the 4–3 transitions. However, differences are observed all over the rest of the spectral range. The 3–3 transitions structure appears at higher wavelengths with respect to the measured structure in the range of 85 – 120 Å, and its relative intensity is underestimated. Also, the code does not give any transitions structures in the band of 50 – 85 Å. The code convergence with the measured spectrum exhibits the same characteristics up to 2 ns. At 3.9 ns, the 4–3 structure coincides with the measured structure around 35 Å, but its relative intensity is underestimated. An agreement is clearly observed between the measured structure in the range of 85 – 120 Å and the 3–3 transitions calculated by the code.

Discussion of the experiment/AVERROES comparison for xenon and krypton

The common point in the analysis of both elements is the relatively good theoretical reproduction of the emission structures at low wavelengths, and the lack of coincidence for the other emission features. The difficulty to trace the observed differences between the synthetic and the measured spectra lies on the wide unresolved emission structures, without discrete ionic features, which prevent us to obtain a rough estimation of the probed plasma state. Here we restrict ourselves to mention some potential sources of the observed deviations.

The intensity deviations of the synthetic xenon 5–4 and the krypton 4–3 structures, observed at different times, could be attributed to the scheme of the plasma time evolution used as input parameters for the code TRANSPEC. A more consistent approach would require the simulation of the laser–plasma interaction with a hydrodynamic code. The difficulty is the three–dimensional (3D) open geometry expansion of the plasma. However, simulations performed with the 1D code MULTI [32] give an advanced convergence at low wavelengths, enforcing the intention to continue this analysis in its 3D approach.

A second potential error source, concerning also the plasma parameters, is the assumed spatial homogeneity implied by the single–cell mode of the code TRANSPEC used here. Even though now the probed region along the laser axis is rather small (~ 200 μm), the XUV radiation recorded by the spectrograph is emitted from all the plasma region perpendicular to the laser axis (~ 1 mm long), along which we should expect the plasma to show gradients (see Fig. 4.2). This is reasonable, insofar as the plasma homogeneity is not justified even for the finer probing scale of the Thomson diagnostics. So, apart from the time evolution, to improve the convergence between the synthetic and the measured spectra the hydrodynamic simulation should include also the plasma spatial profile normal to the laser axis.

The presence of spatial gradients can be partly explained by the large scale of the produced plasma and its open (3D) heating geometry. An additional hypothesis of the observed non–homogeneities of the plasma is the poor thermal–smoothing that it shows to the laser intensity pattern of the random phase plate (RPP). As we explained in paragraph 3.2.2, the operation of the RPP is based on the production of an intensity distribution of very closely spaced peaks, for the spatial scale of which the thermal conduction provides an adequate smoothing mechanism. The large line–shape focal spot (1 mm x 150 μm) in conjunction with the gas–jet target, which shows a rather low thermal smoothing with respect to the solid targets, can produce an non–homogeneous plasma with randomly distributed hot spots. In this case the plasma behaves as a bath of a mean low temperature value, in which there are “islands” of high temperature plasma. Even though this scheme differs from the stereotype of the “gradient”, with regard to the diagnostics it is equivalent : we have the recording of radiation from plasma regions with very different properties. We should notice that initially the specific focal spot, with the large width and the small height, was choosen to fullfil two requirements : (1) to heat all the gas–jet in order to avoid the cold jet around the plasma absorbing the radiation (large spot width), and (2) to minimize the width of the plasma source seen by the Bragg spectrograph in order to improve its spectral resolution (small spot height).

Finally, we should mention that the code AVERROES predicts no emission line in the bands 70 – 100 Å for xenon, and 50 – 85 Å for krypton. Here the question concerns both the accounting of the transitions included in the SCs and the accuracy of the obtained transitions rates used in determining the population kinetics. From this point of view the measured rich time–resolved XUV emission spectra provide an interesting benchmark for the future development of the code model.

4.7 Conclusions

The time–integrated emission spectra in the keV range, as well as the time–resolved XUV emission spectra have been measured for both the xenon and krypton. The plasmas were generated by irradiating gas–jet targets with a laser beam, which in parallel probes the plasmas to characterize their parameters in the so called “self–scattering” Thomson scheme. The Thomson diagnostics provide the necessary parameters of density and temperature used by the collisional radiative superconfiguration code TRANSPEC/AVERROES to simulate their emission spectra in the keV and the XUV spectral ranges.

The time–integrated spectra in the keV range showed the presence of different ion species in the iso–electronic sequence from Ni–like (Xe^{26+}) to V–like (Xe^{31+}) for the xenon, and in the sequence from Na–like (Kr^{25+}) to F–like (Kr^{27+}) for the krypton plasma. The variation of the experimental conditions of gas–jet pressure and laser energy proved the dependence of the ions populations on these parameters. The measurements of the time–resolved XUV spectrum confirmed for both elements its time dependence determined by the variation of the plasma parameters of density and temperature.

The comparison of the synthetic with the measured keV spectra proved the ability of the code to calculate the atomic structures and transition rates of medium–Z elements, as well as to solve the NLTE populations kinetics problem with these data. However, the observed disagreements showed a problematic point. In a review of our experimental approach, we should mention that this problem is introduced by the large spatial scale of the plasma, initially chosen to avoid the cold gas around the produced plasma which absorbs the emitted x–ray radiation. However this scale, either due to the open expansion geometry, or to the hot spots induced by the RPP, give a non–homogeneous plasma, the behavior of which is difficult to be simulated. This concerns partly the divergence between the Thomson diagnostic and the estimation of the plasma state obtained by the Bragg spectrograph. But most important, it explains the observed gradients which introduce difficulties in following the variations of the plasma with the code.

The situation becomes more complicated when dealing with the XUV spectra, because here is introduced additionally the parameter of time. In this range, the code can reproduce the low wavelength emission features corresponding to the 5–4 transitions of xenon and to the 4–3 transitions of krypton. However, it can not predict the other wide emission structures appearing in the measured spectra. A next step to improve the code/experiment agreement is to perform simulations with a 3D hydrodynamic code in order to follow more accurately the plasma time evolution, which affects strongly the emission in the XUV range, as shown in our measurements.

References of Chapter 4

[1] L. B. Da Silva *et al.*, Absorption Measurements Demonstrating the Importance of $\Delta n = 0$ Transitions in the Opacity of Iron, Phys. Rev. Lett **69**, 438 (1992).

[2] J. D. Lindl *et al.*, The physics basis for ignition using indirect–drive targets on the National Ingition Facility, Phys. Plasmas **11**, 339 (2004).

[3] A. Bar–Shalom *et al.*, Super–transition–arrays : A model for the spectral analysis of hot, dense plasma, Phys. Rev. A **40**, 3183 (1989).

[4] O. Peyrusse, A superconfiguration model for broadband spectroscopy of non–LTE plasmas, J. Phys. B : At. Mol. Opt. Phys. **33**, 4303 (2000).

[5] O. Peyrusse, A model for the simulation of nonequilibrium line transfer in laboratory plasmas, Phys. Fluids B **4**, 2007 (1992).

[6] S. H. Glenzer, *et al.*, Thomson Scattering from High-*Z* Laser-Produced Plasmas, Phys. Rev. Letters **82**, 97 (1999).

[7] Bo Bai, *et al.*, Thomson scattering measurements of gold plasmas produced with 0.351 μm laser light, Phys. Plasmas **8**, 4144 (2001).

[8] S. H. Glenzer, *et al.*, Ionization Balance in Inertial Confinement Fusion Hohlraums, Phys. Rev. Letters **87**, 045002 (2001).

[9] C. Chenais–Popovics *et al.*, X-ray emission of a xenon gas jet plasma diagnosed with Thomson scattering, Phys. Rev. E **65**, 0464181 (2002).

[10] S. Bastiani–Ceccoti *et al.*, Analysis of the X-ray and time-resolved XUV emission of laser produced Xe and Kr plasmas, High Energy Density Phys. **3**, 20 (2007).

[11] V. Nagels–Silvert, Validation expérimentale des codes de physique atomique des plasmas hors équilibre thermodynamique local, thesis Ecole Polytechnique, 2004.

[12] J. E. Rice, et *al.*, X-ray observation of 2*l*–*nl*' transitions and configuration-interaction effects from Kr, Mo, Nb and Zr in near neon-like charge states from tokamak plasmas, J. Phys. B : At. Mol. Opt. Phys. **33**, 5435 (2000).

[13] V. Nagels et *al.*, Spectra of Laser Irradiated Xenon and Krypton in the Wavelength Range 0.5–1.0 nm, Phys. Scripta **68**, 233 (2003).

[14] V. Malka, *et. al.*, Characterization of neutral density profile in a wide range of pressure of cylindrical pulsed gas – jet, Rev. Sci. Instrum. **71**, 2329 (2000).

[15] R. L. Kelly, Atomic and Ionic Spectrum Lines below 2000 angstroms: Hydrogen through Krypton, J. Phys. Chem. Ref. Data **16**, Suppl. 1 (1987).

[16] Henke *et al.*, High energy x-ray response of photographic films: models and measurement, J. Opt. Soc. Am. B **3**, 1540 (1986).

[17] B. L. Henke, E. M. Gullikson, J. C. Davis, X-Ray Interactions : Photoabsorption, Scattering, Transmission and Reflection at E = 50-30,000 eV, Z = 1-92, At. Data Nucl. Data Tables **54**, 181 (1993).

[18] A. Burek, Crystals for astronomical x-ray spectroscopy, Space Sci, Instrum. **2**, 53 (1976).

[19] Center for X-ray Optics (CXRO), X-Ray Interaction With Matter Tabulated Data, http://henke.lbl.gov/optical_constants/

[20] B. L. Henke, J. P. Knauer, K. Premaratne, The characterization of x-ray photocathodes in the 0.1 – 10 keV photon energy region, J. Appl. Phys. **5**, 1509 (1981).

[21] C. Reverdin, *et al.*, Absolute brightness measurements at the LURE synchrotron with a bolometer and application to the absolute calibration of the photodiodes and photocathodes, Laser and Particle Beams **12**, 573 (1994).

[22] Reverdin et al., Sensibilite spectrale des photocathodes XUV minces en transmission, rapport interne CEA–DIF (1993).

[23] J–R Marques *et al.*, Mesure par diffusion Thomson de l'évolution de la température et de la densité électronique de plasmas de xénon ou de krypton créés par laser, Rapport LULI (2003).

[24] Y. Klimontovich, "The statistical theory of non–equilibrium processes in a plasma", Pergamon Press, 1967.

[25] J. Sheffield, Plasma Scattering of Electromagnetic Radiation, Academic Press, 1975.

[26] S. H. Glenzer *et al.*, Thomson scattering from laser plasmas, Phys. Plasmas **6**, 2117 (1999).

[27] D. Bohm, E. P. Gross, Theory of Plasma Oscillations. A. Origin of Medium Like Behavior, Phys. Rev **75**, 1851 (1949).

[28] C. Bauche-Arnoult *et al.*, Variance of the distribution of energy levels and of the transition arrays in atomic spectra. III. Case of spin-orbit-split arrays, Phys. Rev. A **31**, 2248 (1985).

[29] C. Chenais–Popovics et al., L-band x-ray absorption of radiatively heated nickel, Phys. Rev. E **65**, 016413 (2001).

[30] A. Bar-Shalom, M. Klapisch, J. Oreg, J. Quant. Spec. Radiat. Transfer **71** 169 (2001).

[31] R. Ramis, R. Schmalz and J. Meyer–Ter–Vehn, MULTI – A computer code for one – dimensional multigroup radiation hydrodynamics, Comp. Phys. Communications **49**, 475 (1988).

Chapter 5 XUV absorption spectroscopy of radiatively heated ZnS and Al plasmas

5.1 Introduction

Thin solid foils irradiated by short and intense pulses of x–ray fluxes provide a source for investigating the absorption properties of hot and dense plasmas in local thermodynamic equilibrium (LTE). These plasmas are found in many fields of fundamental and applied research, such as laboratory astrophysics [1–4], Inertial Confinement Fusion (ICF) [5] and x–ray source development.

In astrophysics, the study of the opacities are of particular importance for the development of accurate atmosphere models, as they rule the energy exchange in stellar interiors through the mechanism of radiation transport [6]. This holds particularly for the opacities of medium–Z elements in the XUV range from 50 to 1000 eV, where lies the maximum of the Planck function for the temperatures reached inside the stars. Medium–Z elements represent only a small fraction of the total stellar mass, but they are mostly responsible of radiative transfer as their ionic species emit and absorb a rich XUV spectrum, unlike the fully ionized hydrogen and helium plasmas [7]. In the indirect ICF scheme, the capsule ablation is driven by the thermal x–ray radiation confined in the interior of a cavity made of gold or other high–Z material. Here the opacity of the cavity materials affects crucial parameters for ICF as the temperature and the homogeneity of the radiation field [8]. During last years, the x–ray sources have also received much attention because of their technological applications, as the extreme ultraviolet lithography (EUVL) used for the development of new generation processors (node size < 50 nm). In this field the opacities of high–Z plasmas are important for investigating the radiation transport and thus the conversion efficiencies of the sources [9].

The necessity for accurate theoretical models describing the plasmas opacities has led to the development of various plasma atomic physics codes, such as the code SCO [10–12] which calculates the absorption spectrum of medium and high–Z LTE plasmas based on the superconfiguration formalism [13]. The opacities of plasma mixtures are of particular importance mainly due to their application in astrophysics. The SCO theoretical model has been recently developed to describe them [12]. The subject of the present work could be viewed as a part of a more general development of experimental techniques that can provide benchmarks for mixture modeling.

In this experiment the opacities of zinc sulfide (ZnS) and aluminium (Al) plasmas in LTE are characterized by measuring their absorption spectra in the XUV range [14]. ZnS and Al foils are heated by the x–ray radiation confined in the interior of a spherical gold cavity. The compound ZnS was chosen because the sulfur $n = 2$–3 and zinc $n = 3$–4 transitions, where n is the principal quantum number, lie in the same spectral range between 20–180 Å and do not overlap. Thus it gives the ability to investigate the opacities of a plasma mixture which is more homogeneous than in the multi–layered target foils approach [15]. The ZnS absorption spectrum is analyzed by comparing the experimental measurements with the theoretical calculations of the code SCO. Al plasma was chosen because its absorption spectrum in the XUV range has been studied extensively in previous experiments [16,17], where it was proved that it can provide an independent means of inferring the absorbing plasmas parameters [16]. Its absorption spectrum is analyzed with the detailed atomic code HULLAC [18] to obtain an estimation of the ZnS foil heating conditions achieved in our experiment.

5.2 Experimental setup and data processing

5.2.1 Laser beams and targets description

Laser beams

Figure 5.1 shows the top–view of the experimental setup used to measure the plasmas XUV absorption spectrum generated by the radiative heating of zinc sulfide (ZnS) and aluminium (Al) foils. In this experiment the two neodymium doped laser beams of the LULI2000 facility are used. Both laser beams are frequency–doubled ($\lambda = 0.53$ μm) by using two KDP crystals with a frequency doubling efficiency of ~ 35 %. The pulse duration of the laser beams is 500 ps.

One of the two laser beams – hereafter called “main beam” – falls on the entrance hole of the spherical cavity, which is placed in the center of the experimental chamber. This is achieved by coupling a $f = 800$ mm lens with a random phase plate (RPP) providing a focal spot with a nominal value of 500 μm diameter FWHM on the conversion foil covering the cavity entrance hole. The energy of the main beam at 0.53 μm wavelength varies in the range of 70 – 140 J (nominal flux : $10^{14} - 1.4\ 10^{14}$ W/cm^2).

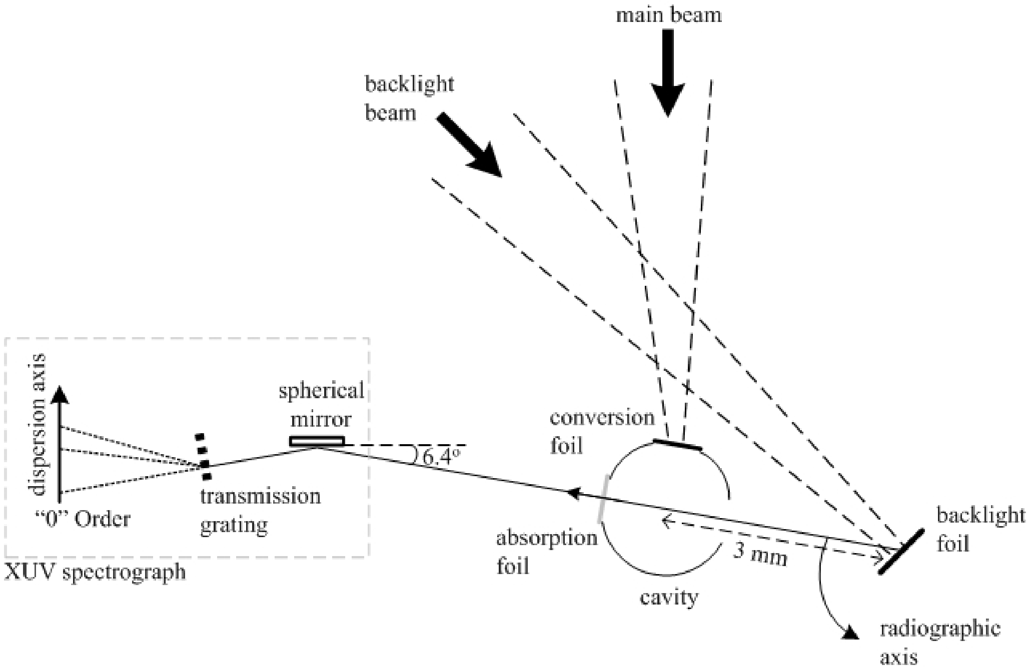

Figure 5.1 Experimental setup used to measure the time resolved XUV absorption spectrum of radiatively heated ZnS and Al foils.

The second laser beam – hereafter called “backlight beam” – heats a 20 μm thick gold foil, and the produced plasma provides the XUV emission source (“backlight”) used to probe the absorption foil (see Fig. 5.1). The backlight foil is aligned on the line of sight determined by the diagnostic holes of the cavity and the XUV spectrograph spherical mirror (“radiographic axis”). Its plane is oriented slightly differently from the normal to the laser axis to avoid back–reflection of the backlight beam. At the same time, this provides a proper radiation angular distribution to obtain a high intensity backlight signal for the absorption probing, while its 3 mm distance from the cavity prevents the absorption foil heating. The backlight beam is focused on the gold foil by coupling a $f = 800$ mm lens with a RPP of 4.2 mm x 0.37

mm element size, giving an elliptical focal spot with 150 µm horizontal size at 50 % of the laser intensity maximum, and 1 mm vertical size at 10 % of the laser intensity maximum. The energy of the backlight beam at 0.53 µm wavelength varies in the range of 20 – 40 J (nominal flux: 3.4 10^{13} – 6.8 10^{13} W/cm^2). Given the backlight beam energy, the focal spot geometry ensures an increased energy flux heating the gold foil (small horizontal dimension), while it makes the backlight alignment of the radiographic axis easier (large vertical dimension).

The synchronization of the two beams is adjusted to obtain the backlight 800 ps after the main beam. Taking into account the time resolved nature of our measurements, this choice fulfills the following antithetical constraints :

1. The absorption probing is performed early enough to ensure that the ablative plasma produced at the rear of the conversion foil has not reached the radiographic axis due to its expansion ("plasma filling"), preventing the overlapping of its emission spectrum with the backlight.
2. It is performed late enough to minimize the temperature gradients introduced by the thermal expansion of the absorption foil.
3. It is performed late enough to ensure that the radiative emission of the cavity is very low, and of the order of the background noise, a necessary condition to deduce the plasma absorption from the measured backlight spectra (cf §5.3.1).

Spherical gold cavities and absorption foils

The radiative heating of the absorption foils is realized by using a spherical gold cavity. Its geometrical characteristics are summarized in Figure 5.2(a). Its diameter is 1.2 mm, and it contains three holes : the two diagnostic holes of 250 µm diameter, and an entrance hole of 700 µm diameter. The entrance hole is covered with a 130 nm thick gold foil, which transforms the deposited coherent laser energy to the incoherent x–ray source heating the cavity. The two diagnostic holes lie on a line defining the radiographic axis for the absorption probing. One of the two diagnostic holes is covered with a thin foil of the material (ZnS, Al), the absorption of which is measured. The foil thicknesses used are : 48.9 nm for ZnS, and 74 nm for Al both corresponding to 20 µg/cm^2 areal mass. The absorption foils are coated on both sides with 35.3 nm thick carbon (C) tampers corresponding to 8 µg/cm^2 areal mass (see Fig. 5.2(b)). The tampered configuration was chosen as it improves the homogeneity of the probed plasma by reducing the density and temperature gradients along its expansion axis [19,20].

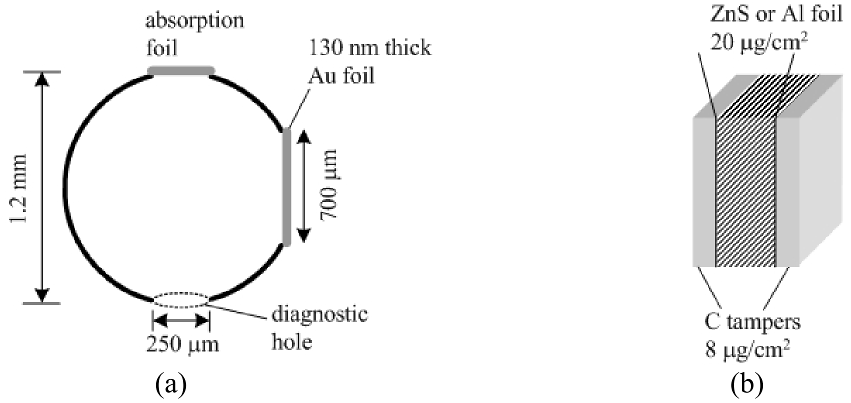

(a) (b)

Figure 5.2 (a) Geometrical properties of the spherical gold cavity. (b) Tampered configuration of the absorption foils.

Concerning the confinement of the radiation inside the cavity the important physical quantity is the x–ray opacity of the wall material, and gold is an optimum choice as a high–Z element [8,21]. For the radiation field temperature in the interior of the cavity, the important parameter is the conversion efficiency of the laser beam energy into x–rays at the rear of the conversion foil. This is determined by : (1) the material of the conversion foil, (2) its thickness, and (3) the range of the laser beam flux. The energy conversion efficiency of different materials was studied in [22] by irradiating planar targets with laser fluxes similar with those in our experiment ($\lambda = 0.53$ μm, $S = 1.3\ 10^{13}$ W/cm^2). The analysis of the absolutely calibrated emission spectra shows an increased efficiency as the atomic number of the element is increased, with gold targets being the optimum choice. Also, for the fluxes used in the experiment (~ 10^{14} W/cm^2) the gold planar targets exhibit an optimum conversion efficiency [23]. Finally, given the material and the laser energy range, previous works showed that the conversion efficiency is strongly dependent on the thickness of conversion foil. The 130 nm thickness chosen here provides a high conversion efficiency, ensuring that the plasma expansion speed is low enough to avoid a fast plasma filling of the cavity [24].

5.2.2 Diagnostic Instruments

XUV spectrograph

The measurement of the backlight emission spectrum probing the absorption plasma is performed with the XUV spectrograph described in paragraph 3.4.2. The spectrograph is coupled with a Kentech streak camera and records the time evolution of the absorption spectrum. We recall that the XUV spectrograph is composed of a 5200 mm curvature radius Ni spherical mirror coupled with a 2000 lines/mm gold transmission grating. In the specific setup, the mirror is placed at a grazing angle of 6.4° to cut off the high energetic photons below 20 Å (see also Fig. 4.1). Also, the distances *plasma source–spherical mirror* and *spherical mirror–streak camera*, are adjusted properly to obtain a magnification factor $G = 1$ and an optimized spectral resolution of 2.7 Å (see §3.4.2). This resolution is mainly determined by the apparent diameter ~ 250 μm of the backlight plasma source, which is defined by the diameter of the diagnostic holes of the cavity. The streak camera deflection speed is 4 mm/ns, giving a time resolution of 50 ps.

Pinhole cameras

The focal spot of the main beam is monitored with a x–ray pinhole camera composed of three entrance holes of 5, 10 and 20 μm diameter, respectively, arranged in a triangle of 1 mm side. The recording device is an ARP CCD camera, and a 23 μm thick beryllium filter is used to bound the spectral integration range of the instrument. The arrangement *plasma source–pinhole–CCD* lies in the same plane as the propagation direction of the laser beam, and it forms a 36° angle with the horizontal plane of the experimental chamber, i.e. with the main laser beam axis. The distance *plasma source–pinhole* is set to 170 mm, and the distance *pinhole–CCD* to 600 mm. Thus, the nominal value of the magnification factor is ~ 3.5.

The backlight focal spot is monitored with a single–hole pinhole camera of 23 μm diameter. The images are recorded on a COHU CCD camera, in front of which is placed a filter composed of 23 μm beryllium plus 100 μm Mylar. The magnification factor of this pinhole is ~ 2 ($r = 70$ mm, $R = 140$ mm).

To analyze the absorption foils hydrodynamics, we have to determine the main beam flux heating the conversion foil. The measurements obtained with the pinhole give a focal spot diameter of ~ 460 μm. For the 500 ps pulse duration of the main beam, and given the laser energy, the heating flux varies in the range of $1.1\ 10^{14} - 1.5\ 10^{14}$ W/cm^2.

5.2.3 Experimental data processing

Figure 5.3 shows a typical absorption time–resolved spectrum image measured with the XUV spectrograph. It is obtained with a radiatively heated ZnS plasma (20 μg/cm^2 areal mass ZnS) absorbing the backlight XUV source. The main and the backlight beam energies at 0.53 μm wavelength are 99 and 23 J, respectively. The spectrum time evolution is recorded along the vertical axis, and its dispersion along the horizontal axis. The weak spectrum feature appearing first as time evolves corresponds to the radiative emission of the cavity, and the second feature corresponds to the backlight emission spectrum absorbed by the ZnS plasma.

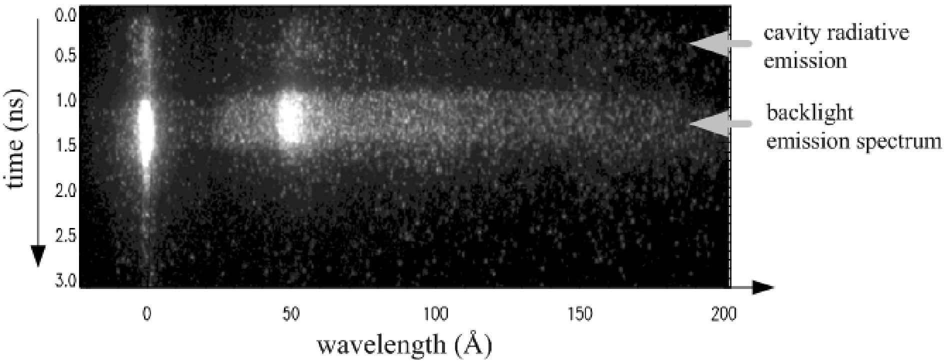

Figure 5.3 Time–resolved XUV absorption spectrum image obtained by probing with the backlight source a ZnS plasma obtained from a radiatively heated 20 μg/cm^2 areal mass foil.

The processing steps applied to the measured spectrum are : (1) the correction of the spectrum image deformation introduced by the intensifier, (2) the calibration of the dispersion and time axis, and (3) the correction of the spectral deformation introduced by the spectrograph components to the measured intensity of the spectrum (see Chapter 3).

Dispersion axis calibration

According to the Eq. (3.13) of paragraph 3.4.2, the wavelength calibration of the dispersion axis is performed by using the linear formula :

$$m\lambda = a_1(pixel) + a_0 \tag{5.1}$$

where a_1 is the spectrograph dispersion coefficient, and a_0 an offset coefficient due to the small shifts of the zero transmission order. The calculation of a_1 is performed by measuring the K–edge position by inserting on the backlight spectrum a 1 μm thick Be filter, which is placed in front of the XUV spectrograph. For this, the emission spectrum of a 12.5 μm thick gold foil, heated by a backlight beam of 17 J energy at 0.53 μm wavelength, was measured. The spectrum profile is given as the full line in Figure 5.4. The Be K–edge appears at pixel 587 and the zero transmission order appears at pixel 278. The theoretical absorption spectrum of a cold solid Be foil (dashed line) shows a sharp K–edge at 110.85 Å [25]. Thus, the dispersion coefficient for the specific setup of the XUV spectrograph is, a_1 = 0.36 Å/pixel.

Time axis calibration

The time calibration is performed by measuring with the streak camera the 800 ps delay between the backlight and the main beam, which is very accurately determined near the front end of the laser. In this way, a calibration of the streak camera deflection speed is also obtained, i.e. an estimation for the accuracy of its nominal value given by the manufacturer.

Figure 5.5 gives a spectrum profile obtained along the time axis of the spectrum image of Fig. 5.3. The rising half maximum of the cavity radiative emission appears at 405 pixels, and the rising half maximum of the backlight emission at 457 pixels. Assuming the temporal coincidence between the spectrum emission features and the laser beams producing them, the time delay between the two laser beams is Δt = 52 pixels. Thus, the time coefficient is a_{time} = 0.0154 ns/pixel.

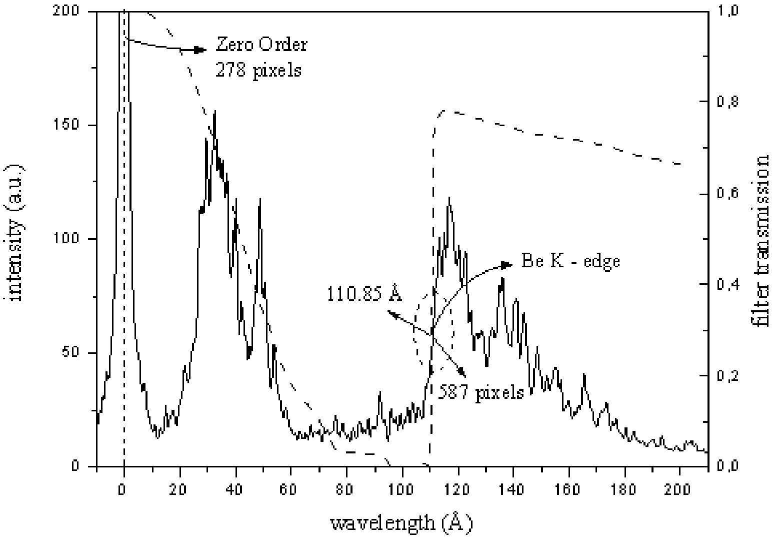

Figure 5.4 Spectrum allowing the calculation of the dispersion coefficient a_l of Eq. (5.1). Full line : emission spectrum of a 12.5 μm thick gold foil heated by a backlight beam of 17 J energy at 0.53 μm. Dashed line : 1 μm thick Be foil transmission curve.

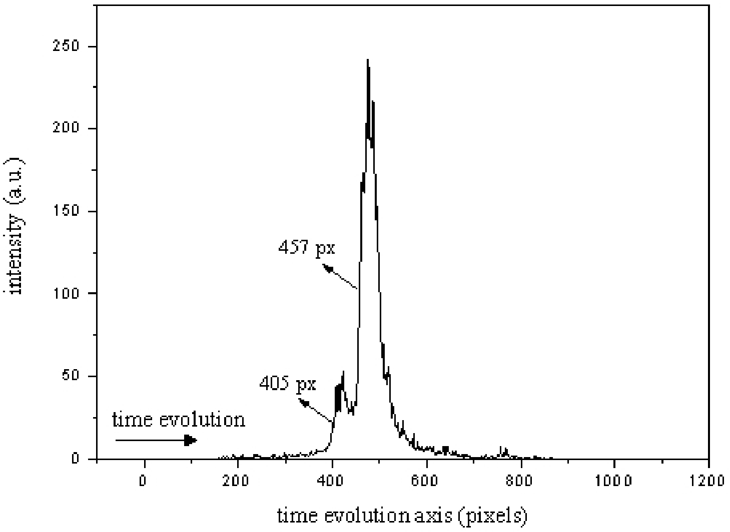

Figure 5.5 Lineout along the time axis of the spectrum image given in Fig. 5.3 used to determine the time coefficient of the XUV spectrograph. The first spectrum feature, as time evolves, corresponds to the cavity radiative emission, and the second one to the backlight emission.

The nominal value of the streak deflection speed measured on the phosphor plate is 4 mm/ns. To give this value in ns/pixel measured on the CCD camera, we have to take into account both the magnification of the intensifier (G_{int} = 4/5) and the fiber optics configuration (G_{fo} = 1/3). For the 13 µm pixel size of the Andor CCD camera, this transformation gives a deflection speed nominal value of 0.013 ns/pixel, which agrees with the measured one (deviation ~ 15 %).

5.3 Experimental methods

5.3.1 Deduction of the plasma transmission

The study of the plasma absorption is reduced to the experimental determination of its spectral opacity. We recall that the radiation transport through an absorbing medium is ruled by the formula

$$I_v = I_{v,o} \exp[-\kappa_v(\rho,T)\cdot \Delta l \cdot \rho] \tag{5.2}$$

where $I_{v,o}$, I_v are respectively the incident and the transmitted radiation intensity, $\kappa_v(\rho, T)$ is the massive spectral opacity of the medium, Δl is the medium length crossed by the transmitted radiation, and ρ its matter density.

The quantity deduced from our measurements is the spectral transmission of the absorbing plasma. It is defined as the ratio of the radiation intensity transmitted through the absorbing plasma to the backlight radiation intensity, or from Eq. (5.2),

$$\tau \equiv \frac{I_v}{I_{vo}} = \exp[-\kappa_v(\rho,T)\cdot \Delta l \cdot \rho] \tag{5.3}$$

The measurement of the plasma transmission determines directly the absorption properties of the radiatively heated plasma, i.e. its spectral opacity. Experimentally, it is necessary to measure : (1) the backlight radiation passing through the absorbing plasma, hereafter called “absorption measurement”, and (2) the backlight radiation without the absorbing plasma between the backlight source and the XUV spectrograph, or “backlight measurement”.

The plasma transmission, and as a consequence its opacity, are not measured directly but they are deduced from two different measured signals. This intrinsic characteristic of the absorption experiments enforces us to determine the conditions under which those signals can be used to provide properly the plasma absorption [19]. This is discussed in the next two paragraphs.

Normalization of the backlight signals

To study the time resolved XUV absorption spectra we use a streak camera for the measurements of the backlight radiation [1]. Unlike the point projection experiments [26,27], this technique does not allow to measure the spectrum with spatial resolution [19]. As a consequence, the absorption and the backlight measurements are obtained in different experimental shots. Ideally, to deduce the plasma transmission we should have an absolute coincidence between the different experimental conditions, but more realistically the coincidence of the backlight beam energies is sufficient. The finite number of shots performed, and the unavoidable variations of the laser energy from shot to shot, introduce deviations between the different backlight and absorption measurements. To overcome these deviations, we normalize the intensities of the different spectra. One has thus to analyze the variation of the backlight intensity as a function of the laser energy, as well as the absorption properties of the Al and ZnS foils.

Figure 5.6 gives two backlight emission spectra obtained by irradiating a 20 μm thick gold foil with different energies of the backlight beam (E_{BL} = 20 and 28 J at 0.53 μm); these values represent the maximum energy difference obtained in our measurements. The gold plasma emission spectrum contains an intense broad structure around 50 Å corresponding to the O–band transitions [22], while above 55 Å it is characterized by a fairly flat emission structure without discrete transition features. Concerning the intensity level of the emission spectrum, in the range of 55 – 180 Å it varies rather linearly with the laser energy. This does not hold for the O–band emission feature around 50 Å. Thus, the deduction of the transmission should be restricted to the spectral range 55 – 125 Å. At lower wavelengths the non linearity of the backlight does not permit to correlate the intensity level of two different shots, while for higher wavelengths the intensity is too low (see Fig. 5.6 (b)).

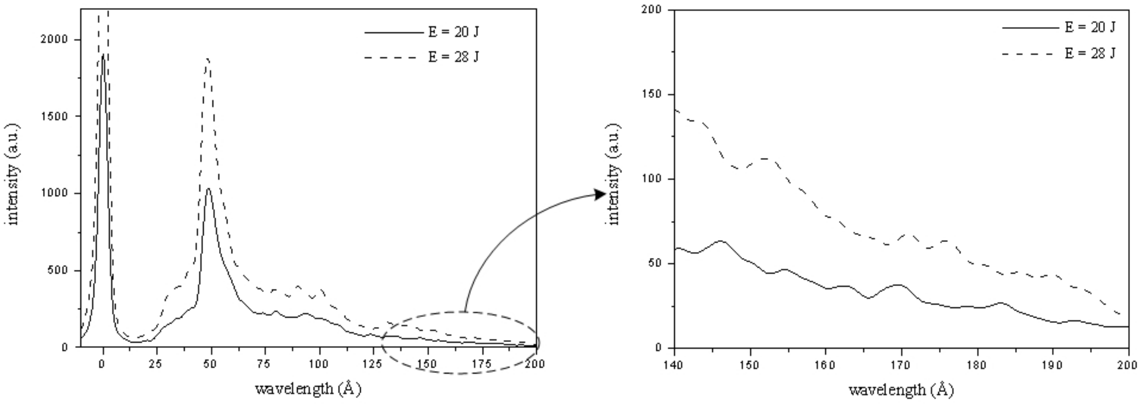

(a) (b)

Figure 5.6 (a) Comparison of backlight emission spectra obtained for different energies of the backlight beam. (b) Magnification of the spectral range of 145 – 180 Å used to normalize the Al absorption. The spectra are obtained from the streak spectrum images with a time average corresponding to 500 ps. (The curves are convolved with a 2.7 Å FWHM gaussian).

Let us now look at the absorbing plasmas properties. Figure 5.7 gives the spectral transmission of Al (solid line) and C (dotted line) plasmas calculated with the atomic code HULLAC [18], and of a ZnS plasma (dashed line) calculated with the code SCO [10,11]. The transmissions curves are obtained for typical plasma parameters corresponding to the conditions achieved in the experiment. Both Al and C plasmas show a very low absorption in the spectral window of 145 – 180 Å, which could be considered as negligible. Provided that the backlight energy does not vary significantly between the backlight and the absorption measurements, this spectral window could be used as a reference to determine a normalization factor, f_{Al}, for the calculation of Al transmission [24,28]. If $\widetilde{I}^{W}$ is the average intensity of the backlight signal in the non absorbing spectral window, the normalization approximation could be written

$$\tau_{Al} = f_{Al} \times \frac{I_{absorption}}{I_{backlight}} \quad , \quad f_{Al} = \frac{\widetilde{I}^{W}{}_{backlight}}{\widetilde{I}^{W}{}_{absorption}} \tag{5.4}$$

On the other hand, the ZnS plasma does not show an extensive low absorption region in the whole spectral range of 20 – 200 Å. In this case the normalization is provided by the linear variation of the backlight intensity with the energy. Thus, for ZnS the normalization approximation is

$$\tau_{ZnS} = f_{ZnS} \times \frac{I_{absorption}}{I_{backlight}} \quad , \quad f_{ZnS} = \frac{E_{backlight}}{E_{absorption}} \tag{5.5}$$

For both elements, the necessery condition to normalize the backlight to the absorption measurement is the negligible variation of the backlight energy between the two shots. In the case of Al this provides the coincidence of the spectra in the non absorbing spectral window, and for ZnS it ensures the linearity requirement. The advantage with the normalization approach of Eq. (5.4) used for Al, is that it permits to account for the variations of the backlight intensity introduced by the aligment backlight/cavity.

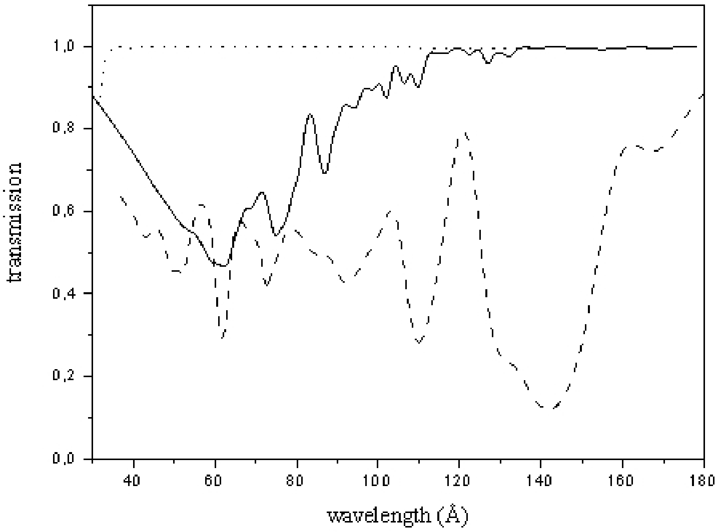

Figure 5.7 Theoretical transmissions of Al and C calculated with the atomic code HULLAC[18], and of ZnS calculated with the code SCO[10–11]. Full line : 20 μg/cm^2 areal mass Al plasma with T_e = 20 eV and ρ = 2 mg/cm^3. Dashed line : 20 μg/cm^2 areal mass ZnS plasma with T_e = 16 eV and ρ = 2.5 mg/cm^3. Dotted line : 8 μg/cm^2 areal mass C plasma with T_e = 20 eV and ρ = 1 mg/cm^3. (The curves are convolved with a 2.7 Å FWHM gaussian).

Characterization of the cavity radiative emission

The cavity radiation emission heating the absorption foil, and which is recorded by the XUV spectrograph with the measured backlight spectrum, should be subtracted like a noise signal [24]. The time resolved approach solves this problem when a time delay between the main beam and the backlight beam is introduced. Thus, we ensure that during the probing of the absorption plasma the cavity emission is of the order of the background noise [29].

Figure 5.8 shows an image obtained by measuring the backlight and the emission spectrum of a cavity without absorption foil (20 J backlight and 78 J main beam at 0.53 μm). The 800 ps time delay between the two 500 ps duration laser beams ensures that the absorption plasma probing starts 300 ps after the end of the cavity heating. In this interval, the cavity emission feature becomes very weak. To show this, Figure 5.9 gives two 300 ps temporal width lineouts sampling, respectively, the cavity emission at the time interval between the two laser beams (dashed line), and the backlight maximum (full line). In the range of 55 – 125 Å the cavity radiation is of the order of ~ 18 counts over the background noise, while the corresponding mean level of the backlight is ~ 230 counts. As the cavity emission decreases with time, we expect that, during the backlight pulse, its level will be of the same order of magnitude as the background noise (~ 10 counts). Thus, its elimination is provided by the correction of the background noise applied to the spectrum.

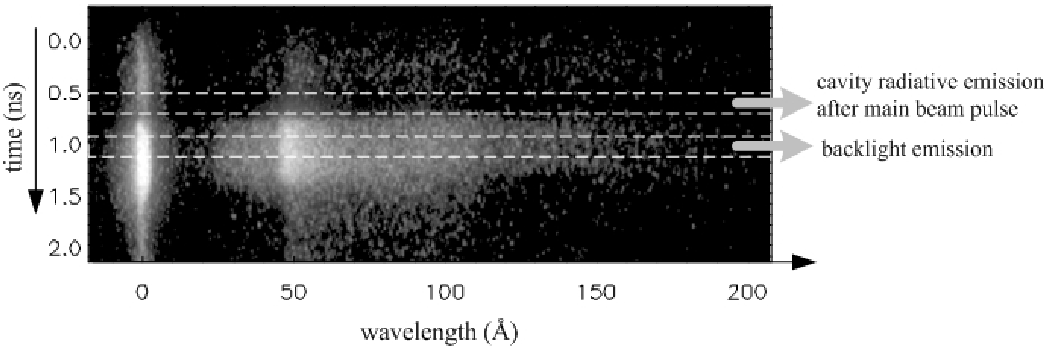

Figure 5.8 Backlight and cavity emission spectrum image obtained with a 20 J backlight and 78 J main beam at 0.53 μm (cavity without absorption foil). The cavity emission profile is obtained after the end of the main beam, and that of the backlight emission at the maximum of the backlight signal (profiles time integration ~ 300 ps).

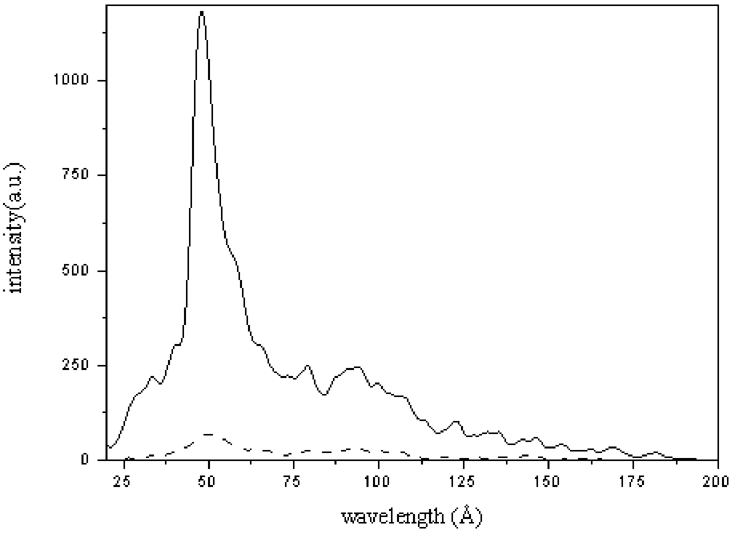

Figure 5.9 Comparison of the lineouts obtained from Fig. 5.8. Full line : backlight emission, dashed line : cavity emission. (The curves are convolved with a 2.7 Å FWHM gaussian).

5.3.2 Al and ZnS plasmas absorption spectra

Experimental measurements

Table 5–I gives the characteristics of the different measurements used to deduce the transmissions of Al and ZnS plasmas. Figure 5.10 shows the profiles sampled from the recorded XUV spectrum images of both materials. The profiles are averaged over a 500 ps time interval to improve the signal to noise ratio, and convolved with a 2.7 Å FWHM gaussian to account for the spectral resolution of the XUV spectrograph. The spectrum profiles are corrected for the background noise and the self emission.

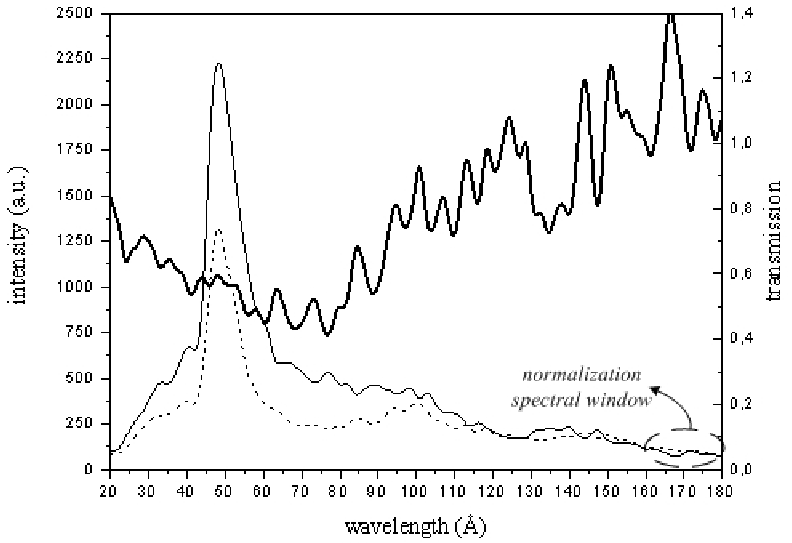

(a)

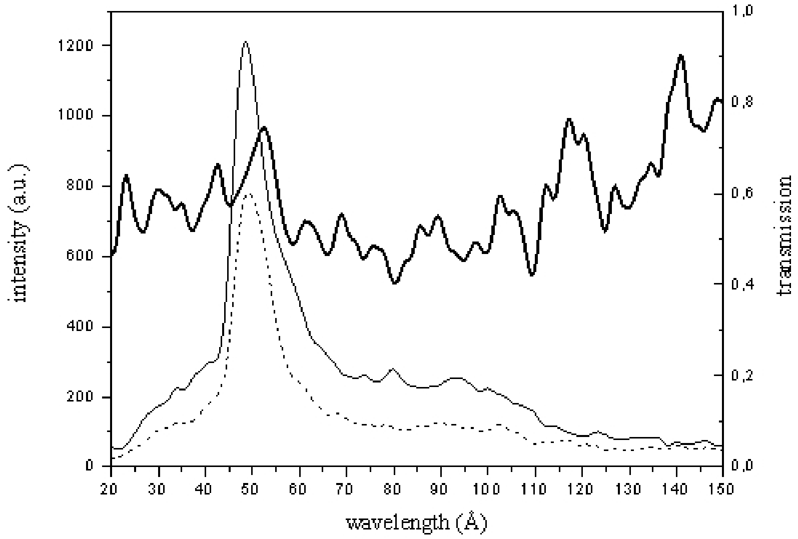

(b)

Figure 5.10 Experimental transmission curves (thick solid line) measured by probing : (a) 20 μg/cm^2 Al foil, (b) 20 μg/cm^2 ZnS foil. The transmissions are obtained by dividing the absorption (dashed line) with the backlight spectrum profiles (solid line).

		main beam (0.53 μm)		backlight beam (0.53 μm)	areal mass (μg/cm^2)
		E (J)	Flux (W/cm^2)	E (J)	
Al	absorption	139	1.5 10^{14}	36	C/Al/C 8/20/8
	backlight alone	–	–	40	
ZnS	absorption	99	1.1 10^{14}	23	C/ZnS/C 8/20/8
	backlight alone	–	–	20	

Table 5–I : Characteristics of the absorption and backlight measurements used to deduce the transmissions curves of Al and ZnS plasmas.

For the Al case of Fig. 5.10(a), the backlight spectrum (full line) is normalized with respect to the absorption spectrum (dashed line) according to Eq. (5.4), using the non absorbing spectral window of the Al plasma in the range of 160 – 180 Å. For the ZnS foil of Fig. 5.10(b), the normalization of the backlight spectrum (full line) to the absorption spectrum (dashed line) is performed according to Eq. (5.5), using the ratio of the backlight beam energies. The transmissions obtained by dividing the absorption and the backlight profiles are given in the figures as thick full lines.

Analysis method of the measured absorption spectra

For the heating conditions achieved in our experiment, and for both absorbing materials, the plasma parameters are expected to vary in the range of 15 – 30 eV for the electron temperature and of 2 – 5 mg/cm^3 for the matter density (cf. §5.4.2, 5.6.2). Under those conditions the plasmas are expected to be in a state of local thermodynamic equilibrium (LTE). To calculate the absorption spectrum with the LTE code SCO [10,11], or with the atomic code HULLAC employed with a Saha–Boltzmann statistics [18], the determination of the plasma parameters is necessary. The theoretical method that we use to obtain these parameters involves : (1) the calculation of the radiation heating the absorption foils given by the Basko model [30] and the view factor approach [31], and (2) the simulation of the foils hydrodynamics with the code MULTI [32], using the x–ray radiation obtained in step (1) [17,28,33].

The methodological question arising here concerns the independent experimental determination of the plasma parameters, for the conditions under which the absorption measurements are performed [19,34]. Like in [16] the technique applied in this work consists in measuring the Al absorption spectrum. The analysis of the Al absorption provides an independent diagnostic of the cavity radiative temperature, because its spectrum shows well characterized discrete absorption features of different ions, which additionally are sufficiently sensitive to the variations of the plasma temperature and matter density. The difference with the approach used in [16] is that here Al gives an estimation for the validity of the theoretical method, rather than a direct measurement of the plasma parameters. This is due to the different hydrodynamic conditions that might prevail for the two plasmas, and which result from the difference in their experimental conditions.

In the next paragraph the calculation of the Al plasma hydrodynamics is given, and in paragraph 5.5 the validity of the method is checked, comparing the *ab initio* calculations of the Al absorption spectrum obtained by HULLAC with the measured spectrum. Then, in paragraph 5.6 the same procedure is applied for the analysis of the ZnS absorption spectrum.

5.4 Hydrodynamics of the radiatively heated Al absorption foil

5.4.1 Calculation of the radiation heating the Al foil

Simulation of the x–ray radiation source

To obtain the x–ray radiation source heating the 20 μg/cm^2 Al absorption foil a simulation is performed with MULTI [32]: a 130 nm thick gold foil is irradiated with a laser beam of 500 ps duration and 1.5 10^{14} W/cm^2 energy flux at 0.53 μm wavelength, according to the experimental conditions of the measurement (see §5.3.2). The calculated spectrum and temporal dependence of the radiation emitted at the rear of the gold foil are given in Figures 5.11(a), (b).

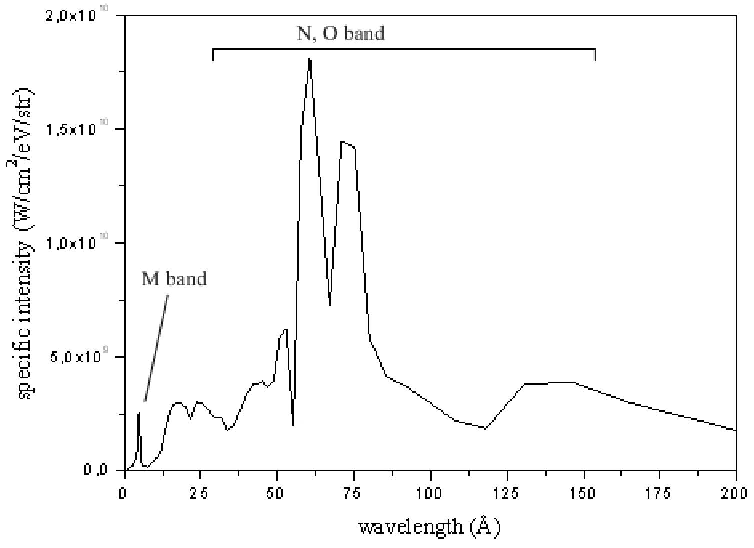

(a)

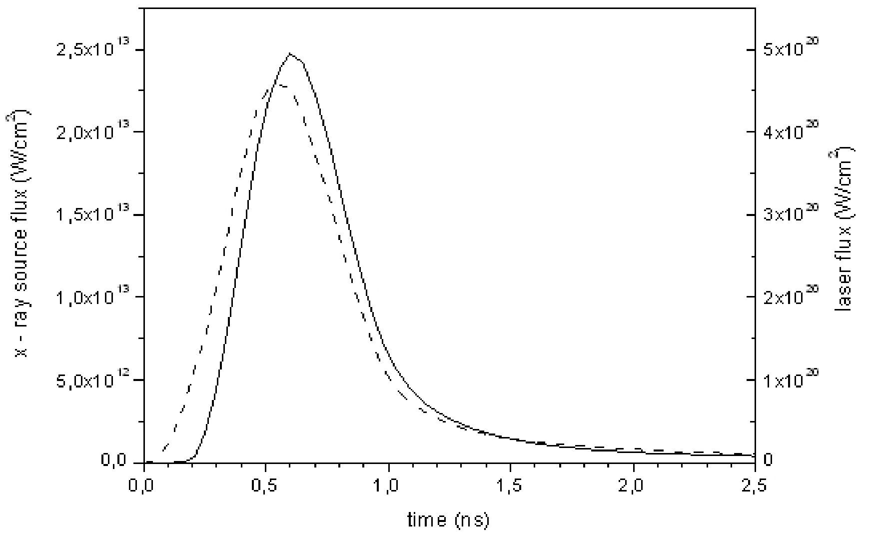

(b)

Figure 5.11 Simulation results of MULTI for the x–ray radiation emitted at the rear of a 130 nm thick gold foil heated by a laser beam (1.5 10^{14} W/cm^2, 0.53 µm, 500 ps). (a) Specific intensity calculated at the maximum of the laser pulse. (b) Full line : mean x–ray flux as a function of time, obtained by integration over the frequency and angle groups, dashed line : laser beam flux.

Figure 5.11(a) gives the spectral intensity of the x–ray obtained at the maximum of the laser pulse. The energy is mainly confined in the spectral range of 50 – 80 Å corresponding to the N (n = 4) and O (n = 5) band transitions, while the intensity of the relatively hard M (n = 3) band transitions is very low. The conversion of the laser light energy into x–rays by gold foils was studied analytically in a previous work of our research group [24,28]. In this experiment, absolutely calibrated x–ray spectra emitted at the front and the rear of gold foils were measured for different thicknesses close to 130 nm (100, 120 nm), irradiating them with a similar laser flux (~ 5 10^{13} W/cm^2, 0.53 µm, 500 ps). Comparison with the theoretical spectra obtained with MULTI, using the group emissivities/opacities calculated with the code

POTREC [35], showed that the simulation reproduces adequately the various emission features, but it introduces a small spectral shift toward the high wavelengths, a disagreement attributed to the accuracy of POTREC. The spectral distribution of the radiation obtained by MULTI is used directly in our work for simulating the absorption foils hydrodynamics (cf. §5.4.2).

Figure 5.11(b) gives in a common graph the time evolution of the laser flux heating the gold foil (dashed line), and the flux emitted at its rear (full line) integrated over the frequency and the angle groups used with the simulation of MULTI. Apart from a small time delay, the x–ray flux follows the evolution of the laser beam and has a maximum of 2.5 10^{13} W/cm^2. Having calculated the source flux, we can now apply the Basko model and the view factor approach to calculate the flux heating the absorption foil.

Total radiation coupled with the Al foil

Table 5–II summarizes the geometrical characteristics of the spherical gold cavities used in our experiment, as well as the values of the fractional area factors n_S and n_W determining the energy exchange in its interior. A_C is the surface of the closed cavity with no holes, A_S is the surface of the x–ray source (here the gold conversion foil), and $A_H = A_F$ is the area of the diagnostic holes. $A_W = A_C - (A_S + 2A_H)$ is the surface of the cavity wall. We recall that n_W determines the incident flux on an arbitrary wall element due to the total radiation emitted from the cavity wall, and n_S the incident flux on a wall element due to the radiation emitted from the x–ray source surface.

Ø (mm)	A_C (mm^2)	A_W (mm^2)	A_S (mm^2)	A_H (mm^2)	A_F (mm^2)	η_W	η_S
1.2	4.52	4.23	0.196	0.049	0.049	0.93	0.043

Table 5–II : Geometrical characteristics of the spherical gold cavity used in the experiment

The flux of the x–ray source emitted at the rear of the conversion foil multiplied by the fractional area factor η_S represents the input of the Basko model [30], which rules the thermal radiation transport through the cavity wall, and gives the radiative flux reemitted by each wall element. Using the source flux of Fig. 5.11(b) we obtain the radiation emitted by the cavity wall given in Fig. 5.12 as full line. The reemitted flux increases rapidly, following the x–ray source time evolution (dashed line), and has a maximum of 5 10^{11} W/cm^2. After the end of the laser pulse, implying the rapid decrease of the source flux (0.6 – 1 ns), the reemission of the cavity also decreases, though with a lower rate after 1 ns.

From the reemitted flux and the Stefan–Boltzmann law ($S = \sigma T_R^4$; σ Stefan constant, T_R the radiative temperature), the equivalent radiative temperature of the cavity is calculated and shown in Fig. 5.13 (full line). Following the variation of the x–ray source, the temperature increases rapidly in the first 600 ps, up to a maximum of 48 eV. After the end of the laser pulse, the temperature gradually decreases to 20 eV at 4 ns.

The dashed line in Fig. 5.13 represents the reemission factor

$$R(t) = S_r(t)/[S_i(t) + S_s(t)] \tag{5.6}$$

which is the ratio of the flux reemitted to the total flux received by each wall element. R starts from a low value, and at the rising half of the x–ray source (till 0.7 ns) it shows an regular increase with time. As in this time interval the incident flux S_i appearing in the denominator of Eq. (5.6) also increases, the evolution of R implies the increase of the reemitted flux S_r, or the wall gradual heating. At the falling half of the x–ray source (0.7 – 1 ns) R continues to increase, but now this results from the slow decrease rate of S_r with regard to S_s, expression of the confinement of the radiation in the interior of the cavity.

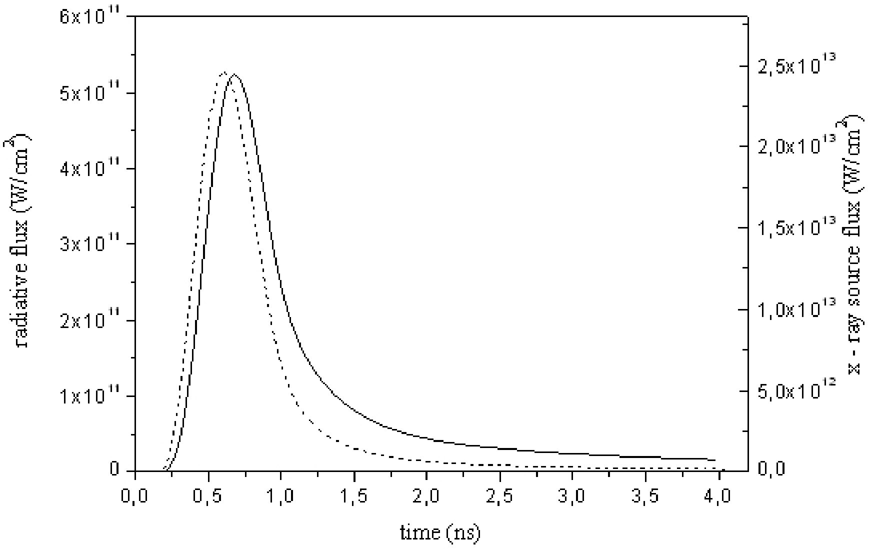

Figure 5.12 Full line : Radiative flux S_r reemitted from the cavity wall calculated with the Basko model [30] and the view factor approach [31]. Dashed line : x–ray source flux S_0 calculated in Fig. 5.11(b).

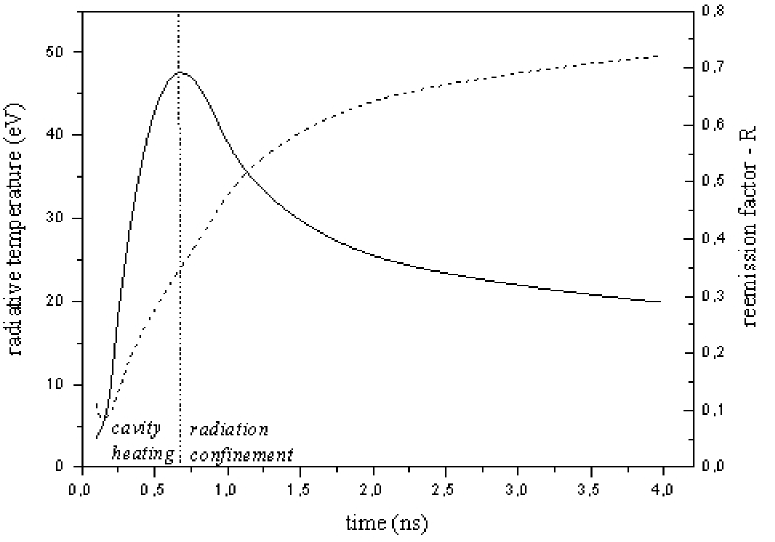

Figure 5.13 Full line : radiative temperature of the cavity wall obtained from the flux of Fig. 5.12 using the Stefan–Boltzmann law. Dashed line : reemission factor characterizing the x–rays confinement in the interior of the cavity.

Then, we calculate the flux heating the absorption foil due to the cavity emission, $S_{i,Wall}$, and to the emission of the source $S_{i,Source}$, as well as their sum corresponding to the total heating flux $S_{i,Total}$, and the results are summarized in Fig. 5.14. The total flux $S_{i,Total}$ (full line) shows a maximum of 1.5 10^{12} W/cm^2 corresponding to an equivalent planckian temperature of 62 eV. A simple inspection of the figure shows that : $S_{i,Source,max} = 2\ S_{i,Wall,max} = 10^{12}$ W/cm^2. As the flux directly coming from the conversion foil is dominant, we choose to simulate the absorption foil hydrodynamics by coupling with it directly the flux emitted at the rear of the conversion foil (source flux), weighted properly to correspond to the total flux heating it. To this purpose, we have to calculate the ratio between the total heating flux and the source flux $a(t) = S_{i,Total} / S_0$ (see Eq. (2.43)). Using for the time–varying reemission factor its mean value, $R = 0.3$, averaged in the interval $t = 0.4 - 1$ ns, we find that $a = 0.06$, i.e. the total flux heating the absorption foil is equal to 6% of the total flux emitted from the x–ray source.

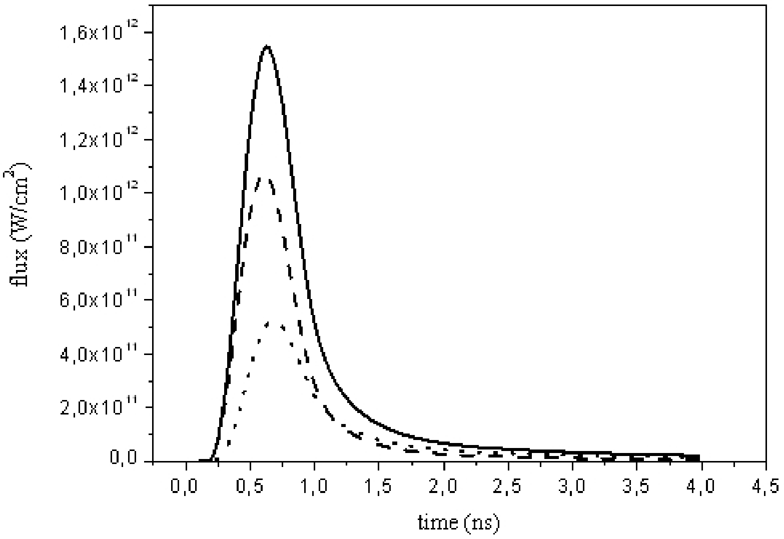

Figure 5.14 X–ray radiation fluxes heating the absorption foil. Dotted line: flux emitted from the cavity wall; dashed line : flux emitted from the conversion foil; full line : total flux.

5.4.2 Hydrodynamic simulation of the Al foil expansion

To simulate with MULTI the hydrodynamic expansion of the Al foil we use as heating driver the x–ray radiation emitted at the rear of the conversion foil rather than an equivalent Planckian radiator [16]. This choice is justified because of the dominant contribution of the conversion foil flux in the heating of the absorption foil, and it permits to take into account the spectral distribution of the heating radiation, improving the simulation accuracy [20,28].

To this purpose, 6 % of the x–ray flux emitted at the back side of a 130 nm thick gold foil, heated by a 500 ps duration Gaussian pulse with 1.5×10^{14} W/cm^2 flux at 0.53 μm wavelength (see Fig. 5.11), was used to irradiate a 20 μg/cm^2 Al foil, coated on each side with 8 μg/cm^2 C tampers. Here, for this second simulation, the x–ray radiation is assumed to be coupled on the vacuum border of the right C tamper, as Figure 5.15 shows. The simulation results are summarized in Fig. 5.16, 5.17; for reference Fig. 5.16 gives also the time evolution of the heating flux (gray full line).

Fig. 5.16(a) gives the time evolution of the plasma electron temperature. The three curves obtained at the right C/Al cell (dashed line), at the center of the Al plasma (black full line), and at the left C/Al cell (dotted line), cover the whole range of the plasma spatial expansion. The temperature shows a fast rise giving at the central plasma cell a maximum of 30 eV at 0.9 ns (absolute maximum of 35 eV at the right C/Al plasma cell), and then the plasma gradually cools to 15 eV as time evolves to 4 ns. Considering the plasma evolution during the probing pulse (grayed region of Fig. 5.16(a)), we see that initially the spatial gradients of the temperature are rather high (22 – 30 eV), and they are slightly smoothed out as time evolves

(18 – 23 eV at the end of the pulse). Fig. 5.16(b) gives the time evolution of the plasma mean ionization number; which at the center of the plasma and during the probing, it varies around ~ 5.5 – 6.

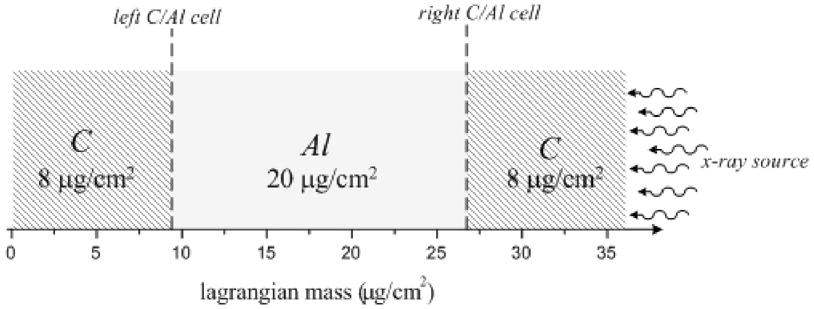

Figure 5.15 One–dimensional Lagrangian representation of the Al absorption foil tampered configuration. The x–ray radiation is coupled on the vacuum border of the right C tamper.

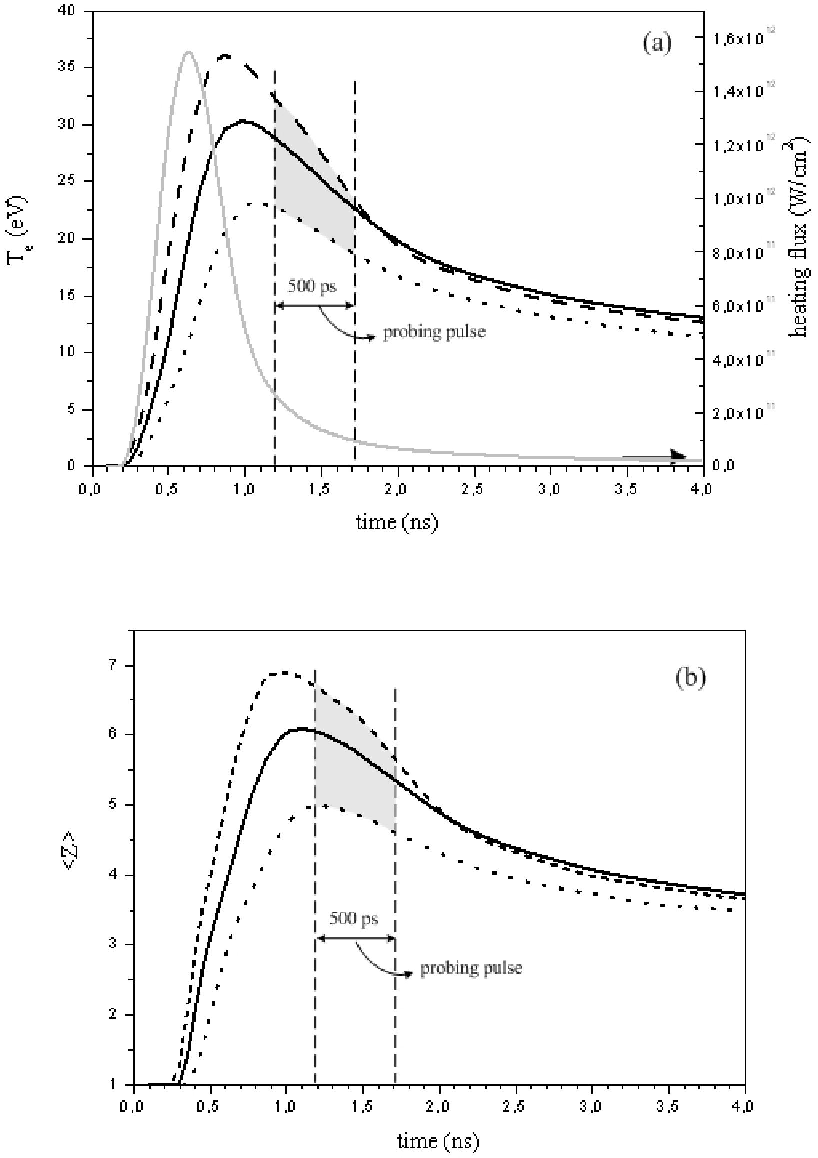

Figure 5.16 Time evolution of (a) T_e, (b) <Z> calculated with MULTI for a 20 µg/cm^2 Al foil tamped with 8 µg/cm^2 C foils. Full black line : T_e at the center of Al, dashed line : at the right C/Al cell, and dotted line : at the left C/Al cell. Full grey line in (a) : total flux heating the foil.

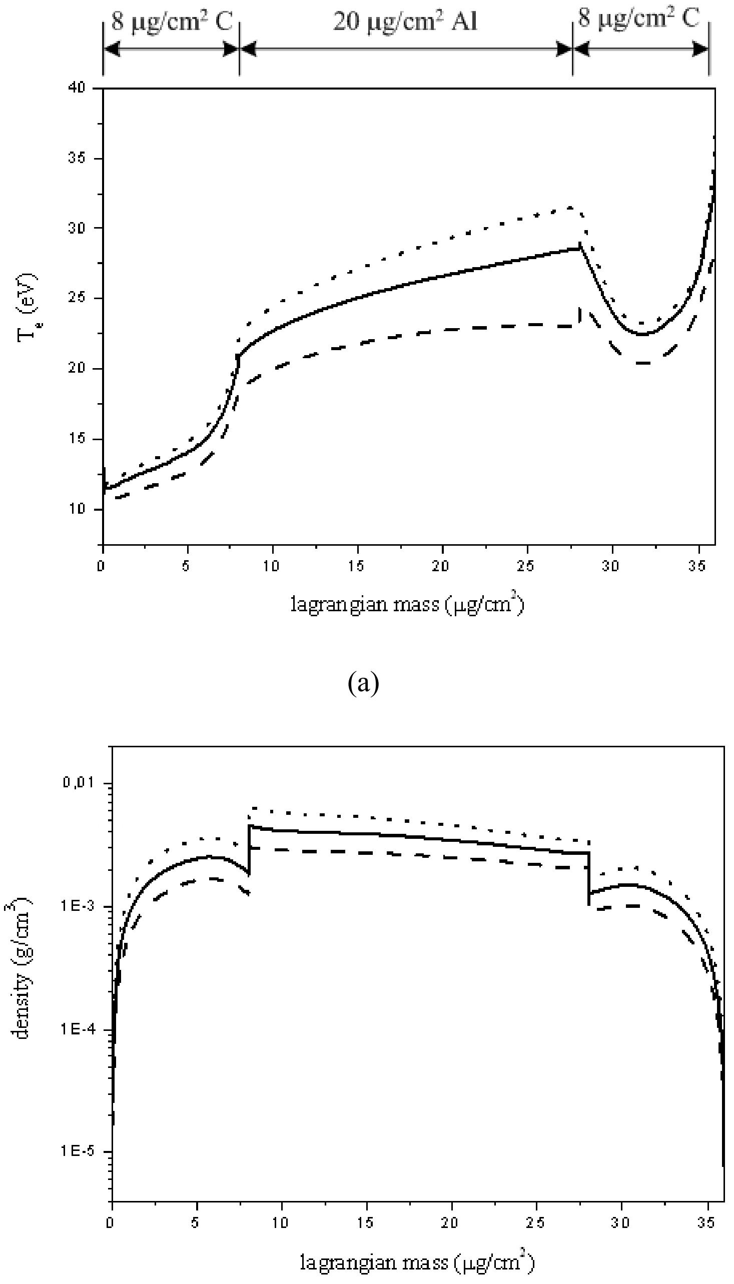

(a)

(b)

Figure 5.17 MULTI simulation results of the plasma hydrodynamic parameters as a function of the Lagrangian mass. (a) Electron temperature, and (b) matter density at the rising half–maximum (dotted line), at the maximum (full line), and at the falling half–maximum of the probing pulse (dashed line).

The gradients of the plasma temperature and density are illustrated more clearly in Figure 5.17, which gives their variation as a function of the Lagrangian mass. The different curves are obtained at three times corresponding to the rising half–maximum, to the maximum, and to the falling half–maximum of the probing pulse, providing, also, an image of the plasma time evolution. Fig. 5.17(a), gives the spatial variation of the plasma temperature. The temperature is higher in the Al plasma than in the C tampers (except the small region at the extreme right where the x–ray radiation heats the foil). This behavior could be attributed to the materials opacities in conjunction with the spectral distribution of the gold foil emission spectrum used as the heating driver. In Fig. 5.17(b) showing the matter density, on can see that the Al plasma exhibits a density higher than the C tampers density which decreases very fast at both plasma–vacuum borders. This implies the strong expansion of the C plasmas, and shows that the Al plasma is confined in this tampered foil configuration. Initially, the matter density shows a spatial variation of 3 – 6 mg/cm^2 (rising half–maximum), and gradually smoothes out, following an evolution similar to the electron temperature: 2.5 – 4 mg/cm^2 (maximum), 2 – 3 mg/cm^2 (falling half–maximum).

5.5 Analysis of the Al plasma absorption spectrum

5.5.1 Characterization of the Al absorption spectrum

The experimental absorption spectrum of paragraph 5.3.2, obtained from a 20 μg/cm^2 areal mass Al foil is given as the solid curve in Figure 5.18. The absorption features of the measured spectrum are identified with the atomic code HULLAC [18], which gives the ability to calculate the relative intensities of the different atomic transitions associated with each Al ion species. For this, an estimation of the ion populations contributing to the measured absorption is necessary. According to the simulation results of MULTI [32], and taking into account both the temporal and spatial gradients of Al plasma, its matter density varies in the range of 2 – 6 mg/cm^3 and its electron temperature in the range of 18 – 30 eV.

The ionic distributions calculated with the Saha–Boltzmann law for an Al plasma of 2 mg/cm^3 matter density, and different values of the electron temperature spanning the expected experimental range, are given in Table 5–III. The ions contributing significantly to the plasma population belong to the sequence of Al^{3+}–Al^{8+}, and the identification procedure is reduced to the calculation of their transitions. For each ion the relative intensities of the atomic transitions are calculated with the atomic code HULLAC, and the identification is shown in Fig. 5.18 with a simple superposition of the calculated transitions (grey lines) with the measured spectrum (Note: The comparison with Al^{3+} ion transitions is not given, as HULLAC predicts that its spectrum is confined in the range above 130 Å, where the experimental measurement is ambiguous).

T_e (eV)	<Z>	% Al^{3+}	% Al^{4+}	% Al^{5+}	% Al^{6+}	% Al^{7+}	% Al^{8+}
16	4.0	17	**62**	21	0	0	0
18	4.4	7	46	44	3	0	0
20	4.8	3	27	**57**	13	0	0
22	5.2	1	14	53	30	2	0
24	5.5	0	6	40	47	7	0
26	5.9	0	3	25	**54**	18	0
28	6.2	0	1	14	50	32	3
30	6.5	0	0	7	39	**45**	9

Table 5–III Ions distributions of an LTE Al plasma obtained for 2 mg/cm^3 matter density and different electron temperatures spanning the hydrodynamic range of the measured plasma.

To confirm the identification of Fig. 5.18, the same procedure is performed for the ions in the sequence of Al^{5+}–Al^{8+}, using now the tabulated atomic data of NIST database [36]. The relative intensities of the atomic transitions are obtained from the NIST database assuming an LTE plasma. For each ion the calculation is performed by using the temperature where its Saha distribution is maximum, and a roughly estimated electron density of 2 10^{20} cm^{-3}. These results are compared with the measured absorption spectrum in Fig. 5.19.

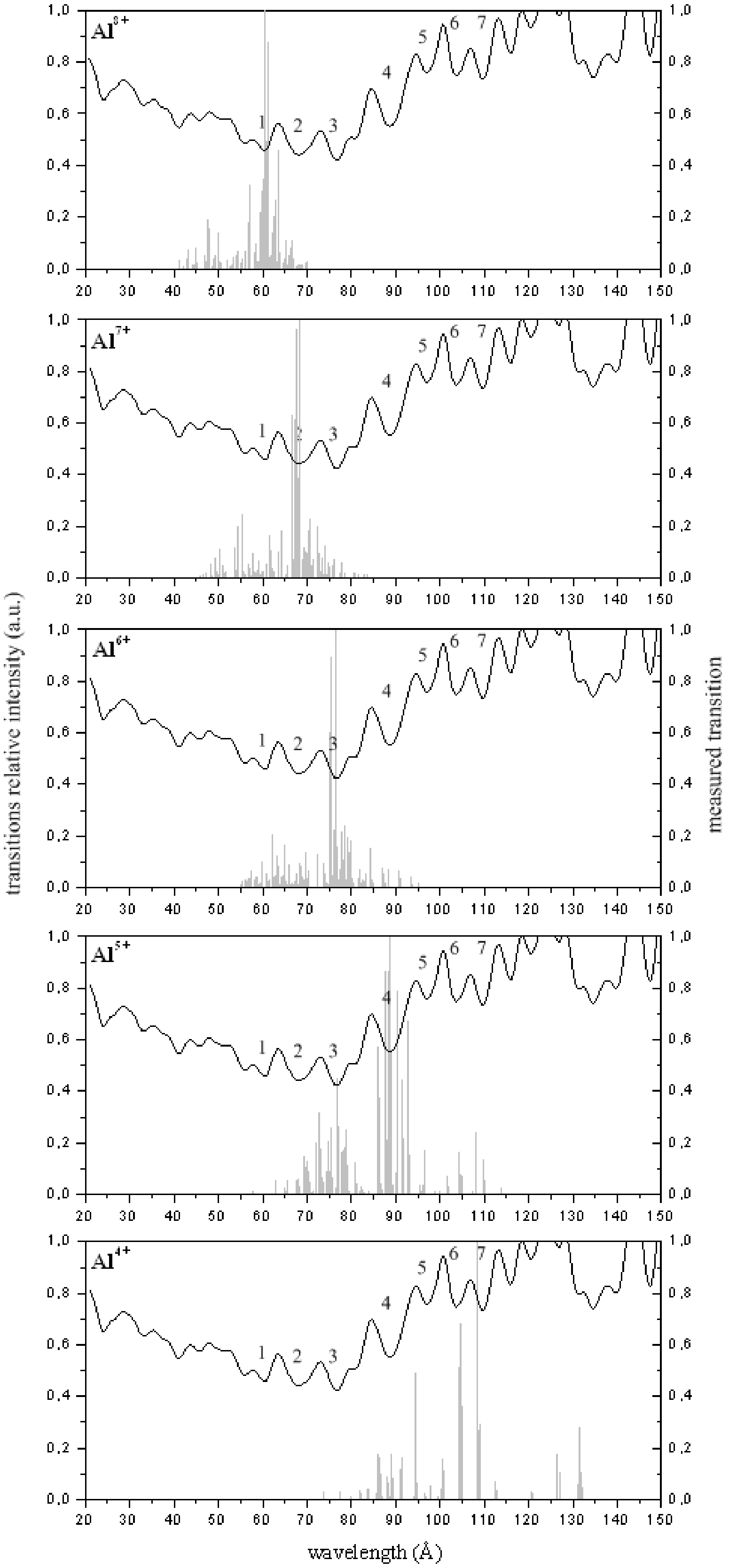

Figure 5.18 Identification of the ions contributing to the absorption of Al plasma with HULLAC. Full line : experimental spectrum; grey bars : relative intensities of the atomic transitions calculated ion by ion with the detailed atomic code HULLAC [18].

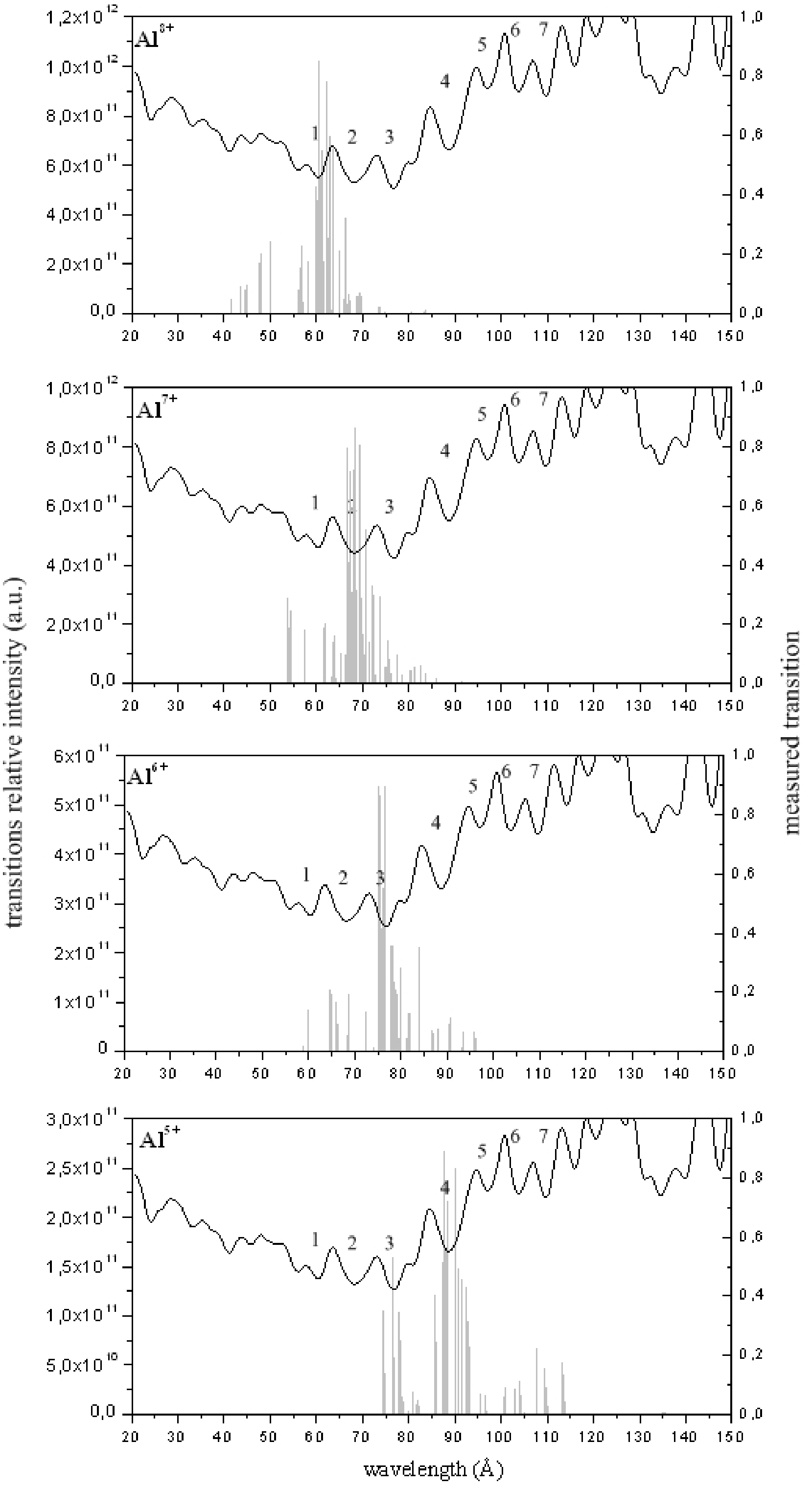

Figure 5.19 Identification of the ions contributing to the absorption of Al plasma with the NIST database [36]. Full line : experimental spectrum; grey bars : relative intensities of the atomic transitions obtained from NIST database.

From both figures, a straightforward correspondence is noticed between the major absorption features in the spectral range of 55 – 120 Å and the atomic transitions of the different ionic species. These results are summarized in Table 5–IV. The first column gives the labels of the absorption features identified in Fig. 5.18 and 5.19. The second and third columns give, respectively, the wavelengths of the ionic transitions contributing strongly to the absorption, according to the calculations of HULLAC and the NIST data. The wavelengths of the measured features are given in column 4. Finally, column 5 gives the experimental wavelengths of the absorption structures measured in Ref. [17] and also observed in our spectrum. Thus we provide an independent confirmation of the ionic species identification. We should remark that the wavelengths of columns 4, 5 represent simply the central values of the observed structures and not a strict identification of transition lines. The rough estimation of the plasma average charge of $<Z_{Al}> \approx 5-7$, as well as the rather broad ionic distribution, both inferred by the table data, suggest the presence of gradients, in agreement with the simulation results of MULTI.

label	λ_{HULLAC}(Å)	λ_{NIST}(Å)[36]	λ_{exp}(Å)	λ_{exp}(Å)[17]	ion	low level	high level
1	60.57	60.59	60.41	///	Al^{8+}	$2s2p^2$	$2s2p3d$
2	68.39	68.38	68.09	///	Al^{7+}	$2s^22p^2$	$2s^22p3d$
3	76.64	75.28	76.86	///	Al^{6+}	$2s^22p^3$	$2s^22p^23d$
	76.91	76.62		///	Al^{5+}	$2s^22p^4$	$2s^22p^33d$
4	88.86	87.78	88.56	///	Al^{5+}	$2s^22p^4$	$2s^22p^33d$
5	95.32	95.97	96.97	100.5	Al^{6+}	$2s2p^4$	$2s2p^33s$
	96.34	96.44			Al^{5+}	$2s2p^5$	$2s2p^4\mathrm{3s}$
6	104.5	103.94	103.91	105.5	Al^{5+}	$2s^22p^4$	$2s^22p^33s$
	104.7				Al^{4+}	$2s^22p^5$	$2s^22p^43d$
7	108.5		109.4	110	Al^{4+}	$2s^22p^5$	$2s^22p^43d$
	109.6	109.52			Al^{5+}	$2s^22p^4$	$2s^22p^33s$

Table 5–IV Identification of the different ions and their corresponding atomic transitions contributing to the observed absorption features of the Al plasma.

5.5.2 Comparison of the HULLAC synthetic Al spectrum with the measured absorption

Ab initio calculation of the Al absorption spectrum

The theoretical calculation of the Al absorption spectrum is performed with the detailed atomic code HULLAC [18], using the hydrodynamic parameters calculated with the hydrocode MULTI [32]. Additionally to the spatial gradients of the plasma parameters, the time integration of the measured absorption enforce us to account also for their temporal variation. First, a set of discrete times, t_n, are picked covering the evolution of the Al plasma which corresponds to the absorption measurement (plasma probing). Then, at each time t_n, both Al and C plasmas are divided in a number of i–cells of constant matter density and temperature, using discrete steps $\Delta\rho$, ΔT_e for the hydrodynamic parameters. This splitting attributes at each cell an areal mass density $\sigma_i(t_n)$ satisfying the matter conservation,

$$\sigma_{Foil} = \sum_i \sigma_i(t_n) \tag{5.7}$$

Calculating with HULLAC the spectral opacity, $\kappa_{i,v}(\rho_i, T_{i,e})$, of each cell ($\sigma_i$, ρ_i, $T_{i,e}$), its transmission is

$$\tau_i(t_n) = e^{-\kappa_i \sigma_i} \tag{5.8}$$

and the plasma transmission at t_n is calculated as the product of all the i–cells transmissions,

$$\tau(t_n) \equiv \prod_i \tau_i(t_n) = \prod_i e^{-\kappa_i \sigma_i} \tag{5.9}$$

Then, we account for the temporal evolution of the plasma by taking the average of the transmissions calculated at different times,

$$\tilde{\tau} = \frac{1}{N}\sum_{n=1}^{N} \tau(t_n) \tag{5.10}$$

The determination of the steps $\Delta\rho$ and ΔT_e was made with the aid of HULLAC. The absorption spectra of Al and C were calculated for different plasma parameters to determine the maximum steps for which their variations are not significant. Concerning the electron temperature, the absorption variation is followed accurately with ΔT_e = 2 eV for the Al and with ΔT_e = 4 eV for the C plasma. The low step accuracy of C is justified by the characteristics of its absorption spectrum introducing only a continuum lowering without discrete features, and which is calculated to improve the accuracy of the continuum absorption level.

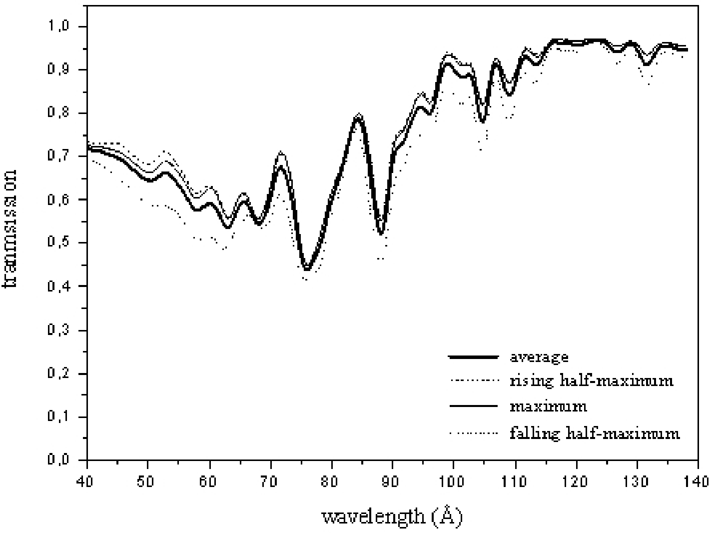

Figure 5.20 Theoretical absorption curves of a 20 μg/cm^2 Al foil calculated with HULLAC [18] and the hydrodynamic results of MULTI [32] for the electronic temperature profiles of Fig. 5.17(a) calculated at three times. The figure gives, also, their time average according to Eq. (5.10).

Concerning the matter density, the calculations of HULLAC showed that it does not affect significantly the absorption features of Al. Thus, as a first approximation, a mean value of 2 mg/cm^3 is used for Al and of 1 mg/cm^3 for C. For the temporal discretization, the criterion is to cover the evolution during the plasma probing, ensuring that the absorption spectrum between two times varies smoothly. Calculations with HULLAC showed that this condition is satisfied averaging on three samples at the rising half–maximum, at the maximum, and at the falling half–maximum of the backlight pulse (Fig. 5.17 of §5.4.2). The absorption profiles calculated for the three times, as well as their average are shown in Figure 5.20.

Comparison with the experimental absorption

The comparison of the averaged theoretical curve (full line) of Fig. 5.20 with the measured absorption of the 20 μg/cm^2 areal mass Al foil (dashed line) is given in Fig. 5.21. The theoretical curve reproduces with good accuracy the measured structures corresponding to the Al^{5+} and Al^{6+} transitions, and which are identified in the spectral range of 72 – 107 Å. Deviations are observed at the extremity of the spectrum. The two discrete 2*p*–3*s* absorption structures of Al^{5+} around 104, 110 Å (where the 2*p*–3*d* transitions of Al^{4+} ion also contribute) show an inverse intensity ratio with respect to the measured one. Below 72 Å, the theoretical curve shows systematically a lower absorption level with respect to the measured absorption. This is particularly obvious for the 2*p*–3*d* structure of Al^{7+} ion around 68 Å. Finally, the measured absorption structure identified with the 2*p*–3*d* transitions of Al^{8+} show a relative shift of ~ 2 Å with respect to the theoretical.

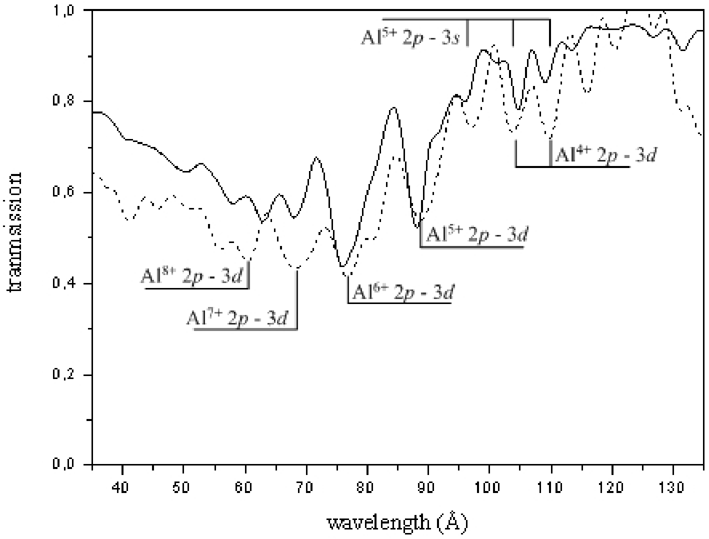

Figure 5.21 Comparison of the theoretical absorption spectrum (full line) calculated with HULLAC [18] with the measured absorption of the 20 μg/cm^2 Al foil (dashed line).

Concerning the low absorption level below 72 Å, a possible explanation could be the underestimation of the Al density due to the approximation used in our calculations. Indeed calculations run with HULLAC [18] for different densities in the range of 1 – 5 mg/cm^3 show that the absorption level increases with density, particularly in the spectral range of 20 – 80 Å. This is due to an increase of the continuum photoionization absorption on which the discrete features are superimposed. However, the situation is more complicated as the decrease of the temperature leads also to an increased continuum absorption. Indeed, calculations with HULLAC show that in the range of 20 – 80 Å the photoionization absorption of Al^{4+} and Al^{5+} is much stronger than that of Al^{6+} (see Fig. 5.22). Thus, the observed deviation could be also explained by an underestimation of the lower charged ions in the HULLAC calculation in LTE. As concerns the continuum absorption, a problem linked to the gold O–band cannot be excluded.

The relative shift of the structure identified with the 2*p*–3*d* transitions of Al^{8+} can also be attributed to an inappropriate ionic distribution. Here, we find that the theoretical absorption structure observed around 63 Å corresponds to the 2*p*–4*d* transitions of Al^{6+}. A high population of this Al^{6+} ion can lead to a strong contribution to the absorption spectrum of these relatively low intensity 2*p*–4*d* transitions (see Fig. 5.18). To be more specific, let us take the rising half–maximum profile of Fig. 5.17(a). For this temperature spatial variation, and assuming a Saha statistics, Al^{6+} represents 46% of the ions populations while Al^{8+} is only 3%. So now, the deviation observed around 63 Å could be attributed to an underestimation of the Al^{8+} population in the HULLAC calculation.

Consequently, the measured plasma is compatible with a wider ionic distribution than the LTE distribution used for the HULLAC calculation, with relatively higher populations at the extremity of the identified ionic sequence. This may signify that : (1) there is a wider variation of the electron temperature with respect to the one predicted by MULTI, or (2) there are deviations from the Saha statistics implying the NLTE behavior of the produced plasma [28]. Taking LTE as valid, the narrow variation of the plasma temperature could be attributed to the accuracy limits of the atomic physics used by MULTI. This may concern both the opacities of the gold plasma heating the cavity and the absorption foil, and the Al plasma determining its interaction with the radiation field. The description of the cavity radiation given by the Basko model [30] can also be questionable.

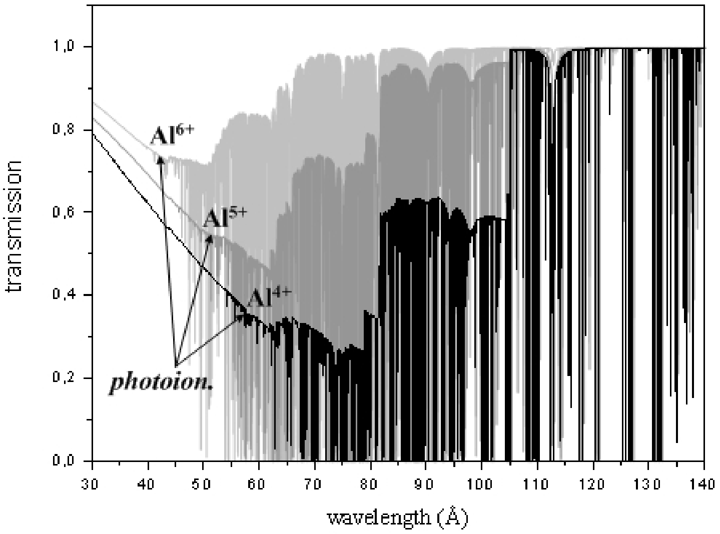

Figure 5.22 Transmission curves of a 20 μg/cm^2 Al plasma showing the photoionization continuum (no smoothing by the experimental line width). The curves are calculated with HULLAC [18] for 16 (black line), 20 (gray line) and 26 eV (light gray line) temperatures corresponding respectively to the maximum ionic populations of Al^{4+}, Al^{5+}, and Al^{6+} according to Saha law (see Table 5–IV); matter density 2 mg/cm^3.

Conclusions on the analysis method

In the XUV range, the observed absorption spectrum presents characteristic structures due to bound–bound transitions. But also, the continuum absorption associated with photoionization contributes significantly with the characteristic bound–bound transitions, to the formation of the observed absorption structures. The matter density and temperature gradients make the simulation of the spectrum more complicated, even if we assume LTE conditions. Their presence makes difficult the ability to "measure" the parameters with the XUV spectroscopy as in [16], something that exceeds the context of our work. Now, restricting ourselves to an evaluation of the plasma hydrodynamics accuracy, we can say that the *ab initio* calculations reproduce fairly well the measured spectrum of Al. So, under the given experimental conditions, the theoretical method followed is acceptable and we now apply it to the analysis of the ZnS absorption spectrum.

5.6 Analysis of the ZnS plasma absorption spectrum

5.6.1 Characterization of the ZnS absorption spectrum

The experimental ZnS absorption spectrum, already shown in Figure 5.10(b), obtained from a 20 μg/cm^2 areal mass foil is given in Fig. 5.23 with an identification of the different transitions contributing to the spectrum of the plasma mixture. This identification is obtained by comparing the measured absorption with analytical calculations performed with the code SCO [10,11]. In the spectral range of 55 – 120 Å various absorption features of different zinc and sulfur ions are observed. Table 5–V summarizes the correspondence of labels shown in Fig. 5.23 with the different ions (3rd column) and their transitions (4th, 5th columns) (Note : the experimental wavelengths given in the 2nd column are the peak values around which the absorption structures appear).

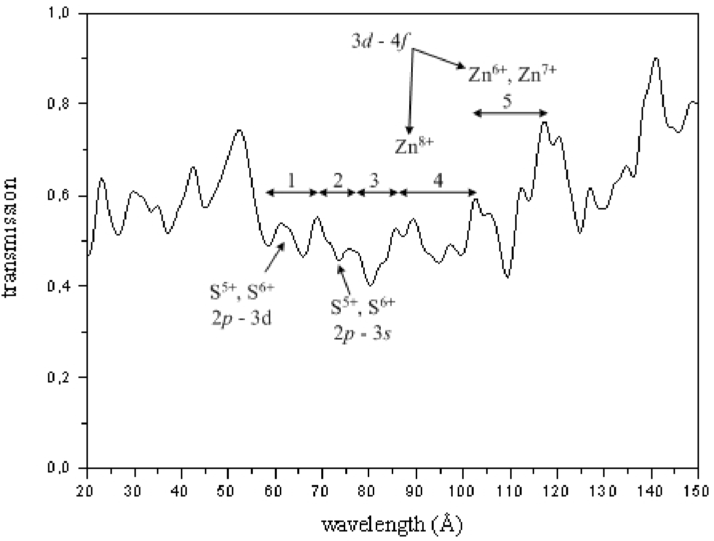

Figure 5.23 Measured absorption spectrum of a 20 μg/cm^2 ZnS foil, tamped with 8 μg/cm^2 C foils on both sides (see Fig. 5.10(b)). Figure shows the labels of the identified transitions given in Table 5–V.

label	λ_{exp}(Å)	ion	low level	high level
1	61	S^{5+}	$2p^6 3s$	$2p^5 3s 3d$
		S^{6+}	$2p^6$	$2p^5 3d$
2	73	S^{5+}	$2p^6 3s$	$2p^5 3s^2$
		S^{6+}	$2p^6$	$2p^5 3s$
3	80	Zn^{8+}	$3d^4$	$3d^3 5f$
4	95	Zn^{8+}	$3d^4$	$3d^3 4f$
5	109	Zn^{6+}	$3d^6$	$3d^5 4f$
		Zn^{7+}	$3d^5$	$3d^4 4f$

Table 5–V Identification of the different ions of zinc and sulfur species, and their transitions contributing to the measured absorption spectrum.

In the range of 103 – 120 Å the $3d$–$4f$ transitions of Zn^{6+} and Zn^{7+} ions can be identified (label 5). The $3d$–$4f$ transitions of Zn^{8+} (label 4) show two discrete absorption structures : a dominant one in the range 90 – 103 Å, and a rather weak one around 87 Å. The structure in the range of 75 – 85 Å (label 3) may corresponds to the $3d$–$5f$ transitions of Zn^{8+}. At lower wavelengths the 2*p*–3*s* transitions of S^{5+}, S^{6+} ions are identified in the narrow structure appearing in the range of 70 – 75 Å (label 2). The identified ions give a rough estimation of the plasma mixture ionization, $<Z_{ZnS}> \approx 6$.

5.6.2 Hydrodynamic simulation of the ZnS foil

As for the Al case, first the radiation emitted at the rear of a 130 nm thick gold foil is simulated with MULTI [32], irradiating it with a 500 ps duration laser pulse of 1.1 10^{14} W/cm^2 flux at 0.53 μm. The x–ray source is used as input in the Basko model [30], from which we obtain that the x–ray flux heating the absorption foil corresponds to 6% of the total flux emitted at the rear of the gold foil; equivalently the heating flux corresponds to a Planckian radiation of 55 eV temperature. The simulation of the ZnS hydrodynamics is performed using the gold foil emission spectrum obtained by MULTI. A 20 μg/cm^2 areal mass ZnS foil coated on each side with 8 μg/cm^2 C tampers is heated by 6% of the radiation calculated in the first simulation. The heating radiation is coupled at the C/vacuum interface of the right C tamper. The results are summarized in Figures 5.24, and 5.25.

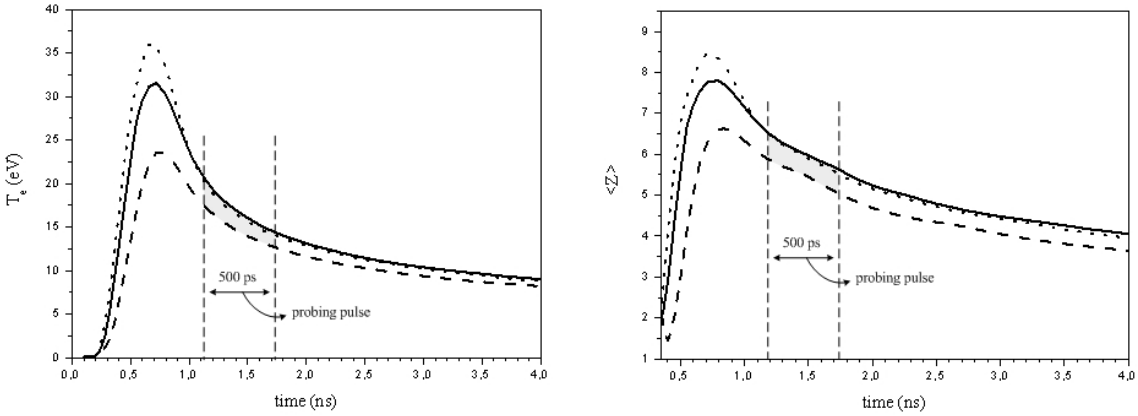

(a) (b)

Figure 5.24 Time evolution of the ZnS plasma hydrodynamic parameters obtained at the right C/ZnS spatial cell (dotted line), at the center of the ZnS plasma (full line), and at the left C/ZnS cell (dashed line). (a) Electron temperature, (b) mean ionization number.

Fig. 5.24(a) gives the time evolution of the plasma electron temperature. The three samples covering the plasma spatial expansion, are obtained at the left C/ZnS cell (dashed line), at the center of the ZnS plasma (full line), and at the right C/ZnS cell (dotted line). The temperature rises fast due to the foil heating, giving at the central plasma cell a maximum of 31 eV (absolute maximum of 36 eV at the right C/ZnS cell). Then the plasma gradually cools to 8 eV as time evolves to 4 ns. During the backlight pulse (grayed region), the temperature variation of each cell is about 5 eV. In particular, at the beginning of the backlight the temperature exhibits a spatial distribution of 16 – 20 eV, which becomes at the end of the pulse 12 – 15 eV. Thus, the gradients appearing on the averaged measured plasma are mainly due to the time evolution of the temperature during the probing pulse, and not because of its spatial variation. Fig. 5.24(b) gives the time evolution of the plasma mean ionization number. Its value at the center of the plasma during the backlight pulse (grayed region) varies between 5.7 – 6.5 in accordance with the experimental rough estimation obtained from the ions identification.

The electron temperature and the matter density of the ZnS plasma are given as a function of the Lagrangian mass in Fig. 5.25(a), (b). The three curves are obtained at the rising half–maximum, the maximum and the falling half–maximum of the backlight pulse. From Fig. 5.25(a) we see that the temperature of the ZnS plasma is more uniform than in the Al plasma shown in Fig. 5.17(a); at the three times, it varies in the range of 17 – 20 eV, 14 – 16 eV, and 13 – 14 eV. The relative spatial homogeneity is also seen for its matter density (Fig. 5.25(b)), which at the three times takes values in the range of 4 – 5 mg/cm^3, 3 – 4 mg/cm^3, and 2.5 – 3 mg/cm^3.

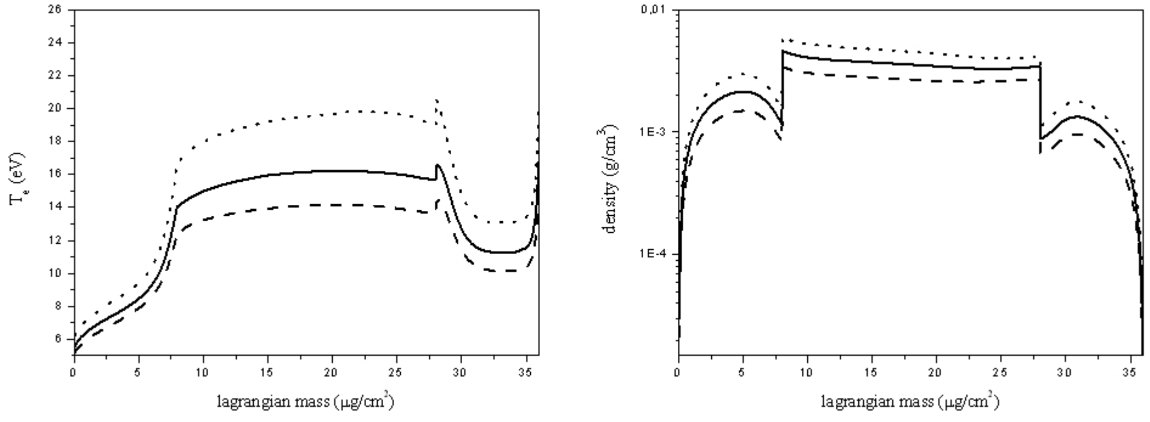

(a) (b)

Figure 5.25 Lagrangian representation of the ZnS plasma hydrodynamic parameters obtained at the rising half–maximum (dotted line), at the maximum (full) line, and at the falling half–maximum (dashed line) of the backlight. (a) Electron temperature, (b) matter density.

5.6.3 Comparison of the SCO synthetic ZnS spectrum with the measured absorption

Ab initio **calculation of the absorption spectrum**

The hydrodynamic parameters of the ZnS plasma obtained with the code MULTI [32] are post–processed with the code SCO [10,11] to calculate its absorption spectrum. As with the Al plasma, the temporal and spatial variations of the temperature are taken into account, while in a first approximation the matter density is fixed. Concerning the temperature, calculations with SCO showed that its temporal variation during the plasma probing is adequately approached with the three samples of Fig. 5.25(a). Further, the spatial variation for each of the time is followed by dividing the plasma in discrete cells of constant temperature, using steps of 2 eV for the ZnS and 4 eV for the C plasmas. The matter density is fixed at 2.5 mg/cm^3 for ZnS and 1 mg/cm^3 for C.

In each cell of constant ρ, T_e the absorption of the sulfur and zinc plasmas are calculated with SCO. The opacity of each component of the mixture accounts for the total electronic density via the ionic distribution and therefore is sensitive to the presence of the other component. The transmission of the plasma mixture cell is simply

$$\tau_i(t_n) = e^{-\kappa_{i,S}\sigma_{i,S}} \cdot e^{-\kappa_{i,Zn}\sigma_{i,Zn}} \qquad (5.11)$$

where the partial areal mass of Zn and S are :

$$\sigma_{i,Zn} = \frac{A_{Zn}}{A_{ZnS}} \sigma_{i,ZnS} \tag{5.12.a}$$

$$\sigma_{i,S} = \frac{A_S}{A_{ZnS}} \sigma_{i,ZnS} \tag{5.12.b}$$

A_{Zn}, A_S and A_{ZnS} are respectively the atomic weights of the zinc, sulfur and zinc sulfide. Then, the plasma transmission at each time is calculated as the product of all the *i*–cells according to Eq. (5.9), and their time average is calculated by Eq. (5.10). The results for the three times of the probing pulse and their average are shown in Figure 5.26.

An inspection of the three times synthetic spectra shows that the part of the absorption associated with the zinc ionic transitions varies strongly with the temperature in comparison with the corresponding sulfur part. In particular, as the temperature decreases : (1) the mean absorption level increases especially at high wavelengths, and (2) a deformation is observed in the absorption feature around 85 Å corresponding to the Zn^{8+} 3*d*–4*f* transitions. This behavior could be attributed to the relative variation of the absorption continuum (photoionization) of zinc with regard to its discrete absorption features (bound–bound absorption transitions) as explained in the Al case (see § 5.5.2).

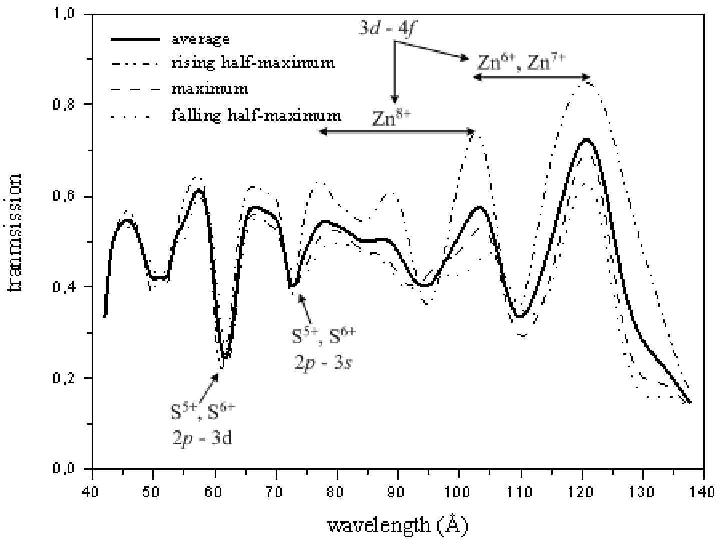

Figure 5.26 Theoretical absorption profiles calculated with the code SCO [10,11], using the temperature spatial variation of the three times profiles of Fig. 5.25(a). The figure gives also their time average according to Eq. (5.10).

Comparison with the experimental absorption

The comparison of the averaged theoretical curve (full line) of Fig. 5.26 with the measured absorption of the 20 µg/cm^2 areal mass ZnS foil (dashed line) is given in Fig. 5.27. The two absorption structures in the range of 84 – 120 Å, which are identified with the 3*d*–4*f* transitions of the Zn^{6+}–Zn^{8+} ions, are in a good agreement. The theoretical spectrum reproduces also the absorption structure around 74 Å corresponding to the 2*p*–3*s* transitions of the S^{5+}–S^{6+} ions.

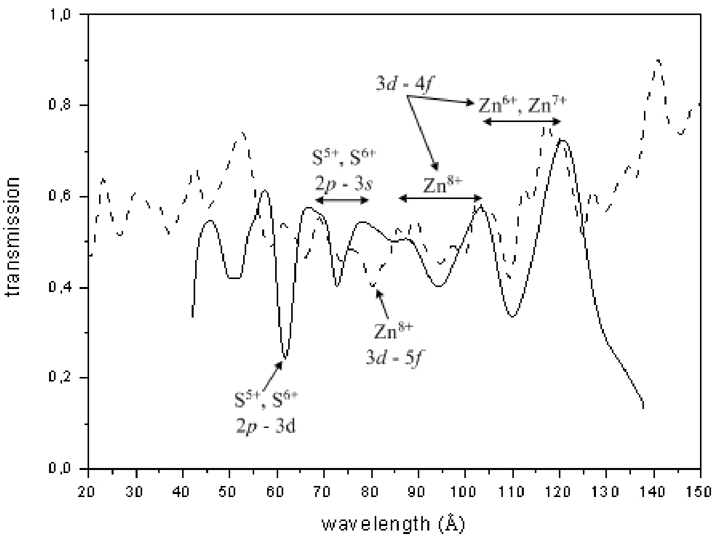

Figure 5.27 Comparison of the theoretical absorption spectrum calculated with SCO code [10,11] (full line) with the measured absorption of a 20 μg/cm^2 areal mass ZnS foil (dashed line).

In the absorption part corresponding to the sulfur ions a deviation is observed at the 2*p*–3*d* transitions of S^{5+}–S^6 in the range of 58 – 70 Å. In the absorption part of the zinc ions a deviation appears in the range of 76–84 Å. The calculations performed with SCO give that this structure may be attributed to the 3*d*–5*f* transitions of Zn^{8+} ion, and its interesting characteristic is the strong variation with respect to the matter density. Also, SCO predicts an intense and broad absorption structure in the range of 120 – 160 Å (see also Fig. 5.28), which is in a striking disagreement with the measured spectrum.

To check the accuracy of the super transitions arrays formalism of SCO [10,11] we have performed some preliminary calculations of the ZnS absorption spectrum with the detailed atomic code HULLAC [18]. Figure 5.28 compares the experimental spectrum with the results of the two codes for a 20 μg/cm^2 areal mass ZnS plasma of 2.5 mg/cm^3 matter density and 16 eV temperature. Except for the difference of the absorption levels, the two codes give similar shapes for the features in the range of 50–80 Å. Therefore, the observed deviation of the experimental spectrum in the range of the sulfur 2*p*–3*d* transitions around 60 Å should be attributed to the measurement accuracy at low wavelengths. The remarkable result is the relative agreement of the experiment with the HULLAC calculations in the range of 120 – 140 Å, and its deviation from the SCO calculations. According to HULLAC this absorption structure corresponds to the 3*d*–4*f* transitions of the Zn^{5+}–Zn^{6+} ions. However the result of HULLAC has to be taken with care, due to the difficulty to handle the huge number of the transitions involved in the calculations of the zinc absorption spectrum, and due to the very preliminary character of these computation results. This experimental "confirmation" of the HULLAC calculations and the disagreement between SCO and HULLAC could be viewed as an interesting point for further theoretical investigation on this XUV spectral range.

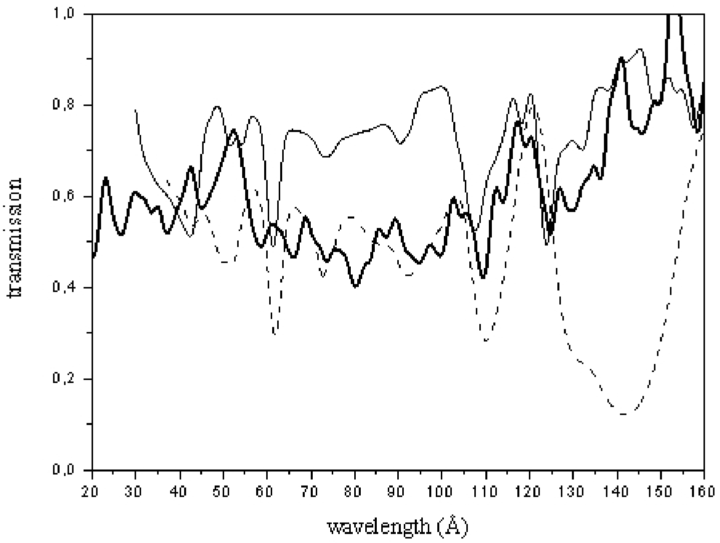

Figure 5.28 Comparison of the SCO [10,11] (dashed line) and HULLAC [18] (thin full line) calculations with the measured absorption (thick full line); the codes use the plasma parameters: 20 μg/cm^2 areal mass, 2.5 mg/cm^3 matter density and 16 eV temperature.

5.7 Conclusions

The time resolved XUV absorption spectra of ZnS and Al foils heated by the thermal radiation of a gold cavity have been measured. The simulation of the spectra necessitates the determination of the hydrodynamics parameters, and this was performed with the hydrodynamic code MULTI and the theoretical calculation of the radiation heating the absorption foils. The method for determining the cavity radiation is based on the Basko model giving the radiation temperature of the heated wall, and the view factor approach describing the energy redistribution in the interior of the cavity. Given the laser flux range heating the cavity, these calculations gave x–ray fluxes heating the absorption foils which correspond to equivalent Planckian radiation temperatures in the range of 55–60 eV.

The theoretical approach was verified by the analysis of the Al absorption spectrum. Using the code HULLAC as post–processor of the Al hydrodynamics, the main absorption features identified with the 2*p*–3*d* transitions of Al^{5+}–Al^{6+} were reproduced with very good accuracy, validating the method ability to estimate the plasmas heating for the given experimental conditions. The deviations between the theoretical predictions with the measured spectrum were also extensively discussed. An interesting conclusion concerns the limitations of the XUV absorption spectroscopy as a temperature and matter density diagnostics in the presence of temperature and density gradients, and in particular, their influence on the photoionization continuum.

Based on the estimation of the cavity heating conditions, the ZnS plasma hydrodynamic expansion was simulated with MULTI. The results were post–processed with the code SCO to calculate its absorption spectrum. Comparison showed the dominance of the 3*d*–4*f* transitions of Zn^{6+} and Zn^{7+} ions. Also, spectral features corresponding to the 3*d*–4*f* and 3*d*–5*f* transitions of Zn^{8+} were identified. The deviations of the theoretical transmission in the range corresponding to Zn^{8+} 3*d*–5*f* transitions suggests a correlation between the matter density and the occurrence of the transitions, an interesting point which needs further exploration. For sulfur, the 2*p*–3*s* transitions of S^{5+}–S^{6+} ions have been identified. The observed deviation between experiment and theory in the range corresponding to the 2*p*–3*d* transitions have been checked with the detailed atomic code HULLAC. As the HULLAC and SCO calculations are in accordance for these sulfur transitions, the deviations were attributed to the measurement accuracy at low wavelengths, in the vicinity of the gold spectrum O–band emission feature which may extend above 50 Å. The large deviation between the SCO calculations and the measured absorption in the range of 120 – 160 Å was also analyzed with HULLAC. Preliminary calculations with the detailed code gave a good agreement with the measured absorption structure in the range of 120 – 140 Å identified with the 3*d*–4*f* transitions of Zn^{5+}–Zn^{6+}. The confirmation of the HULLAC calculations and their large deviation from the calculations of SCO is also an interesting point which should be investigated further in the context of the theoretical models used to simulate the plasmas absorption spectra.

References of Chapter 5

[1] L. B. Da Silva *et al.*, Absorption Measurements Demonstrating the Importance of $\Delta n = 0$ Transitions in the Opacity of Iron, Phys. Rev. Lett **69**, 438 (1992).

[2] F. J. Rogers and C. A. Iglesias, Science **263**, 50 (1994).

[3] C. Chenais–Popovics *et al.*, Astrophys. J., Suppl. Ser. **127**, 275 (2000).

[4] M. Sako *et al.*, Astron. Astrophys. **365L**, 168 (2001).

[5] J. D. Lindl *et al.*, The physics basis for ignition using indirect–drive targets on the National Ignition Facility, Phys. Plasmas **11**, 339 (2004).

[6] D. Mihalas, Stellar atmospheres, W. H. Freeman and Company (1978).

[7] C. Chenais–Popovics, Astrophysics in laboratory : Opacity measurements, Laser Part. Beams **20**, 291 (2002).

[8] S. Atzeni, J. Meyer-Ter-Vehn, The Physics of Inertial Fusion, Beam plasma interaction, Hydrodynamics, Hot dense matter, pp. 302 – 303, Oxford Science Publications, 2004.

[9] S. Fujioka *et al.*, Opacity effect on Extreme Ultraviolet Radiation from Laser–Produced Tin Plasmas, Phys. Rev. Letters **95**, 2350041 (2005).

[10] T. Blenski, A. Grimaldi and F. Perrot, Hatree–Fock statistical approach to atoms and photoabsorption in plasmas, Phys. Rev. E **55**, R4889 (1997).

[11] T. Blenski, A. Grimaldi and F. Perrot, A superconfiguration code based on the local density approximation, J. Quant. Spec. Radiat. Transfer **65**, 91 (2000).

[12] J. C. Pain and T. Blenski, Self-consistent approach for the thermodynamics of ions intense plasmas in the superconfiguration approximation, J. Quant. Spec. Radiat. Transfer **8**, 355 (2003).

[13] A. Bar–Shalom *et al.*, Super–transition–arrays : A model for the spectral analysis of hot, dense plasma, Phys. Rev. A **40**, 3183 (1989).

[14] N. Kontogiannopoulos *et al.*, Measurement of XUV–absorption spectra of ZnS radiatively heated foils, High Energy Density Phys. **3**, 149 (2007).

[15] C. Chenais–Popovics *et al.*, Absorption measurements of radiatively heated multi–layered Al/Ni foils, J. Quant. Spec. Radiat. Transfer **71**, 249 (2001).

[16] G. Winhart *et al.*, XUV opacity measurements and comparison with models, J. Quant. Spec. Radiat. Transfer **54**, 437 (1995).

[17] G. Winhart *et al.*, Measurements of extreme uv opacities in hot dense Al, Fe and Co, Phys. Rev. E **53**, R1332 (1996).

[18] A. Bar–Shalom *et al.*, HULLAC, an integrated computer package for atomic processes in plasmas, J. Quant. Spec. Radiat. Transfer **71**, 169 (2001).

[19] T.S. Perry et *al.*, Absorption experiment on x-ray-heated mid-Z constrained samples, Phys. Rev. E **54**, 5617 (1996).

[20] F. Thais et *al.*, Absorption of local thermodynamic equilibrium aluminum at different densities, J. Quant. Spec. Radiat. Transfer **81**, 473 (2003).

[21] Y. B. Zel'dovich, Y. P. Raizer, Physics of Shock Waves and High-Temperature Hydrodynamic Phenomena, Academic Press, 1966.

[22] K. Eidmann, T. Kishimoto, Absolutely measured X–ray spectra from laser plasmas with targets of different elements, App. Phys. Letters **49**, 377 (1986).

[23] P. D. Goldstone *et al.*, Dynamics of High-Z plasmas produced by a short-wavelength laser, Phys. Rev. Letters **59**, 56 (1987).

[24] F. Gilleron, Etude du transfert radiative et de l'opacité d'un plasma crée par rayonnement X, thesis, Ecole Polytechnique (2000).

[25] Center for X-ray Optics (CXRO), X-Ray Interaction With Matter Tabulated Data, http://henke.lbl.gov/optical_constants/

[26] T. S. Perry et *al.*, Opacity Measurements in Hot Dense Medium, Phys. Rev. Letters **67**, 3784 (1991).

[27] H. Merdji et *al.*, K-Shell spectroscopy of radiatively heated aluminium, J. Quant. Radiat. Transfer **58**, 773 (1997).

[28] F. Gilleron, et *al.*, LTE absorption spectroscopy of an X–ray heated boron plasma, J. Quant. Spec. Radiat. Transfer **69**, 217 (2000).

[29] C. Chenais-Popovics *et al.*, L-band x-ray absorption of radiatively heated nickel, Phys. Rev. E **65**, 0164131 (2001).

[30] M. Basko, An improved version of the view factor method for simulating inertial confinement fusion holraums, Phys. Plasmas **3**, 4148 (1996).

[31] G. D. Tsakiris, Energy redistribution in cavities by thermal radiation, Phys. Fluids B **4**, 992 (1992).

[32] R. Ramis, R. Schmalz and J. Meyer–Ter–Vehn, MULTI – A computer code for one – dimensional multigroup radiation hydrodynamics, Comp. Phys. Communications **49**, 475 (1988).

[33] H. Merdji et *al.*, Phys. Rev. E **57** 1042 (1998)

[34] T.S. Perry et *al.*, Quantitative measurement of mid-Z opacities, J. Quant. Spectrosc. Radiat. Transfer **54**, 317 (1995).

[35] A. Mirone *et al.*, J. Quant. Spec. Radiat. Transfer **58**, 791 (1997).

[36] NIST Atomic Spectra Database, http://physics.nist.gov/PhysRefData/ASD/ index.html (2006).

Conclusions and perspectives

In this work we performed experiments of emission and absorption spectroscopy of laser produced plasmas, to provide *well characterized* spectral data which permit to benchmark atomic physics codes. More precisely, we produced xenon and krypton plasmas in NLTE conditions and studied their emission spectra. In a second experiment, we characterized the absorption spectra of zinc sulfide and aluminium plasmas in LTE conditions.

Xenon and krypton emission spectroscopy

In this experiment the time–integrated emission spectra in the keV range, and the time–resolved XUV emission spectra of laser irradiated NLTE xenon and krypton plasmas were measured. The states of the plasmas were characterized independently with the Thomson scattering technique in order to precise their heating conditions (density and temperature). The spectroscopic data were compared to simulations performed with the code TRANSPEC /AVERROES using the Thomson plasma parameters.

In the keV spectral range the code reproduces rather well the spectra of the xenon and krypton plasmas, but with different temperatures than those measured with the Thomson diagnostics. In the time–resolved measurements in the XUV range, the code reproduces the low wavelength (around 40 Å) emission structures for both the xenon and krypton plasmas, but differences appear for longer wavelengths. The study of the experimental measuring conditions showed that the incompatibilities between the Bragg spectrograph and the Thomson diagnostics have to be attributed to the inhomogeneity of the produced plasmas. Here, we should recall that the antithetical experimental constraints that produced the plasma non homogeneity are : (1) the large heating scale of the gas–jets (1 mm focal spot width) used to avoid the cold gas absorbing the emitted radiation, and (2) the large ellipticity of the laser focal spot, obtained with a random phase plate used to improve the Bragg crystal spectrograph spectral resolution. Concerning the XUV spectrum, the problem seems to be open also from its theoretical side. However, we have to underline that the intrinsic inability to precise experimentally the space and time evolution of the plasmas heating conditions restricts the improvement of the code calculations.

The design of a future experiment should be oriented in avoiding the plasmas non homogeneities observed here. First the laser focal spot should be more carefully chosen to exclude any potential introduction of hot spots. Second, the spatial scale of the plasma should be reduced to improve its homogeneity. Finally, given the plasma scale, the instruments should ensure a more accurate coincidence between the probed regions of the plasma.

Concerning the potential limitations of the TRANSPEC/AVERROES calculations in the XUV spectral range, our experimental measurements are a useful database provided that we can determine the plasma temporal and spatial evolution. This can be done by performing a simulation of the laser/gas–jet interaction with a 3D hydrodynamic code. Also, for the rather simple spectra in the keV range, it would be interesting to analyze them using detailed atomic codes as HULLAC, coupled to a NLTE collisional radiative solver.

Zinc sulfide and aluminium absorption spectroscopy

In this experiment we measured the time resolved XUV spectra of ZnS and Al radiatively heated foils under LTE conditions. The Al absorption spectrum analyzed with the code HULLAC provided an independent estimation of the heating conditions achieved with the 1.2 mm diameter gold cavities used in the experiment. It confirmed the validity of the theoretical calculations giving radiative temperatures in the range of 55–60 eV. The comparison of the ZnS measured spectrum with the calculations performed with the code SCO gave in general a good agreement for different absorption features of both zinc and sulfur ions. However, disagreements were also noticed at high and low wavelength of the experimental spectral range, which suggest further experimental and theoretical work.

Concerning the experimental side we should recall the variations of the backlight conditions from shot to shot, which become particularly important in the vicinity of the backlight O–band emission around 55 Å. Due to the non linear variation of the backlight intensity with the laser energy in this spectral range, the normalization procedure followed in the case of ZnS may introduce some accuracy limitations.

Spatial and temporal variations of the plasma parameters during the probing of the plasma introduces difficulties in providing the proper parameters to be post–processed by the SCO code. This is specially important due to the strong variation of the XUV absorption spectrum with both the temperature and the density. In a future experiment, these effects should be reduced.

Concerning the theoretical limitations of SCO, we have to notice the large deviation of the code predictions from the measured spectrum in the range of 120 – 140 Å in which the $3d$–$4f$ transitions of the Zn^{5+}–Zn^{6+} ions appear. The preliminary calculations performed by the detailed code HULLAC seems to confirm the validity of our measurements. In this case our spectroscopic data provide a good experimental reference to check further the SCO calculations. Further detailed analysis with HULLAC is also desirable here. From a theoretical point of view, the 55 – 120 Å range at $T \sim 15$ eV presents an interesting challenge to detailed codes as it involves the $3d$–nl transitions of Zn ions with an almost half–filled $3d$ subshell (about 24 bound electrons) giving rise to complicated absorption structures (UTA).

Perspectives

In both experiments the plasmas inhomogeneities, introduced due to the spatial or temporal probing scale, proved to be an strong limiting factor in analysing the experimental data. This holds especially for the XUV emission and absorption spectroscopy, due to the additional theoretical complications that one finds in this spectral range. The inference following from both experiments is that the lack of the plasma homogeneity restricts the ability to characterize experimentally its state, regardless of the experimental technique that we apply (Thomson scattering or XUV spectroscopy). Thus, a common request concerns the realization of experiments with more homogeneous probed plasmas.

From this point of view, and as concerns the absorption spectroscopy, the new PICO2000 laser facility of LULI laboratory, which provides power laser pulses of picosecond time duration, gives advanced possibilities. The main advantage of PICO2000 laser facility is the ability to probe the absorbing plasma evolving the nanosecond scale with backlight pulses of picosecond scale time duration. In this way the plasma gradients introduced due to its time evolution are avoided, ensuring its improved homogeneity.

This advanced approach will be applied for the first time in an experiment planned in the year 2008 concerning the characterization of the absorption spectra in the keV range of different medium–Z elements foils (Fe, Ni, Cu, Zn, Ge) heated radiatively at similar temperatures. The results of this work will be very important for the future development of the absorption spectroscopy of hot and dense plasmas. In the mid–term future, experiments on great laser facilities, like LIL–PETAL, LMJ, should permit investigations on large volumes of hot plasmas with consequently a important improvement in the quality of the results.

Appendix A Elements of the Thomson scattering theory

A.I Introduction

An electromagnetic wave interacting with a charged particle induces its acceleration and the emission of electromagnetic radiation. The result of this interaction is the scattering of the incident radiation. When the frequency of the incident wave is sufficiently low and the quantum effects can be neglected this process is referred as Thomson scattering [1,2].

Thomson scattering was introduced in the domain of laser produced plasmas as a diagnostic method which permits to obtain the density and the electronic temperature, measuring simultaneously the scattered spectra due to the plasma ionic and electronic fluctuations [3,4]. The underlying theory of the Thomson scattering from plasmas is rather complicated, involving the microscopic fluctuations induced on the density of the plasma species, as described by kinetic theory, by its medium–like reaction on the electromagnetic radiation. The description of the plasma scattered radiation followed in this work, is based on the formalism of the *spectral density function* introduced by Salpeter [2,5]. Here we give some basic elements of the Salpeter theory permitting to correlate the spectral characteristics of the scattered radiation with the plasma parameters. A more rigorous description can be found in [2].

A.II Scattered electromagnetic radiation from plasma

A simple description of the Thomson scattering from a plasma is given in Figure A.1. Fig. A.1(a) shows an electromagnetic wave incident on a plasma scattering volume V, along the direction defined by the wave number k_i. The plasma electrons within V show a uniform electronic density on the average, but on a microscopic scale there are fluctuations due to their random thermal motion. The incident electromagnetic wave imposes an additional perturbation on the thermally fluctuating profile of the electronic density, the net effect of which is the emission of a scattered electromagnetic wave by the plasma in the direction of k_s, which forms with k_i an angle θ. Thus, the collective effect of the plasma Thomson scattering can be viewed equivalently as the result of the elastic interaction between the incident electromagnetic wave, the perturbation wave of the electronic density and the scattered electromagnetic wave (see Fig. A.1(b)).

The three interacting waves obey to the conservation laws of energy and momentum :

$$\omega_s = \omega_i \pm \omega \tag{A.1.a}$$

$$\bar{k}_s = \bar{k}_i \pm \bar{k} \tag{A.1.b}$$

Further, for the incident and the scattered electromagnetic waves we have their usual dispersion relations [1],

$$\omega_i^{\ 2} = \omega_{pe}^{\ 2} + k_i^{\ 2} c^2 \tag{A.2.a}$$

$$\omega_s^{\ 2} = \omega_{pe}^{\ 2} + k_s^{\ 2} c^2 \tag{A.2.b}$$

where $\omega_{pe} = \sqrt{n_e e^2 / \varepsilon_o m_e}$ is the electron plasma frequency, e is the electron charge, m_e the electron mass, n_e the electron density, and ε_o the vacuum dielectric constant. Of course, when the medium–like behavior of the plasma is determined by the reaction of its ions, in Eq. (A.2) we have the ion plasma frequency $\omega_{pi} = \sqrt{n_i e^2 / \varepsilon_o m_i}$, where n_i, m_i are the ion density and mass, respectively.

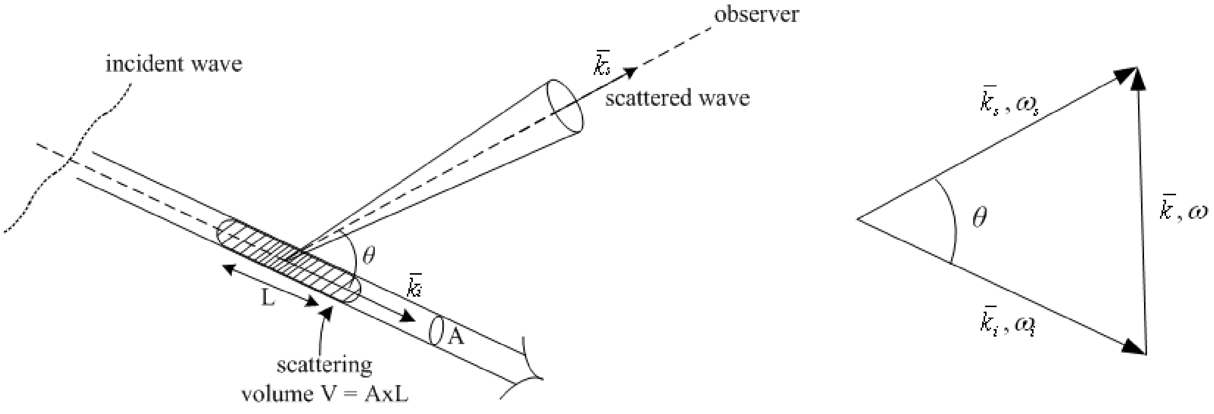

(a) (b)

Figure A.1 (a) Scheme of the Thomson scattering of electromagnetic radiation from a plasma of finite volume *V*. (b) Geometry of Thomson scattering interacting waves.

A few comments are necessary for the wave quantities (k, ω) of the electron density perturbation inserted in Eq. (A.1). The spatial variation of the electron density, in the observation direction θ and for constant time, is determined by the differential wavenumber k, which in fact is the spatial harmonic component of the density perturbation imposed by the incident electromagnetic field [2]. From Fig. A.2(b) it follows that this two quantities are related by the formula

$$k = (k_i^{\,2} + k_s^{\,2} - 2k_i k_s \cos\theta)^{1/2} \tag{A.3}$$

Because the scattered radiation in the direction θ results from the spatial variation of the electron density in this direction, Eq. (A.3) can be viewed as the dispersion equation of the medium–like plasma reaction to the incident electromagnetic radiation. In this approach θ is the dispersion angle along which the radiation scattering occurs, for a given perturbation k of the electron density. The time evolution of the electron density, at a given spatial point, is determined by the frequency ω, which is the time harmonic component of the imposed electron density perturbation. This time evolution reflects the double Doppler effect taking place due to the electron velocity with respect both to the frame of the incident electromagnetic wave, as well as to the frame of the observer.

Up to now, the problem of the radiation scattering has been considered in its most general form, as the interaction of an electromagnetic wave with a plasma showing a medium–like behavior, without investigating the conditions under which this behavior occurs. It can be proved that the mode of the plasma reaction on the incident wave is characterized by the following parameter [2] :

$$\alpha = \frac{1}{k\lambda_D} = \frac{\lambda}{2\pi\lambda_D} \tag{A.4}$$

The range of α is determined by the ratio of the wavelength λ of the electron density perturbation to the Debye length λ_D,

$$\lambda_D = \sqrt{\varepsilon_o k_B T / e^2 n_e} \tag{A.5}$$

and depending on its value two regimes of the radiation scattering may be discriminated :

(i). $\alpha << 1$: In this range, the length of the resultant perturbation λ is much less than λ_D. This means that the incident electromagnetic wave interacts with randomly distributed charges in a scale where each charge is not subjected to the shielding of the neighbor charges, and therefore it is seen as "free". The scattering in this regime is called *incoherent scattering*, and is determined by the sum of the radiations scattered independently by each single charge. The main characteristic of the incoherent scattering spectrum is that it reflects the shape of the electron velocity distribution. As this scattering regime is not used in our experiment we are not analyze it further here.

(ii). $\alpha \geq 1$: In this range, λ is comparable to, or greater than λ_D, and the incident electromagnetic wave interacts with charges which are additionally subjected to their mutual screening through the long range Coulomb forces. Due to this, the plasma shows a collective reaction on the perturbation imposed by the incident wave, and therefore it behaves like a medium. Radiation scattering from the plasma under these conditions is characterized as *coherent scattering*, and this is the regimes that holds in our experiment.

The spectral characteristics of the scattered radiation in the coherent regime are determined by the disturbances of the plasma particles density (electrons, ions) that are excited and propagated through the plasma. Assuming a collisionless plasma, with a Maxwellian velocity distribution of the plasma charges, there are two different mechanisms for the plasma waves excitation.

A. High perturbation frequencies, $\omega > \omega_{pi}$

For high perturbation frequencies $\omega > \omega_{pi}$ (ω_{pi}, the ion plasma frequency), the scattering is determined by the electrons behavior, as the much heavier ions can not respond at such high frequencies and may be viewed as an immobile neutralizing background. In this range, electron plasma waves are excited which presents a resonance frequency ω_{oe} given by the Bohm–Gross dispersion relationship [6] :

$$\omega^2{}_{oe} \cong \omega^2{}_{pe} + (3k_B T_e / m_e)k^2 = \omega^2{}_{pe}(1 + \frac{3}{\alpha^2}) \tag{A.6}$$

where k_B is the Boltzmann constant and T_e the electron temperature. Due to the resonance of the longitudinal electrons waves, the scattered power spectrum shows two resonance peaks at $\omega_s = \omega_i \pm \omega_{oe}$, which are called *electronic satellites*. As in the coherent regime $\alpha^2 >> 1$, in a first approximation we find from Eq. (A.6) that the resonance occurs at $\omega_{pe} = \sqrt{n_e e^2 / \varepsilon_o m_e}$. Thus, the shift of the peaks with respect to the frequency of the incident electromagnetic wave is proportional to the square root of the electron density. The above are shown in Figure A.2(a), where the scattered power spectrum of a Maxwellian collisionless plasma is given, which is obtained numerically with the spectral density function approach [2].

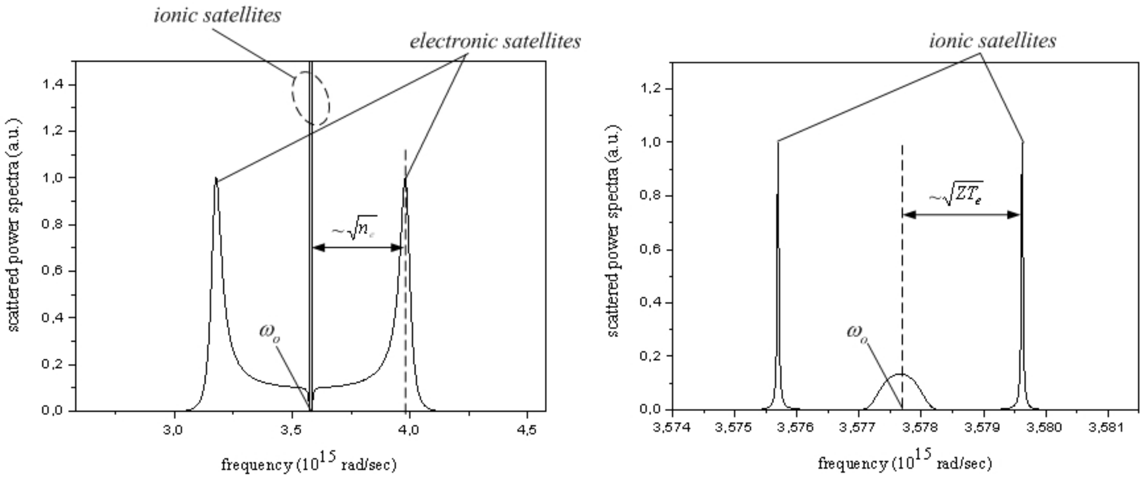

(a) (b)

Figure A.2 Scattered power spectra of a xenon plasma at two different ranges of the perturbation frequency : (a) $\omega > \omega_{pi}$ where appear the resonance peaks of the electron plasma waves ("electronic satellites"), and (b) $\omega \sim \omega_{pi}$ where appear the resonance peaks of the acoustic waves ("ionic satellites"). The curves were calculated using the spectral density function of a Maxwellian collisionles plasma (Typical values of the plasma parameters : T_e = 200 eV, T_i = 20 eV, Z = 26, $n_e = 3\text{x}10^{19}$ cm^{-3}).

B. Low perturbation frequencies, $\omega \sim \omega_{p\mathrm{i}}$

For low perturbation frequencies, $\omega \sim \omega_{p\mathrm{i}}$, the excitation of ion acoustic plasma waves takes place. In the case of a strongly non isothermal plasma, with $T_e >> T_i$, the ion acoustic waves show a resonance frequency

$$\omega_{ac}{}^2 \cong k^2(k_B(\frac{a^2}{1+a^2})\frac{\langle Z\rangle T_e}{m_i}+\frac{3k_BT_i}{m_i}) \tag{A.7}$$

or, in a first approximation at

$$\omega_{ac} \cong \upsilon_s k \tag{A.8}$$

where $\upsilon_s = \sqrt{\langle Z\rangle k_B T_e / m_i}$ is the sound velocity of the ion acoustic waves determined by the electrons temperature and the ionic mass [7]. Similarly with the electron plasma waves, in this spectral range the scattered power spectrum shows two peaks at $\omega_s = \omega_i \pm \omega_{ac}$ showing a shift with respect to ω_i which is proportional to $\sqrt{\langle Z\rangle T_e}$ (see Fig A.2(b)).

When the plasma electronic density is such that $\omega_{pe} << \omega_i$, the dispersion Eq. (A.2.a) and (A.2.b) give

$$\omega_i \approx k_i c \tag{A.9.a}$$

$$\omega_s \approx k_s c \tag{A.9.b}$$

Substituting Eq. (A.9) in the energy conservation law of Eq. (A.1.a) we obtain

$$k_s = k_i \pm k \frac{\upsilon_s}{c} \approx k_i \qquad \text{(A.10)}$$

due to the low value of the sound velocity ($\upsilon_s/c << 1$). With this approximation, Eq. (A.3) becomes

$$k \approx 2k_i \sin(\frac{\theta}{2}) \qquad \text{(A.11)}$$

The incident wavenumber k_i is given in terms of the critical density by the formula [3],

$$k_i = \frac{\omega_o}{c} \sqrt{1 - \frac{n_e}{n_{cr}}} \qquad \text{(A.12)}$$

where the critical density n_{cr} in practical units is

$$n_{cr}(cm^{-3}) = 1.110^{21} / \lambda_i(\mu m) \qquad \text{(A.13)}$$

Having determined the reduced value of k_i from Eq. (A.12), and thus the scattering wavenumber k from Eq. (A.11), Eq. (A.8) (or more accurately Eq. (A.7)) permits to determine the product $<Z>$ T_e of the electron temperature with mean ionization number. Thus, if one of these two parameters is independently known, the ionic scattering spectrum provides directly the other.

Appendix B Mach–Zehnder interferometry experiment

In this appendix we describe the Mach–Zehnder interferometer experiment performed in the gas–jet facility of the LULI laboratory, to characterize the neutral density profile of the gas–jet targets. The gas–jets are produced by the 1mm diameter output conical copper nozzle used in the xenon–krypton experiment.

The experimental setup is given in Figure B.1 [8]. A 532.5 nm wavelength He–Ne laser is expanded and collimated to a 1 cm diameter beam. The beam is splitted and propagates to the two optical arms of the Mach–Zehnder interferometer, with the gas–jet nozzle placed in one of them. The output beamsplitter, in conjunction with the *f/5* collecting lens, recombine the two beams in the entrance of an 8–bit CCD camera, where the produced interference fringes are recorded. The flow of the gas–jet is controlled by a solenoid electro–valve, which opens for a specific time interval when it is triggered. The duration of its operation has been measured independently with a Schlieren shadowgraph experiment, and was found ~ 140 ms. The backing pressure of the gas–jet is adjusted and measured with a pressure transducer, and the pressure of the vacuum chamber is fixed to be less than 10^{-2} mbar with the aid of a baratron sensor. The time evolution of the gas–jet is obtained using a 2 ms optical shutter. As the time response of the shutter is much less than the electro–valve duration, this is accomplished by changing the time delay of the shutter trigger to probe different times of the gas–jet evolution.

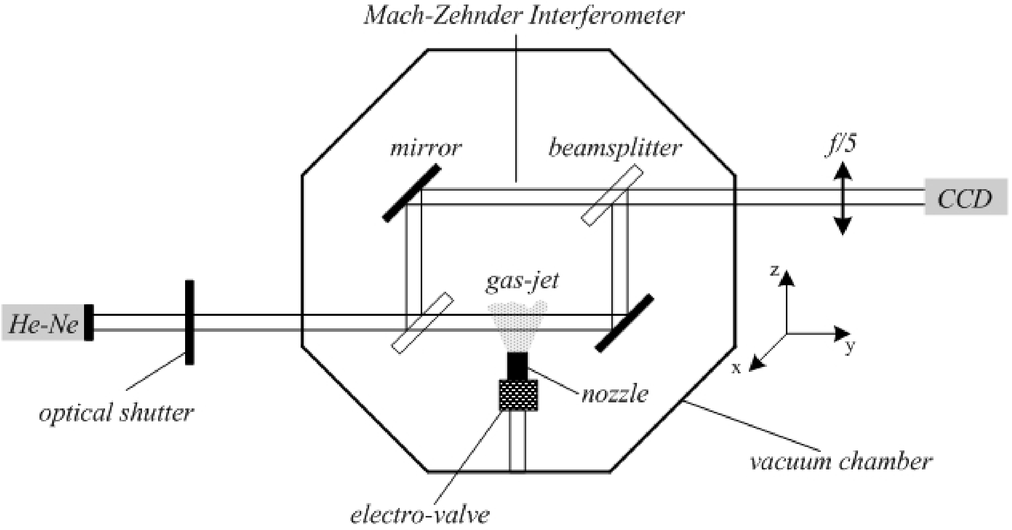

Figure B.1 Top view of the experimental setup used to characterize the density profile of the neutral gas–jet injected by a 1 mm diameter nozzle.

Initially, and when there is no gas flow, the Mach–Zehnder interferometer is regulated properly to gives the interference fringes shown in Fig. B.2(a). When the nozzle injects the gas–jet, the refractive index in the one arm, and along the optical path of the beam propagating through the gas–jet, is changed. This variation causes an additional phase shift to the beam propagating through the gas–jet, which has as result the displacement of the fringes pattern, as can be seen in Fig. B.2(b). The intensity of the interference pattern along the axis of the gas–jet flow (z–axis of Fig. B.2) is then written

$$I(z) = I_o[1 + \cos(\frac{2\pi z}{d} + \varphi(z))] \tag{B.1}$$

where *d* is the initial distance of the fringes, and *φ*(*z*) is the phase shift introduced by the gas–jet. Therefore, in a first step, by comparing the two fringes patterns it is possible to deduce *φ*(*z*) at each point along the perpendicular to the propagation direction of the laser beam (x–axis of Fig. B.2).

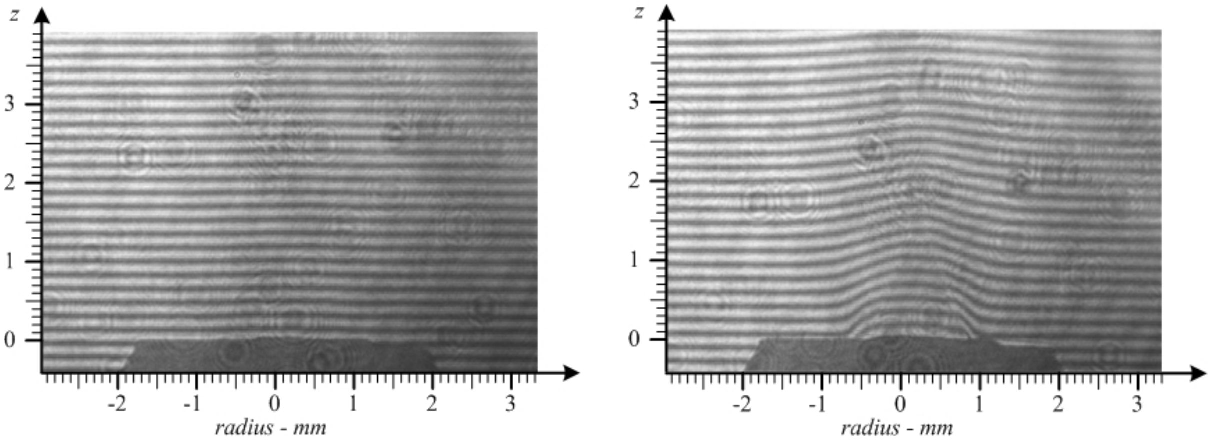

(a) (b)

Figure B.2 (a) Mach–Zehnder fringes pattern without gas–jet flow. (b) Shift of the fringes pattern due to the flow of 20 bar Ar gas–jet.

In terms of the gas–jet refractive index *n*(*r*), the difference of the phase shift between the two optical arms is given by the formula

$$\delta\varphi(x) = \frac{4\pi}{\lambda_o}\int_0^{s/2}[n(r)-1]dy \tag{B.2}$$

where λ_o is the wavelength of the laser beam, and the integration is taken along the optical path *s* of the beam propagating through the gas–jet (see Fig. B.3). In cylindrical coordinates the above formula becomes

$$\delta\varphi(x) = \frac{4\pi}{\lambda_o}\int_x^{r_0}\frac{[n(r)-1]rdr}{\sqrt{r^2-x^2}} \tag{B.3}$$

where r_0 is the gas–jet radius. Due to the cylindrical symmetry of the gas–jet flow, Eq. (B.3) can be solved in terms of (*n*(*r*) – 1) using the inverse Abel transform

$$\frac{2\pi[n(r)-1]}{\lambda_o} = -\frac{1}{\pi}\int_r^{r_o}\frac{d\varphi}{dx}\frac{dx}{\sqrt{x^2-r^2}} \tag{B.4}$$

Then the density distribution of the gas–jet can be calculated, as it is proportional to the gas refractive index, by the simple formula

$$\frac{N(r)}{N_o} = \frac{(n(r)-1)}{(n_o-1)} \tag{B.5}$$

where n_o is the refractive index and N_o the density of atoms at the standard temperature and pressure (for argon, $n_o = 1.000281$, and $N_o = 2.68 \times 10^{19}$ cm^{-3}).

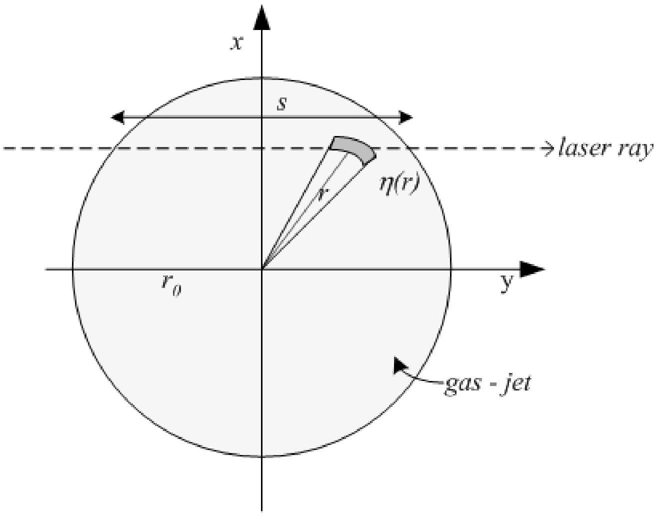

Figure B.3 Phase difference inserting the gas–jet in a laser ray propagating along a path *s* normal to the x–axis.

Fig. B.4 gives the density radial distributions obtained at a distance of 0.5 and 1 mm from the nozzle, for a 20 bar argon gas–jet. The density decreases with the distance, but it shows a similar parabolic profile as a function of the jet radius. At 1 mm distance from the nozzle and for an angular aperture of 1 mm diameter, which is determined by the random phase plate of the laser beam, the density varies between $9 \times 10^{18} - 3 \times 10^{19}$ cm^{-3}.

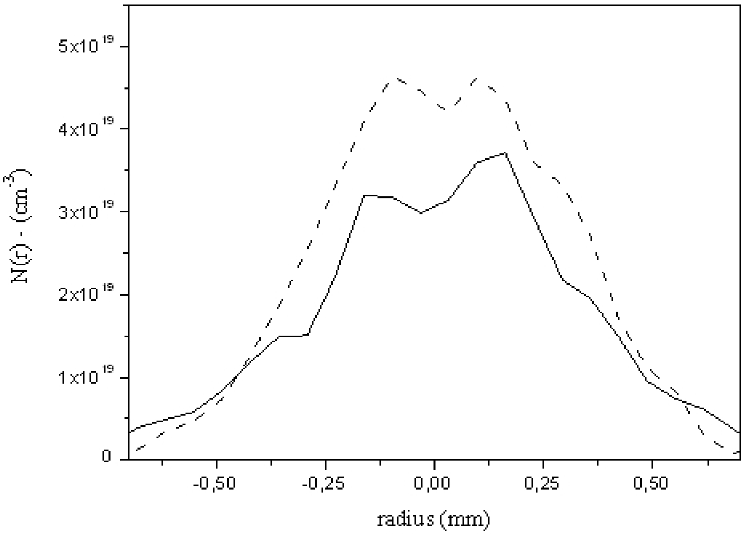

Figure B.4 Neutral density profile of 20 bars argon gas–jet at 0.5 (dashed line) and 1 mm (full line) distance from the nozzle.

References of Appendixes

[1] J. D. Jackson, Classical electrodynamics, Wiley, 1999.

[2] J. Sheffield, Plasma Scattering of Electromagnetic Radiation, Academic Press, 1975.

[3] S. H. Glenzer *et al.*, Thomson scattering from laser plasmas, Phys. Plasmas **6**, 2117 (1999).

[4] S. H. Glenzer, *et al.*, Ionization Balance in Inertial Confinement Fusion Hohlraums, Phys. Rev. Letters **87**, 045002 (2001).

[5] E. E. Salpeter, Electron Density Fluctuations in a Plasma, Phys. Rev. **120**, 1528 (1960).

[6] D. Bohm, E. P. Gross, Theory of Plasma Oscillations. A. Origin of Medium Like Behavior, Phys. Rev **75**, 1851 (1949).

[7] Y. L. Klimontovitch, The kinetic theory of electromagnetic processes, Springer 1983.

[8] V. Malka, *et. al.*, Characterization of neutral density profile in a wide range of pressure of cylindrical pulsed gas – jet, Rev. Sci. Instrum. **71**, 2329 (2000).

Appendix C Publications

C.I Analysis of the X-ray and time-resolved XUV emission of laser produced Xe and Kr plasmas

C.II Measurement of XUV-absorption spectra of ZnS radiatively heated foils

Available online at www.sciencedirect.com
ScienceDirect
High Energy Density Physics 3 (2007) 20–27
High Energy Density Physics
www.elsevier.com/locate/hedp

Analysis of the X-ray and time-resolved XUV emission of laser produced Xe and Kr plasmas

S. Bastiani-Ceccotti [a,*], N. Kontogiannopoulos [a], J.-R. Marquès [a], S. Tzortzakis [a], L. Lecherbourg [a], F. Thais [b], I. Matsushima [c], O. Peyrusse [d], C. Chenais-Popovics [a]

[a] *Laboratoire pour l'Utilisation des Lasers Intenses (LULI), Ecole Polytechnique, CNRS, CEA, UPMC; Route de Saclay, 91128 Palaiseau, France*
[b] *CEA/DSM/SPAM, Centre d'Etudes de Saclay, 91191 Gif-sur-Yvette Cedex, France*
[c] *National Institute of Advanced Industrial Science and Technology, Tsukuba 3058568, Japan*
[d] *CELIA, UMR 5107 Université Bordeaux 1-CEA–CNRS, 33405 Talence, France*

Abstract

A frequency-doubled laser beam of the Nd:glass kilojoule nanosecond LULI2000 facility (1.5 ns duration, 200–400 J energy, 0.53 μm wavelength) was focused on a Xe or Kr gas jet. The plasma was simultaneously diagnosed with X-ray (in the wavelength range of 6–8 Å for Kr and of 12–15 Å for Xe) and time-resolved XUV (20–200 Å) emission spectroscopy. Electron density and temperature as well as the ionization charge were measured by time-resolved Thomson scattering of the heating laser pulse. The spectra are compared with the calculations performed with the NLTE collisional-radiative code AVERROES/TRANSPEC. Best fits of the X-ray and XUV spectra obtained are presented. The measured charge distribution and dynamics is analyzed using the simultaneous Thomson scattering diagnostic.

PACS: 52.50.Jm; 52.25.Os; 32.70.Fw; 52.70.La

Keywords: Plasma spectroscopy; Non-LTE plasmas; High-Z plasmas; L-shell spectra; M-shell spectra; XUV emission

1. Introduction

Multicharged ions are present in hot dense plasmas and play a major role in radiation transport in stellar atmospheres and in inertial confinement fusion plasmas. High atomic number *Z*, multi-charged ion plasmas are also ideal for the production of bright X-ray sources. These high-*Z* plasmas are usually not in local-thermodynamic-equilibrium (NLTE) and are described by complex atomic physics models, which are the subject of much research and numerous discussions [1,2]. The primary reason is that calculation of complete spectra of high-*Z* elements by traditional detailed atomic structure codes coupled to population kinetics models incorporating several ions requires an unmanageably large number of transitions and energy levels. Thus, statistical approaches involving groupings of levels, e.g., configurations [3] and superconfigurations [4,5], prove to be very efficient when combined with the Unresolved Transition Array (UTA/SOSA) formalism [6] and/or the SuperTransition Array (STA) formalism [7]. Further, there are recent efforts to develop hybrid calculations mixing detailed levels and configurations [8,9]. In addition to, and in support of, the theoretical effort there is a need for experimental benchmarks from measurements of well-diagnosed plasmas [10–14].

In the present experiment, we attempt to create quasi-homogeneous, quasi steady-state, large scale (millimeter size) plasmas by focusing a nanosecond laser pulse into a gas jet. Both time-integrated X-ray and time-resolved XUV spectra emitted by plasmas of xenon and krypton were recorded. The Thomson scattering diagnostic provided the mean electron temperature and density of the plasma, and its average charge. In contrast to the previous studies performed with

---

[*] Corresponding author.
E-mail address: serena.bastiani@polytechnique.fr (S. Bastiani-Ceccotti).

1574-1818/$ - see front matter © 2007 Elsevier B.V. All rights reserved.
doi:10.1016/j.hedp.2007.01.004

the LULI facility [12–15], the simultaneous measurement of time-resolved XUV spectra is implemented here, and krypton spectra have been measured. Calculations performed with the AVERROES/TRANSPEC NLTE collisional-radiative superconfiguration code [5] are compared with experimental results.

2. Experimental setup

The experiment was performed on the LULI2000 facility where we focused a flat-top, 1.5 ns duration, frequency-doubled neodymium laser beam ($\lambda = 0.53$ μm) on a Xe ($Z = 54$) or Kr ($Z = 36$) gas jet, with a $f = 800$ mm lens coupled to a random phase plate (RPP) to obtain an elliptic focal spot of 1 mm (horizontal) × 150 μm (vertical) size, measured between the zeros of the intensity distribution function. The laser energy was varied from 100 to 400 J, corresponding to intensities from 0.5 to 2×10^{14} W/cm^2, respectively. The laser was focused at a distance of 750 μm from the exit plane of a 1 mm diameter supersonic gas nozzle. At this distance, the radial density profile of the gas jet, measured by Mach-Zehnder interferometry, has a super-Gaussian-like shape, with a 0.25 mm gradient at its border, followed by a 1 mm diameter homogeneous plateau. The horizontal width of the focal spot has been chosen to match the 1 mm diameter to minimize the reabsorption effects of a surrounding cold gas layer. On the other hand, the vertical size of the focal spot was chosen to minimize the effect of source broadening, so to optimize the spectral resolution of the Bragg crystal spectrograph. The gas jet backing pressure was varied from 1.3 to 7.0 bar, giving an ion density in the focal volume varying linearly with the pressure from 1.7 to 9.0×10^{18} cm^{-3}.

The laser energy absorption by the plasma was measured with a calorimeter set in front of the incident beam. The calorimeter was calibrated by measuring the beam energy without the gas jet, i.e. without absorption. The laser absorption increased from 28% to 55% when the gas pressure was varied from 1.3 to 7 bar. The laser–gas interaction region was monitored with an X-ray pinhole camera. We simultaneously recorded the time-integrated X-ray spectra in the keV range and the time-resolved XUV spectra emitted from the plasma at 90° from the laser axis. In previous experiments, it was demonstrated that the keV X-ray photons are emitted during the laser pulse and that the spectral shape of the emission remains almost the same for the duration of the laser pulse [12]. So, we measured the time-integrated keV emission with a double Bragg crystal spectrograph, composed by a TlAP crystal and an ADP crystal. The TlAP crystal recorded the 3d-4f transitions of xenon, in the 12–15 Å range, and the ADP crystal covered the 2–3 and 2–4 transitions of krypton, in the 6–8 Å range. The spectral resolution was 38 mÅ and 16 mÅ for the Xe and Kr spectra, which was limited by the 150 μm height of the laser focal spot, respectively. A vertical, 200 μm width slit in front of each crystal yielded a 330 μm spatial resolution along the laser axis. The spectra were registered on Kodak DEF films. Unlike the X-ray spectral measurement, time resolution is required to measure the XUV emission. Indeed, we previously observed that the XUV spectra have a strong time dependence as the plasma emits during the recombination phase that occurs after the laser pulse [13]. For gas jet experiments the use of a streak camera is complicated by the need for protection from the sudden pressure increase when the gas jet is triggered. To circumvent this we implemented a differential pumping system through a 500 μm width slit. The XUV spectra were measured in the 20–200 Å range with a 2000 l/mm transmission grating coupled to a 5.2 m radius spherical imaging nickel mirror. The resolution of the spectrograph was 2.5 Å, and the time resolution of the camera was around 50 ps.

The plasma electron density and temperature were obtained by the analysis of the Thomson self-scattering signal. The incident laser beam, backscattered at 135° from the laser propagation direction, was collected with a *f*/6 lens and relayed to two spectrometers coupled to streak cameras with temporal resolution better than 20 ps, one with a high (0.2 nm) spectral resolution to resolve the ionic component, and the other with a lower resolution (6.4 nm) to record the full electron component. The observed volume, defined by the collecting lens aperture and by the spectrometer and streak camera slits, was 50(height) × 200(width) × 300(depth) μm^3, and thus probed the heated plasma volume. Comparison between measured and theoretical spectra permits one to infer (i) the value of the product of the average charge by the electronic temperature ZT_e, from the ionic component, (ii) the electron density n_e from the electron component [16]. A few Mach-Zehnder interferometry measurements were performed with helium gas to determine the ion density at a given backing pressure, irrespectively of the nature of the gas.

3. Experimental results

3.1. Thomson self-scattering diagnostic

An example of the Thomson scattering raw data for xenon at 2 bar backing pressure and 120 J laser energy is displayed in Fig. 1a and b for the time-resolved ion and electron features. For the ion feature spectrum, we see the two satellites on both sides of the laser wavelength. The wavelength separation between the satellites is proportional to the ion sound velocity:

$$c_s \approx \sqrt{\frac{ZT_e}{m_i}\left(\frac{1}{1+(k\lambda_D)^2}+\frac{3T_i}{ZT_e}\right)}$$

where m_i is the ion mass, k the plasma perturbation wavenumber, λ_D the Debye length, and T_i the ionic temperature. In our experiment, the plasma and the diffusion geometry are such that $k\lambda_D < 1$ and $T_i \ll ZT_e$, then the separation is mainly dependent on ZT_e. Fig. 1a shows that the separation increases very rapidly (as ionization and temperature increase), with a rise time similar to that of the laser pulse (about 0.2 ns), and then remains constant during the laser pulse duration. For all the experiments we observed that the red satellite is brighter than the blue one. This can be explained by the presence of

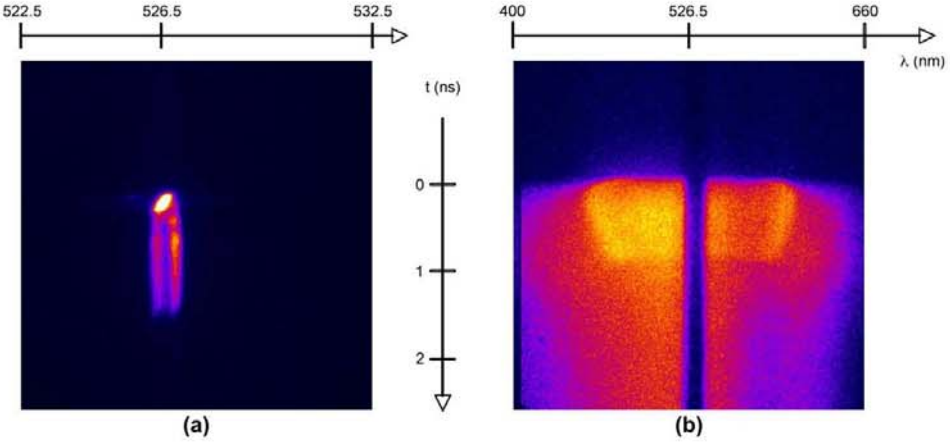

Fig. 1. Thomson self-scattering spectra measured on xenon (2 bar, 120 J). (a) Ionic satellites; (b) electronic satellites (the dark region in the middle of the spectrum corresponds to the ionic component attenuated by an interferential filter).

a Brillouin instability, or by a velocity drift of the electrons with respect to the ions (estimated to about 10^4 m/s).

On the electron feature spectrum, the dark region in the middle of the spectrum is centered on the laser wavelength and corresponds to the ion component, which is strongly attenuated by an interference filter placed at the spectrometer entrance. The separation between the maxima on both sides of this central region is proportional to the Bohm–Gross frequency:

$$\omega_{\mathrm{BG}} = \omega_{\mathrm{pe}}\sqrt{1+3(k\lambda_{\mathrm{D}})^2}$$

where ω_{pe} is the electron plasma frequency. One can see in Fig. 1b that at the beginning of the signal, the edges of the electron feature satellites separate very rapidly due to the rapid ionization of the plasma. Later in time, this separation slowly decreases due to a slow reduction of electron density. This reduction is typically of the order of 10^{19} cm^{-3}/ns, in good agreement with the expansion by thermal pressure. As several additional mechanisms modify the maximum and width of the satellites, the analysis of these spectra was performed with a parametric fit of the measured spectra using theoretical plots [13]. The experiments obtained for different laser energies and gas pressures of Xe and Kr gave the following parameters: $n_e = 0.2\text{–}1.2 \times 10^{19}$ cm^{-3}, $Z = 12\text{–}24$, $T_e = 160\text{–}500$ eV.

3.2. XUV spectroscopy

Typical streak camera images of the time-resolved XUV emission of xenon and krypton are shown in Fig. 2, for a gas pressure of 4 bar and a laser energy around 360 J. The wavelengths were calibrated using the Be filter K-edge and Al filter L-edge. The origin of the wavelength axis is the zero order of the grating. It is immediately obvious that the emission lasts longer than the 1.5 ns laser pulse. The time dependence is especially visible around 50 Å for xenon, where a bright structure disappears earlier than the rest of the spectrum. Previous calculations had shown that the xenon Co-like ions (Xe^{27+}) emit around 50 Å [15]. So, the present result shows that this highly ionized charge state disappears after about 1 ns. For krypton, the structures observed below 50 Å disappear at around 2 ns, i.e., more quickly than the rest of

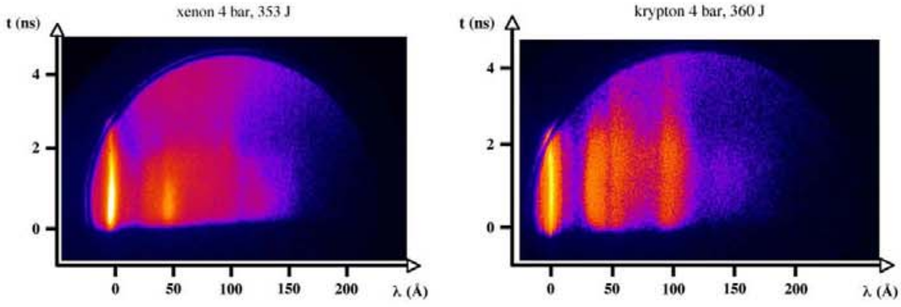

Fig. 2. XUV streaked images recorded for xenon and krypton at 4 bar gas pressure and about 360 J laser energy.

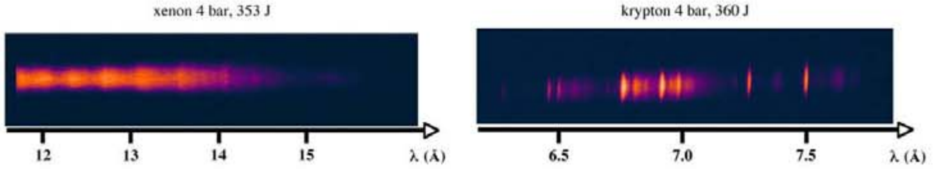

Fig. 3. Raw X-ray images recorded for xenon and krypton at 4 bar gas pressure and about 360 J laser energy. The vertical axis is the plasma image along the laser axis.

the spectrum. This behavior is expected, as the recombining plasma emits at lower photon energies.

3.3. keV X-ray spectroscopy

An example of the raw spectra obtained with the X-ray spectrograph is shown in Fig. 3, for same condition as shown in Fig. 2. We observe that the plasma is quite homogeneous in the laser propagation direction (vertical axis on the images). In Fig. 4 we present the lineouts of the X-ray spectra obtained at the center of the gas jet for different gas pressures and laser energies. The xenon spectrum is composed of 3d-4f Unresolved Transition Arrays emitted by different ion stages from Ni-like (Xe^{26+}) to V-like (Xe^{31+}). For krypton, the spectrum is dominated by the $n=2-3$ and $n=2-4$ transitions from Na-like (Kr^{25+}) to F-like (Kr^{27+}). For both elements one observes that the transition arrays intensity ratios follow the ionization, which increases with incident laser intensity and gas pressure, that are directly related to absorbed energy. The dependence with Kr gas pressure on the F-/Ne-like intensity ratios is especially clear in the 6.4–6.7 Å spectral range. For Xe, the spectra measured for 2 bar – 127 J and 1.3 bar – 420 J are very similar, showing that the absorbed laser energy is similar for these two different conditions. Further, the spectrum obtained for Xe, for 1.3 bar pressure and 420 J energy is very similar to the results of previous experiments [12]. It is important to note that there is a disagreement between the Z inferred from Thomson scattering and that extracted from the observed emission. This point is discussed further below in the text.

4. AVERROES/TRANSPEC calculations

We compare the measured XUV and X-ray spectra to *ab initio* calculations performed with the AVERROES/TRANSPEC (A/T) superconfiguration code [5]. AVERROES first calculates the collisional and radiative rates, and the superconfiguration energies. Second, these data are used in the collisional-radiative model TRANSPEC, which computes NLTE populations and generates synthetic spectra using given ion density and electron temperature. These parameters are provided, ideally, by the Thomson scattering (TS) diagnostic. To calculate the time evolution of the XUV emission, we assume a temporal profile for the electron temperature characterized by a fast rise, 0.2 ns, followed by a 0.25 ns duration plateau at the TS deduced value for the temperature, and then followed by a relatively slow decay, giving a total duration of 4.5 ns.

4.1. Xenon spectra

A typical result for the xenon case is plotted in Fig. 5. The dashed lines are the XUV spectra measured at different times during the plasma expansion, for an experiment having 2 bar backing pressure and 355 J laser energy. The spectra are then compared to the calculation from the A/T code, obtained with

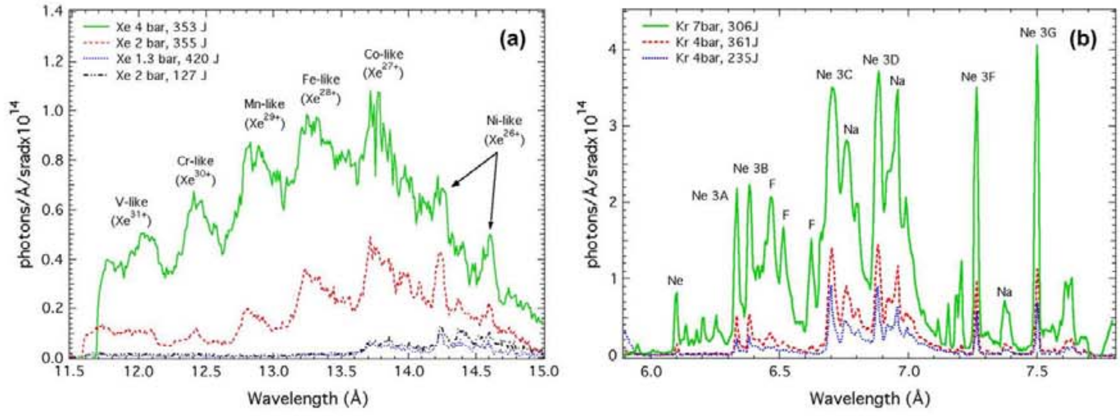

Fig. 4. X-ray spectra traced at the center of the gas jet, as a function of gas pressure and laser energy. (a) Xenon, and (b) krypton.

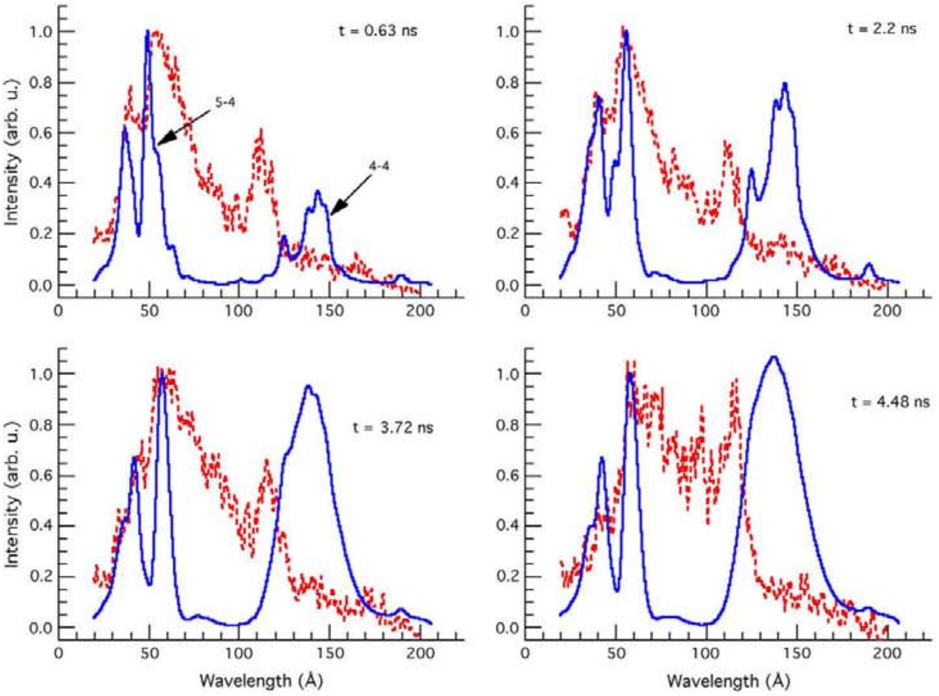

Fig. 5. Xenon XUV spectra recorded at different times, for 2 bar gas pressure and 355 J laser energy (dashed lines). The AVERROES calculations (full lines) are performed with the plasma parameters deduced by the TS diagnostic ($N_i = 2.57 \times 10^{18}$ cm^{-3} and $T_e = 330$ eV).

the TS deduced values for this shot ($N_i = 2.57 \times 10^{18}$ cm^{-3} and $T_e = 330$ eV). We observe that the agreement is better for the short wavelength part of the spectra. The relative intensity of the two 5–4 structures is well reproduced, although the width is underestimated. The situation is problematic on the long wavelength side of the spectra, where the code reproduces neither the experimental wavelengths of the 4–4 structures nor their intensity.

The experimental X-ray spectrum recorded for xenon at 4 bar and 350 J is compared to A/T calculations in Fig. 6. The experimental X-ray spectrum shows that Xe^{27+} and Xe^{28+} are the main ion stage emitting, in contradiction with the value of $Z = 24.3$ given by TS, which also yields $T_e = 390 \pm 40$ eV, and $n_e = (1.2 \pm 0.5) \times 10^{20}$ cm^{-3}. However, for an A/T calculation to generate the Xe^{26+} ionic species, which dominates the spectrum, requires a T_e of 600 eV. For all the recorded X-ray spectra, the ionization measured by TS seems to be systematically lower than that inferred from the ion stages observed in the spectra. We can also observe in Fig. 6 that the quite strong sensitivity of the calculated spectra on the electronic temperature allows a precision better than 10% on the best fit temperature value.

In Fig. 7, we show the XUV spectra at different times obtained on Kr, at 4 bar and 230 J compared with the A/T calculations. For the early times there is quite good agreement for the short wavelengths, whereas for later times the agreement is better on the long wavelength side. For the X-ray emission, Fig. 8, the theoretical fit is complicated by the inaccurate treatment of the optical depth of the Ne-like lines. The figure shows that the 6.5–7 Å region is well reproduced by the code, whereas for the shorter wavelengths the reabsorption is slightly underestimated, and it is overestimated for the longer wavelength region. As the spectrum has been calculated with the SOSA formalism, this disagreement could be due to a poor treatment of the coupling between the populations

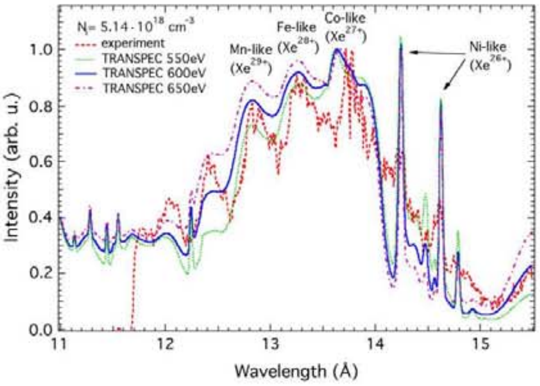

Fig. 6. Xenon X-ray spectrum recorded for 4 bar gas pressure and 350 J laser energy, compared with AVERROES/TRANSPEC calculations for 550 eV, 600 eV and 650 eV electronic temperatures ($N_i = 5.14 \times 10^{18}$ cm^{-3}).

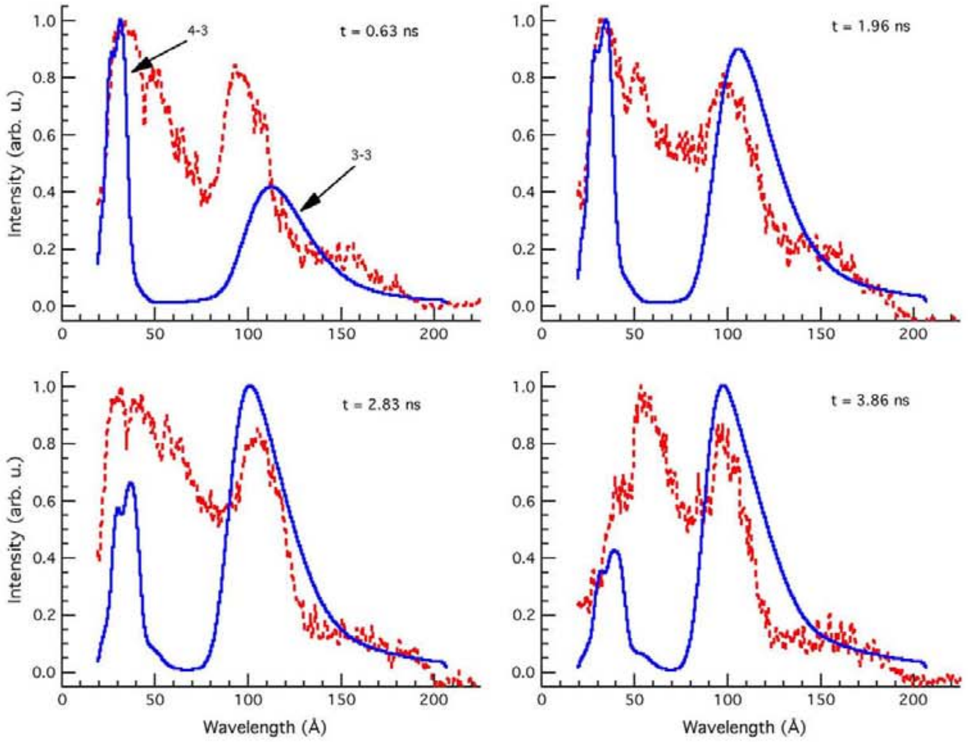

Fig. 7. Krypton XUV spectra at different times during the plasma evolution, for 4 bar gas pressure and 230 J laser energy (dashed lines). The AVERROES calculations (full lines) are performed using the TS deduced plasma parameters ($N_i = 5.12 \times 10^{18}$ cm^{-3}, $T_e = 170$ eV, and $Z = 23$).

and the radiation, which cannot be accurately treated within the SOSA approach. The use of a Detailed Level Accounting (DLA) approach coupled to a proper treatment of line transfer [17] might provide better results. It has to be stressed that, as in the case of Xe, the X-ray spectrum has been calculated using a temperature value (500 eV) higher than that measured with the TS diagnostic (170 eV).

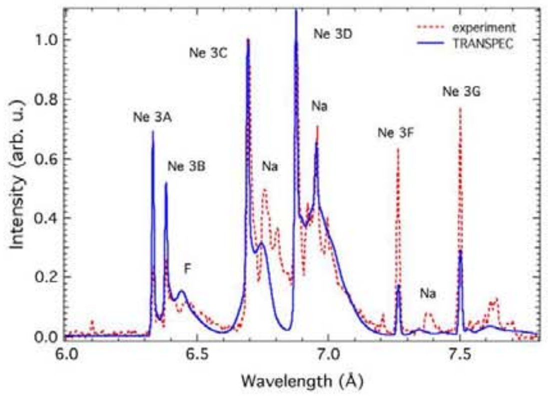

Fig. 8. Krypton X-ray spectrum recorded on the same shot than the XUV spectra in Fig. 7 (4 bar, 230 J), compared with AVERROES/TRANSPEC calculations for $N_i = 5.12 \times 10^{18}$ cm^{-3} and $T_e = 500$ eV.

5. Discussion

A first step to improve the agreement between calculated and measured XUV spectra consists of using a hydrodynamic code to obtain a more accurate description of the plasma parameter evolution as a function of time. The difficulty is the 3D character of the irradiation geometry. However, as a start, we have performed 1D simulations using the MULTI hydrocode [18]. In Fig. 9 we show the temperature profile as a function of time obtained with MULTI in the case of Xe, at 2 bar and 355 J, compared to the profile used to obtain the previous analysis shown in Fig. 5.

Fig. 10 shows the spectra obtained using the MULTI temperature profile in the TRANSPEC calculations, compared to the previous calculations. The width of the short wavelength structure and the shift of the long wavelength structure towards slightly shorter wavelengths yield better agreement with the experimental data. This provides encouragement to use 2D or 3D hydrodynamic simulations of the plasma.

The disagreement between the observed X-ray emission and the TS *Z* requires discussion. A first hypothesis to explain the discrepancy is that the homogeneity of the plasma is not

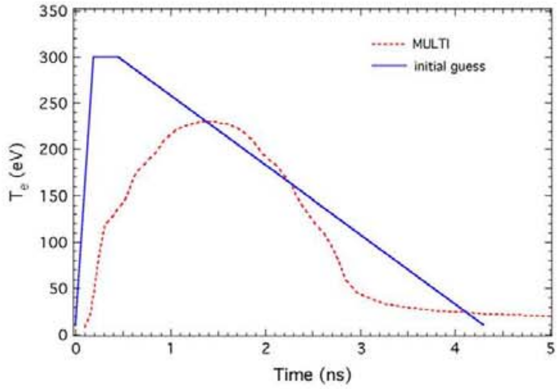

Fig. 9. Temperature profile issued from the MULTI simulation for the case of xenon, at 2 bar pressure, irradiated with 355 J laser energy, compared to the temperature profile used in the simulations of Fig. 5.

achieved in the experiment. The far-field intensity distribution of an RPP has, in general, an intensity envelope, which is essentially an Airy function, superimposed to a fine speckle pattern [19]. If this intensity pattern impinges on a solid target, the thermal conduction is sufficiently high to smooth the intensity of the speckle pattern. On the other hand, for a gas target the thermal conduction may be too small to obtain such a smoothing [20]. In this case, the plasma behaves like a “bath” with given average electron temperature and density, with hot spots, generated by the speckles of the RPP. In this case, the XUV radiation, which is emitted by the whole plasma, is representative of a lower average temperature than the X-ray keV radiation, which is emitted only by the hot spots. If this hypothesis is correct, then the agreement between the XUV and the TS diagnostics could be due to the relatively large plasma region investigated by the TS diagnostic. The large widths of the TS satellites could confirm this scenario.

6. Conclusions and future work

Xenon and krypton X-ray and XUV spectra were recorded to benchmark atomic physics codes such as AVERROES in non-LTE conditions. Electronic and ionic Thomson scattering provided the measurement of electron and ion density, electron temperature and average ionization. An XUV streak camera was operated for gas pressures lower than 10 bar, using a differential pumping system. The dependence of spectra on laser intensity and gas pressure is in general agreement with the laser heating conditions of the gas jet.

Our data clearly show that the XUV emission vary in time, so the time resolution for this diagnostic is necessary. The spectra show that the ionization increases with pressure and

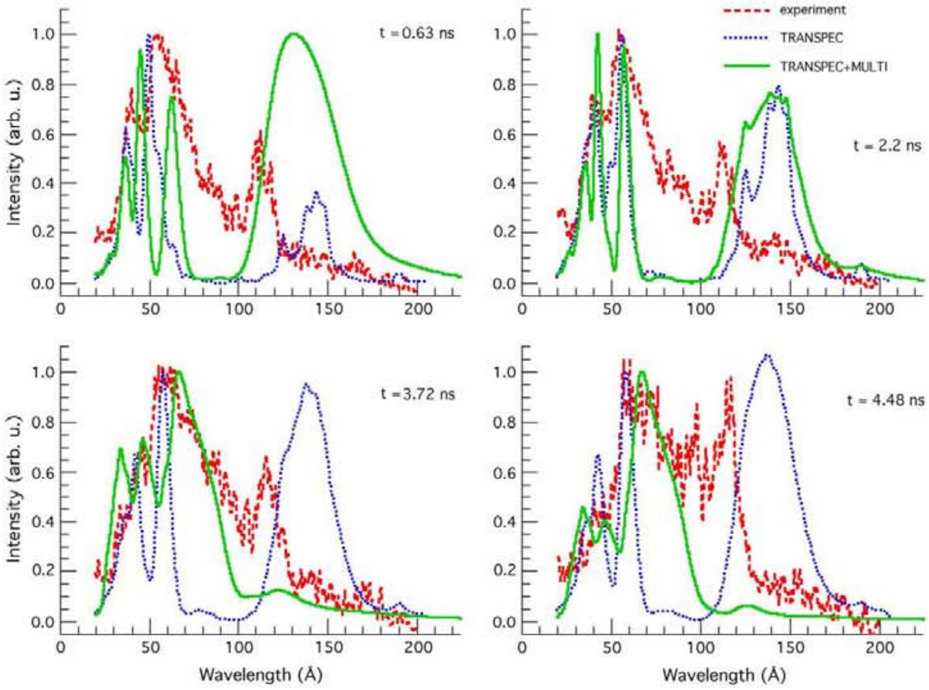

Fig. 10. Xenon XUV spectra measured for 2 bar gas pressure and 355 J laser energy (dashed lines) compared with the AVERROES/TRANSPEC calculations (full lines) performed using the MULTI temperature profile of Fig. 9. To the sake of a better comparison, the figure shows again (dotted lines) the same A/T calculations of Fig. 5.

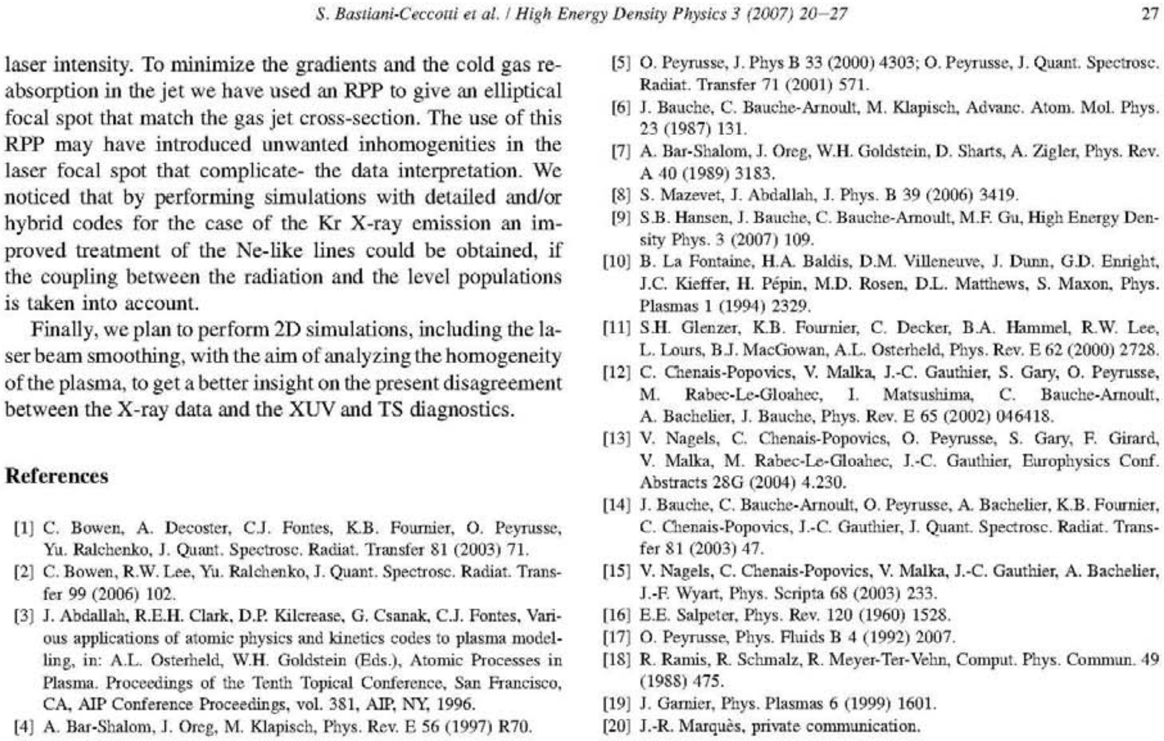

laser intensity. To minimize the gradients and the cold gas reabsorption in the jet we have used an RPP to give an elliptical focal spot that match the gas jet cross-section. The use of this RPP may have introduced unwanted inhomogenities in the laser focal spot that complicate- the data interpretation. We noticed that by performing simulations with detailed and/or hybrid codes for the case of the Kr X-ray emission an improved treatment of the Ne-like lines could be obtained, if the coupling between the radiation and the level populations is taken into account.

Finally, we plan to perform 2D simulations, including the laser beam smoothing, with the aim of analyzing the homogeneity of the plasma, to get a better insight on the present disagreement between the X-ray data and the XUV and TS diagnostics.

References

[1] C. Bowen, A. Decoster, C.J. Fontes, K.B. Fournier, O. Peyrusse, Yu. Ralchenko, J. Quant. Spectrosc. Radiat. Transfer 81 (2003) 71.

[2] C. Bowen, R.W. Lee, Yu. Ralchenko, J. Quant. Spectrosc. Radiat. Transfer 99 (2006) 102.

[3] J. Abdallah, R.E.H. Clark, D.P. Kilcrease, G. Csanak, C.J. Fontes, Various applications of atomic physics and kinetics codes to plasma modelling, in: A.L. Osterheld, W.H. Goldstein (Eds.), Atomic Processes in Plasma. Proceedings of the Tenth Topical Conference, San Francisco, CA, AIP Conference Proceedings, vol. 381, AIP, NY, 1996.

[4] A. Bar-Shalom, J. Oreg, M. Klapisch, Phys. Rev. E 56 (1997) R70.

[5] O. Peyrusse, J. Phys B 33 (2000) 4303; O. Peyrusse, J. Quant. Spectrosc. Radiat. Transfer 71 (2001) 571.

[6] J. Bauche, C. Bauche-Arnoult, M. Klapisch, Advanc. Atom. Mol. Phys. 23 (1987) 131.

[7] A. Bar-Shalom, J. Oreg, W.H. Goldstein, D. Sharts, A. Zigler, Phys. Rev. A 40 (1989) 3183.

[8] S. Mazevet, J. Abdallah, J. Phys. B 39 (2006) 3419.

[9] S.B. Hansen, J. Bauche, C. Bauche-Arnoult, M.F. Gu, High Energy Density Phys. 3 (2007) 109.

[10] B. La Fontaine, H.A. Baldis, D.M. Villeneuve, J. Dunn, G.D. Enright, J.C. Kieffer, H. Pépin, M.D. Rosen, D.L. Matthews, S. Maxon, Phys. Plasmas 1 (1994) 2329.

[11] S.H. Glenzer, K.B. Fournier, C. Decker, B.A. Hammel, R.W. Lee, L. Lours, B.J. MacGowan, A.L. Osterheld, Phys. Rev. E 62 (2000) 2728.

[12] C. Chenais-Popovics, V. Malka, J.-C. Gauthier, S. Gary, O. Peyrusse, M. Rabec-Le-Gloahec, I. Matsushima, C. Bauche-Arnoult, A. Bachelier, J. Bauche, Phys. Rev. E 65 (2002) 046418.

[13] V. Nagels, C. Chenais-Popovics, O. Peyrusse, S. Gary, F. Girard, V. Malka, M. Rabec-Le-Gloahec, J.-C. Gauthier, Europhysics Conf. Abstracts 28G (2004) 4.230.

[14] J. Bauche, C. Bauche-Arnoult, O. Peyrusse, A. Bachelier, K.B. Fournier, C. Chenais-Popovics, J.-C. Gauthier, J. Quant. Spectrosc. Radiat. Transfer 81 (2003) 47.

[15] V. Nagels, C. Chenais-Popovics, V. Malka, J.-C. Gauthier, A. Bachelier, J.-F. Wyart, Phys. Scripta 68 (2003) 233.

[16] E.E. Salpeter, Phys. Rev. 120 (1960) 1528.

[17] O. Peyrusse, Phys. Fluids B 4 (1992) 2007.

[18] R. Ramis, R. Schmalz, R. Meyer-Ter-Vehn, Comput. Phys. Commun. 49 (1988) 475.

[19] J. Garnier, Phys. Plasmas 6 (1999) 1601.

[20] J.-R. Marquès, private communication.

Available online at www.sciencedirect.com

ScienceDirect

High Energy Density Physics 3 (2007) 149–155

High Energy Density Physics

www.elsevier.com/locate/hedp

Measurement of XUV-absorption spectra of ZnS radiatively heated foils

N. Kontogiannopoulos [a,*], S. Bastiani-Ceccotti [a], F. Thais [b], C. Chenais-Popovics [a], P. Sauvan [c], R. Schott [a], W. Fölsner [d], Ph. Arnault [e], M. Poirier [b], T. Blenski [b]

[a] *Laboratoire pour l'Utilisation des Lasers Intenses, CNRS UMR7605, Ecole Polytechnique, 91128 Palaiseau, France*
[b] *DSM/DRECAM/SPAM, CEA-Saclay, 91191 Gif-sur-Yvette Cedex, France*
[c] *Departamento de Ingeniería Energética, UNED, Juan del Rosal 12, 28040 Madrid, Spain*
[d] *Max-Planck Institut für Quantenoptik, Garching, Germany*
[e] *Centre DAM-Ile-de-France, BP 12, 91680 Bruyères-le-Châtel, France*

Abstract

Time-resolved absorption of zinc sulfide (ZnS) and aluminum in the XUV-range has been measured. Thin foils in conditions close to local thermodynamic equilibrium were heated by radiation from laser-irradiated gold spherical cavities. Analysis of the aluminum foil radiative hydrodynamic expansion, based on the detailed atomic calculations of its absorption spectra, showed that the cavity emitted flux that heated the absorption foils corresponds to a radiation temperature in the range 55–60 eV. Comparison of the ZnS absorption spectra with calculations based on a superconfiguration approach identified the presence of species $Zn^{6+}-Zn^{8+}$ and $S^{5+}-S^{6+}$. Based on the validation of the radiative source simulations, experimental spectra were then compared to calculations performed by post-processing the radiative hydrodynamic simulations of ZnS. Satisfying agreement is found when temperature gradients are accounted for.

PACS: 52.50.Jm; 52.25.Os; 52.70.La

Keywords: XUV absorption spectroscopy; Laser produced plasma; X-ray heated plasma; LTE-plasma; Plasma mixture

1. Introduction

The energy exchange in stellar interiors is dominated by radiative transfer, which is determined by the absorption of medium-Z elements, even though they represent only a small fraction of the stellar mass [1,2]. This stems from the strong absorption structures of medium-Z elements in the X-ray and XUV range that match the Planckian spectrum of the radiated flux. Further, the study of absorption coefficients is of great interest for the indirect scheme of inertial confinement fusion, where the deposited energy is dominated by the radiative properties of the atomic species used in hohlraums and pellets layers [3].

In the present experiment the absorption coefficients of zinc sulfide (ZnS) and aluminum plasmas in local thermodynamic equilibrium (LTE) conditions were characterized by measurements of their absorption spectra. ZnS and Al foils were heated by the radiation emitted by a gold spherical cavity. The ZnS absorption spectra were analyzed by comparing the experimental measurements with the theoretical predictions of the SCO atomic physics code [4,5], based on the superconfiguration approximation [6].

Measurements of the absorption spectra of plasma mixtures are timely and important as they can provide benchmarks for recently developed theoretical models [7]. Such models are of particular interest especially in astrophysics

---

* Corresponding author.
E-mail address: kontogia@greco2.polytechnique.fr (N. Kontogiannopoulos).

1574-1818/$ - see front matter © 2007 Elsevier B.V. All rights reserved.
doi:10.1016/j.hedp.2007.02.011

where plasma mixtures dominate stellar behavior. The compound ZnS was chosen because the sulfur $n = 2–3$ and zinc $n = 3–4$ transitions, where n is the principal quantum number, lie in the same spectral region and do not overlap. Finally, the Al study was performed because its absorption spectra have been previously measured [8,2] and as a low-Z element its absorption spectra can also be accurately predicted by detailed atomic physics codes such as HULLAC [9,10]. Thus, it provides an independent means of inferring the foil temperature achieved under the specific experimental conditions.

2. Experimental setup and methods

2.1. Experimental setup

The experiment was performed at the LULI2000 laser facility, where two frequency-doubled ($\lambda = 0.53$ μm), 500 ps pulse duration, Nd-glass laser beams were used. A schematic of the experimental setup is given in Fig. 1. The first beam, hereafter called the "main beam", heated the spherical gold cavity. It was focused with a $f = 800$ mm lens coupled with a random phase plate (RPP) to obtain a 500 μm diameter FWHM focal spot at the entrance hole of the cavity. The energy of the main beam at 0.53 μm wavelength was ~130 J giving an average intensity of 1.3×10^{14} W/cm^2.

A 1.2 mm diameter spherical gold cavity was used for the radiative heating of the absorption foils. The main beam heated a 130 nm thick gold foil located at the entrance hole of the cavity (∅ 700 μm). The radiation emitted from the back side of this foil was absorbed by the wall of the cavity producing a plasma layer on its interior, which then emitted radiation that was confined in the cavity. An absorption foil placed on one of the two diagnostic holes (∅ 250 μm) was heated by the radiation emitted from the cavity and by the directly-irradiated Au foil.

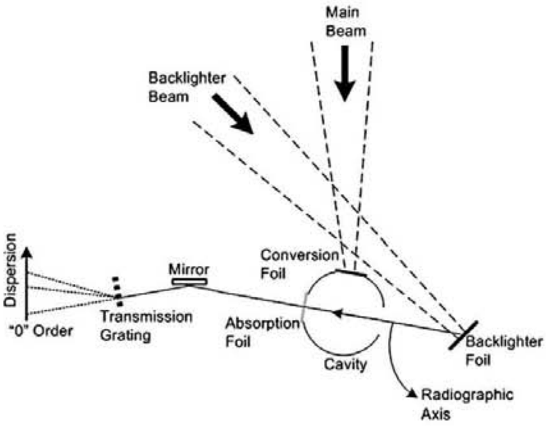

Fig. 1. Experimental setup for the absorption measurement of ZnS foils heated by the X-rays radiative emission of a gold cavity.

Two foils thicknesses were used: 48.9 nm or 97.8 nm for ZnS and 74 nm or 148 nm for Al, which correspond to 20 and 40 μg/cm^2 areal mass, respectively. The absorption foils of both types were coated on both sides with 35.3 nm thick carbon tampers corresponding to 8 μg/cm^2 areal mass. The tampered configuration was used to reduce the density and temperature gradients along the plasma expansion axis, and thus to improve the homogeneity of the probed plasma [11].

The second laser beam, delivering an energy of 30 J at 0.53 μm wavelength – hereafter called the "backlight beam", or BL beam – was focused on a 20 μm thick gold foil to produce a XUV absorption source, or backlight, used to probe the radiatively heated foils. The backlight producing gold foil was placed at a distance of 3 mm from the cavity to prevent the heating of the absorption foils. The BL beam was delayed by 800 ps with respect to the main beam. This delay ensures that the absorption probing occurs late enough to minimize the temperature gradient of the target plasma introduced by its hydrodynamic expansion, but early enough to prevent the plasma obscuring the line of sight along from the BL to the spectrometer defined by the cavity diagnostic holes (see Fig. 1). Furthermore, with this delay, the probing occurs when the radiative emission of the cavity is small, being on the order of the background level.

Both laser focal spots were monitored using two X-ray pinhole cameras. The backlight spectra were time-resolved using an XUV spectrograph coupled with a X-ray streak camera. The spectrograph was composed of a 2000 lines/mm gold transmission grating with a Ni spherical mirror with curvature radius 5200 mm. The mirror was placed with a grazing incidence angle of 6.4° to reject the energetic X-ray photons with wavelengths below 20 Å. Due to the spectrograph dispersion, the streak camera recorded photons up to 200 Å. Thus, the spectrograph covered the spectral range 20–200 Å with a resolution of 2.4 Å. The time resolution provided by the streak camera was 50 ps.

2.2. Backlighter spectrum characterization

Fig. 2 shows a raw time-resolved spectrum of a 20 μg/cm^2 Al absorption foil. The weak spectral feature emitted first corresponds to the self-emission of the cavity transmitted by the foil, while the second feature corresponds to the transmitted backlighter emission. The backlight spectra were obtained from the streak images with temporal average corresponding

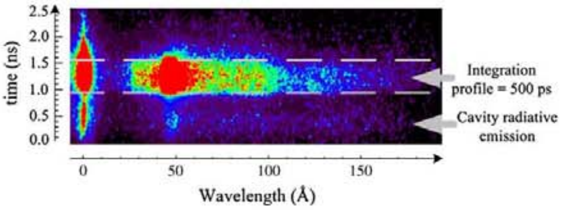

Fig. 2. Time-resolved Al XUV-absorption image recorded on the streak camera.

to an integration of 500 ps, in order to minimize the noise on the measured spectra.

As the spectra of the backlight and of the backlight absorbed by the foil were measured in different experiments, it was necessary to normalize the absorption spectra to the spectra of the backlight used in each shot and scaled from the laser energy. The gold emission is characterized by a fairly flat spectrum without discrete emission lines, except for a broad structure in the region around 50 Å (O – band transitions). The normalization was performed taking into account the linear dependence of the spectral intensity level as a function of the BL laser energy. The spectral range for the analysis was limited to 55–125 Å, as the O-band structure below 55 Å had a strong non-linear dependence on the BL laser energy, and the BL emission level was too low above 125 Å.

2.3. Method of analysis of the spectra

ZnS and Al spectra were analyzed by comparison of the experimental spectra with the results of the codes SCO [4,5,7] and HULLAC [9], respectively, used to post-process the output of the radiative hydrodynamic code MULTI [12]. The detailed atomic physics code HULLAC provides the transmission of individual ion stages. HULLAC uses the energy levels and the oscillator strengths for each single ion species calculated and tabulated by RELAC, which is based on the relativistic parametric potential method [10]. Then the plasma transmission is calculated using a Saha–Boltzmann distribution of the ion populations for the conditions provided by MULTI.

On the other hand, the version of SCO used here is based on the statistical theory for the description of the super-transition arrays in LTE plasmas [4–7]. SCO can calculate the absorption and transmission spectra of all elements separately as well as the total absorption and transmission spectrum of the mixture. The ion-in-cell model [4-6] is used for all elements in the mixture so that all the ions are screened by a plasma having the same electron density [7]. In the present work, the Thomas–Fermi model of mixtures is used self-consistently to find the effective mass density of each element corresponding to the free electron density. The ions of the mixture and of the carbon tamper are represented by hundreds of superconfigurations, the structure of which are calculated self-consistently in a neutral atomic sphere corresponding to the effective mass density of the element [4,5]. The absorption spectra are calculated separately for each superconfiguration and the total absorption spectrum is the sum over all superconfiguration weighted by their relative probabilities [4,5,7]. For each superconfiguration SCO does not calculate detailed lines but uses instead a statistical approach both for terms [13] and for configurations [4–7] resulting in unresolved absorption structures (UTA or SOSA). For each one-electron transition between two configurations a continuous envelope with the UTA or SOSA width and center of gravity represents the array of corresponding detailed lines. These envelopes are averaged over all configurations belonging to the superconfiguration [4–6]. The orbital relaxation corrections have been included for all relevant transitions [5].

The determination of the hydrodynamic parameters, used by SCO and HULLAC, necessitates two simulations with the code MULTI because the radiative heat flux driving the absorption foil and the associated radiative temperature are not known. In a first simulation, the laser irradiated conversion foil expansion and the radiative flux emitted at the rear of this foil are calculated. Then the theoretical model proposed by Basko [14] is used to determine the energy balance in the cavity, which provides the radiative flux that heats the absorption foil. A second simulation is then performed to calculate the hydrodynamic behavior of the absorption foil. Aluminum spectra are used here to check the validity of the method and the evaluation of the radiative flux heating the absorption foil.

3. Determination of the heating radiative flux from the analysis of the Al spectra

3.1. Al absorption spectra

The analysis was performed for a 20 μg/cm^2 areal mass Al foil, where the main laser beam flux was 1.4 × 10^{14} W/cm^2 at 0.53 μm. The experimental absorption spectrum averaged over the probing pulse duration is given in Fig. 3 where the dominant transitions are due to the 2p–3d transitions of Al^{7+} to Al^{5+}, at 68, 76 and 88 Å, respectively. The Al^{5+} 2p–3s transitions are observed at 105 and 110 Å. The NIST tables [15] suggest that the transition close to 96 Å may originate in Al^{6+} 2p–3s transitions, but the HULLAC transitions strengths are weak for these lines, so additional spectroscopic data would be useful. This ionization distribution, broader than those in previous works [8], suggests the presence of gradients – most likely in the temperature – in the heated Al.

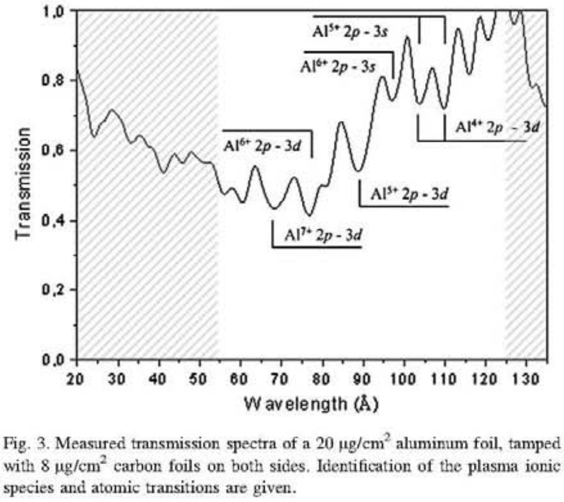

Fig. 3. Measured transmission spectra of a 20 μg/cm^2 aluminum foil, tamped with 8 μg/cm^2 carbon foils on both sides. Identification of the plasma ionic species and atomic transitions are given.

3.2. Calculation of the radiation flux heating the aluminum foil

The Basko model, used to calculate the cavity heating and flux on the Al foil, is based on the modified asymptotic self-similar solution for the heating of a planar medium, in conjunction with a view factor approach for the description of the energy balance inside the cavity [14,16–18].

The X-ray flux emitted at the rear of the conversion foil was calculated in a first simulation with MULTI. A 130 nm thick gold foil was heated on one side (front) by a Gaussian laser pulse of 500 ps duration and 1.4×10^{14} W/cm^2 flux at 0.53 μm wavelength. This radiative flux was then used as an input to the Basko model, where the reemission factor (albedo) of the cavity wall was found equal to 0.3. Taking into account the view factors between the absorption foil, the conversion foil and the cavity wall, the flux emitted by the cavity wall heating the absorption foil was estimated to be 2% of the total flux emitted by the conversion foil, while 4% of the total flux emitted by the conversion foil directly heats the absorption foil, i.e., twice the flux emitted by the cavity which is comparable to the results reported in Ref. [19]. The total heating flux, characterized by the sum of the two fluxes, corresponds to 6% of the total flux emitted by the conversion foil. The equivalent temperature of the total incident flux on the absorption foil corresponds to a radiative temperature of 60 eV. Note that the spectrum emitted by the conversion foil deviates from a Planckian distribution so that an equivalent temperature is a valid concept for the total flux only and not for its spectral distribution [11,20].

3.3. Hydrodynamic simulation of the aluminum foil expansion

To simulate with MULTI the hydrodynamic expansion of the Al foil, the X-ray emission from the rear of the gold foil calculated above was used as the heating source. This choice was justified because the contribution of the conversion foil flux is dominant for the heating of the absorption foil. Furthermore, it permits one to account for the spectral distribution of the heating radiation to give a more accurate simulation than that using a Planckian source [11,20]. To this end, 6% of the X-ray flux emitted at the back side of a 130 nm thick gold foil, obtained by MULTI for a 500 ps duration Gaussian pulse with 1.4×10^{14} W/cm^2 flux at 0.53 μm wavelength, was used to irradiate a 20 μg/cm^2 Al foil, coated on each side with 8 μg/cm^2 carbon tampers. In Fig. 4 are the electron temperature and the matter density as a function of the Lagrangian mass at three times corresponding to the rising half-maximum (1.2 ns), maximum (1.4 ns) and falling half-maximum (1.7 ns) of the probing pulse. Those profiles cover the measurement integration interval of 500 ps, and permit one to follow the temporal evolution and spatial distribution of the hydrodynamics. We observe in Fig. 4(a) that the temperature spatial gradients of Al are initially large (22–30 eV at 1.2 ns and 20–28 eV at 1.4 ns) and smooth out as time evolves (18–23 eV at 1.7 ns). In Fig. 4(b), we see that the matter density spatial variations are 3–6 mg/cm^3 at 1.2 ns, 2.5–4 mg/cm^3 at 1.4 ns, and 2–3 mg/cm^3 at 1.7 ns.

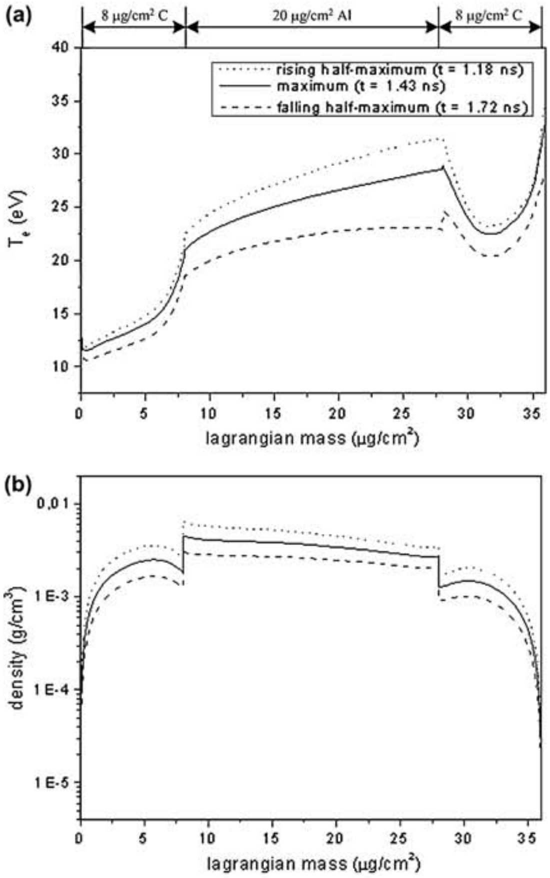

Fig. 4. Multi-simulation results of a 20 μg/cm^2 aluminum foil tamped with 8 μg/cm^2 carbon foils on both sides. (a) Electron temperature and (b) density as function of Lagrangian mass at the rising half-maximum (1.2 ns), at the maximum (1.4 ns) and at the falling half-maximum (1.7 ns) of the probing pulse.

3.4. Calculation of aluminum absorption spectra – comparison with the measured absorption

The hydrodynamic parameters of the Al foil given by MULTI were used to calculate *ab initio* the Al absorption spectra with the detailed code HULLAC. The spatial variation of the Al electron temperature was represented by dividing each time profile into a number of constant temperature cells using discrete steps of 2 eV. Because calculations with HULLAC showed that the matter density does not affect significantly the structures of the absorption of Al, a mean value of 2 mg/cm^3 was used as a first approximation. The carbon foils introduce only a lowering of the transmission due to the continuum absorption. Their contributions were taken into account to provide an absolute value of the absorption. Thus, for the tampers the spatial variation of their electron temperature was discretized using 4 eV steps, while their matter density was fixed to a mean value of 1 mg/cm^3. Then, the total transmission for each time profile was calculated by the product:

$$\tau(t_n) = \prod_i \mathrm{e}^{-K_i \sigma_i}$$

where $K_i(\rho, T_i)$ is the opacity of the i-th spatial cell given by HULLAC for the mean density ρ and the cell constant temperature T_i; σ_i is the i-th cell areal mass, and the product includes both Al and carbon cells. The temporal variation, for the interval covering the time integration of the measured absorption, was approximated by calculating the average of the three time profiles using the formula:

$$\bar{\tau} = \frac{1}{3}\sum_{n=1}^{3} \tau(t_n)$$

where the time profiles are considered at $t = 1.2$ ns, 1.4 ns and 1.7 ns, respectively.

The averaged transmission is shown in Fig. 5 together with the measured transmission. The theoretical transmission reproduces with good accuracy the measured structures corresponding to the Al^{5+} and Al^{6+} transitions identified in Fig. 5. However, below 75 Å the theoretical absorption level is systematically lower than the measured one. This is particularly obvious for the structure around 68 Å corresponding to the transitions of Al^{7+} and from 100 to 110 Å where Al^{4+} ions contribute to the absorption. These discrepancies may be attributed to the deviations of the ion populations from the Saha–Bolztmann statistics that have been reported in similar works [19,20].

This analysis of the Al spectra suggests that the equivalent temperature of 60 eV given by the Basko model can be an adequate estimate of the radiative flux heating the Al absorption foil. Taking into account the energy variations of the main beam, according to the Basko model, the equivalent temperatures of the heating flux are expected to be in the range of 55–60 eV for the different experimental shots.

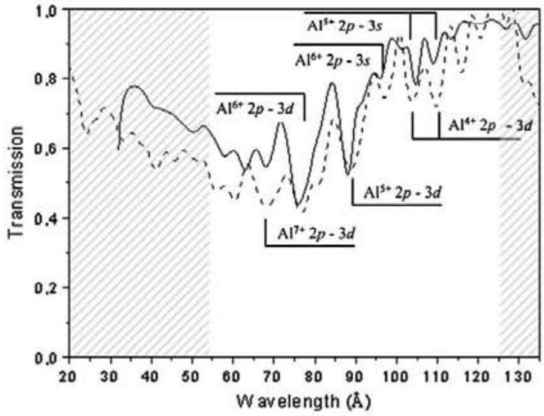

Fig. 5. Comparison of the experimental transmission (thin dashed line) with the averaged transmission calculated with HULLAC code (thick full line). The density and the electron temperature are calculated with MULTI. The time evolution gradients are included calculating separately the transmissions given by the spatial gradients distributions at three times and taking their average. (Reliable measured range is 55–125 Å.)

4. ZnS absorption spectra analysis

The ZnS transmission spectra were analyzed with SCO. First, SCO permitted the identification of the atomic transitions of the various zinc and sulfur observed ion species. Second, SCO was coupled as a post-processor of MULTI output to calculate the transmission spectra of the ZnS plasma taking into account its spatial distribution and its time evolution.

In Fig. 6 is presented the measured transmission spectrum of a 20 μg/cm^2 ZnS foil. The main beam flux on the conversion foil was 10^{14} W/cm^2 at 0.53 μm. In the spectral range between 55 and 120 Å we observed various absorption structures corresponding to the transitions of both zinc and sulfur ions. In particular, the 3d–4f transitions of Zn^{6+} and Zn^{7+} are dominant in the range 103–120 Å. The 3d–4f transitions of Zn^{8+} appear as two structures between 84–90 Å and 90–103 Å. At lower wavelengths 2p–3s transitions of the ions S^{5+}–S^{6+} have been identified as the narrow structure observed between 70 and 75 Å.

For the experimental conditions of Fig. 6, according to the Basko model, the radiative flux heating the ZnS foil corresponds to an equivalent Planckian radiation of 55 eV. Following the same procedure as for Al, the hydrodynamic simulation of ZnS was performed coupling directly the

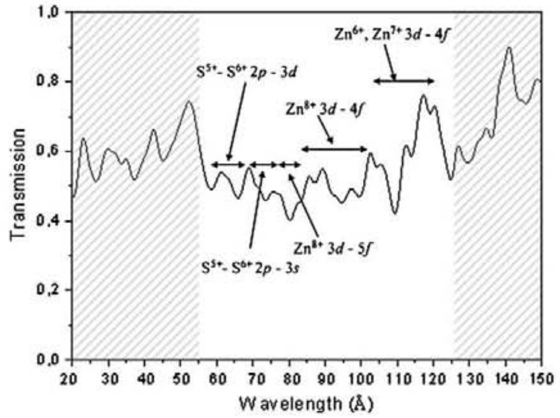

Fig. 6. Measured transmission spectra of a 20 μg/cm^2 ZnS foil, tamped with 8 μg/cm^2 carbon foils on both sides. Identification of the plasma ionic species and of the corresponding atomic transitions structures.

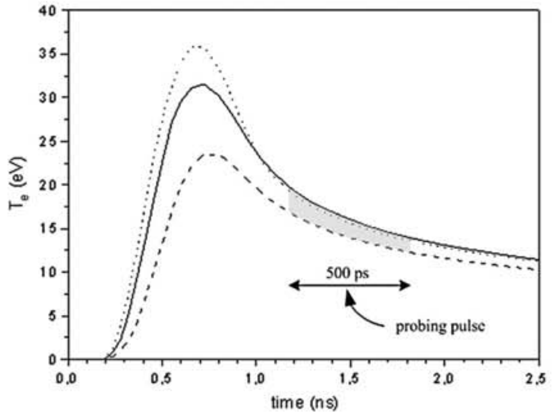

Fig. 7. Multi-simulation results of the temperature time evolution of 20 μg/cm^2 ZnS foil tamped with 8 μg/cm^2 carbon foils on both sides, at three interfaces covering the plasma spatial expansion. Dashed line: right carbon/ZnS interface. Full line: Interface at the center of ZnS. Dotted line: left carbon/ZnS interface.

radiation emitted at the back side of a gold foil, rather than using a Planckian driver.

The electron temperature time evolution of ZnS is given in Fig. 7. During the probing pulse, the temperature variation of each cell (ZnS center cell and C/ZnS interfaces) is about 5 eV. The electron temperature and the matter density as a function of the Lagrangian mass at three times corresponding to the rising half-maximum (1.2 ns), the maximum (1.4 ns) and the falling half-maximum (1.7 ns) of the probing pulse are given in Fig. 8. According to Fig. 8(a), the temperature spatial gradients are initially 17–20 eV at 1.2 ns and smooth out as time evolves to 14–16 eV at 1.4 ns and 13–14 eV at 1.7 ns. That is, MULTI predicts that the temperature gradients are mainly due to the time evolution. Further, in Fig. 8(b), the matter density presents a spatial variation of 4–5 mg/cm^3 at 1.2 ns, of 3–4 mg/cm^3 at 1.4 ns, and of 2.5–3 mg/cm^3 at 1.7 ns, respectively.

The results calculated by MULTI have been post-processed with SCO to determine the transmission as was done for Al case. As a first approximation, the calculations were performed using a constant matter density of 2.5 mg/cm^3 for ZnS and of 1 mg/cm^3 for carbon, respectively.

The theoretical results are compared to the measured transmission in Fig. 9, where good agreement between the two is found in the range 84–120 Å, corresponding to the 3d–4f transitions of Zn^{6+}–Zn^{8+}. However, there is a difference in the range 76–84 Å. In particular, the measured transmission has an absorption feature around 80 Å that does not appear in the theoretical transmission. Identification of supertransitions arrays with SCO shows that this feature could correspond to the Zn^{8+} 3d–5f transitions. For these conditions the theory seems to follow only the weak narrow structure in the range 84–90 Å, which correspond to the 3d–4f transitions of Zn^{8+}. For the absorption of the sulfur ions S^{5+}–S^{6+}, the theoretical transmission is in agreement with the narrow absorption feature of the 2p–3s transitions between 70 and 75 Å; however, a large deviation is observed in the absorption feature of the 2p–3d transitions in the range 58–70 Å.

We note that the ZnS matter density used for the calculations is a first approximation. Calculations with SCO showed that the zinc transmission spectrum is sensitive to the density. This dependence affects the absorption and could explain the observed deviations of the absolute value of the transmission. Further, and more interestingly, the matter density affects the shape of the transmission spectra, in particular as concerns the Zn^{8+} 3d–5f transitions. This needs further analysis. The deviation for sulfur around 60 Å is probably due to the lower experimental accuracy at low wavelengths. Further analysis using HULLAC is needed to clarify this situation for the transmission [21].

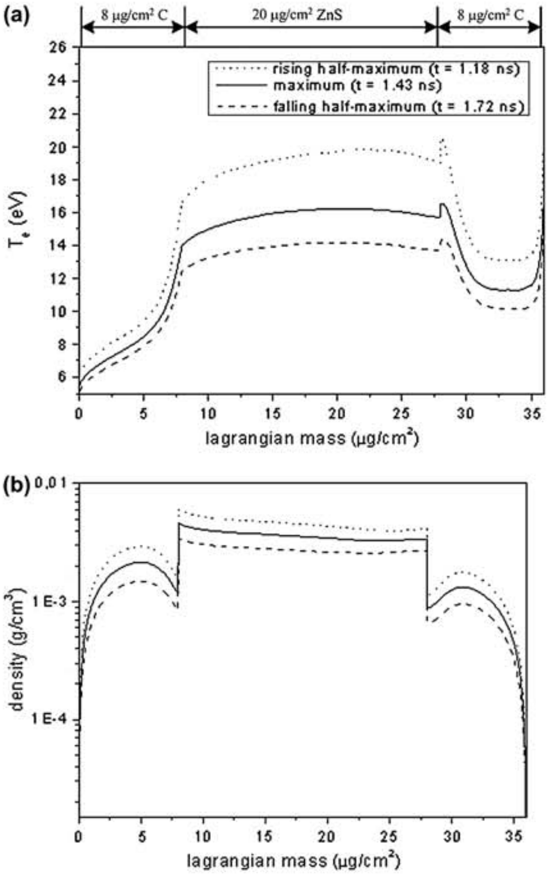

Fig. 8. Lagrangian representation of plasma hydrodynamic parameters. (a) Electron temperature and (b) density at the rising half-maximum (1.2 ns), at the maximum (1.4 ns) and at the falling half-maximum (1.7 ns) of the probing pulse.

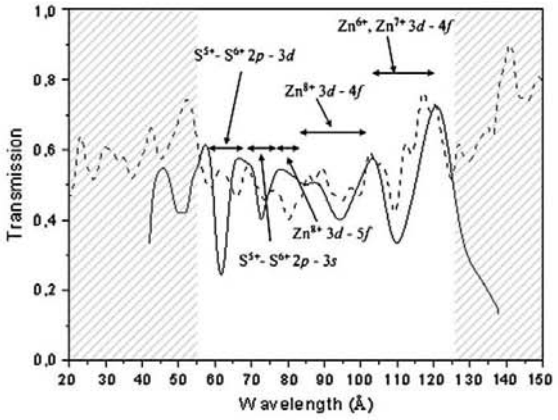

Fig. 9. Comparison of the experimental transmission (thin dashed line) with the averaged transmission calculated with the SCO code (thick full line). The density and the electron temperature are calculated with MULTI. The time evolution gradients are included calculating separately the transmissions given by the spatial gradients distributions at three times and taking their average. (Reliable measured range is 55–125 Å.)

5. Conclusions

The time resolved XUV absorption spectra of ZnS and Al foils heated by the thermal radiation of a gold cavity have been measured. Analysis of the Al absorption spectra with HULLAC post-processing the hydrodynamic output of MULTI, showed that the Planckian equivalent temperatures of the radiative flux heating the absorption foil was in the range of 55–60 eV. Based on this estimate of the cavity heating conditions, the ZnS foil hydrodynamic expansion was simulated with MULTI. The results were used by SCO to calculate the transmission spectra of ZnS. Comparison showed the dominance of the 3d–4f transitions of Zn^{6+} and Zn^{7+} ions. Also, spectral features corresponding to the 3d–4f and 3d–5f transitions of Zn^{8+} were identified. The deviations of the theoretical transmission in the range corresponding to Zn^{8+} 3d–5f transitions suggests a correlation between the matter density and the occurrence of the transitions, an interesting point which needs further exploration. For sulfur, the 2p–3s transitions of S^{5+}–S^{6+} ions have been identified. The observed deviation between experiment and theory in the range corresponding to the 2p–3d transitions will be further analyzed with the detailed code HULLAC.

Acknowledgements

The authors acknowledge the invaluable support of the LULI laser operations staff, in particular Marc Rabec-Le-Gloahec, Luc Martin and A. M. Sautivet. A special thank to the Max Planck Institute members, Klaus Eidmann and George Tsakiris for helpful discussions and assistance for the holraum targets definition. T. Blenski, M. Poirier and F. Thais acknowledge a partial support from EURATOM.

References

[1] D. Mihalas, Stellar Atmospheres, W.H. Freeman and Company, San Francisco, 1978.
[2] C. Chenais-Popovics, Laser Part. Beams 20 (2002) 291 (and references herein).
[3] S. Atzeni, J. Meyer-Ter-Vehn, The Physics of Inertial Fusion – Beam Plasma Interaction, Hydrodynamics, Hot Dense Matter, Oxford Science Publication, 2004.
[4] T. Blenski, A. Grimaldi, F. Perrot, Phys. Rev. E 55 (1997) R4889.
[5] T. Blenski, A. Grimaldi, F. Perrot, J. Quant. Spec. Radiat. Transfer 65 (2000) 91.
[6] A. Bar-Shalom, J. Oreg, W.H. Goldstein, D. Shvarts, A. Zigler, Phys. Rev. A 40 (1989) 3183.
[7] J.C. Pain, T. Blenski, J. Quant. Spec. Radiat. Transfer 8 (2003) 355.
[8] G. Winhart, K. Eidmann, C.A. Iglesias, A. Bar-Shalom, Phys. Rev. E 53 (1996) 1332.
[9] A. Bar-Shalom, M. Klapisch, J. Oreg, J. Quant. Spec. Radiat. Transfer 71 (2001) 169.
[10] M. Klapisch, J.L. Schwob, B.S. Fraenkel, J. Oreg, J. Opt. Soc. Am. 67 (1977) 148.
[11] F. Thais, S. Bastiani, T. Blenski, C. Chenais-Popovics, K. Eidmann, W. Fölsner, J.-C. Gauthier, F. Gilleron, M. Poirier, J. Quant. Spec. Radiat. Transfer 81 (2003) 473.
[12] R. Ramis, R. Schmalz, J. Meyer-Ter-Vehn, Comput. Phys. Commun. 49 (1988) 475.
[13] J. Bauche, C. Bauche-Arnoult, M. Klapisch, Adv. Atom. Mol. Phys. 23 (1988) 131.
[14] M. Basko, Phys. Plasmas 3 (1996) 4148.
[15] NIST Atomic Spectra Database.<http://physics.nist.gov/PhysRefData/ASD/index.html> (2006).
[16] R. Pakula, R. Sigel, Phys. Fluids 28 (1985) 232.
[17] R. Sigel, R. Pakula, S. Sakabe, G.D. Tsakiris, Phys. Rev. A 38 (1988) 5779.
[18] G.D. Tsakiris, Phys. Fluids B 4 (1992) 992.
[19] F. Gilleron, H. Merdji, M. Fajardo, O. Henrot, J.C. Gauthier, C. Chenais-Popovics, W. Fölsner, K. Eidmann, J. Quant. Spec. Radiat. Transfer 69 (2001) 217.
[20] F. Gilleron, Étude du transfert radiatif et de l'opacité d'un plasma créé par rayonnement X, thesis École Polytechnique, 2000.
[21] C. Chenais-Popovics, M. Fajardo, F. Gilleron, U. Teubner, J.C. Gauthier, C. Bauche-Arnoult, A. Bachelier, J. Bauche, T. Blenski, F. Thais, F. Perrot, A. Benuzzi, S. Turk-Chieze, J.P. Chieze, F. Dorchies, U. Andiel, W. Foelsner, K. Eidmann, Phys. Rev. E 65 (2001) 016413.